The aerodynamic effects of the cornering flow conditions

Author:
Keogh, James

Publication Date:
2016

DOI:
https://doi.org/10.26190/unsworks/19191

The Aerodynamic Effects of the Cornering Flow Conditions

James Keogh

A thesis submitted in fulfilment of the requirements
for the degree of Doctor of Philosophy

UNSW Australia

School of Mechanical and Manufacturing Engineering
Faculty of Engineering

July 2016

THE UNIVERSITY OF NEW SOUTH WALES
Thesis/Dissertation Sheet

Surname or Family name: Keogh

First name: James Other name/s: Michael

Abbreviation for degree: PhD

School: Mechanical and Manufacturing Engineering Faculty: Engineering

Title: The Aerodynamic Effects of the Cornering Flow Conditions

Cornering is a commonly-encountered condition for vehicles, yet one where the aerodynamic implications are not well understood. The curved path results in relative curvature of the freestream flow, causing a continuous change in the angle of yaw along the length and across the width of a vehicle. As this motion occurs within a rotating reference frame a radially orientated centrifugal acceleration acts on the flow at the surface, in addition to a freestream velocity which varies according to the radial displacement.

Flow around a reference automotive bluff body was analysed using Large Eddy Simulations to gain insight into the flow effects attributed to this condition. The yawed condition was initially investigated to gain an understanding of the geometry's sensitivity to flow angle. In this condition the formation of longitudinal vortices due to the oncoming flow angle promoted attached flow and resulted in vortex-induced lift. A side force and an increase in aerodynamic drag also occurred due to an increased frontal area and angled orientation of the wake.

Within the steady-state constant-radius cornering condition, cumulative effects resulted in the flowfield differing from the yawed condition. Acceleration due to the rotating reference frame caused a radially orientated pressure gradient which induced an external side-force directed toward the centre of the corner. The change in flow angle along the length of the bluff body resulted in a yawing moment which acted in a direction that would oppose the yaw rotation within a corner. A contraction of the wake separation bubble caused an increase in aerodynamic drag and an increase in magnitude of the periodic wake bursting mechanism. The bluff body geometry also demonstrated a heightened yaw sensitivity within the cornering condition. Force coefficient changes occurred that were up to three times the magnitude of those for different yaw angles in straight flow.

Finally a new experimental method was developed for the cornering condition, with a proof of concept constructed and an initial experimental analysis conducted. Through conceiving a design that continuously delivered flow to a rotating test-section, the correct relative curvature was able to be achieved within a rotating reference frame.

FOR OFFICE USE ONLY Date of completion of requirements for Award:

THIS SHEET IS TO BE GLUED TO THE INSIDE FRONT COVER OF THE THESIS

COPYRIGHT STATEMENT

Signed …….....

Date 29/03/16 …….....

AUTHENTICITY STATEMENT

Si…….....

Date 29/03/16 …….....

ORIGINALITY STATEMENT

'I hereby declare that this submission is my own work and to the best of my knowledge it contains no materials previously published or written by another person, or substantial proportions of material which have been accepted for the award of any other degree or diploma at UNSW or any other educational institution, except where due acknowledgement is made in the thesis. Any contribution made to the research by others, with whom I have worked at UNSW or elsewhere, is explicitly acknowledged in the thesis. I also declare that the intellectual content of this thesis is the product of my own work, except to the extent that assistance from others in the project's design and conception or in style, presentation and linguistic expression is acknowledged.'

Signed

Date 24/10/16

UNSW AUSTRALIA

Abstract

Doctor of Philosophy

The Aerodynamic Effects of the Cornering Flow Conditions

by James Keogh

Cornering is a commonly-encountered condition for vehicles, yet one where the aerodynamic implications are not well understood. The curved path results in relative curvature of the freestream flow, causing a continuous change in the angle of yaw along the length and across the width of a vehicle. As this motion occurs within a rotating reference frame a radially orientated centrifugal acceleration acts on the flow at the surface, in addition to a freestream velocity which varies according to the radial displacement.

Flow around a reference automotive bluff body was analysed using Large Eddy Simulations to gain insight into the flow effects attributed to this condition. The yawed condition was initially investigated to gain an understanding of the geometry's sensitivity to flow angle. In this condition the formation of longitudinal vortices due to the oncoming flow angle promoted attached flow and resulted in vortex-induced lift. A side force and an increase in aerodynamic drag also occurred due to an increased frontal area and angled orientation of the wake.

Within the steady-state constant-radius cornering condition, cumulative effects resulted in the flowfield differing from the yawed condition. Acceleration due to the rotating reference frame caused a radially orientated pressure gradient which induced an external side-force directed toward the centre of the corner. The change in flow angle along the length of the bluff body resulted in a yawing moment which acted in a direction that would oppose the yaw rotation within a corner. A contraction of the wake separation bubble caused an increase in aerodynamic drag and an increase in magnitude of the periodic wake bursting mechanism. The bluff body geometry also demonstrated a heightened yaw sensitivity within the cornering condition. Force coefficient changes occurred that were up to three times the magnitude of those for different yaw angles in straight flow.

Finally a new experimental method was developed for the cornering condition, with a proof of concept constructed and an initial experimental analysis conducted. Through conceiving a design that continuously delivered flow to a rotating test-section, the correct relative curvature was able to be achieved within a rotating reference frame.

Acknowledgements

I would firstly like to acknowledge the guidance and technical assistance provided by my project supervisors, Assoc. Prof. Tracie Barber, Asst. Prof. Graham Doig, and Dr Sammy Diasinos. I greatly appreciate all your time and effort. I was particularly fortunate to have three supervisors who all remained very actively involved throughout my candidature and were always there to provide me with valuable feedback. I would also like to thank you all for continuing to support me as I commenced full-time work in a different country, even with a thesis still needing to be submitted.

I would like to thank the technical staff at the university for their help with the experimental component of this project. Particularly Dr Zebb Prime whose expertise with instrumentation was highly valuable. The amount and quality of the results would not have been the same without his contribution.

I have been fortunate to also have the support of several fellow research students, particularly Dave Fulker, Reza Keshavarzi, Kyll Schomberg, and Kyle Forster. Special mention has to go to Kyle Forster, who selflessly donated large amounts of his time to provide help with the experimental component of this project (this willingness correlated very closely with the associated risk of the activity). His ideas and endless engineering knowledge were always valuable.

I would like to thank my family for their support of everything I do, and their willingness to assist me in any way they can. Circumstantially my parents endured an extended period where their house became temporary storage for partially-completed wind tunnel components, for which I offer my apologies.

Finally I must thank Yolanda Nijmeijer for her support and enduring my constant complaints. Your encouragement and the faith you have in my abilities always helps give me the courage to pursue my ideas — even when they are a little bit unconventional.

Related Publications

Keogh J, Barber T, Diasinos S, and Doig G *The Aerodynamic Effects on a Cornering Ahmed Body*, Journal of Wind Engineering and Industrial Aerodynamics, 154, pp. 34-46, 2016

Keogh J, Barber T, Diasinos S, and Doig G, *A New Type of Wind Tunnel for the Evaluation of Curved Motion*, AIAA Scitech, January 2016

Keogh J, Barber T, Diasinos S, and Doig G, *Techniques for Aerodynamic Analysis of Cornering Vehicles*, No. 2015-01-0022. SAE Technical Paper, 2015.

Keogh J, Doig G, Diasinos S, and Barber T, *Detached Eddy Simulation of the Cornering Aerodynamics of the Ahmed Reference Model*, FISITA World Automotive Conference, Maastricht, the Netherlands, June 2014

Keogh J, Doig G, Diasinos S, and Barber T, *The influence of cornering on the vortical wake structures of an inverted wing*, Proceedings of the Institution of Mechanical Engineers, Part D: Journal of Automobile Engineering (2015): 0954407015571673

Keogh J, Doig G, Barber T, and Diasinos S, *The Aerodynamics of a Cornering Inverted Wing in Ground Effect*, Applied Mechanics and Materials, 553, pp. 205-210, 2014

Contents

List of Figures

List of Tables

Symbols

a_c	centripetal acceleration	ms^{-2}
A	area	m^2
A_{ref}	reference area of Ahmed body = 0.112032	m^2
C_D	coefficient of drag	
C_{Fx}	coefficient of force in the x-direction	
C_f	coefficient of skin friction	
C_L	coefficient of lift	
$C_{M\psi}$	yawing moment coefficient, measured about the point (-0.5,0,0)	
$C_{M\theta}$	pitching moment coefficient, measured about the point (-0.5,0,0)	
$C_{M\phi}$	rolling moment coefficient, measured about the point (-0.5,0,0)	
C_P	coefficient of static pressure	
C_S	coefficient of side force	
COR	centre of rotation	
E	voltage	V
H	height	m
I	turbulence intensity	%
k	turbulent kinetic energy	$\mathrm{m}^2\mathrm{s}^{-2}$
L	length of Ahmed body = 1.044	m
p	static pressure	Pa
P_{abs}	absolute pressure	Pa
q	dynamic pressure	Pa
R	radius	m
R^2	coefficient of determination	
RSS	root-sum-square	
Str	strouhal number = $\frac{fH}{U_\infty}$	
t	time	s
T_0	calibration temperature	K
T_a	ambient temperature	K
T_w	hot-wire temperature	K

u_a	absolute velocity	ms^{-1}
u_r	relative velocity	ms^{-1}
U_∞	freestream velocity	ms^{-1}
$U_{\infty,m}$	mean freestream velocity	ms^{-1}
U_{RMSD}	velocity root-mean-square derivative	ms^{-1}
u	x-velocity	ms^{-1}
v	y-velocity	ms^{-1}
w	z-velocity	ms^{-1}
x	cartesian rectilinear co-ordinate directed positive from front to rear	m
$x*$	cartesian rectilinear co-ordinate directed positive down the backlight surface	m
y	cartesian rectilinear co-ordinate directed positive from left to right	m
z	cartesian rectilinear co-ordinate directed positive vertically up	m
β	linear least-squares fit	
Γ_A	normalised circulation strength	
δ	thickness	m
Δ	difference	m
θ	angular cylindrical co-ordinate	$^\circ$
κ	curvature	m^{-1}
ρ	density	kgm^{-3}
σ	standard deviation	
ψ	angle of yaw	$^\circ$
ω	angular velocity	rads^{-1}
Ω_n	normal vorticity	s^{-1}
Ω_x	x-vorticity	s^{-1}
Ω_y	y-vorticity	s^{-1}
Ω_z	z-vorticity	s^{-1}

Chapter 1

Introduction

The phenomena which affect the motion of a bluff body through a fluid can be deceptively complex, and remain a topic of both practical and academic interest. An improved understanding of these factors will continue to have implications for engineering design in a wide range of industrial applications. In the automotive industry the expense of energy and an increasing environmental awareness has resulted in the average consumer carefully considering the efficiency of their potential new vehicle before making a purchase. At highway cruising speeds, aerodynamic drag can be the most significant component of the overall resistance the motor needs to overcome, so small gains in aerodynamic efficiency can have a large impact. This has led manufacturers to now regularly publish aerodynamic drag figures with the release of their latest models. Aesthetics still is the dominant consideration in consumer decision-making, but investing heavily in aerodynamic design is now a common feature of the automotive industry, and no longer restricted to high performance vehicles and motorsport.

Low aerodynamic drag is a desirable trait for almost any vehicle, but it is not the only important aerodynamic quality, and optimising the external design to the nearest millimetre in the low turbulence, steady-flow of a wind tunnel does not reflect the real environment a vehicle will be exposed to. The roads are not all straight, the air is rarely perfectly still, and the turbulence intensity is often much higher [1]. Vehicles also interact with each other through the disturbances they create in the air, which can cause vehicle proximity to have a significant influence [2]. Aerodynamic characteristics can also be desirable from a safety perspective, or used to improve dynamic capabilities.

Cornering is a condition that introduces a unique combination of changes to the freestream flow conditions experienced by motor vehicles. Only a few recent studies have investigated the aerodynamic effects of the cornering condition [3–5], and none have yet presented a detailed explanation of the associated flow phenomena within this condition.

For some vehicles aerodynamic performance through corners will be more critical than performance in a straight-line. Circuit-based racing cars, hill-climb racing cars and a wide variety of modern performance vehicles are aerodynamically designed to produce downforce which compromises straight-line speed in order to allow large gains to be made in the corners through increased levels of grip [6–8]. The cornering condition can result in flow conditions that significantly differ from the straight-line condition and is thus an area of industrial relevance that is yet to receive thorough investigation.

1.1 The Dynamics of Cornering

Before investigating the aerodynamics of cornering it is first necessary to have an understanding of how a vehicle travels through a corner. For any vehicle the only contact between the vehicle and the road surface is where the tyres meet the road. This area between the deformed pneumatic tyre and road surface is referred to as the print [9], and the interaction between the vehicle and the road at this location defines the motion of the vehicle.

Acceleration is most commonly associated with the force that pushes the passenger back in the seat when the straight-line speed is increased, but acceleration also occurs when travelling in a corner. The magnitude of this acceleration is proportional to the instantaneous radius R the vehicle is turning through and the tangential velocity, or angular velocity, about that location. The lateral load then becomes a function of both the vehicle mass, and the lateral acceleration.

As a result of this acceleration the print of the tyre will deform due to the lateral force. This deformation will be further dependent on all moments and forces acting on the vehicle as well as the properties of the tyre. Due to the point of contact being deformed, the tyre no longer assumes a path aligned with its longitudinal axis. The trailing edge of the print, which is under lower vertical load, will begin to slip over the road surface, while the front portion will deform and retain contact, as is shown in Fig. 1.1. The deviation of the tyre's path from its longitudinal axis is referred to as the slip angle. As the lateral force increases, so will the slip angle, however there will also be a gradual increase in the amount of the print that is sliding over the road surface. Eventually the maximum lateral load that can be sustained will be reached and breakaway occurs with the tyre completely sliding across the road surface.

Racing cars use the beneficial effects of aerodynamic downforce, or increased vertical load, to increase the lateral force that a tyre can sustain. The increased vertical load due to downforce can occur in the absence of additional lateral force, as the vehicle mass

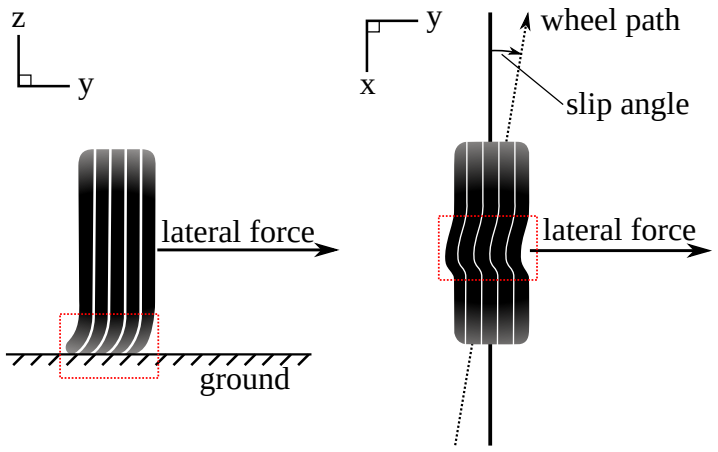

FIGURE 1.1: Diagram of tyre deformation resulting in a slip angle within the cornering condition

does not increase. The result is that higher cornering speeds can be achieved, typically permitting an overall decreased lap time around a circuit [6, 7, 9, 10].

A bicycle model is a simple way of considering a vehicle in the cornering condition. Instead of including all four tyres, the front and rear are approximated as a single tyre each. The front tyre path is defined by the steering angle minus the slip angle, whereas the rear tyre path is defined according to the slip angle only (in the absence of any rear wheel steering). The front is where the driver interacts with the vehicle and controls its path through a corner, so the attitude of the car through the corner is defined based on rear slip angle. From the rear slip angle the vehicle slip angle can be calculated at the intersection of the vehicle's roll axis with its centre of mass (defined as the origin of the vehicle's motion).

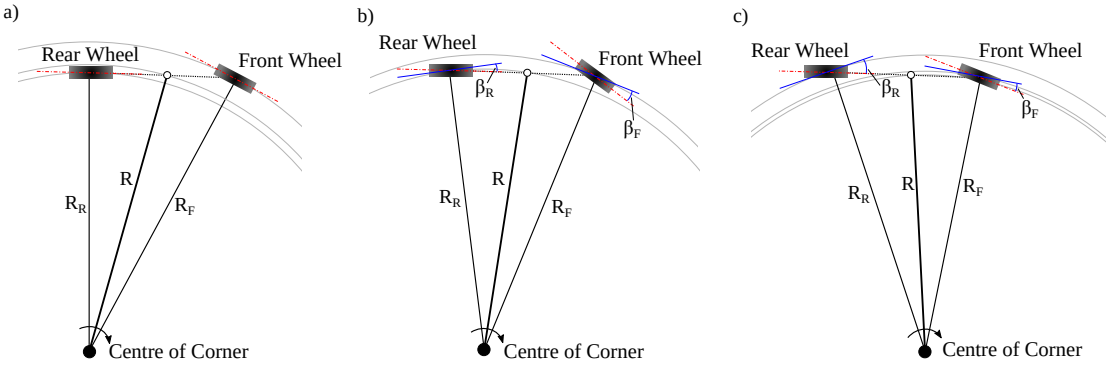

FIGURE 1.2: Bicycle model diagram demonstrating the dynamic effect of cornering: a) Negligible lateral force, b) larger rear-slip angle, c) smaller rear slip angle

For very low-speed corners the rear slip angle approaches zero due to a negligible lateral force, and results in the type of motion shown in Fig. 1.2a). As the velocity of the

vehicle increases through a corner, or the corner radius decreases while maintained the same tangential velocity, the lateral load increases and so does the rear slip angle. This will result in motion bearing greater similarity to Fig. 1.2b) or c). As vehicle speeds increase, aerodynamic effects also become more influential.

Different vehicle configurations will also affect the angle of a vehicle through a corner. Neutral steer is a configuration under which, as the lateral force increases, the rate of change of the front slip angle will equal that of the rear. Most passenger vehicles, and even racing cars, will favour a set-up that tends towards understeer, where the rate of change of the front slip angle exceeds that of the rear slip angle.

Typical slip angles will vary greatly between different types of tyres as well as road surfaces. Racing tyre data presented in Milliken and Milliken [9] indicate maximum slip angles in the range of 6 degrees. Some tyres on passenger vehicles can exceed these slip angles however these vehicles are far less likely to be driven to the point where they are on this limit.

While this only serves as an introduction to a complex topic, it is necessary to consider these parameters to ensure the aerodynamic modelling of the vehicle through a corner is representative of the scenario in reality. The dynamic characteristics will differ between vehicles, and must be evaluated for each case before undertaking a specific analysis of any vehicle.

1.2 The Cornering Flow Conditions

Under ideal, still conditions, a car travelling through a corner assumes a curved path through stationary air. Considered in the reference frame of the vehicle, curved airflow is observed to pass over the car. This flow observed from the reference frame of the vehicle is shown in 1.3. The most fundamental type of curved motion is that of a constant radius arc. This instantaneous flowfield can be described as an angular velocity about a fixed external point, located at the centre of the corner. The tangential velocity at any location is:

$$U_\infty = \omega R \tag{1.1}$$

Where R is the distance from the centre of rotation.

Regarding the vehicle as a rigid body, the tangential velocity becomes linearly proportional to the radius — and as a result the velocity of the oncoming flow passing over the vehicle is no longer constant. The outer side of the vehicle, referred to as the outboard side, is in a local region of higher relative flow velocity, and the inboard side is in a

local region of lower velocity. This results in the relative total pressure increasing with radius, and thus the available relative energy in the flow from the vehicle's reference frame. Within this frame the vehicle will also perceive a centrifugal acceleration which will similarly vary according to radius, being greatest at the furthest outboard location.

It can be observed in Fig. 1.3 that the front and rear of the vehicle may be positioned at radii which are greater or lesser than the centre — as a rigid body the front, rear and centre can never follow the same radius. For tighter radii corners, these changes become proportionally greater, and the cornering-specific effects are more apparent.

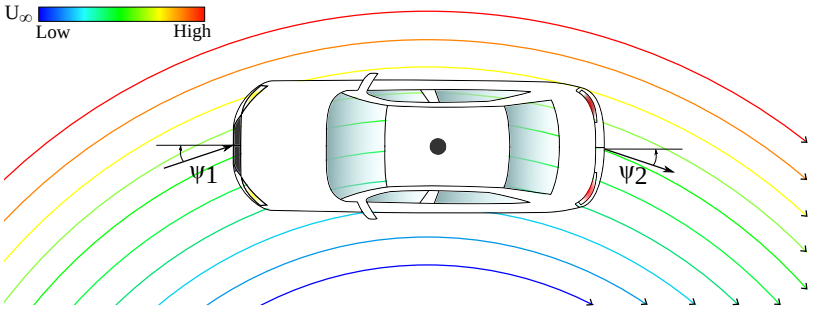

FIGURE 1.3: The steady-state cornering flow conditions

In addition to the change in velocity of the flow, the curvature of the flow is inversely proportional to the radius at any given location:

$$\kappa = \frac{1}{R} \tag{1.2}$$

This means that for regions of proportionally decreased velocity, there is increased flow curvature.

The angle at which the flow approaches and leaves the body is effectively an angle of yaw. By definition the greater the flow curvature, the greater the change in yaw angle both along and across the width of any body. Thus the shape of the body becomes influential in the aerodynamic changes that occur in cornering. This becomes readily observable for the geometries shown in Fig. 1.4. The blade of a wind turbine would be an example of a body that would experience a very large change in local freestream velocity from root to tip, whereas a submarine travelling through a corner would experience a very large flow angle change from front to rear, with a less significant change in freestream velocity. However a wind turbine will use a blade profile which accommodates its rotary motion, while automobiles or submarines are designed for the straight-line conditions in which they more commonly operate.

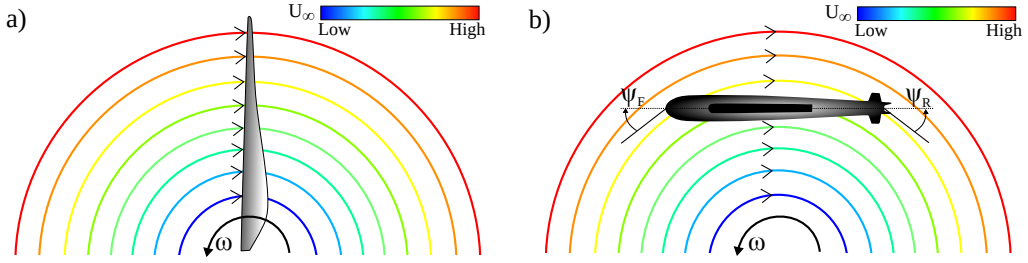

FIGURE 1.4: The influence of geometric shape on the aerodynamic characteristics in a curved flowfield

1.2.1 Cornering Aerodynamics

Analysis of the aerodynamic performance of a vehicle is typically conducted through a combination of computational modelling and wind tunnel testing, with these results generally supplemented by some on-road data. A holistic understanding of the true aerodynamic performance of any geometry requires the consideration of the range of conditions a vehicle will be exposed to in the real world, including cornering. Motorsport is a specific example where the aerodynamic performance of a vehicle can become most critical in the cornering condition. In this application performance gains are achieved through the addition of aerodynamic devices which, in turn, results in the higher cornering speeds [7].

The cornering condition has been a topic of investigation in applications pertaining to passenger vehicles in addition to motorsport. A two-part study by Okada et. al [3] and Tsubokura et. al [4], investigated two variants of a simple passenger car geometry on-road and numerically to examine the aerodynamic, and resultant dynamic, effects experienced during sinusoidal motion and high speed cornering. For on-road analysis flow measurements were taken using surface static pressure disk probes, with total pressure also measured in the front wheel wake. The difficulties associated with gaining meaningful results using this method on the driving vehicle were acknowledged, and all on-road forces were reported as estimates based on integration of the surface pressure measurements, which were calibrated using wind tunnel data of the vehicle in the yawed condition. The two vehicle geometries used in the studies differed in the amount of open space around the wheel in the wheel well, the A-pillar shape, undertray geometry, and side-skirt profile, as shown in Fig. 1.5.

A yawing moment was identified to occur within the cornering condition which was directed against the yaw rotation of the vehicle, resulting in an aerodynamic damping effect. However, the small geometric differences between the two vehicles were enough to cause a maximum 49% change in this yawing moment. Supplementary Large Eddy

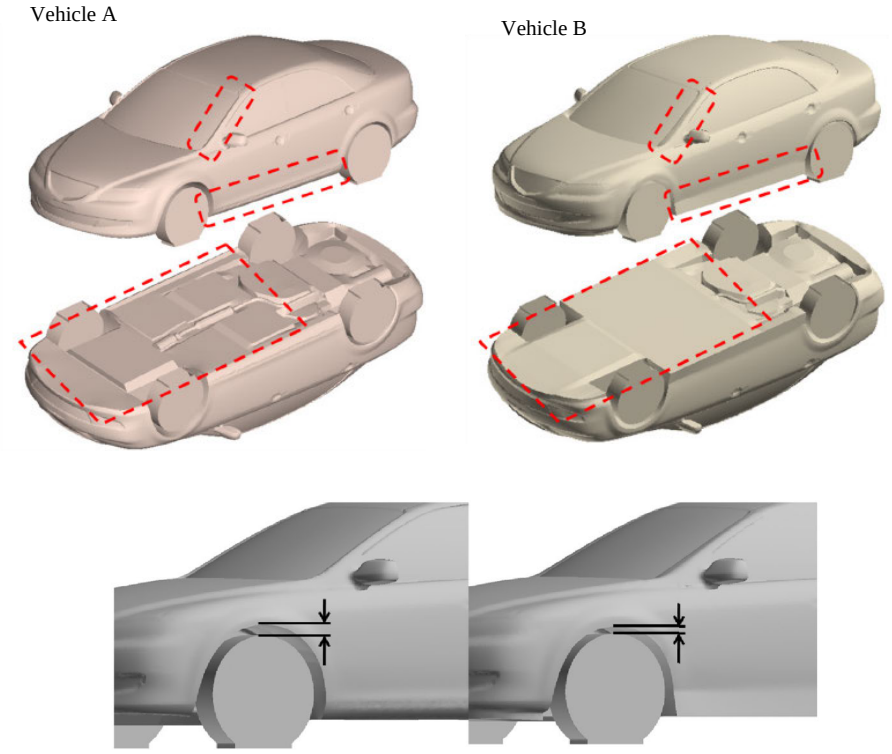

FIGURE 1.5: The two vehicle geometries used by Tsubokura et. al [4] for analysis of the high-speed cornering condition and sinusoidal motion, indicating the locations of geometric differences. *Reprinted with permission from SAE International.*

Simulation (LES) results identified a stronger inboard vortex to be generated within the wheel well for vehicle A which enhanced this moment. Their analysis also revealed varied temporal response during sinusoidal motion.

The primary shortcoming of this study was the authors' neglect to relate any of the results to a cornering-specific parameter. Thus the effect of the flowfield curvature and the change in angle along the length of the body was not addressed, nor any implications of the rotating non-inertial reference frame. Results were curiously ascribed to only an average instantaneous yaw angle as opposed to the cornering condition, and limited the ability to draw conclusions.

A computational analysis of an open wheeled racing car during cornering motion was conducted by Nara et. al [5]. Three sections of track from the Fuji Speed Way Circuit were selected and used to plot paths for the vehicle's motion. The simulations included the deceleration and acceleration of the vehicle in addition to the multiple variable curvatures within each of these sections. Results focussed on the variation in negative lift and side force during the different paths simulated, with an absence of discussion regarding the flow structures. They identified the side force to vary most significantly

through the track sections, while the downforce was more affected in the low-speed tight-radius corners. Similar to the analysis of Tsubokura et. al [4] these results were related to vehicle slip angle (as a representative measure of yaw) as opposed to any cornering parameters.

In a further study relating to motorsport, an isolated inverted wing travelling in the path of a corner was considered by Keogh et. al [11]. The work identified significant changes to the structure of the vortical wake during cornering and highlighted potentially detrimental aerodynamic effects due to the dependence of such vehicles on vortex-induced suction. A local Reynolds number increase across the span resulted in an uneven aerodynamic loading and caused a rolling moment which increased the outboard load, while the angle of the flow at the endplates resulted in a side force and yawing moment.

The curved motion of the flow relative to a vehicle necessitates a departure from the conventional methodology for numerical models. The vehicle must be in a rotating non-inertial reference frame to create the correct relative freestream dynamic pressure gradient in the absence of a static pressure gradient, in addition to the acceleration. The boundary conditions and computational modelling techniques used to achieve this have differed amongst previous investigations.

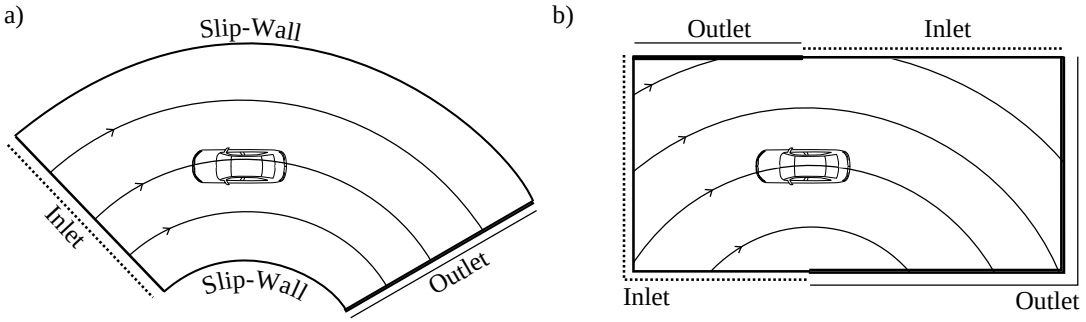

FIGURE 1.6: The different numerical domain configurations used for cornering simulation: a) the curved domain, b) the rectangular domain

Tsubokura et. al [4] used a rectangular computational domain, with variable inlet and outlet conditions along the walls, as is shown in Fig. 1.6b). Nara et. al [5] used the same technique with the addition of the Arbitrary Langrangian-Eulerian (ALE) method for the boundary conditions. With the ALE method the inlet and outlet conditions were continually modified to enable the modelling of a vehicle's motion over the path of a race-track. While Van Djick [12] alternatively favoured the use of a curved domain for a motorcycle aerodynamic analysis, as is shown in Fig. 1.6a). In this method the domain was curved to match the path of the flow, instead of modifying type of boundary conditions in order to accommodate the flow path.

The difficulty in experimentally analysing the cornering condition (discussed in Section 1.3), has led to the use of approximate methods [6]. Of these methods, placing a wind tunnel model at an angle of yaw is the most commonly utilised and is occasionally incorrectly believed to be equivalent. Such an example was the study by Albukrek et. al [13] which investigated the performance of an open-wheeled racing car through (what was stated as) a corner. In this instance the employed methodology assumed the cornering flow conditions to be equivalent to the vehicle being placed in the yawed condition, at a yaw angle equal to the chassis slip angle, and thus neglected the true curved path of cornering. Johansson and Katz [14] also used yaw as an experimental estimation of the cornering condition in a wind tunnel, for the analysis of a sprint car. It must be noted that the equivalence of yaw and cornering was not suggested, and the specific vehicle type for which this was conducted will operate at very high slip angles within corners — making the adoption of this methodology an understandable compromise. However the assumption that analysing a vehicle in yaw is a method for approximating of the aerodynamic effects experienced during cornering (in the absence of a known, published quantitative comparison) highlights the importance of not only an investigation into the true cornering condition, but also the need to compare and contrast these results with the yawed condition.

1.3 Experimental methods for analysis in curved flow

An accurate experimental technique for cornering must create the following conditions:

- Flow curvature relative to the model
- A relative velocity gradient which is proportional to the radius
- Centrifugal acceleration in the reference frame of the model
- Constant freestream static pressure
- Continuous and repeatable conditions
- Achieve the correct flow conditions in close proximity to a surface representing the ground

Currently, to the best knowledge of the author, there is no existing experimental facility that can meet all these requirements [6]. The ability to analyse the condition on a track or road has always been possible, but the variability of real-world conditions, and the restricted amount of data that can be obtained from an actual vehicle [3], have both been limitations associated with this approach.

The lack of previous investigation can be partially attributed to the wind tunnel remaining the primary tool for experimental aerodynamic analysis. Wind tunnels were initially designed for testing aircraft in free-flight, rather than vehicles in close ground proximity. The automotive industry initially adopted aerodynamic testing techniques directly from the aeronautical industry, and it has taken time for the technology to evolve to meet their specific needs. Testing and simulation can now correlate more closely to on-road performance and there is a large number of dedicated automotive facilities.

The present work sought to investigate the feasibility of a solution that could offer the cornering flow conditions within a controlled experimental environment. As such, it was first necessary to review the existing experimental facilities and techniques that are capable of reproducing similar flow conditions.

1.3.1 Dynamic Track

One solution could be to create a track with curved sections within a controlled environment. Facilities are in operation which use abandoned rail tunnels for straight-line aerodynamic testing of vehicles [15]. Flow measurement is restricted compared to what can be achieved in a wind tunnel, however it is foreseeable that such an experiment could be designed to permit the same analysis with the inclusion of corners. A limitation would be that this would likely necessitate the construction of a completely new facility rather than modification of existing infrastructure, which would come at a greater expense.

The Princeton Dynamic Model track was a unique experimental design created for testing dynamic stability parameters of aircraft [16] and used a similar principle. A carriage was accelerated along rails with servomechanisms used for the lateral motions, a simple diagram of which is shown in Fig. 1.7. The facility was housed in a building 229 m long, and had effective test-section cross-sectional dimensions of 10.66×9.14 m. Using this method a 0.6g lateral acceleration could be achieved (and allowed the analysis of curved paths) however the speed was limited to 12.19 m/s. The facility was primarily utilised for rotorcraft studies with the model advancing at low speeds [17]. Adapting such a concept for automotive applications would not require a cross-sectional area quite so large, but would inevitably require a large amount of space and would need to be able to operate at higher speeds to achieve representative Reynolds numbers at a feasible model scale.

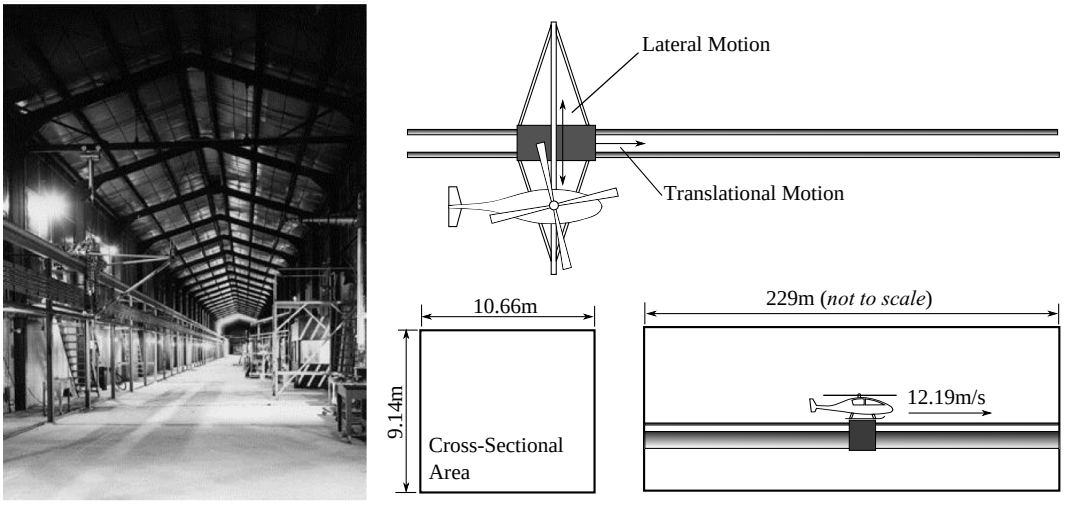

FIGURE 1.7: A simplified schematic of the Princeton Dynamic Model Track [16]

1.3.2 Curved test section

A curved test section is an example of a previous method that has been used to force curved flow over a model. In 1939 the Langley Research Centre built a wind tunnel designed to be capable of testing an aircraft in rolling, pitching and yawing. The Langley Stability Tunnel used interchangeable test-sections, one of which was capable of curving the walls [18], as is shown in Fig. 1.8.

FIGURE 1.8: A view inside the Langley Stability Tunnel curved test section

Forcing flow to follow the shape of a curved test-section ultimately compromises the flow quality due to the centrifugal force. In this condition the flow is accelerated due

to its curved path, whereas in reality the model itself is under acceleration. A large body of work exists for flows in curved ducts [19] and when a fluid travels in a curved path, the centrifugal force will be balanced by a radial static pressure gradient [20]. In a stationary duct the outer duct surface is a concavity which experiences an increase in pressure, while the inner convex surface experiences a decrease in pressure. This effect occurs for both laminar and turbulent flow [21, 22]. An imbalance between these has been identified to result in secondary flow feature formation due to induced cross-flow — an undesirable consequence when seeking to achieve uniform flow for an experimental facility.

Furthermore, through a curved test-section the natural velocity profile for constant total pressure is the opposite of what occurs during cornering. The inner radius is accelerated due to the convex shape and the outer radius is decelerated due to the concavity. These effects increase in severity as the radius of curvature is decreased, leading to flow conditions which are most compromised for small radii corners.

To correct the variable velocity profile within a curved tunnel the NASA stability tunnel used non-uniform screens consisting of vertical wires to provide the necessary asymmetric total pressure loss across the width of the test section. This method was based on the principle that a mesh screen will result in a pressure loss approximately proportional to the square of the flow speed [23]. In a typical wind tunnel this makes such screens very effective in smoothing non-uniformities where a local region of high velocity will experience a proportionally higher loss, while a low velocity region experiences a smaller loss [24]. However, this effect is based on the assumption of uniform screens. Thus the non-uniform screen intentionally created a non-uniform dynamic loss to correct the velocity distribution to be representative of what occurs in the cornering condition, as shown in Fig. 1.9. This required the use of different non-uniform screens for the different curvatures of the test section to accommodate the change in velocity profile.

Chambers et. al [25] presented results that demonstrated the velocity distribution compared favourably to the theoretically correct value at the centre of the test section, but they noted it was compromised both upstream and downstream. They measured a low static pressure along the inner wall of the test-section, and a high pressure region along the outer wall. The static pressure exhibited a linear change across the width of the test section, and the variation from inside to outside was equal to a pressure coefficient of four, presumed to be for the smallest radius corner but not specifically stated.

Bird et. al [26] used the facility to investigate curved flow effects on a swept wing aircraft model. The authors noted the dissimilarity of the condition to the true condition and discussed the effect of the static pressure gradient. This gradient exerted a side-force acting on the model directed towards the centre of the corner, and drew the boundary

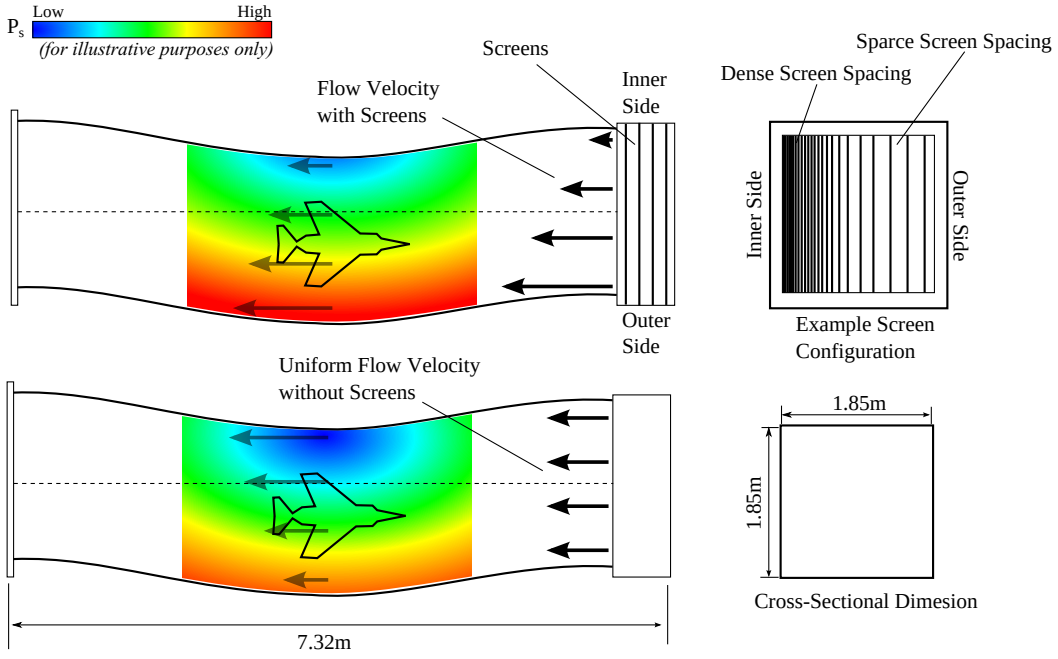

FIGURE 1.9: The effect of the non-uniform screens used in the Langley Stability Tunnel, based on Chambers et. al [25]

layer across the model surface. The authors noted they would expect the exact opposite to occur in the true condition due to acceleration. They dismissed the boundary layer effects as being small, but how this was determined was not specifically stated. The non-uniformity of the distribution of turbulence was noted as a secondary effect of the non-uniform screen, but was stated to have a comparatively smaller effect, although this was also not quantitatively determined.

1.3.3 Distorted model

To re-create the change in flow angle over a body within the straight-flow of a standard wind-tunnel a proposed solution has been to curve the shape of the model itself, rather than the flow, as is shown in Fig. 1.10. The theory is that for any given location along the body, the relative angle between the freestream flow and the model is accurate. However, successful execution would need to accommodate the change in yaw angle and curvature occurring both across the span, as well as along the length. The idea was initially utilised within the aeronautical industry [27, 28], but has also been proposed for automotive applications [6, 29].

Aerodynamically the method is unable to recreate all aspects of the correct condition. The curved shape causes one side of the model to become longer than the other. Somewhat counter-intuitively the side that extends in length, is the side representative of the

inside of the corner, as can be seen in Fig. 1.10. This results in higher local Reynolds numbers occurring on the side closest to the inside of the corner, and lower local Reynolds numbers on the outside. In this way the method can come close to representing the correct flow angles and can achieve this at a constant static pressure, but then does not recreate the relative local Reynolds gradient due to an outboard dynamic pressure increase observed in the true cornering condition.

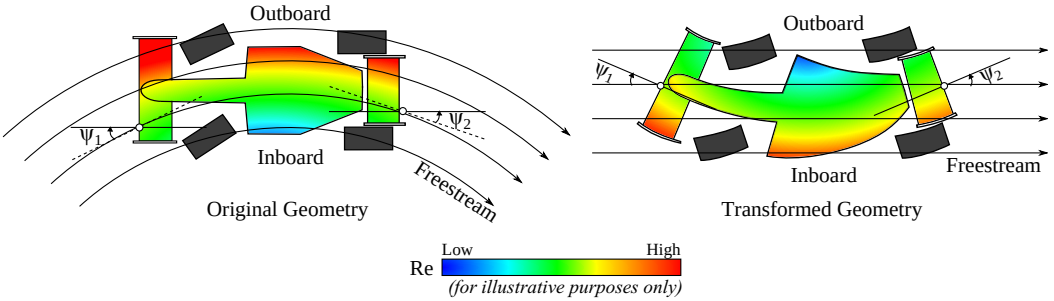

FIGURE 1.10: A car geometry travelling in the path of a left-handed corner and an example of the wind tunnel model bending method used to attempt replicate the cornering condition. An incorrect change in local Reynolds due to model bending is indicated.

There would be the possibility that a non-uniform screen could be used to partially correct this effect, however the induced gradient would have to be severe. Furthermore the effects due to acceleration wouldn't be captured due to the model remaining in an (relatively-speaking) inertial reference frame. A more practical issue is the feasibility of physically constructing such a model. The aspect ratios of geometric features must change due to the distortion, and would be further source of error. The wheels would also have to be curved along a second axis, and yet still rotating – requiring their shape to change as they spin to be truly accurate. A new model is also required for each type of corner, which would significantly increase the cost in most circumstances.

1.3.4 Whirling arm

The whirling arm preceded the wind tunnel and is nearly the ideal experimental rig to replicate the cornering condition. The experiment operates by moving the model in a circular motion through the air about a central vertical axis, shown in Fig. 1.11a). The first was built by an English mathematician Benjamin Robins in 1746 [30]. His whirling arm was driven by a falling weight and had arm length of 1.2 m with a maximum tip tangential velocity of approximately 1 m/s. Further experiments were conducted by Sir George Cayley with an improved design that permitted higher speed where he considered various aerofoil shapes to record lift and drag values.

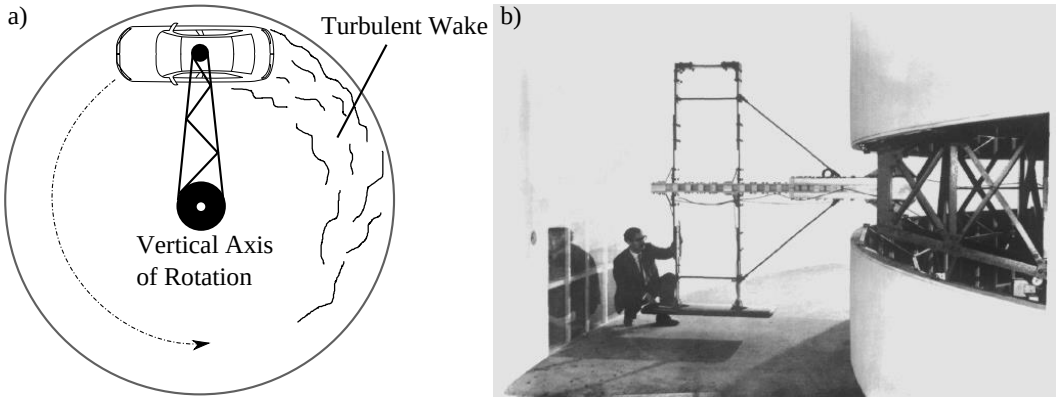

FIGURE 1.11: a) The motion of a model in a whirling arm facility. b) The Cranfield whirling arm facility, showing the model positioned in the test section.

This motion is accurate for replication of the aerodynamic conditions experienced by vehicles travelling through a corner. The motion of the model past the fixed ground would mean a rolling road is no longer required to capture the correct interaction between a vehicle and the ground, and if the freestream flow were stationary as the model passed through it, then the cornering condition would be achieved. However, the flaws of this design were apparent to the first users. The spinning arm meant the model would always be travelling through its own wake and this led to a high level of turbulence and swirl in the flow which ultimately compromised any analysis.

Despite the known issues, the National Physics Laboratory (NPL), in the United Kingdom, built a whirling arm in 1908 [31]. The rig was driven by an electric motor with a design radius of 9 m. It was initially intended for the testing of airships (the most promising form of air travel at that time). Three re-designs were undertaken by the NPL from 1908 to 1942 before the rig was transferred to Cranfield University, with the facility shown in Fig. 1.11b). Modifications attempted to reduce the swirl in the flow through the use of baffles and the removal of any unnecessary bulky measurement devices in the test section. The swirl itself was dependent on the drag of the model and strut in use, but varied from 7.5-22.5% across various configurations. This meant that the flow was also in motion with the model, and would begin to be subject to the effects of curvature Experiments considering a wing in ground effect, hovercraft and aircraft were conducted, but very few results were published [31, 32].

1.3.5 Dynamic test rig

With aircraft becoming more manoeuvrable, testing of dynamic stability parameters became an important consideration [33]. The implementation of dynamic testing rigs within wind tunnels allowed the aeronautical industry to move past deformed models or

curved test sections to simulate a wide range of motions. These are continuing to become more advanced and offer multiple degrees of freedom [34]. The type of motion most similar to a vehicle cornering is coning – this is where the model will be rotated about an axis parallel to the freestream direction. The resultant path then becomes helical as is shown in Fig. 1.12, and thus overcomes the issue of the model running through its own wake, such as is experienced for a whirling arm. A primary limitation is the varying proximity of the model to the test section walls during operation. This commonly results in unsteady interference due to the wall interaction with vortices, particularly at high angles of attack [35].

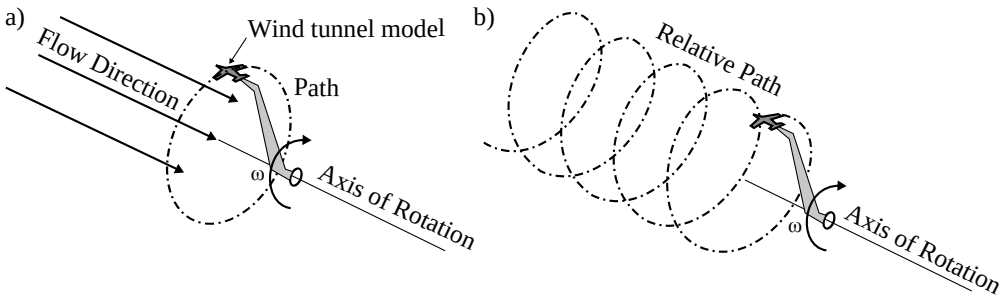

FIGURE 1.12: Steady-state coning motion of a wind tunnel model, as produced by a rotary rig: a) In the absolute reference frame b) In the reference frame of the model

Large or open test sections are already required to allow for the blockage caused by a bluff-body. To use this type of rig would then require either a much larger test-section or the use of a small wind tunnel model. A further issue would be accurately capturing the interaction and relative motion that a vehicle has with the ground. The model could be designed as attached to a fixed ground plane, or be in motion with a moving ground, but both options could become exceedingly complex and result in an increased blockage ratio.

A dynamic yawing method was used by Garry and Cooper [36] for aerodynamic analysis of a tractor-trailer configuration where the model was rotated about it's centre dynamically. The combination of vehicle rotation and the oncoming flow velocity meant that for a given fluid particle it would be possible to observe one angle of yaw at the front and a different angle at the rear — such as occurs during cornering. The relative change in velocity would also be correct due to the tangential component due to rotation. However, the condition could not be achieved instantaneously, that is to say the front and rear of the model wouldn't have ever been at different angles of yaw at any given point in time — nor was it the intention of the authors to achieve such a condition.

Watkins et. al [37] discussed how the combination of rotation and translational motion could achieve a dynamic curvature within a wind tunnel, as is shown in Fig 1.13. Such a

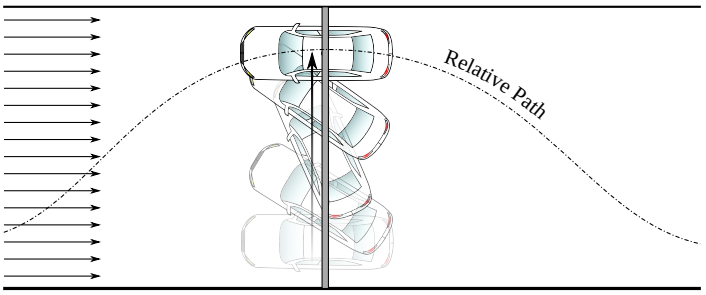

FIGURE 1.13: Sinusoidal curved motion achieved through use of rotation and translation with a wind tunnel traverse

method would permit sinusoidal motion, and there are modern facilities that are capable of achieving such conditions [38]. The practical difficulties associated with using this technique has prevented it from becoming commonplace and the method is still unable to offer cornering conditions for a sustained period as it is limited by the size of the test-section. In addition there are several issues that arise with the use of the technique. For a constant flow velocity, the speed of the model relative to the air increases to a maximum at the middle of the test section due to the additional translational component, and reduce to a minimum at each side. Thus the model would experience multiple components of variable acceleration. Potentially fan speed modulation could be used to create pulses of high and low speed flow to match the model motion and correct this additional acceleration component. A similar flow condition could also theoretically be created through the use of alternating side-wind gust generators positioned on either side of the test section, however any attempts of such methods are yet to be published, and this still would not recreate the correct rotating non-inertial reference frame.

While methods exist that are capable of recreating some aspects of the cornering flow conditions, there is yet to be a method that is capable of sustaining the correct flow conditions for aerodynamic development. Thus investigation into the cornering condition has been partially hindered by to the inability to conduct experimental analysis. The development of a new technique to overcome these limitations would allow investigation to supplement numerical analyses and allow understanding of this condition to further develop.

1.4 Automotive Aerodynamics

In the public domain, research in automotive aerodynamics has favoured the use of simple shapes over detailed car geometries to ensure findings are more likely to be universally applicable. These shapes are generally geometrically simple with a large

separated region forming at the rear due to the blunt shape. The aerodynamic drag is typically dominated by the pressure component due to the significant losses that occur in the wake.

A review of previous bluff-body research for automotive aerodynamics was conducted by Le Good and Garry [39]. The authors detail seventeen different generic car shapes that have been used within publicly available research. The variety of different shapes are largely intended to be representative of different vehicle types. The authors emphasized the value of new research continuing to use the existing geometries where possible to build on prior findings, rather than the continually proposing new reference models and investigating geometric nuances. The "Ahmed Body" [40] was identified as the most thoroughly investigated model.

Recent areas of interest have included efforts to understand the flow environment that a vehicle geometry is likely to experience on-road. Real-world conditions have been identified to be very different to the low turbulence levels and steady flow created in most wind tunnels [1, 41]. These studies have included research into the effects of transient cross-wind gusts [42–46], dynamic pitching and yawing motions [47–50], and following other vehicles in close proximity [2, 51].

For numerical studies there continues to be effort toward improving the methods used to model the complex flow structure, as well as understanding the flow [52–60]. While LES has proved most reliable in its capability to accurately replicate the findings of experimental studies, the computational expense can remain prohibitive for development of a vehicle [52, 55, 58, 59]. There exists a need to further develop hybrid techniques such as Detached Eddy Simulation (DES) [61] to enable accurate simulation to be achieved within a shorter time-frame.

1.4.1 The Ahmed Body

The Ahmed body was first introduced and analysed experimentally in the benchmark study conducted by Ahmed et. al [40]. Dimensions of the experimental model at a backlight angle of 25° are shown in Fig. 1.14. The original motivation behind the design of the geometry was to maintain attached flow over the front to permit detailed investigation into flow features occurring over the sloping rear face called the backlight and also in the near wake. This rear angle results in a number of flow effects common to those observed on hatchback/fastback vehicles, and causes significantly different flow effects in comparison to the simpler square-back model (with no rear sloping face).

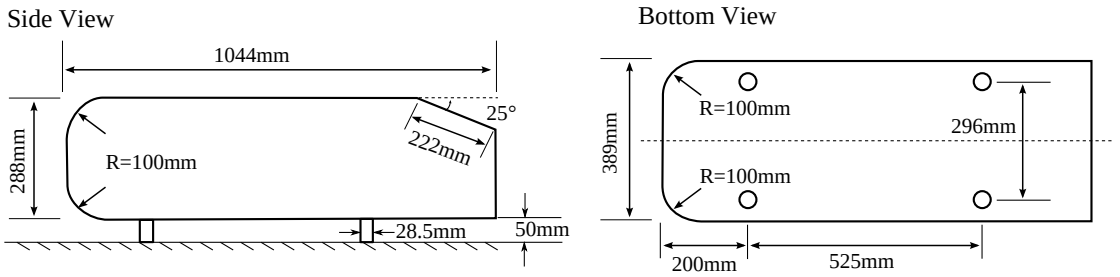

FIGURE 1.14: Geometric dimensions of the Ahmed reference vehicle model

The time-averaged structure in the near wake has been a popular topic of investigation [10, 40, 53, 58, 62–65] and consists of both longitudinal and spanwise structures which are indicated in Fig. 1.15. The rear flow structure has also been closely related to the dominant pressure component of aerodynamic drag. Due to the highly unsteady nature the true time-dependent flowfield significantly differs from the time-averaged. A number of distinct transient flow mechanisms have also been identified, and this continues to be an ongoing topic of further investigation [55, 57, 59, 66–76].

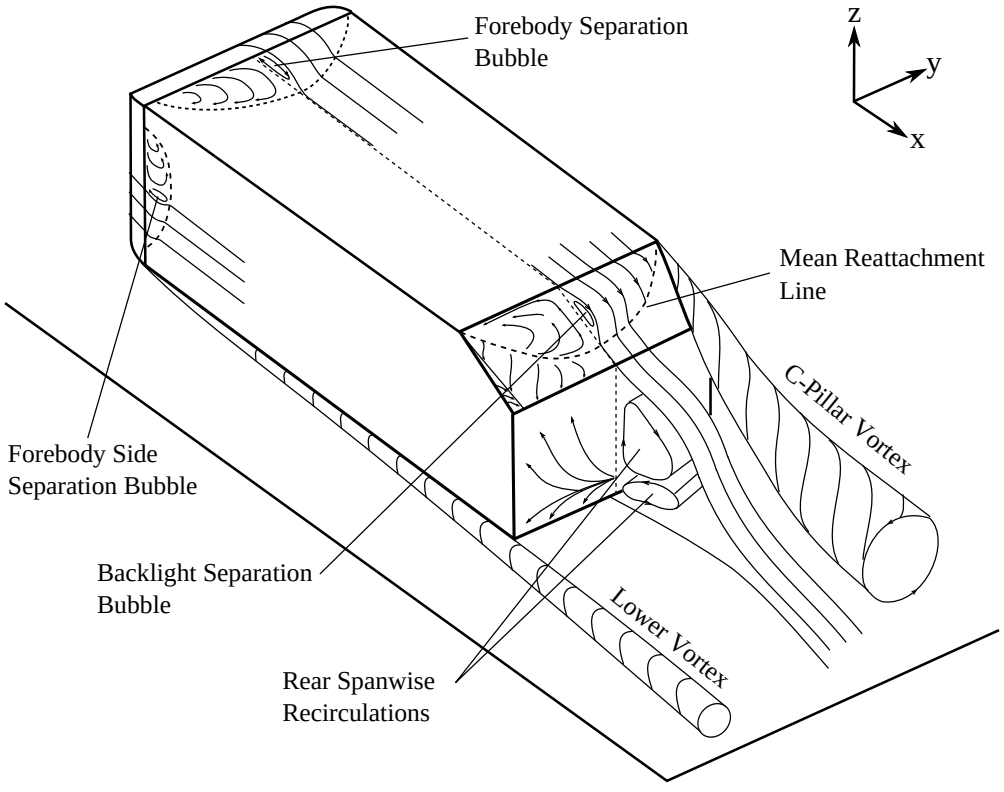

FIGURE 1.15: The flow features of the 25° backlight angle Ahmed body

The original study by Ahmed et. al [40] identified a number of the key aerodynamic

features. They confirmed drag was primarily related to the pressure component, contributing 85% to the overall number. Most of this drag was generated due to the separated region occurring at the rear of the body. Due to the acceleration of the flow down the backlight surface, the shear layer separated off the sides of the body at the C-pillar locations to form a longitudinal vortex at either side. For a backlight angle of 12.5° to 25° the flow separated at the start of the surface and reattached prior to the trailing edge, as shown in Fig. 1.15. Changing the backlight angle affected the strength of the C-pillar vortices, and also the arched vortex structure within the separation bubble at the rear face. At 35° the separation bubble failed to reattach completely and the flow was found to exhibit improved stability in addition to an overall reduction in drag.

Other studies have aided in further developing an understanding of the flow and have identified features that were initially unrecognised. Examples include the separation bubbles forming near the nose over the upper and side surfaces [10, 55, 59, 77], as well as the lower longitudinal vortices forming along either side of the base [59, 62].

The most commonly investigated backlight angle is 25° [10, 40, 53, 57–59, 62–65, 67–71, 73–75], and for numerical studies the separation and reattachment of the flow over the backlight has evaded most numerical methods other than LES. The popularity of both the Ahmed body, and this specific angular configuration made it favourable as a reference model for the present study and meant that findings could be compared to a wide range of previous investigations.

1.4.1.1 Experimental Studies

Lienhart and Becker [63] conducted an experimental study of the original configuration and found close correlation with the work of Ahmed et. al[40]. They used Laser Doppler Anemometry (LDA), hot-wire probes and static pressure measurements to analyse both the 25° and 35° rear angles. Their results included the velocity distribution on downstream planes, as well as boundary layer profiles and wake deficits along the symmetry plane. Additionally, they used an array of pressure sensors over the backlight surface to extract the pressure coefficient distribution. The intention of the publicly funded study was to create a reference data set to enable validation of computational models[78], which was also utilised in the present work.

The transition between different drag regimes for the Ahmed body is characterised according to whether the flow reattaches on the backlight surface. Once the flow completely separates at the start of the backlight, a reduction in drag occurs due to a reduction in the lift-induced component. At an approximate backlight angle of 30° most studies have found the flow fails to reattach, but not all [62, 74]. The critical angle lies close to this

value and would appear to demonstrate sensitivity between experimental configurations. Vino et. al [66] investigated the 30° angle in detail and found the separation bubble to partially reattach near the sides of the backlight, but not at the centre of the face.

Separated flow regions thus present a significant challenge to understanding the flow, and these were classified by Spohn and Gillieron [77] at a Reynolds number of 3×10^4. They detailed the structure of the forebody separation bubble as containing two stable focii, at the end of a separation line. These occurred due to the existence of two vortical structures which turn into the longitudinal plane as they travel downstream, as is shown in Fig. 1.16. In addition, Kelvin Helmholtz vortices were observed to occur within the upper region of this separation bubble. A similar structure was identified for the backlight separation bubble, but occurred in the additional presence of the longitudinal C-pillar vortices.

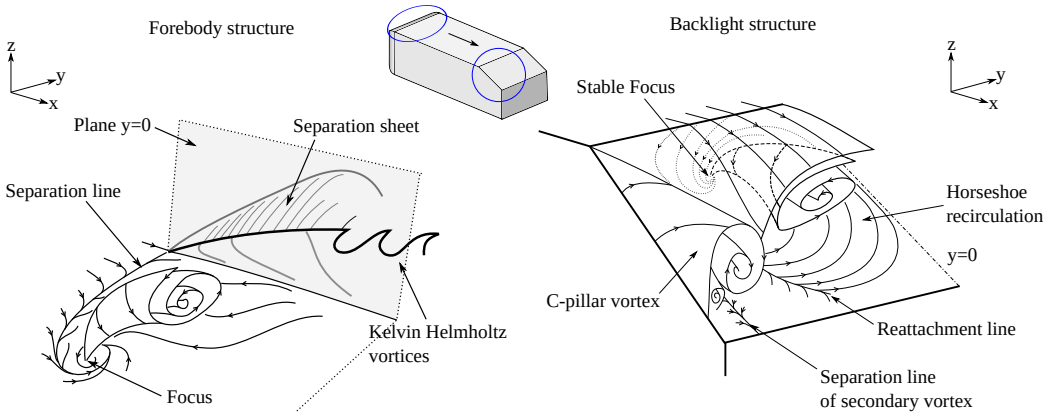

FIGURE 1.16: Adaption of the forebody and backlight separation bubble structure diagrams presented by Spohn and Gillieron [77]

Sims-Williams and Dominy [10] used surface flow visualisation to investigate the same forebody separation at a Reynolds number of 6.2×10^5. They identified the length of this separated region to be less than was observed by Spohn and Gillieron, however did not investigate the structure in comparable detail. Their result could suggest that the feature is less prominent at more realistic Reynolds numbers or higher turbulence intensities.

There have been differences noted between experimental studies, even amongst studies adopting near-identical procedures. This has particularly been the case for the measured drag coefficient, which is discussed further in Chapter 2. Collectively results would suggest either a high level of sensitivity to subtle differences between each experimental configuration, or blockage effects being more substantial than has been previously assumed. Conan et. al [67] attempted to compare results between two different facilities within the same study but acknowledged that too many unknowns limited their ability

to report on the differences they discovered. Despite this, the flow structure has been shown to exhibit a low sensitivity to Reynolds number. From 4.4×10^6 to 1.3×10^7 Bayraktar et. al [64] recorded only a 3.5% decrease in drag coefficient. These findings have been supported by subsequent studies at lower Reynolds number [73, 79]. Joseph et. al explained the mild increase in drag with Reynolds number due to a decrease in the size of the separation bubble which occurred on the backlight surface, allowing the pressure recovery in this region to occur sooner.

The transient wake motions have been of further interest and dominant wake modes have been identified at Strouhal numbers ranging from 0.2 to 0.5 (based on model height)[66, 68–70, 73, 75, 76, 80] which fall into a similar range to investigations conducted on a range of bluff bodies. The large number of interactions occurring within the wake and, as a result, the range of frequencies of flow activity occurring at any given measurement location continue to present challenges when attempting to understand the flow.

Previous transient analyses have been predominantly concerned with pressure and velocity fluctuations on the centreline plane at the rear of the body due to the shear layer shedding off the upper surface, and the unsteadiness within the rear separation bubble. Thacker et. al [69] and Zhang et. al [76] identified dominant frequencies at Str ≈ 0.23 for the rear separation bubble.

Describing why and how these motions of the flow occur has continued to present a challenge. Thacker et. al [69] proposed the backlight surface frequency measurements to be the result of flapping motion of the shear layer off the upper surface. They also identified higher frequencies in the upper part of the backlight flow due to secondary shearing above the rear separation bubble. Zhang et. al [76] identified a second dominant frequency of Str $= 0.31$ to occur closer to the sides of the backlight, and supported a quasi-periodic spanwise vortex roll proposed by Wang et. al [75]. They attributed the common frequency identified between the two studies to be due to the merging of the spanwise vortices in the upper part of the separation bubble, which corresponded to the periodic change in size of the separation bubble region.

For the larger separated region occurring at the trailing face, transient flow activity has been identified to occur at Strouhal numbers ranging from 0.39 to 0.49 [55, 66, 76]. Vino et. al [66] measured Str $= 0.39$ based on surface pressure taps and proposed a von Kármán vortex street mechanism to occur within the wake due to an alternate shedding of the upper and lower shear layers. Through downstream turbulence intensity measurements, alternating stretching of the upper and lower recirculations was identified — with the lower recirculation extending upwards downstream, and the upper extending downwards dowstream. Zhang et. al [76] used a combination of hot-wire and PIV measurements to investigate the same mechanism in greater detail and a multi-phased

quasi-periodic motion of the rear separated region was proposed. Similarly they identified a periodic extension and contraction of the recirculations, however they also found these structures to emanate a fluid parcel downstream within the sequence, as is shown in Fig. 1.17.

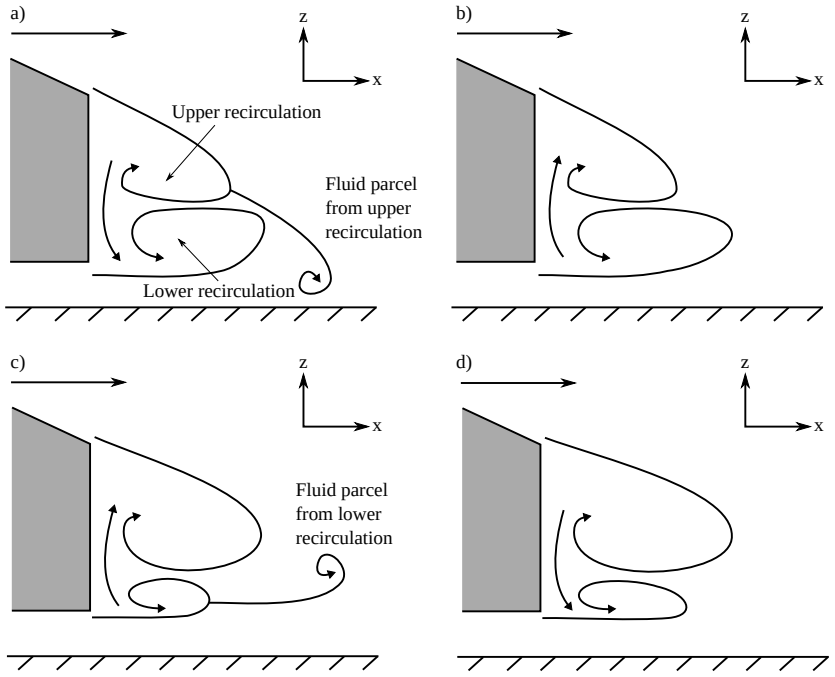

FIGURE 1.17: Sequence of transient mechanism identified in the rear separation bubble as shown by Zhang et. al [76]

They proposed that the recirculation periodically increases in size until a critical core pressure is reached; the structure then bursts releasing a fluid parcel downstream. This mechanism was observed to alternate between the upper and lower structures. In addition they also proposed that flow passed between the upper and lower structures near the boundary due to the pressure difference. They noted that this mechanism could reasonably be expected to be sensitive to specific experimental characteristics such as the surface finish of the wind tunnel model, and turbulence levels; thus possibly explaining the range of reported frequencies amongst studies.

1.4.1.2 Numerical Studies

Adopting a numerical methodology that is capable of accurately capturing the flowfield has presented a challenge. Han [56] published an early investigation into the Ahmed body using Reynolds Averaged Navier Stokes (RANS) simulations. Reported results correlated with the experimental data (to the extent of the prediction of lift, drag, and surface pressure profiles) up to a 20° backlight angle. For the 30° backlight angle the

method failed to predict the discontinuity in trends which is commonly attributed to the transition from the high-drag regime to the low-drag with separation of the flow over the backlight. Incorrectly resolving this critical flow feature had cumulative effects and was stated as a reason for the study focussing on smaller backlight angles.

Higher-order numerical modelling techniques such as LES [81] and DES [61] have been preferred to simulate the unsteady wake region of a wide-range of bluff-bodies. For the Ahmed body particularly LES has proved to be superior in capturing both longitudinal and spanwise structures [55, 58, 59, 65]. Howard and Pourquie[72] used LES to conduct a study which considered the geometry with a 28° backlight angle in the absence of a ground plane. Grid density was hindered due to available computational power with only 1.6×10^6 elements, and necessitated the implementation of a log-law boundary layer approximation. Q-criterion was utilised for visualisation of the vortical structures, and spectral analysis was conducted of the transient flow behaviour within the wake. Drag was estimated to be under-predicted, which was based on experimental results achieved at the angles of 25° and 30° (as there were no experimental results to compare to at a 28° backlight angle). An under-prediction of the viscous drag component was partially attributed to the inability to sufficiently resolve the flow at the boundary.

Krajnović and Davidson [58, 59, 65] conducted wall-resolved LES which highlighted the potential of this method for capturing the flowfield in detail. They used the Smagorinsky Sub-Grid Scale (SGS) model with a fixed Smagorinsky constant of 0.1. Their studies identified a number of phenomena yet to be captured in experimental investigations.

Within the instantaneous flowfield they presented a detailed picture of the backlight flow structure. The rear separation bubble was identified to consist of spanwise vortices which were directed towards the centre plane due to the presence of the C-pillar vortices. These spanwise vortices merged to form larger structures which then briefly assumed a hairpin structure before detaching from from the surface. They also observed a gear-wheel type mechanism to occur for the C-pillar vortex, whereby a counter and co-rotating structure were induced by the rotation of the primary structure. They were the first to identify the existence of the lower vortices, which has since been supported experimentally [62, 75]. The lower longitudinal vortices formed due to the boundary layer growth along the underside of the body, resulting in an increase in pressure on the lower surface. In most experimental configurations the detection of the lower vortices was inhibited by the presence of the lower cylindrical support struts. Krajnović and Davidson also supported the merging of the C-pillar vortex with the upper recirculation downstream, a finding that was initially believed to occur by Ahmed et. al [40] and confirmed by Zhang et. al [76]. These studies were of particularly strong influence as the numerical study was

not only able to support prior experimental findings, but also identify new phenomena which have since been confirmed experimentally.

For the same geometry different techniques have since been adopted in attempts to reduce the computational expense and improve solution stability of LES. Spectral Vanishing Viscosity (SVV) LES was such an example as used by Minguez et. al [55]. This method introduces a viscous term for the highest resolved frequencies, intended to improve solution stability. Suitable correlation with the experimental data was found in most regions, however an over-prediction of the forebody separation bubble was recognised as a source of some discrepancy. They presented a detailed analysis of the flowfield, including frequency analysis at several locations along the symmetry plane of the body. A strong peak was measured at Str = 0.27 in the upper region of the backlight separation bubble, which was similar to the Str = 0.26 value identified by Krajnović and Davidson. In the lower part of the wake Str = 0.42 was identified as the dominant frequency, which was attributed to the recirculations at the trailing face — although a specific transient mechanism was not proposed. From approximately one body-length downstream the authors identified the turbulence to be largely homogeneous and isotropic with energy decreasing according to the Kolmogorov rate $k^{-}5/3$, however, in the near wake region the anisotropy indicated more geometry dependent mechanisms operating across a wide range of frequencies.

Minguez et. al [55] and Krajnović and Davidson [58, 59, 65] have since remained the benchmark numerical studies. A more recent study by Aljure et. al [53] investigated four further LES-based methods for both the Ahmed body and the Asmo generic car model. Grids were unstructured and the finest resolution was only 1.6×10^6 cells. Within the study the authors attempted to propose that significantly coarser grids could be used capture the flowfield to an acceptable degree of accuracy. However they failed to address the flow features developing over the body in any significant depth. No details were provided of the separated flow regions that have challenged prior investigations, allowing limited assessment of the true fidelity achieved. The drag coefficient values were within 7% of experimental values, however the contribution of the viscous component was five times less than was identified in the experiments of Ahmed et. al [40]. Thus it was a significant over-prediction of the pressure component and under-prediction of the viscous component which resulted in a similar prediction of the total value.

Serre et. al [52] contrasted a range of LES-based methods which included the Smagorinsky SGS model with a wall model, the Dynamic Smagorinsky model, the SVV-LES method, and a DES simulation with the k-ω SST [82] model at the boundary. The separation bubble on the backlight was only able to be correctly captured by one of the four methods, which was the SVV-LES, as was adopted by Minguez et. al [55]. The authors

noted this was a substantial challenge towards accurately predicting the flowfield. This difficulty was also discussed in more detail by Minguez et. al [55] who attributed the demonstrated inadequacy of other models to the turbulent stresses resulting from the Kelvin Helmholtz instabilities of the separation bubble. Specifically that these stresses far exceed those for which most turbulence models will be calibrated, thus necessitating the features to be resolved. In the study by Serre et. al this single feature most strongly influenced their conclusion that the SVV-LES model was most appropriate for the body.

While this model performed best in terms of flow geometry, a hindrance was an over-prediction of aerodynamic drag by 44%. This was attributed to an over-prediction of the forebody separation bubble increasing the effective frontal area. What the authors did not consider in this assessment was the 8.24% blockage ratio of the computational domain — which was almost double that used for the other methods, which all predicted the drag coefficient more closely.

Serre et. al demonstrated that DES was able to achieve a result with a significantly lower computational expense, but acknowledged it failed to offer the same accuracy as LES. The future potential of such methods will hopefully allow studies to be conducted within a much shorter time-frame, however it currently has not developed to the stage where suitable accuracy can be achieved. These findings were further supported in a more detailed publication of the same DES method by Guilmineau et. al[54].

1.4.2 Bluff Bodies in Yaw

Investigation of the Ahmed body in the yawed condition has been limited in comparison to the extensive body of work in the straight-line condition. An early experimental study of the Ahmed body with a rear sloping face in the yawed condition was conducted by Bayraktar et. al [64]. Their study utilised the NASA Langley full scale tunnel which allowed the investigation of the body at Reynolds numbers which are typical of a bus or truck. Results only presented drag values for the yawed condition and identified an increase to occur. The sensitivity to yaw was dependent on backlight angle with the 12.5° and 0° angles experienced a proportionally greater increase in drag due to yaw than the 25° case.

More recently an investigation by Meile et. al [83] considered both the 25° and 35° rear angles at in the yawed condition. Force and moment coefficients were measured for both configurations at angles of yaw up to 25°, with 2.5° increments. The study focussed on the bi-stable nature of the 35° backlight angle wake in these conditions. Between yaw angles of 11 to 15° the authors noted 'random' fluctuations in the wake structure based on long sampling periods of up to 10 minutes. These corresponded to the partial

reattachment of the flow down the backlight surface, which resulted in an increase in the lift coefficient generated through a reduction in surface pressure over the rearward part of the car. An additional finding was an increase in the side force and yawing moment as yaw angle increased, as well as an increase in strength of the windward side C-pillar vortex.

An alternative bluff body with a square-back was experimentally evaluated at yaw by Golkhe et. al [84]. The geometry lacked the defined edges and features found on the Ahmed body with a continuous rounded surface over most of the body, as is shown in Fig. 1.18. Up to a 30° angle was considered, and specific yaw flow effects were classified according range of angles across which they occurred. A yawing moment and side force were identified to result from the flow angle. The side force continued to increase up to the maximum measured yaw angle of 30°, which would be expected due to the increasing area normal to the direction of the flow. Yawing moment acted in the positive direction (turning the forebody in the direction of the flow angle) and increased linearly up to 18°. From 18° to 30° the moment continued to increase albeit at a reduced rate. The contribution toward the yawing moment was divided between the forebody and rear section through analysis of the surface pressure distribution. The forebody continued to have a greater contribution to the yawing moment across the range of angles, however the counter moment induced by the leeward rear side became more significant at the higher flow angles. The development of the vortical flow structure on the leeward side was also analysed using PIV and is shown in Fig. 1.18. They identified the lower structure to remain attached up to angles of 20° and then separate beyond this point. They also noted the beneficial effects of these vortices towards aiding in cross-wind stability.

FIGURE 1.18: The development of the leeward flow structure in a cross-wind, as identified by Gohlke et. al [84]

The same geometry was modelled numerically by Guilineau et. al [60] using DES with the k-ω SST turbulence model at the wall. The study primarily sought to validate the numerical method against the experimental results. Correlation was assessed based on comparison with surface pressure data, and PIV results. The force trends were in agreement across the two studies, and the flow structures exhibited close similarity. The only major discrepancy was the pressure deficit near the base on the leeward side, which

was unable to be matched in magnitude by the numerical study and was identified as a limitation of the model.

The study by Volpe et. al [85] was an exception to the common focus on the time-averaged flow effects in yaw, with their study investigating the transient flow structures occurring behind a squareback Ahmed model. They identified common wake modes to occur at low frequencies of Str = 0.08 and 0.13 (based on model height) attributing the dual recirculation structure occurring in the wake. They also identified high sensitivity of these effects to only slight changes in yaw angle, where a 0.4° yaw angle change was enough to result in a 30% reduction in the characteristic frequency. Krentel and Nitsche [86] also investigated the same geometry with the addition of an active drag control mechanism which used compressed air jets positioned at the rear of the body. These jets interacted with the shear layer off the respective sides of the body and resulted in a 3.5% reduction in the force coefficient in the x-direction at a 15° angle of yaw. In the straight-line condition a smaller 2.2% reduction occurred for the same configuration, highlighting the additional benefit of the jets toward the asymmetric wake structure in the yawed condition.

The transient cross-wind or gust condition has also been a topic of investigation [42, 44, 45, 50, 87], particularly from the perspective of safety. A driver can be easily caught unprepared due to the very strong aerodynamic forces which may result[46, 88]. The force response of a vehicle to a gust will typically be out of phase with the onset of the condition, and this phase shift will vary dependent on geometry. Ferrand [89] identified the magnitude of the forces to either exceed, or be less, than what is recorded in the static condition due to hysteresis effects. For harmonic transient gusts the frequency also affects the magnitude of difference between the static yawed case, with lower frequency typically demonstrating a wider range of forces. However, these effects are more likely to bear relevance for a transient cornering motion, much less the steady-state cornering condition analysed in the present work.

Importantly these findings for generic bluff-bodies have been shown to extend to vehicles, with common effects being the introduction of a side force and yawing moment, in addition to an increase in aerodynamic drag. Baker [90] presented a summary of a number of different vehicles and their force and moment response to a constant yaw angle, which further supported this. Howell [91] also investigated the effect of yaw for a range of passenger vehicles, as well as the generic Windsor model. He again identified similar effects that occurred for the different geometries, however, the magnitude of this varied amongst different geometries. Seven different vehicles were analysed in each class (saloon, SUV, small hatchback, and MPV) and the spread of different force results among the MPV class was approximately double that of any other category. Results

demonstrated the influence that shape can have on a vehicle's sensitivity to yaw, but also that (in most cases) there are similar characteristics amongst vehicles of a certain type.

1.5 Present Approach

The cornering condition is a common aerodynamic environment experienced by vehicles that is yet to be the topic of detailed investigation. This has been exacerbated by the additional difficulty in numerical modelling, and the inability to create the correct flow conditions within a controlled environment for experimental analysis. The primary aim of the present work is to develop a fundamental understanding of the cornering condition, and the associated flow effects.

The Ahmed body [40] was selected as an appropriate geometry due to its status as one of the most comprehensively investigated generic automotive bodies. The Wall-Resolved LES is validated against experimental data in Chapter 2 where an assessment of the fidelity in capturing both the time-averaged flowfield and temporal effects is conducted. Through resolving the boundary region the method is shown to able to capture the separated flow regions which are critical toward the accurate prediction of aerodynamic characteristics.

A review of current literature identified the yawed condition as the most widely-adopted existing method for experimentally approximating cornering performance [6]. Thus the merit of first investigating the steady yaw condition was twofold. This enabled investigation into the effects of flow angle in isolation, and also further permitted direct comparison between the yawed and cornering conditions with a common platform. Yaw angles ranging from 2.5° to 10° are considered in Chapter 3. These angles are smaller than those often investigated in dedicated cross-wind studies, but were selected to relate more closely to the magnitude of yaw angle that occurs along a vehicle when travelling in the path of a corner.

Chapter 4 consists of a detailed analysis of the aerodynamic effects of the cornering flow conditions. For a steady-state cornering condition radii ranging from a 20 car-lengths to 5 car-lengths are examined. For the smallest radius corner a current model Volkswagen Golf would be capable of maintaining a tangential velocity of approximately 50 km/h (13.9 m/s) [92], corresponding to a length-based Reynolds number of 4.35×10^6, with higher speeds being achievable for more performance-orientated vehicles. These radii were thus selected to be representative of conditions where significant cornering-specific flow were expected to occur, without surpassing a radius where aerodynamic effects

become insignificant due to low speeds. In this chapter the centre of the body remains aligned tangentially to the curved path of the corner, resulting in equal and opposite flow angles occurring at the front and rear.

Within Chapter 5 the results of the yawed and cornering conditions are compared and contrasted to assess the synonymity of the two conditions, allowing the derivation of some initial conclusions. In addition, sensitivity due to yaw angle within the cornering condition is analysed. For a constant corner radius of 10 car-lengths, three different yaw angles of 1.43°, 0°, and -1.43° are compared. The angular increment investigated corresponded to a 0.25L shift in the location at which the flow angle was zero with respect to the body's co-ordinate system. This allowed an assessment of the implications a vehicle's dynamic attributes may have toward aerodynamic performance in the cornering condition.

Finally, a novel experimental method was developed, and is evaluated in Chapter 6. The design is the first to offer the correct and repeatable flow conditions representative of a steady-state corner. Analysis of the aerodynamic principles of operation, and details of the construction of the first working prototype are included. Experimental analysis is conducted of the test-section flow and compared to the ideal flowfield which occurs during cornering. Ultimately the unique development represents a step toward permitting future experimental investigations within the cornering condition, and the potential to corroborate the findings of the computational analysis within the present study.

Chapter 2

Numerical Method

2.1 Large Eddy Simulation

Computational Fluid Dynamics (CFD) simulation of the turbulent flow around bluff-bodies such as cars, trucks, and trains remains computationally demanding. For research applications Detached Eddy Simulation (DES) and Large Eddy Simulation (LES) have become favoured methods. Although more computationally expensive, these techniques allow more detailed simulation of the separated flow structures, and have demonstrated an ability to capture both the transient and time-averaged characteristics of the flow. Direct Numerical Simulation (DNS) is the most numerically simple approach, in that the governing equations are directly discretised and then solved, however this requires all scales of motion to be resolved, and a sufficient number of grid points to achieve this. A computational domain is required to be of sufficient size to resolve the largest scale in the system, and the cell size must be small enough to resolve the smallest scale, which is equivalent to the Kolmogorov length scale. Temporal discretisation must also be sufficiently small to resolve these features. As a result the computational cost becomes proportional to Re^3 [93], and for external automotive aerodynamics this remains prohibitive.

In the present work some preliminary investigation used DES, which combines a RANS approximation at the boundary which blends to LES away from the body. However, poor correlation with experimental data was apparent, in line with findings in prior studies [52], and this method was not further pursued. The RANS boundary layer model has previously been identified to be incapable of capturing the high turbulent stresses within the separated flow regions [55], and poor prediction of these specific areas was identified as the critical inadequacy.

The use of Wall-Resolved LES proved more suitable. LES resolves the large turbulent features and uses a sub-grid scale (SGS) model to approximate the smaller structures. The small and large scales of motion are determined by spatially filtering the velocity field with a kernel that determines scales smaller than the local grid scale. The rationale behind the application of this model is that the momentum, mass, energy, and most other physical properties are mostly transported by the large scale eddies. The large eddies also tend to be the most problem dependent whereas small eddies tend to be more isotropic [93]. Hence an accurate representation of the flowfield can be obtained with a significantly lower computational expense than DNS.

2.2 Governing Equations

For the cornering condition, which forms the central focus of the present work, the relative motion of the flow past the body is considered within a rotating reference frame and thus the Navier-Stokes equations are expressed in a cylindrical co-ordinate system.

Within a Cartesian system the incompressible continuity equation is the sum of the partial derivatives of each velocity component with respect to the same displacement component. When transformed into a cylindrical system this is then expressed in terms of the angular, radial, and vertical velocity components:

$$\frac{1}{r}\frac{\partial}{\partial r}(rv_r) + \frac{1}{r}\frac{\partial v_\phi}{\partial \phi} + \frac{\partial v_z}{\partial z} = 0 \tag{2.1}$$

In general form both can be expressed as:

$$\nabla \cdot \vec{v} = 0 \tag{2.2}$$

due to the zero divergence condition of the velocity field for the incompressible form of the equation.

Within the cylindrical system the momentum equation can be expressed according to the angular, radial, and vertical momentum.

Radial momentum:

$$\rho\left(\frac{\partial v_r}{\partial t} + v_r\frac{\partial v_r}{\partial r} + \frac{v_\phi}{r}\frac{\partial v_r}{\partial \phi} + v_z\frac{\partial v_r}{\partial z} - \frac{v_\phi^2}{r}\right)$$

$$= -\frac{\partial p}{\partial r} + \mu\left[\frac{1}{r}\frac{\partial}{\partial r}\left(r\frac{\partial v_r}{\partial r}\right) + \frac{1}{r^2}\frac{\partial^2 v_r}{\partial \phi^2} + \frac{\partial^2 v_r}{\partial z^2} - \frac{v_r}{r^2} - \frac{2}{r^2}\frac{\partial v_\phi}{\partial \phi}\right] \tag{2.3}$$

Angular momentum:

$$\rho\left(\frac{\partial u_\phi}{\partial t}+v_r\frac{\partial v_\phi}{\partial r}+\frac{v_\phi}{r}\frac{\partial v_\phi}{\partial \phi}+v_z\frac{\partial v_\phi}{\partial z}-\frac{v_r v_\phi}{r}\right)$$

$$=-\frac{1}{r}\frac{\partial p}{\partial \phi}+\mu\left[\frac{1}{r}\frac{\partial}{\partial r}\left(r\frac{\partial v_\phi}{\partial r}\right)+\frac{1}{r^2}\frac{\partial^2 v_\phi}{\partial \phi^2}+\frac{\partial^2 v_\phi}{\partial z^2}-\frac{2}{r^2}\frac{\partial v_\phi}{\partial \phi}-\frac{v_\phi}{r^2}\right] \tag{2.4}$$

Vertical momentum:

$$\rho\left(\frac{\partial v_z}{\partial t}+v_r\frac{\partial v_z}{\partial r}+\frac{v_\phi}{r}\frac{\partial v_z}{\partial \phi}+v_z\frac{\partial v_z}{\partial z}\right)$$

$$=-\frac{\partial p}{\partial z}+\mu\left[\frac{1}{r}\frac{\partial}{\partial r}\left(r\frac{\partial v_z}{\partial r}\right)+\frac{1}{r^2}\frac{\partial^2 v_z}{\partial \phi^2}+\frac{\partial^2 v_z}{\partial z^2}\right] \tag{2.5}$$

Considering curved motion in the absolute reference frame, there are specific terms which become of particular influence. In the radial momentum balance, shown in Eqn. 2.3, it can be observed that a centripetal force term arises due its necessity to maintain the same radial momentum balance for an element rotating about a fixed axis, according to $\frac{v_\phi^2}{r}$.

The body force component of the angular momentum, shown in Eqn. 2.4, is also observed to vary according to the product of the radial and tangential velocity, and is equivalent to the change in rotational inertia of the element. As the radius or angular velocity increase, the body force component of the angular momentum will increase in accordance with the term $\frac{v_r v_\phi}{r}$.

These changes in angular or radial momentum are then respectively balanced by pressure gradients and viscous stresses of the same orientation, introducing inherent resultant flow effects for curved motion.

The terms can then be summarised as the balance of the acceleration and velocity gradients, with the pressure gradient and viscous stresses.

$$\frac{\partial}{\partial t}(\rho\vec{v})+\nabla\cdot(\rho\vec{v}\vec{v})=-\nabla p+\nabla\cdot(\overline{\overline{\tau}}) \tag{2.6}$$

Within the present study these velocity terms were then expressed in relative reference frame of the vehicle.

For a single rotating reference frame the axis of rotation is described by a unit direction vector $\hat{a}$.

$$\vec{\omega}=\omega\hat{a} \tag{2.7}$$

The entire computational domain is then regarded with respect to the rotating frame, where every point is described with respect to its distance from the origin and is given

a position vector $\vec{r}$

$$\vec{v}_r = \vec{v} - \vec{u}_r \tag{2.8}$$

$$\vec{u}_r = \vec{\omega} - \vec{r} \tag{2.9}$$

$\vec{v}_r$ is the relative velocity (the velocity observed within the rotating reference frame), $\vec{v}$ is the absolute velocity (the velocity observed from outside the rotating reference frame i.e. in the absolute reference frame) and $\vec{u}_r$ is the velocity due to the rotation of the reference frame. For the type of flows considered in the present work the relative velocity formulation yielded improved rates of convergence and solution stability, deeming the specification preferable.

Thus these same equations are expressed according to the relative terms:

$$\nabla \cdot \vec{v}_r = 0 \tag{2.10}$$

With the momentum equation being equal to:

$$\frac{\partial}{\partial t}(\rho\vec{v}_r) + \nabla \cdot (\rho\vec{v}_r\vec{v}_r) + \rho(2\vec{\omega} \times \vec{v}_r + \vec{\omega} \times \vec{\omega} \times \vec{r}) = -\nabla p + \nabla \cdot (\overline{\overline{\tau}}) \tag{2.11}$$

With the stress tensor $\overline{\overline{\tau}}$ also calculated according to the relative velocity derivatives are used, as opposed to the absolute.

Due to the rotating frame of reference there is the introduction of centrifugal $\rho\,(\vec{\omega} \times \vec{\omega} \times \vec{r})$ and Coriolis force $\rho\,(2\vec{\omega} \times \vec{v}_r)$ terms, with both being inertial forces that are perceived within a rotating reference frame. The centrifugal force is equivalent to the centripetal force that would be required to maintain the path curvature within the absolute frame. While the Coriolis force expresses the change in momentum according to the radial velocity of each discrete element, due to it's apparent inertia when considered within the relative reference frame.

2.3 Sub-Grid Scale Model

For LES modelling a filter is used to separate eddies whose scales are smaller than the filter width, and differentiates the sub-grid scale from the resolved structures. A filtered variable f is denoted by an overbar and gives:

$$\bar{f}(x) = \int_D f(x')G(x, x')dx' \tag{2.12}$$

Where G is the filter function and D is the entire fluid domain.

Accurate sub-grid scale (SGS) modelling presents a significant challenge to the successful implementation of LES. Multiple factors must be taken into consideration as the SGS model must perform several functions. The model should accurately represent the energy transfer between the resolved scale and the sub-grid scale, accurately predict the turbulent dissipation, and vanish in laminar flow[93].

The original Smagorinsky-Lilly model [81] has demonstrated suitability across a wide-range of different problems, including complex three-dimensional flowfields. While it has demonstrated strength in the modelling of fully turbulent flows, it has often proved too dissipative to capture transition without grid resolutions approaching that of DNS [94]. More complex models are often being proposed that require multiple filtering operations and several coefficients to be evaluated, however, there are two issues that have prevented their wider adoption. Inherently through introducing additional terms required to be computed for each iteration, there is an increase the computational time required for the simulation. Piomelli [95] reported an increase of up to a 31% for a Langrangian model, such as that described in [96], in comparison to the original Smagorinsky-Lilly model [81]. Further to this is that these models are yet to conclusively demonstrate superiority and typically struggle in more complex three-dimensional flows [95].

In the present study LES was adopted to permit high-fidelity analysis of the flow structures developing around a bluff-body, with focus directed towards the flow rather than the numerical model itself. In a practical sense, most vehicles will have geometric features likely to trip the boundary layer near the front — as the forebody separation bubble achieves in the case of the Ahmed body. This meant the ability to capture boundary layer transition was not a critical requirement of the SGS model in this instance. Due to its previously demonstrated success in accurately capturing the flow phenomena of the considered geometry [58, 59, 65, 97], and comparatively superior efficiency, the Smagorinsky-Lilly SGS model was selected.

In ANSYS Fluent 14.5 [98] a mixing length parameter is used to approximate the turbulent length scales and this is calculated according to:

$$L_S = min(\kappa d, C_S \Delta) \tag{2.13}$$

Where L_S is the mixing length, d is the distance to the nearest wall, C_S is the Smagorinsky constant, κ is the von Kármán constant, and Δ is the local grid scale.

The subgrid-scale turbulent viscosity is then modelled according to:

$$\mu_t = \rho L_s^2 |\overline{S}| \tag{2.14}$$

Where $|\overline{S}|$ is proportional to the rate-of-strain tensor from the resolved scale of eddies.

Lilly originally derived a value of $C_S = 0.23$ for homogeneous isotropic turbulence in the inertial subrange [99], however for most engineering flows this value has been found to result in excessive damping of large scale fluctuations.

A proposed alternative to employing a fixed value is the Dynamic Smagorinsky-Lilly model [100]. This determines the Smagorinsky constant (C_S) using two separate filters. The additional test filter is twice the width of the grid filter. The flowfield is then resolved using the grid filter and the test filter, and the difference between the two resolved flowfields is used to determine the model constant. This formulation offers the benefit of not requiring the user to specify a fixed constant but is unstable. As a result the solver utilises local averaging to smooth the values, and additionally bounds the value between 0 and 0.23. While the use of this bounded directional averaging has been shown to permit accurate simulation in simple flows, the method has not demonstrated the same robustness in more complex three-dimensional flows [52].

Alternatively a fixed C_S value has demonstrated suitability for a variety of flows and is adaptable across different applications [101]. For highly three-dimensional flow with large variations in the resolved scales, a fixed Smagorinsky constant of 0.1 has been identified as suitable, and was successfully adopted in prior simulations of the same geometry [58, 59, 65, 102]. Thus it was deemed preferable to adopt a fixed C_S of the same value.

2.4 Discretisation Schemes

The incompressible simulations detailed throughout the present study were conducted using an implicit pressure-based solver. In the pressure-based approach the velocity field is first calculated from the momentum equations, followed by a calculation of the pressure field, with the solution bounded by the constraint of continuity.

For the pressure-velocity coupling a segregated approach was favoured for efficiency, using the SIMPLEC (Semi Implicit Method for Pressure Linked Equations — Consistent) [103] algorithm. The segregated approach solves each solution variable in a consecutive manner, with only one discretised equation stored in memory, permitting a reduction in the instantaneous computational expense compared to coupled methods. SIMPLEC calculates the pressure field by first solving with a guessed pressure field and then applying a correction to both the pressure field and face flux of each cell to satisfy continuity. SIMPLEC differs from the original SIMPLE algorithm in the face flux correction equation. This correction is applied using a coefficient which is expressed as a

function of the under-relaxation factor for pressure. In the present study this method was identified to aid toward more rapid convergence due to the ability to increase the pressure under-relaxation factor, allowing an overall reduction in solve time with a lower number of iterations needed to achieve convergence at each temporal interval.

The governing equations were discretised both spatially throughout the domain and temporally across the considered time interval. In the present study a second-order upwinding scheme was utilised for pressure, a bounded central differencing scheme for momentum, and a bounded second order implicit transient formulation.

The second order upwinding scheme calculates the cell face values using a Taylor series expansion of the upstream cell centred solution. In a first order scheme the face value is simply assumed to be equal to the immediately upstream cell-centred value. In the second order approach the pressure value at the face is based on both the cell centred value, and the gradient based on the further upstream cell, permitting higher solution accuracy due to a more accurate estimate of the pressure value at the face.

The use of a central differencing for momentum has been demonstrated as ideal for LES simulations due to the inherently low numerical diffusion. The central differencing scheme differs from an upwind scheme in that the face value is calculated based on both the upstream and downstream cell-centred value, and the respective gradients. Provided convergence is achieved, this leads to a theoretically pure second order solution. However in practical application this scheme it is often unstable and can introduce non-physical oscillatory flow behaviour. The bounded central differencing scheme adopts a normalised variable diagram approach [104] which allows a composite numerical scheme to be used. This consists of both a pure central differencing scheme, and a blended central differencing and second order scheme. As an additional stability measure, when a corrective boundedness criterion is violated, a first order scheme is applied to stabilise the flowfield. Thus the bounded central differencing scheme has the favourable attributes of permitting low numerical diffusion throughout the domain, and improved solution stability due to the ability to manage severe gradients and highly unsteady regions[98].

For the temporal discretisation a bounded second order implicit scheme was adopted. At each time interval the spatially discretised equations were thus evaluated for the new time step using backward differences in time. The second order scheme calculates the value at the new time-step based on both the current value, and the value calculated one time-step prior, enabling a more accurate second order estimate at the new interval. The bounded implicit scheme relates the value calculated at each cell to those in the surrounding cells, and applies two additional bounding factors which limit the difference between subsequent time intervals to aid in solution stability.

2.5 Boundary Conditions

Two configurations were used to assess the accuracy of the numerical method and are referred to as Configuration A and B. The differences between the configurations are shown in Fig. 2.1

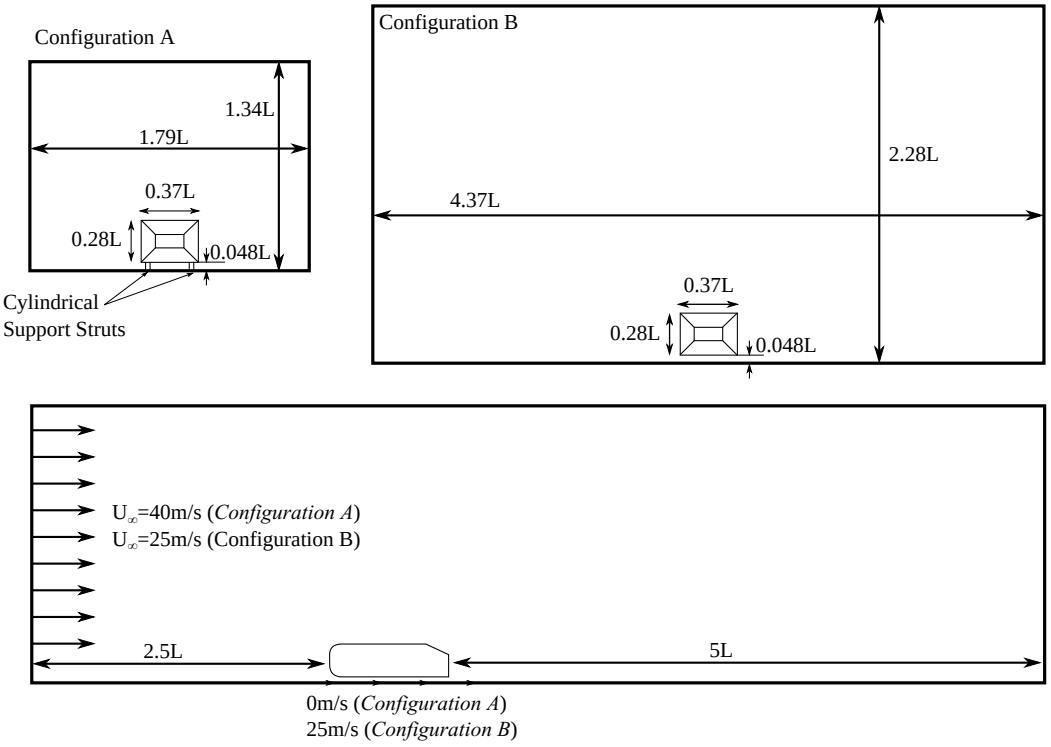

FIGURE 2.1: Overview of the configurations used to assess the numerical method

2.5.1 Configuration A

A numerical model was constructed to closely replicate the experimental configuration of Lienhart and Becker [63]. All data is publicly available and has been widely used for validation of numerical models [52–55, 57–59, 65, 80]. The experiments were conducted in a 3/4 open test-section at a length-based Reynolds number of 2.78×10^6 with an inlet velocity of 40 m/s. The wind tunnel used in their experiments had a low turbulence intensity (0.25%) which permitted the use of a uniform inlet velocity profile.

The inlet was positioned 2.5L upstream, outlet 5L downstream, and the cross-sectional extents of the computational domain were equal to that of the wind tunnel nozzle cross-sectional dimensions, in accordance with the specific ERCOFTAC (European Research Community on Flow, Turbulence and Combustion) guidelines, which were assigned to

the experimental results. The cross-sectional dimensions were thus 1.79×1.34L. Zero-shear slip walls placed on the roof and side walls of the domain, and a stationary non-slip ground condition was used to replicate the experimental configuration.

The surface of the body was defined as a non-slip boundary. Experimentally the boundary layer was tripped using a grit strip located on the nose to ensure a fully turbulent boundary layer. The cylindrical struts used to hold the wind tunnel model in the experiments were also included.

2.5.2 Configuration B

Configuration B was used for a second validation case, as well as the straight-line reference case throughout subsequent chapters. This same configuration was also used for the mesh refinement study, in addition to all yawed and cornering cases.

This configuration was intended to permit investigation of the geometry in the absence of significant interference due to the boundaries. The model was placed in a 'floating' configuration where the cylindrical support struts were removed to isolate the geometry from any localised effects caused by the struts. The domain was then extended in the y and z directions to increase the cross-sectional area and assess a suitable size to prevent any blockage effects. Three different cross-sectional areas were investigated, and are shown in Fig. 2.2, where the roof and side surfaces were moved between distances of 1L and 3L. The small, medium, and large domain sizes corresponded to blockage ratios of 3.3%, 1.0%, and 0.5%.

Blockage will result in local acceleration of the flow past the body due to the reduced cross-sectional area, and will confine the flow to cause further effects that are misrepresentation of reality. In the absence of any interference from the boundaries the static pressure on the walls should approach a constant zero distribution, and thus a freestream velocity identical to that of the inlet velocity.

Due to the computational expense of LES this initial sensitivity analysis was conducted using a RANS approach with a Realizable k-ϵ turbulence model to achieve a steady-state solution. A constant inlet velocity of 25 m/s was used which corresponded to a Reynolds number of 1.7×10^6. A pressure outlet was positioned downstream, with a zero-shear condition for the side-walls and roof, while translational motion the ground plane was also included such that the motion of the ground relative to the freestream flow was zero [105, 106]. The fine grid structure was adopted, and is described in more detail in Section 2.6. Drag and the pressure integral over the wall surfaces were monitored throughout the simulations which converged over 5000 iterations. Drag reached a

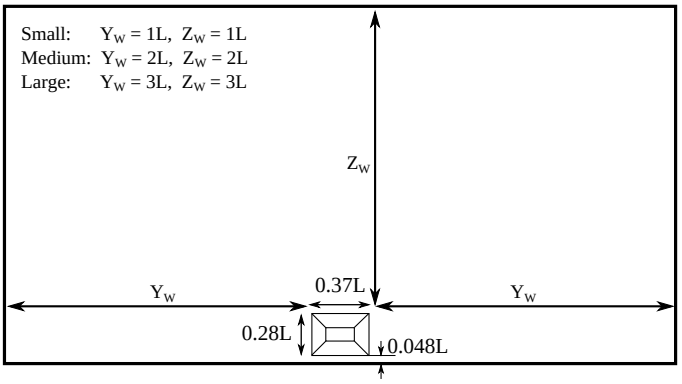

FIGURE 2.2: Cross-sectional dimensions used to assess the influence of blockage ratio and boundary proximity

continuous oscillatory state where the value remained within ±0.21% of the mean over the final 1000 iterations, with the mean value reported. From these results the pressure gradients at the boundaries were analysed to assess the boundary influence with respect to the gradients occurring over the body itself, in line with the method used by Strachan [107].

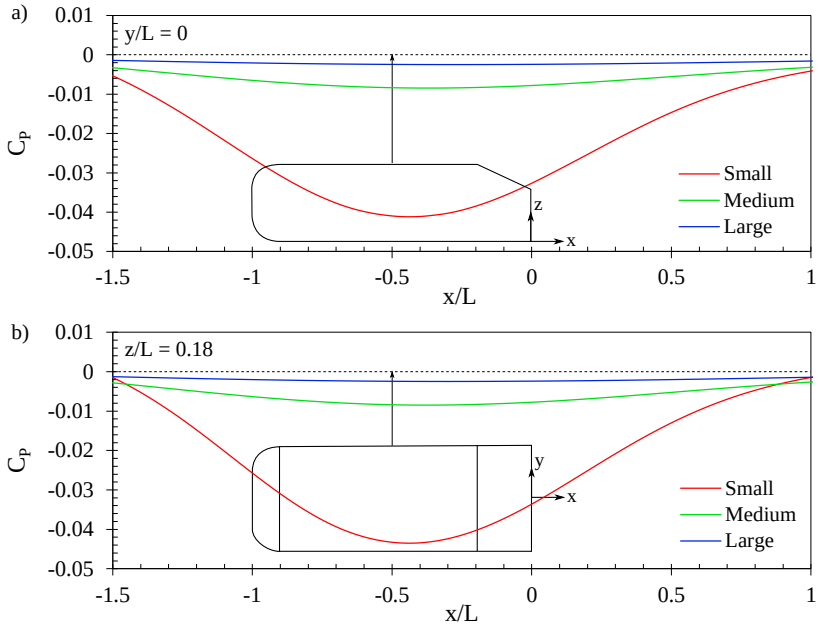

FIGURE 2.3: Pressure coefficient profiles used to assess the boundary influence on the a) roof surface at y/L = 0, b) side surface at z/L = 0.18

Pressure coefficient profiles shown in Fig. 2.3 extended 0.5L upstream of the body and 1L downstream, and were extracted at the centre of the roof surface, and along the side-walls of the domain at z/L = 0.18. For the small domain the maximum wall gradient was $0.046\frac{C_P}{x/L}$ on the roof, and $0.055\frac{C_P}{x/L}$ on the side-walls, where a minimum pressure

coefficient of -0.043 occurred due to the acceleration of the flow past the body due to blockage, correlating to a local increase of 0.011 u/U_∞.

For the medium and large domains the effects were milder, where respective gradients of 0.0067 and 0.0014 occurred over the roof, and $0.0073\frac{C_P}{x/L}$ and $0.0016\frac{C_P}{x/L}$ over the side-walls. Pressure coefficient minima were -0.0085 and -0.0025 for the medium and large domains which corresponded to maximum local freestream velocity changes of 0.0048 u/U_∞ and 0.0026 u/U_∞. Due to these effects the small domain predicted a mean drag value that was 2.92% greater than the large domain, while the medium domain resulted in a milder comparative increase of 0.31% based on the steady-state estimate.

The medium domain was selected as most suitable in the present case, given the minor predicted influence toward the numerical results and moderate computational expense. This resulted in overall cross-sectional dimesions of 4.37×2.28L, with the domain extending 2.5L upstream and 5L downstream, as shown in Fig. 2.1.

2.5.3 Boundary Conditions for Cornering and Yaw

Boundary conditions and the geometric structure of the domain have differed amongst previous studies of the cornering condition [4, 5, 12]. In this instance a rectangular domain configuration was used with inlets and outlets positioned along the walls as is shown in Fig. 2.4a). This method permits the evaluation of multiple corners utilising the same mesh, and would also offer the benefit of allowing dynamic simulations incorporating variable curvatures and directions.

In the present work only steady-state, constant radius corners were considered. The correct flow conditions were achieved through the use of a single rotating reference frame applied to the entire domain, where the motion was defined by prescribing an angular velocity about an external point. The distance of that point to the centre of the body being equal to the corner radius.

The relative velocity formulation was used, thus all velocity values are specified from within the rotating reference frame — considering the fluid in motion rather than the body. The inlet condition was zero in the absolute reference frame. The inlet condition can be understood as representative of the domain moving through stationary flow, rather than flow moving through the domain.

All cornering conditions shown throughout the present study are left-hand corners. Due to the symmetry of the geometry, both left and right-hand corners would be equivalent.

For consistency all cases adopted this specification of using motion of the domain to create the correct flow conditions, rather than an inlet velocity — even for the straight-line

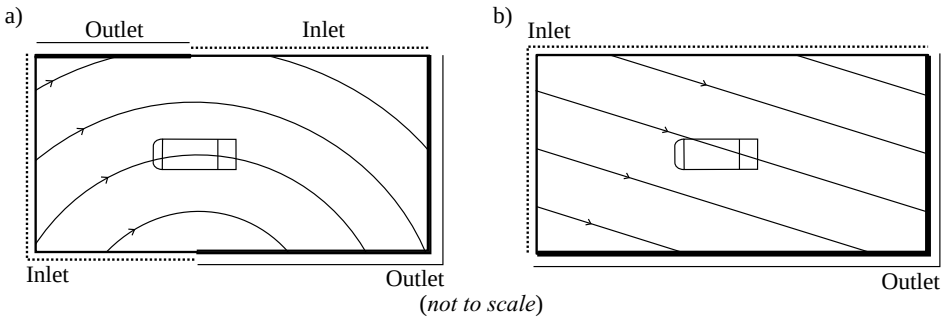

FIGURE 2.4: Inlet and outlet boundary conditions used for a) cornering cases and b) yawed cases

and yawed conditions. Adopting the relative velocity formulation made these conditions synonymous to an inlet velocity. The yawed condition was achieved through positioning an inlet and outlet along the respective sides of the domain, as is shown in Fig. 2.4b). The cross-flow component was specified as directed from right to left in all instances. This ensured that the flow angle was in the same direction leaving the rear of the body and made for improved comparison between the two wake regions. The domain was assigned a translational motion of 25 m/s at the respective yaw angle, in order to reproduce the correct flow angle at the body. This permitted the same grid to be used for simulations and ensured spatial consistency between results.

2.6 Spatial Resolution Requirements

Grid construction is critical for accurate LES, and this stems from the need to ensure that the problem-dependent turbulent structures are resolved. The guidelines proposed by Pope [108] recommend that 80% of the turbulent energy anywhere in the domain must be resolved for an accurate LES simulation, and grid resolution is most critical near the wall.

Since the 1980's the understanding of turbulent boundary layers has rapidly improved through the use of numerical simulation [109]. DNS is typically regarded as being more accurate than experimental results due to the control that can be exerted over the inflow conditions and the ability to measure flow characteristics in the absence of any intrusion [110]. Due to the significant computational expense of this method, it has only been recently that simulation at Reynolds numbers approaching practical values have been achieved.

The majority of the turbulence production will occur within the thin buffer region of the boundary layer, and is attributed to the inflow of high-speed flow, and corresponding

ejection of low-speed fluid parcels [109]. For wall-resolved LES a grid resolution is required that is sufficient to capture these phenomena, which remains prohibitive in most instances. More importantly, in the case of the Ahmed Body geometry, accommodation must be made for the multiple separation bubbles occurring over the body [77]. For separation and reattachment of a turbulent boundary layer over a flat plate Na and Moin [111] identified vortical structures to be lifted from within the inner boundary layer region, up into the shear layer forming above the separated region. The separation bubble was observed to behave similarly to a streamlined body being placed in the flow, transporting boundary layer structures above its location. In the present case it needs to be ensured that cell density remained sufficient above these regions to resolve the small structures exiting into the shear layer.

Thus accurately resolving the separation regions was critical toward the development of the larger flow structures and simulation fidelity in its entirety. Chapman's[112] early estimate of a suitable near-wall resolution was $\Delta x^+ \approx 100$, $\Delta y^+ \approx 20$, with $n_y \approx 10$. More recent estimates suggest a first cell height at the wall giving a $y^+ < 1$, and a streamwise and spanwise resolution of $\Delta x^+ = 50 - 150$ and $\Delta y^+ = 15 - 40$, with $n_y = 10 - 30$ [93, 113] being widely suitable.

Adopting the guidelines of Piomelli and Chasnov [93], Krajnović and Davidson [58] calculated the necessary spatial resolution required for the flowfield around an automotive scale bluff body at Re $\approx 1.8 \times 10^7$ as 6.1×10^8 cells — a number that remains far from practical in most instances. This highlights the present difficulties in using wall-resolved LES for full-scale simulations of a complexly featured geometry, and why it remains a technique more commonly adopted in research.

As a result of the prohibitively high computational expense at full scale Reynolds numbers, the present study considered a smaller scale geometry, and thus reduced Reynolds number. This is a methodology adopted in most previous experimental and numerical studies, and has been identified to be appropriate for the Ahmed body due to the clearly defined geometric features resulting in flow structures retaining their location. Thus Re $= 1.7 \times 10^6$ was adopted and permitted the use of a more manageable final grid size.

Structured grids were constructed using ICEM 14.5 and consisted entirely of hexahedral cells, as is shown in Fig. 2.5. A multi-block method of construction was adopted, and the grid was reflected about the z-x plane to ensure a symmetrical distribution of cells. A separate strategy had to be employed to accommodate the cylindrical struts present in Configuration A, but the number of cells at the surface in the x, y, and z directions remained identical to Configuration B.

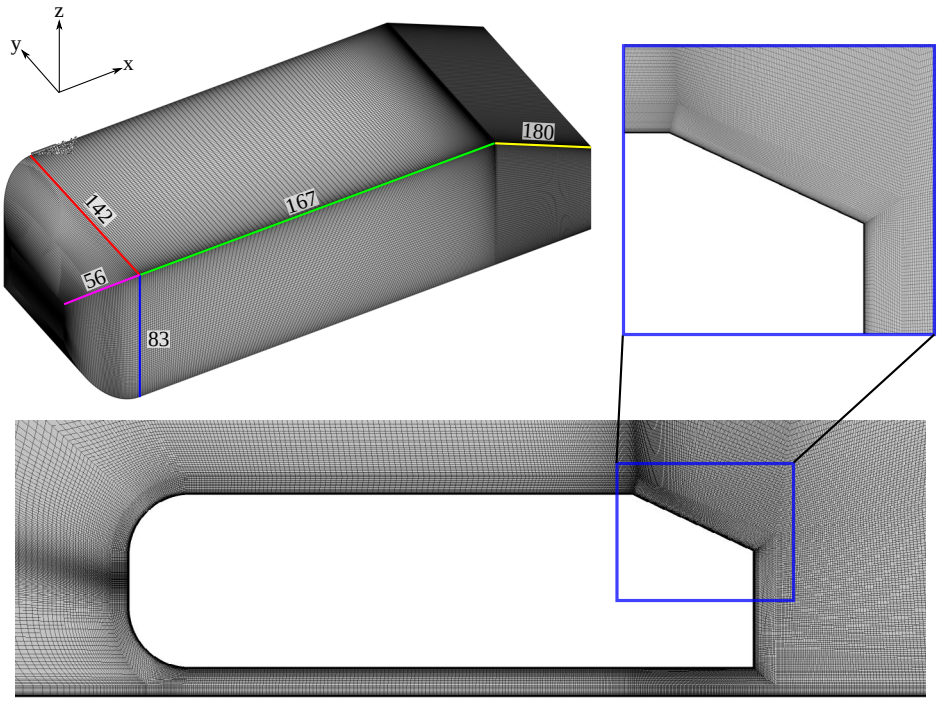

FIGURE 2.5: Element divisions in each direction over the geometry surface for the fine mesh

Cells were concentrated in the backlight region and also in the near wake. A slow growth rate away from the trailing face ensured a high concentration of cells to resolve the near wake region. Other regions of interest were identified to be the forebody region and also near the sharp edges along all sides where an increased resolution was also allocated.

2.7 Grid Convergence Study

In light of the number of different conditions assessed throughout the present study, 3.0×10^7 was the upper limit of a practical grid resolution given available resources and was the cell count for the fine grid. Coarse (1.05×10^7) and medium (1.76×10^7) density meshes were compared to the finest grid asses the effects of spatial resolution on results. The three grid densities were investigated using a common time-step of of 1×10^{-4} L/U_∞, which is explained in more detail in the following section.

The coarse and medium meshes predicted drag coefficients that were 4.23% and 1.95% greater than the fine mesh. While the lift coefficient demonstrated an irregular change between the different grid densities, being only 0.10% lower for the coarse grid but 1.85% higher for the medium grid solution. The pitching moment was higher for the coarse and medium meshes, exceeding the fine mesh value by 2.66% and 0.56% respectively.

TABLE 2.1: Drag, lift and pitching moment coefficient as measured for three mesh densities

Grid Density	No. Cells	C_D	C_L	$C_{M\theta}$
Coarse	1.05×10^7	0.3374	0.2865	-0.1286
Medium	1.76×10^7	0.3300	0.2921	-0.1259
Fine	3.0×10^7	0.3237	0.2868	-0.1252

The separated flow regions around the body are critical to the overall aerodynamic characteristics. Separation bubbles occur at the forebody aft of the nose curvature, and at the start of the backlight. In addition to a region consisting of two recirculations which form at the trailing face, as shown in Fig. 2.6.

As the mesh density increased, the predicted forebody separation bubble increased in size. The coarse grid predicted a maximum height (H_F) that was 52.2% less than the fine grid result, with a separation length (SL_F) that was 46.1% shorter. The fine grid predicted a separation bubble which spanned further across the width of the upper face. This corresponded to the emission of larger vortical structures from within the separation region and further interaction predicted between the front and the rear of the body. This also caused an effective increase in the frontal area, and higher pressure over the nose surface, resulting in a proportionally larger contribution toward the drag coefficient for the fine grid result in comparison to the coarser meshes.

The opposite effect was observed for the backlight separation bubble, whereby the increased cell density corresponded to the prediction of a comparably smaller separated region. In the instantaneous flowfield this region consists of spanwise vortices which merge within the backlight separation region and are ejected. This mechanism has proved elusive in wall-modelled simulations due to the high turbulent stresses [55] and the small spanwise structures which initiate the sequence. For the coarse and medium grids this mechanism still occurred but the initial vortex structures were observed to be correspondingly larger, and enhanced the time-averaged size of this region.

The coarse grid predicted a separation bubble that extended 48.1% further down the backlight face at $y/L = 0$, and had a maximum height that was 81.6% greater than the fine grid prediction. The medium grid predicted a smaller difference, with the bubble again being bigger but only extending 13.3% further down the face. This was attributed to two effects, firstly the reduced interaction between the front and rear of the body for the coarse grid resulted in a loss of energy transfer to the rear separation bubble from the emitted forebody structures. Secondly, the reattachment line fails to continue to the upper corners as the separation bubble assumes a more spanwise orientated shape, differing from the mildly arched shape which begins from a defined point in the fine grid.

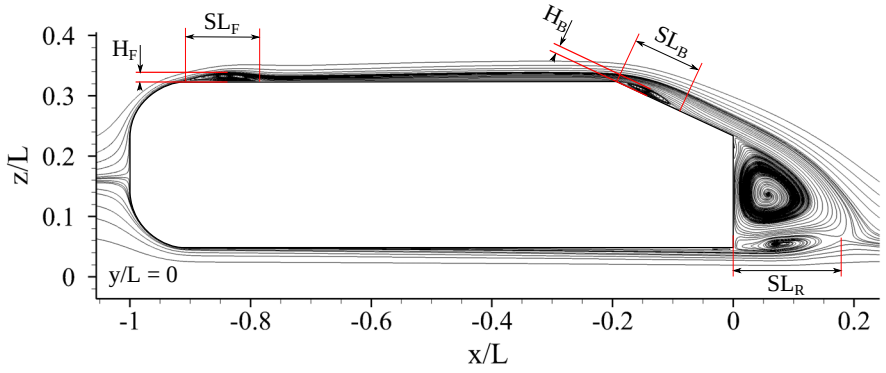

FIGURE 2.6: Separated flow regions around the 25° Ahmed body and their location

TABLE 2.2: Length and height of separated flow regions measured at y/L = 0 for three mesh densities

	Dimension (L)				
Grid Density	SL_F	H_F	SL_B	H_B	SL_R
Coarse	0.076	0.0072	0.185	0.0213	0.154
Medium	0.112	0.0099	0.141	0.0148	0.158
Fine	0.141	0.0151	0.125	0.0118	0.179

The pressure distribution over the upper surface of the body was a further difference noted between grid densities. Figure 2.7 indicates a reduction in the suction peak occurring at the backlight angle due to the increase in size of the separation bubble and the flow assuming a more slight curvature at this location. This was measured to be 11.2% and 1.3% less in magnitude for the coarse and medium meshes. The contraction of the separated region occurring at the rear face also resulted in increased acceleration of the flow down the remainder of the backlight face with a correspondingly reduced surface pressure.

The similar lift prediction between the coarse and fine meshes was due to these two changes having a similar net effect. For the medium grid the lower pressure over most of the backlight surface with only a mild reduction in the suction peak caused a more significant increase in lift coefficient compared to the fine grid, despite the greater similarity between flow structures.

The prediction of the central near wake is shown in Fig. 2.8 with minor differences noted between the three different grid resolutions. For the x-velocity component shown in Fig. 2.8a) the initial wake deficit at x/L = 0.1 was similar for all three cases, however at the further downstream locations the fine grid deficit was observed to exceed that of the coarser meshes. This was due to a comparatively extended separated region at the trailing face of the body. Due to the relative contraction for the coarser grids an

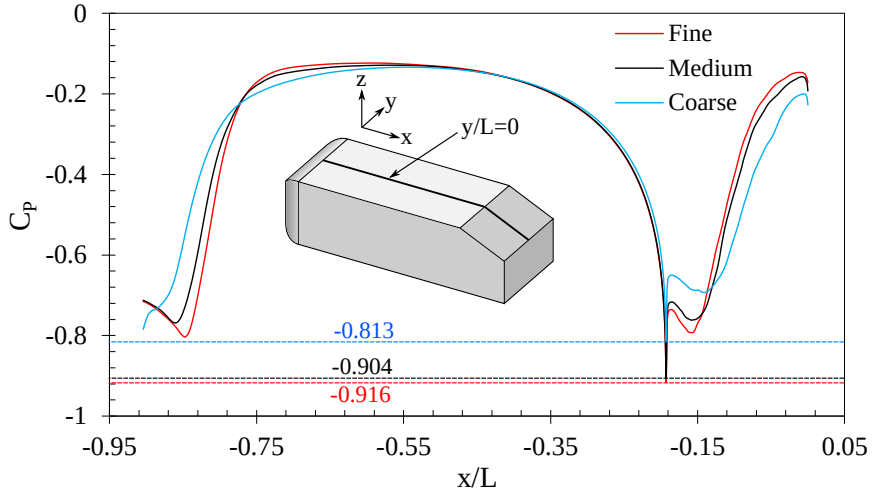

FIGURE 2.7: Pressure distribution over the upper surface for the three grid densities

increased downwash angle was observed off the rear slanted surface causing a lower z-velocity component for the medium and coarse grids.

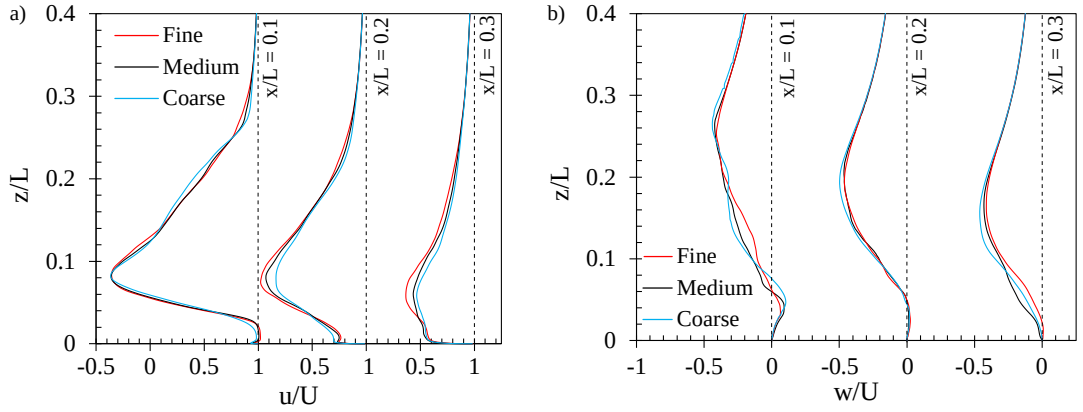

FIGURE 2.8: Wake velocity profiles of the a) x-component, and b) z-component for the three grid densities

The finest achievable grid resolution was deemed most suitable given the selected numerical method, and also the demonstrated effects toward both flow structures and aerodynamic force coefficient predictions. This grid had a consistent first cell height of 0.01 mm over the body surfaces and the ground, which ensured the maximum y^+ value remained below 1. An offset surface of the geometry was used as a guide for the generation of the near-wall layers, which adopted a growth rate of 1.1, and ensured that cells were closely aligned to the normal direction of the surface. At the trailing face a growth rate of 1.05 was applied beyond the near-wall cells and in the downstream direction. An increase in cell-size driven by a cubic spline was applied to the front, top, backlight, and

side surfaces. This ensured cell concentration was maintained in regions with large flow gradients, and relaxed further from the surface.

The average Δ^+ values of the final grid in the streamwise and spanwise directions for each surface are listed in Table 2.3. The distribution highlights the concentration of cells on the nose surface and over the backlight to improve resolution of critical features, resulting in low values of this parameter. The trailing face is omitted in this instance as the flow remained separated over the surface.

TABLE 2.3: Averaged grid Δ^+ in the streamwise and spanwise directions for each body surface

	Δ^+	
Surface	Streamwise	Spanwise
Upper side	169.7	40.5
Under side	101.3	24.1
Backlight	23.5	32.8
Nose	63.6	-
Side	113.1	35.9

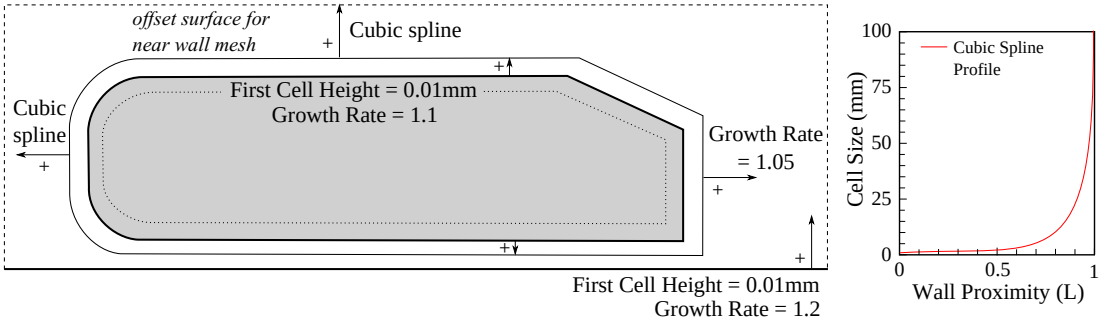

FIGURE 2.9: First cell height and growth rates applied to the surfaces of the Ahmed body geometry for the fine grid

Ultimately the finest grid failed to resolve the boundary layer with turbulent fluctuations falling into the sub-grid scale, despite approaching previously proposed spatial resolution guidelines [93, 113]. More critical was capturing the prominent separated flow regions and the structures ejected from the shear layer, which were favoured as local regions where a high cell concentration was placed.

2.8 Temporal Requirements

The temporal resolution is largely determined by grid dimensions, but must also be suitable to resolve the motion of flow structures. Time was non-dimensionalised according

to the a single fluid particle to travelling the length of the body, and a time-step of 1×10^{-4} $L/U_\infty s$ ensured a maximum CFL number of 0.95 for all simulations, rendering it suitable for the highest frequencies able to be captured by the grid.

The solution was initialized from a Realizable k-ϵ RANS solution and then followed by a series of initial time-steps to bring the flowfield to a developed state before any data was time-averaged or recorded. Frequency analyses based on velocity measurements were conducted at points located within the upper boundary layer, backlight region and near wake. These identified a number of separate peaks in the spectrum for any given location – contributing to the lack of easily recognisable periodic behaviour. Before a developed state was deemed to have been met, it was ensured the median velocity magnitude values fell within 0.5 m/s at all measurement locations for two successive complete passages of the flow over the body. It was determined that 4×10^4 time-steps ensured a suitable initial state was achieved, and this was used for all cases.

In order to obtain the time-averaged aerodynamic characteristics one needs calculate the mean value for each parameter over a series of timesteps. Ideally this time interval should be sufficient such that parameters become independent of time. In reality there will continue to be very small changes in the mean flowfield due to the transient nature of the flow. Dependent on the exact point at which the averaging period is commenced and ended, the time-averaged flowfield will continue to change but to a progressively smaller degree. This is particularly the case for a geometry such as the Ahmed body which exhibits mechanisms operating across a range of time and length scales. In this instance a suitable solution averaging period was found to be $(tU_\infty)/L = 10$ (1×10^5 time-steps).

The length of the averaging period was determined through monitoring of the mean velocity and pressure on downstream planes. In Fig. 2.10 the mean x-velocity between two different points in the time-averaged period are compared to determine the Δu distribution. Both the straight-line condition and a 5 length radius corner were considered. Figure 2.10a) and b) show the difference between time-averaged x-velocity after 2.5×10^4 timesteps and the initial instantaneous flowfield. While Fig. 2.10c) and d) show the difference between time-averaged x-velocity when comparing the final timestep of 1.0×10^5 and the earlier point of 7.5×10^4. In this instance $x/L = 0.5$ is shown as this was a region with low-frequency transient flow mechanisms, and was thus more changeable throughout the averaging time in comparison to other regions around the body. A further assessment used for the straight-line case was also to inspect the flowfield symmetry. In both cases it can be observed that over the final 2.5×10^4 time-steps the time-averaged velocity distribution changed by less than $u/U_\infty = \pm 0.02$, and this finding was consistent for all cases detailed throughout the present work.

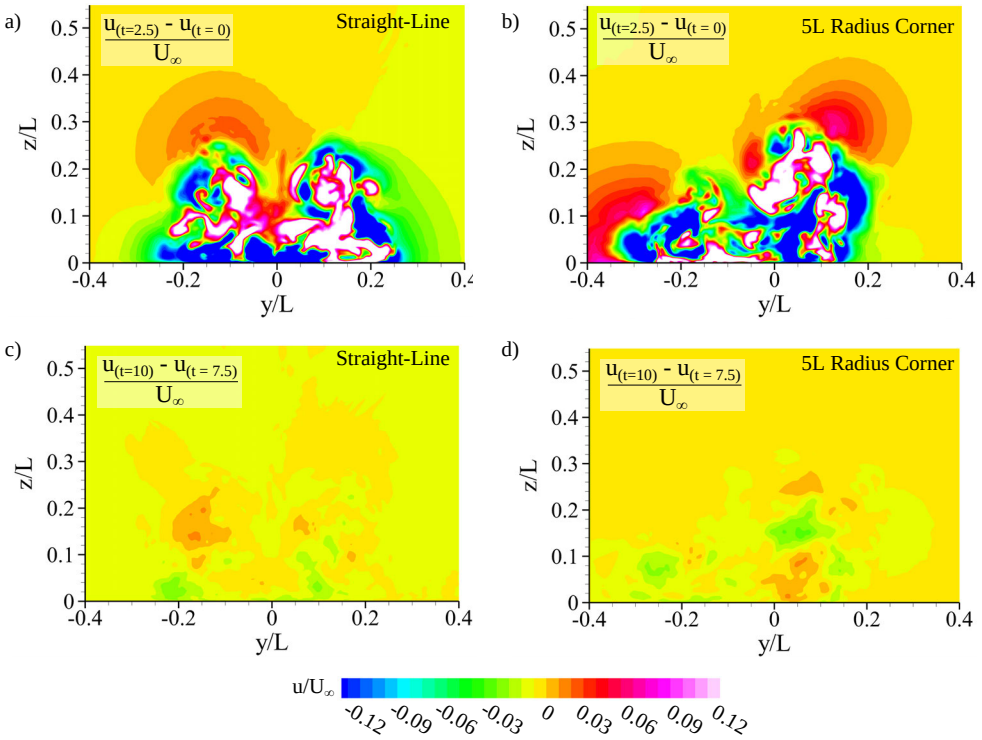

FIGURE 2.10: Difference in the time-averaged velocity field measured on a downstream plane throughout the averaging period for the straight-line and a 5L radius corner

In addition, mean force and moment values, and three point velocity measurements, were monitored to ensure these reached a converged value throughout the averaging period. Results are shown for the straight-line case and the smallest radii cornering case in Fig. 2.11. Over the last 1×10^4 iterations the mean value for all force and moment coefficients ceased to change by more than ± 0.0014. Velocity point measurements varied by an average of ± 0.0034 u/U_∞, and maximum of ± 0.0087 u/U_∞ throughout the same interval. These combined results demonstrated the achievement of a suitable time-averaged flowfield representation.

2.9 Vortex Analysis

Subsonic aerodynamic flowfields are often dominated by vortical structures and thus the adoption of suitable methods for identification and characterisation becomes necessary. Unfortunately therein lies the problem, as there isn't consensus on the best parameter for a quantifying a vortex [114]. The questions surrounding the entire concept of vortices can range from practical to existential. It is a difficult topic to address and continues to be an area of dedicated research. A number of techniques have been proposed, with some more widely adopted than others.

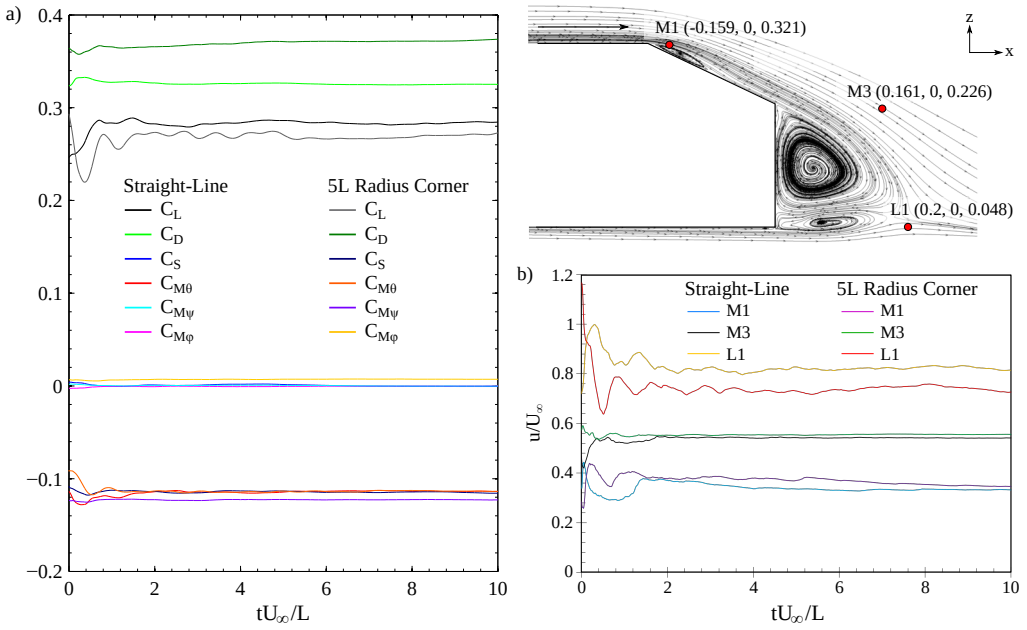

FIGURE 2.11: Convergence of the a) time-averaged force and moment coefficients, and b) point velocity measurements in the wake throughout the averaging interval

A primary complication is the fundamental difficulty in defining a vortex [115]. They are commonly assumed to be regions of high vorticity or coherent structures but these definitions remain qualitative, rather than defined and quantitative. Flows with complex interacting vortices limit nearly every proposed method of identification and quantification. Vorticity can also be high in shear flows where no vortices are present [116], and 'coherent structure' is an ambiguous term in itself. Furthermore, the time-averaged flow is typically of more interest from a design perspective, however this flow structure is simply a mean representation of a typically far more complex field that will occur in reality. In this way a time-averaged vortex can be indistinguishable when observing the instantaneous flow structure. Ultimately, the techniques used in the present work have been selected given the specific context of the problem, and thus can't be considered universally suitable.

Within the field of automotive aerodynamics, the identification criterion that has been most widely adopted is the Q-criterion [117]. This has proven to be a robust parameter that is suitable across a wide range of flows. Q is the second invariant of ∇u and is defined as:

$$Q = \frac{1}{2}(||\Omega||^2 + ||S||^2) \tag{2.15}$$

Where S is the symmetric component of ∇u:

$$S_{ij} = \frac{1}{2}(u_{i,j} + u_{j,i}) \tag{2.16}$$

And Ω is the antisymmetric component:

$$\Omega_{ij} = \frac{1}{2}(u_{i,j} - u_{j,i}) \tag{2.17}$$

Q is a measure of the local balance between shear strain rate and vorticity magnitude [115]. However the use of the criterion necessitates care. The value of Q that is used will only show a trimmed representation of the vortical flowfield, where some features and interactions may be observable in the absence of others.

For a quantitative parameter to give a measure of vortex strength, the total circulation was obtained from integration of vorticity [118], however this again has limitations. For complex vortical structures there are difficulties in defining the vortex boundary and interactions can again skew measurements from being objective [114]. Circulation and decay rate is dependent on the radius from the core. As such, the averaged circulation becomes a more practical value, but cannot be assumed as continuous along a vortex tube.

A vortex will also typically be characterised as having a central low-pressure region — and is a condition for some identification criterion [115, 117]. Pressure minima is a result of the balance between radial forces in rotating flow. Several limitations occur when considering viscous, three-dimensional flows. Flow conditions exist where a pressure minima is not necessary for the existence of a vortex [119], however, this pressure deficit due to the rotating motion occurs in most engineering flows, and can serve as a reasonable further parameter to assess the effect of the structure.

For the Ahmed body the C-pillar vortices are critical flow structures which affect the flow characteristics over the backlight surface, resulting in cumulative effects further downstream. Due to the particular importance of this feature a method was adopted to allow quantification of the strength based on both the circulation and pressure deficit.

Due to the difficulty in determining the boundary of a vortex within a complex system an alternative approach was used. Instead, a simple geometrically defined interrogation region was used which remained constant for all simulations. These regions are shown in Fig. 2.12 and were taken from x/L = 0 to -0.1. The position and size were selected to ensure the vortex core position (identified as the location of maximum Q) for all simulations was contained on the plane and qualitative assessment that the surrounding region of high vorticity was also captured. From the time-averaged flowfield the location of the core position was tracked on these planes over the backlight face and the trajectory measured to be at a negative incline of 18° from the x-axis. There was also a mildly angled trajectory in the y-direction, however this was more asymptotic and realigned with the freestream condition as it continued downstream. The normal vorticity component

aligned with this core trajectory was thus calculated then integrated over the plane to give a measure of circulation strength.

$$\Omega_n = \Omega_x cos(-18) + \Omega_z sin(-18) \tag{2.18}$$

$$\Gamma_n = \int \Omega_n dA \tag{2.19}$$

Similarly the static pressure was integrated over the plane for a second quantitative measure based on the static pressure deficit in the core.

$$C_{p,n} = \int C_p dA \tag{2.20}$$

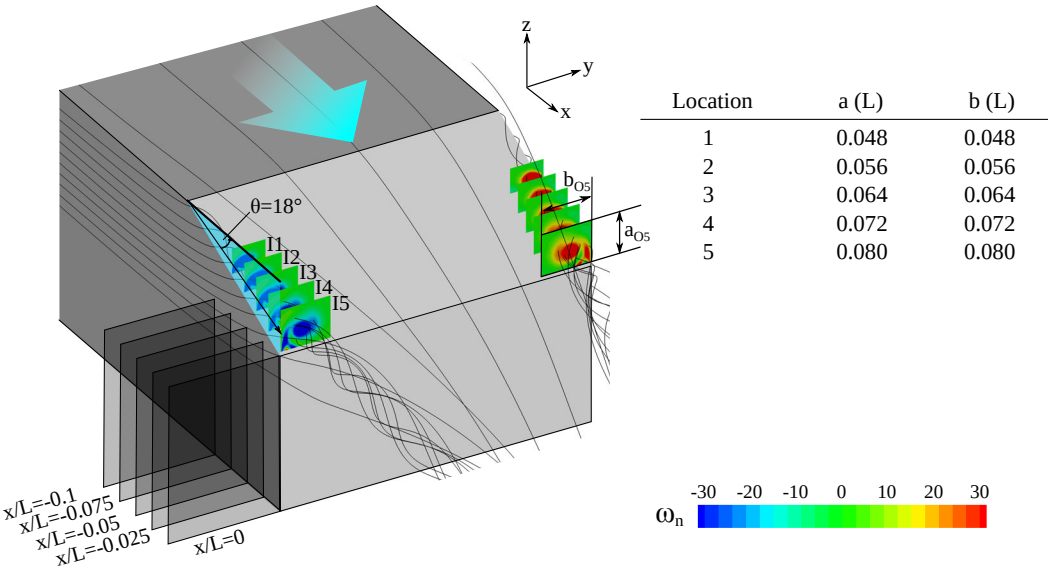

Location	a (L)	b (L)
1	0.048	0.048
2	0.056	0.056
3	0.064	0.064
4	0.072	0.072
5	0.080	0.080

FIGURE 2.12: Locations of measurement planes for determination of circulation strength parameter and pressure deficit

2.10 Critical Point Flow Theory

A method used for detailed analysis was critical-point theory which is often used for interpreting complex flow fields through patterns emerging on a surface[120]. These patterns correspond to the presence of flow structures and can be used to identify features within both the time-averaged and instantaneous flowfield. Examples of the most common type of structures identified are shown in Fig. 2.13.

Nodes are point locations of converging or diverging fluid paths where a stable node is a convergent point, and an unstable node is divergent. Focii occur due to the presence of rotational structures on the plane of observation. Saddle points will emerge at the

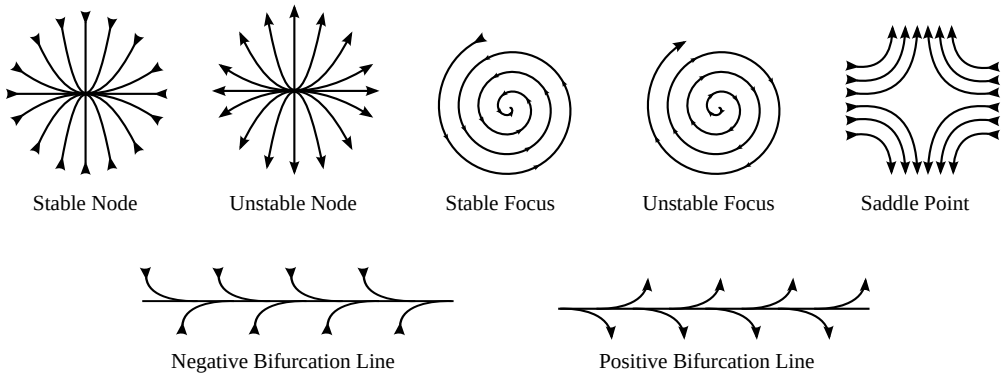

FIGURE 2.13: Critical flow points used to assist in the identification of flow structures

location between two rotating flow structures. Three-dimensional structures can often have different types of motion dependent on the plane upon which they are observed. Combinations of nodes, saddle points, and focii can commonly be observed for different planes taken through the same structure.

In reality, degenerate structures will also form which will not perfectly match the simple structures shown in Fig. 2.13. Dislocated saddle points are common features within a vortex sheet off an object such as a wing, whereby the junction between the vortical structures is offset due to the von Kármán street shedding mechanism. Another example is a star node, where the flow pattern is directly towards a central node, rather than the parabolic curvature shown in Fig. 2.13.

Bifurcation lines show the positions of flow separation and reattachment on a surface and were thus commonly used to quantify flow structures in the present work. They mark the location of intersecting fluid trajectories and form an asymptotic structure. A positive bifurcation is used to identify a line of reattachment on a surface, while a negative bifurcation denotes a line of separation.

2.11 Validation of Numerical Model

The experimental data of Lienhart and Becker [63] was deemed most suitable to be used as the basis for quantitative assessment of the time averaged flow structure. As was discussed in Subsection 2.5 a separate numerical model was specifically created for comparison to these results. The second 'floating' configuration was used for validation against the results of other studies to assess additional criteria.

2.11.1 Rear Flow Structure

The separated flow structures occurring at the rear of the body have been the subject of a large number of prior investigations. The initial assumption made by Ahmed et. al [40] was that the level of interaction between front and rear was minimal, thus making it appropriate to consider the rear in isolation. Recent investigations have demonstrated this to not be the case, and there are indeed flow structures which travel the length of the body and demonstrate front to rear interaction, as will be discussed further.

The rear region consisted of five distinguishable flow features which are shown in Fig. 2.14. In addition to the C-pillar vortices which originated from the edges of the backlight face, two separation bubbles also developed at the rear. One was located at the start of the backlight surface, and the second occured at the trailing face. The backlight separation bubble primarily contained a vortex which assumed a mildly arched shape and initiated near the upper edge. The trailing face separation bubble consisted of two regions of recirculating flow, and formed a dual vortex type structure where the upper recirculation (in the time-averaged sense) was significantly larger than the lower. These regions formed through the rolling of the shear layers off the upper and lower surfaces of the body.

The C-pillar vortices suppressed secondary flow feature formation beneath their location and promoted reattachment of the flow down the backlight surface. The shear layer off the backlight surface was concentrated centrally due to their presence and fed into the upper recirculation about the centre. With the upper recirculation drawing flow at the centre of its span it was observed to spiral outwards towards either side of the body.

In the time-averaged sense the upper recirculation also induced flow from the lower structure into its core region about the either side of the face, observed most clearly in Fig. 2.14b). Alternatively, at the same location, the outer part of the upper recirculation was drawn out and around the C-pillar vortex, while The lower recirculation was also partially induced around the C-pillar vortices. Thus flow exiting the separation bubbles was ultimately drawn into the two longitudinal vortices that resulted in the two large counter-rotating vortical structures downstream.

2.11.2 Near Wake Structure

Wake profiles of both x and z-velocity components along the symmetry plane were taken on several downstream locations and compared to experimental LDA results, as is shown in Fig. 2.15. These indicated both the time-averaged wake deficit and the wake dissipation were captured correctly by the numerical model. Profiles of the vertical

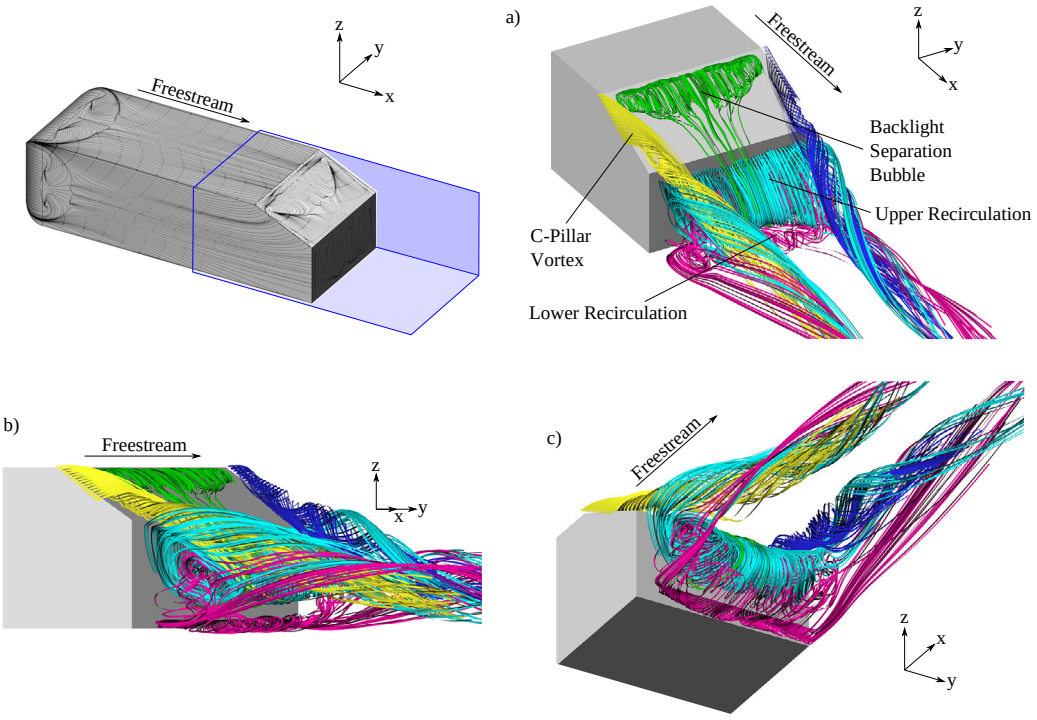

FIGURE 2.14: Streamlines released from within prominent rear flow structures a) upper isometric view b) side view c) lower isometric view

velocity component ensured the flow angles off the backlight and the lower surfaces were also accurately modelled. A noted discrepancy was the under-prediction of the vertical velocity component within the lower part of the wake, as evident on profiles x/L = 0.132-0.228 in Fig. 2.15b). In conjunction with a more significant x-velocity deficit at x/L = 0.228 in the numerical model, this would suggest an over-prediction of the wake separation bubble. Despite this, the largely favourable agreement with the experimental results demonstrated the ability of the numerical model to capture the flow characteristics along the symmetry plane, however further analysis of the entire wake structure was required to assess the validity beyond this location.

Velocity contours from taken on planes at x/L = 0, 0.077, and 0.48 were compared to time-averaged experimental results, as is shown in Fig. 2.16. The shape and position of the dominant C-pillar vortices was captured along with the velocity deficit in the core. A point of difference was the shear layer shedding from underneath the model which also aided toward an explanation of the lower wake discrepancy in Fig. 2.15b). Experimentally, an even layer left from underneath the model however the numerical model indicated a more central concentration of the deficit.

In the numerical model the higher criticality of the backlight, edges, and the forebody dictated the assignment of a high cell concentration in these regions, which was at the

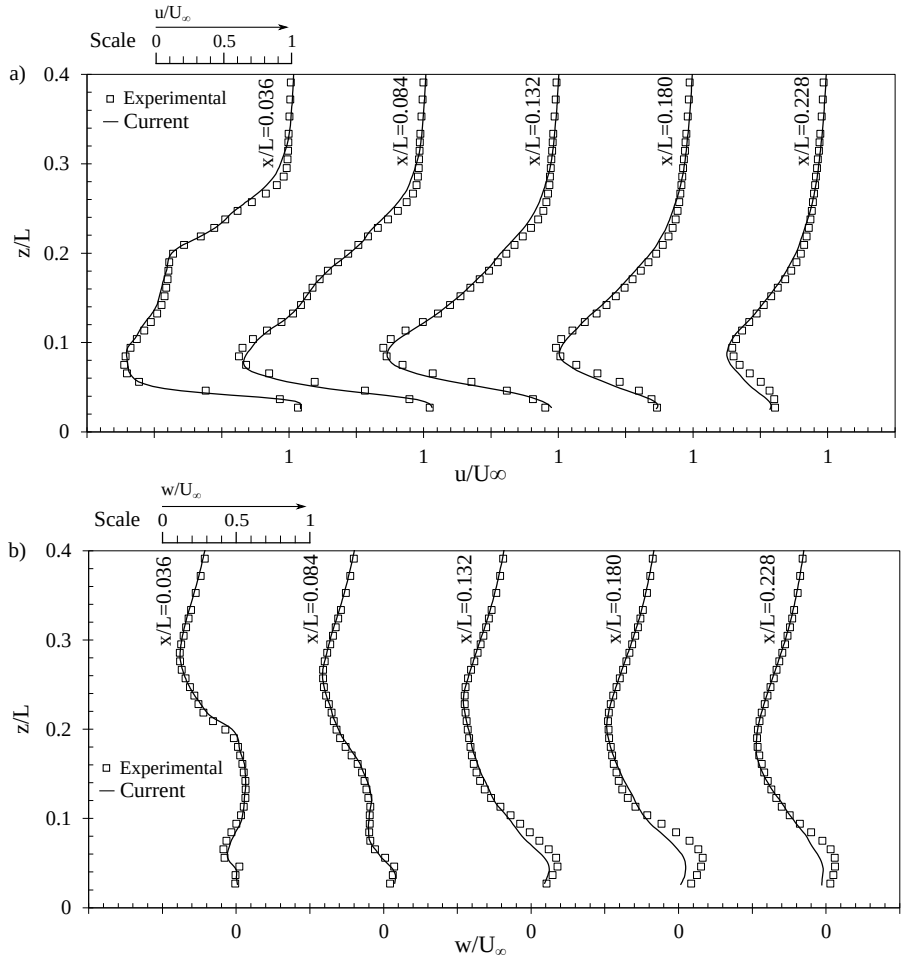

FIGURE 2.15: Experimental and numerical wake profile comparison of a) non-dimensional x-velocity, and b) non-dimensional z-velocity

expense of mesh resolution in regions such as the wake of the struts. While the wake structure of the struts was captured, the cell growth rate off the surface numerically diffused this region contributing to a misrepresentation within the model. As these struts were not present for any further cases this was of lower importance compared to accurately capturing the flow over the backlight and upper surfaces of the body, and was deemed an acceptable compromise.

2.11.3 Backlight Structure

A survey of static pressure coefficient over the backlight surface was undertaken in the reference experiments and this was compared to the numerical simulations, as shown in Fig. 2.17. The results indicated similarity in both the presence of key flow features and their location. The low pressure regions attributed to the presence of the C-pillar vortices extending down either side of the surface are observed in both results, as well

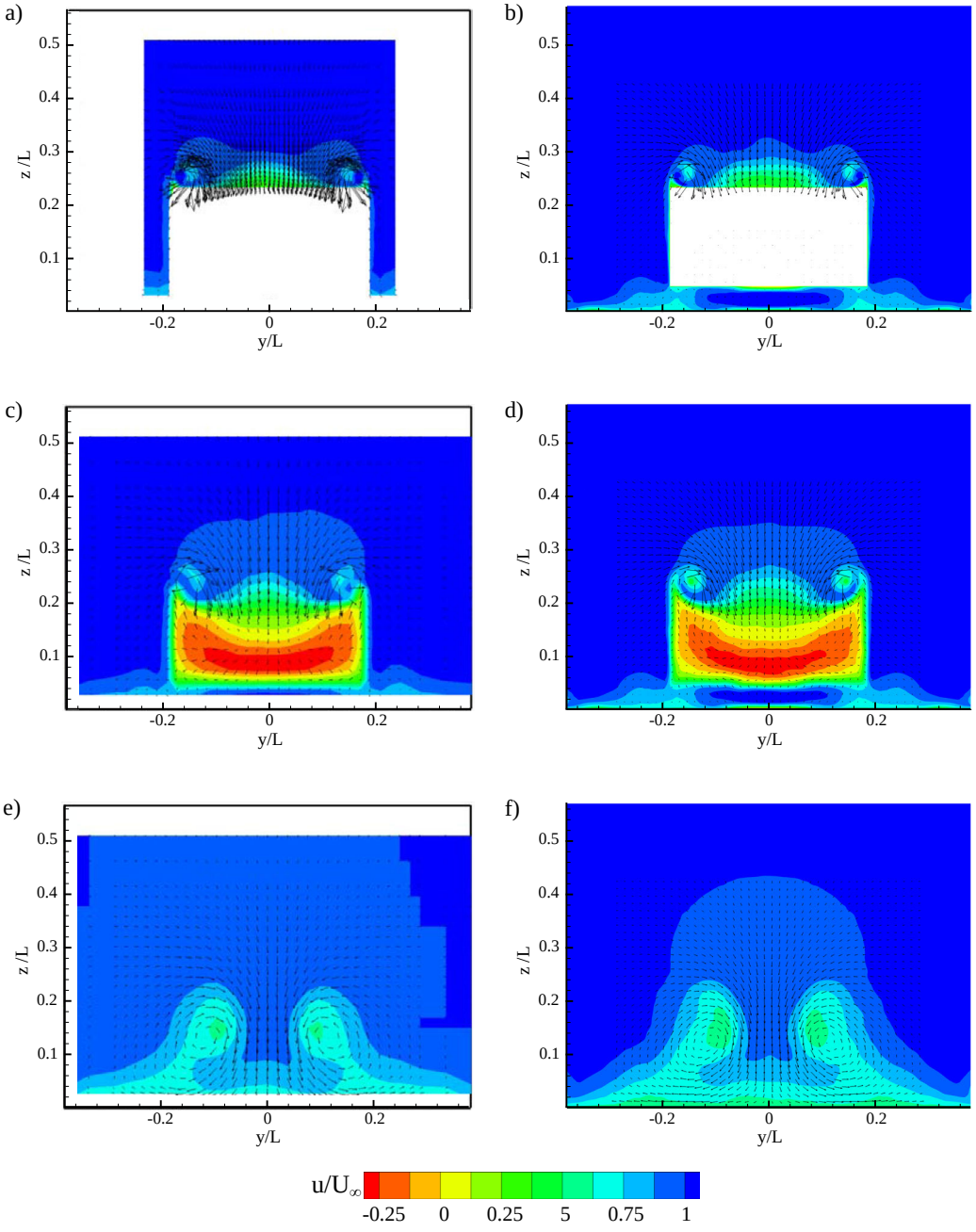

FIGURE 2.16: Contours of x-velocity results comparison a) Experimental x/L = 0, b) Computational x/L = 0, c) Experimental x/L = 0.077, d) Computational x/L = 0.077, e) Experimental x/L = 0.48, f) Computational x/L = 0.48

as the low pressure region beneath the separation bubble which occurred on the upper central part of the face. The reattachment length in the experimental would appear to be shorter due to the reduced surface pressure near the upper edge and rearward increase, however further quantitative assessment would require direct comparison of wall shear which was not included in the experimental study.

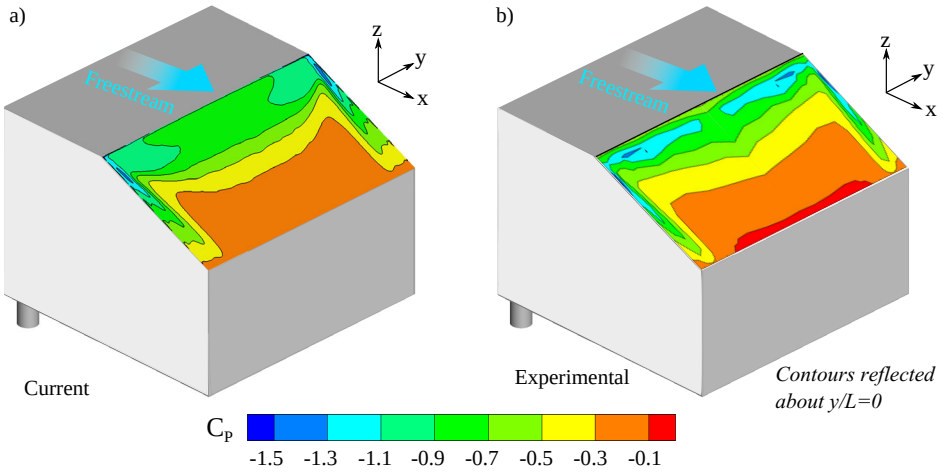

FIGURE 2.17: Surface pressure coefficient distribution comparison between experimental results [63] and the present study

Boundary layer profiles were also compared over the backlight surface between the experimental results and the present study. Profile characteristics matched favourably with the deficit and reversed flow regions within the separation bubble. It must be noted that the experimental results did not extend completely to the surface, hence it can be observed that the numerical results extend beyond the experimental data. The discrepancy within the upper region, where the numerical model predicted a lower velocity in comparison to experimental results, was attributed to an over-prediction of the forebody separation bubble. This resulted in a thicker boundary layer developing over the upper surface. The cumulative effect resulted in a more significant deficit extending the length of the backlight due to the corresponding loss.

Examining the C-pillar vortex in more detail, counter and co-rotating secondary vortices were identified to occur below the primary vortex as shown in Fig. 2.19a), with their associated core pressure deficits shown in Fig. 2.19b). The counter-rotating structure was notably weaker and less easily identifiable. Both the counter and co-rotating secondary vortices remained contained below the primary vortex and were attached along the backlight surface. In the instantaneous flowfield shown in Fig. 2.21, tube structures corresponding to the three separate vortices can also be identified.

Krajnović and Davidson [59] identified this same 'gear-wheel' mechanism in their LES-based study. They noted the secondary co-rotating vortex to remain attached along the

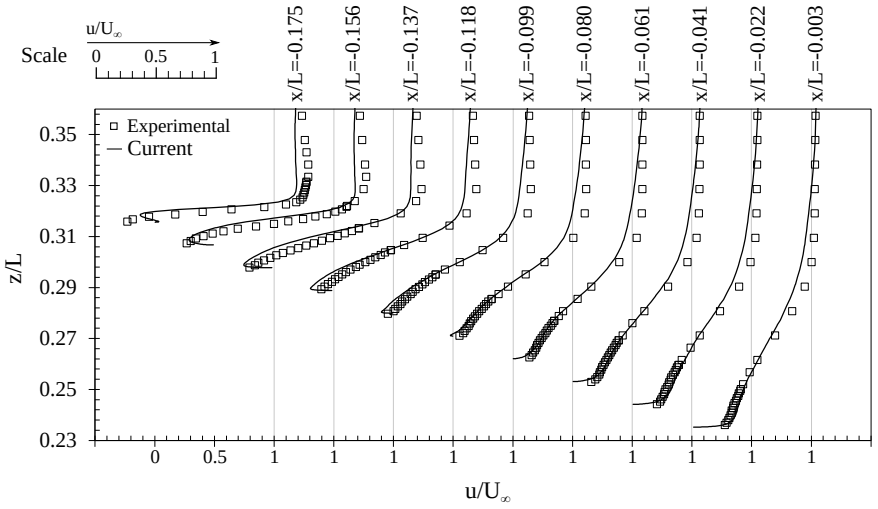

FIGURE 2.18: Comparison of experimental [63] and numerical profiles of non-dimensional x-velocity above the backlight surface

length of the edge, as was identified in the present work, and further drew flow across the C-pillar location. The primary and secondary co-rotating vortices then induced a counter-rotating third vortex. The experimental studies of Ahmed et. al [40], Spohn and Gillierion [77], and Zhang et. al [76] only identified the presence of two vortices which were the primary and secondary counter-rotating vortices. In these works the counter-rotating secondary vortex was attributed to an induced vorticity by the primary vortex. However, they did not detect a co-rotating secondary structure. The lack of experimental identification could be attributed to the difficulty of discerning between regions of positive vorticity occurring due to the primary vortex or the secondary structure rotating in the same direction.

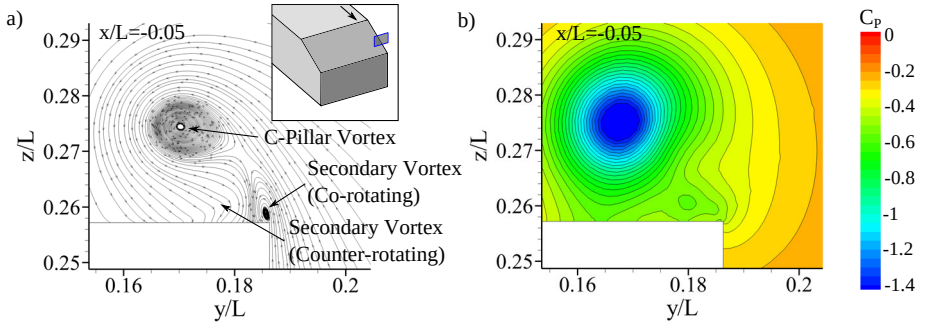

FIGURE 2.19: a) Primary and secondary vortices forming as part of C-pillar 'gearwheel' mechanism, and b) the core pressure deficit within the vortex

In the time-averaged flowfield a separation bubble formed at the start of the backlight surface, as is shown in Fig. 2.20. This was first identified by Ahmed et. al [40] but has proven to be a difficult feature for numerical models to capture due to the high turbulent

stresses that occur within the upper mixing layer [52]. Lienhart et. al [121] measured the peak turbulent kinetic energy at this location ($k_{max}/U_\infty^2 = 0.2$) to significantly exceed that of academic cases typically used for model calibration ($k_{max}/U_\infty^2 \approx 0.035$). This has resulted in DES models, which assume a RANS formulation at the boundary, being incapable of capturing the feature at the 25° backlight angle [52, 54]. Through resolving this structure in greater detail, the present numerical model was able to capture both the primary recirculation within the separation bubble and also an induced smaller counter-rotating secondary structure, as is highlighted in Fig. 2.20.

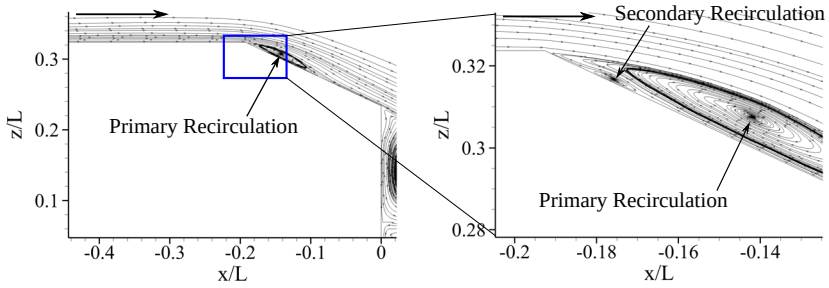

FIGURE 2.20: Location of secondary time-averaged backlight recirculation at y/L = 0

2.11.3.1 Instantaneous Structure

Observing the instantaneous backlight vortex structures with isosurfaces of Q, as shown in Fig. 2.21, a simple separation and reattachment with a single primary structure is no longer apparent. Instead a number of transient flow mechanisms were identified which only amounted to the simple separation bubble in the time-averaged sense.

As the flow passed over the slanted edge an initial separation resulted in the formation of spanwise vortices. The spanwise vortices have been established to occur through a Kelvin Helmholtz type mechanism [75], but it was identified that these evolve downstream in a more three-dimensional manner. The initially small vortices were observed to merge to form larger structures and were also tilted towards the centre of the face. The central span of the merged vortex then lifted off the surface to form a hairpin-type shape. With the centre raised into a region of higher velocity, the hairpin elongated before the legs broke and the structure detached from the surface. This mechanism occurred rapidly and was contained to the upper part of the backlight surface. This evolution into hairpin vortices was in line with the observations of Krajnović and Davidson [59], but is yet to be directly observed experimentally.

However the vortex merging has been previously identified both experimentally and numerically [55, 59, 76] but does not occur across the entire width of the face. In the

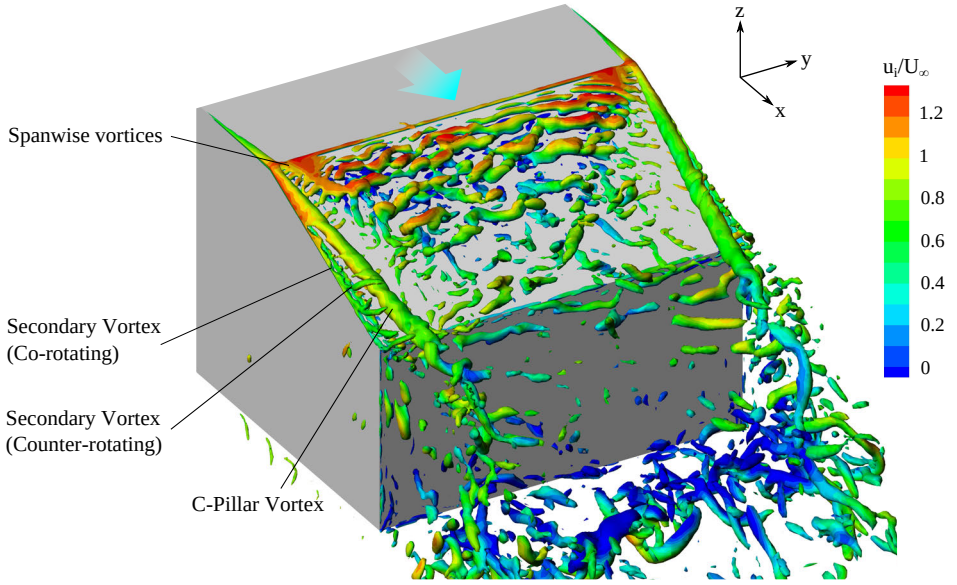

FIGURE 2.21: Instantaneous backlight flow structure observed using isosurfaces of $Q = 1.5 \times 10^6$

present work the C-pillar vortex suppressed the formation of the spanwise structures, as was also experimentally identified by Zhang et. al [76].

2.11.3.2 Transient Effects

Point velocity measurements were taken at four locations on the symmetry plane, and were recorded for each time-step to investigate the presence of dominant frequencies associated with regular transient mechanisms. Two different methods of spectral analysis were used, the first was to extract the wake modes, and the second to observe the shape of the distribution across the frequency range.

To aid in the identification of wake modes a sixth order polynomial curve fit (based on a minimisation of the squared residual error) was subtracted from the raw signal, as shown in Fig. 2.22. This reduced the influence of very low frequency transient motions which have been identified in long (10 minutes) sampling periods taken during experimental analysis [83], but were not feasible to resolve given the present methodology. The power spectral density estimate was then taken of this processed signal and allowed clear identification of the dominant frequencies. Local maxima were extracted from the processed data as peaks where the value exceeded that of either of the neighbouring values, with an additional threshold magnitude criterion that was accordingly adjusted for each spectrum.

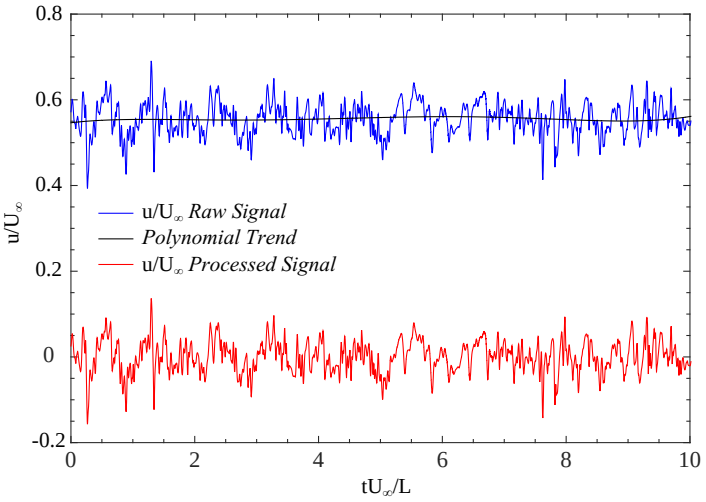

FIGURE 2.22: Example of the velocity signal pre-processing used to aid in identification of characteristic frequencies, as shown for a point wake measurement for a 5L radius corner

Secondly, a power spectral density plot was generated of the raw, unprocessed signal, to generate a result that reflected the magnitude of the wake fluctuations relative to the velocity signal across the considered frequency range. These plots were achieved via adoption of Welch's power spectral density estimate [122] which aided in the removal of noise and improved visual clarity.

For all results a longer sampling period would have improved the accuracy of the distributions, but an inherent disadvantage of numerical simulation is the computational impracticality of achieving these long sampling times. However, an advantage remains the ability to more readily associate these fluctuations in the measured signal to the observed flow mechanisms.

Convergence of the spectrum was monitored throughout the data sampling period to ensure both methods yielded a consistent result. Figure 2.23 shows the power spectral density estimate of the raw signal (upper) and processed signal (lower), with the right vertical axis indicating the magnitude with respect to the difference between the signal and the polynomial curve. For the measured location on the symmetry plane the processed signal converged to indicate a strong wake mode at Str = 0.31, with the raw frequency distribution retaining a similar magnitude across the range but with improved resolution in the low frequency band.

In Fig. 2.24 the inset image shows time-averaged streamlines along the symmetry plane to demonstrate the corresponding locations within the wake structure for each point. At location M1 a peak occurred with a maxima at Str = 0.31. At locations M2 and M3 a clear peak also occurred at a common frequency of Str = 0.31 with the number of peaks

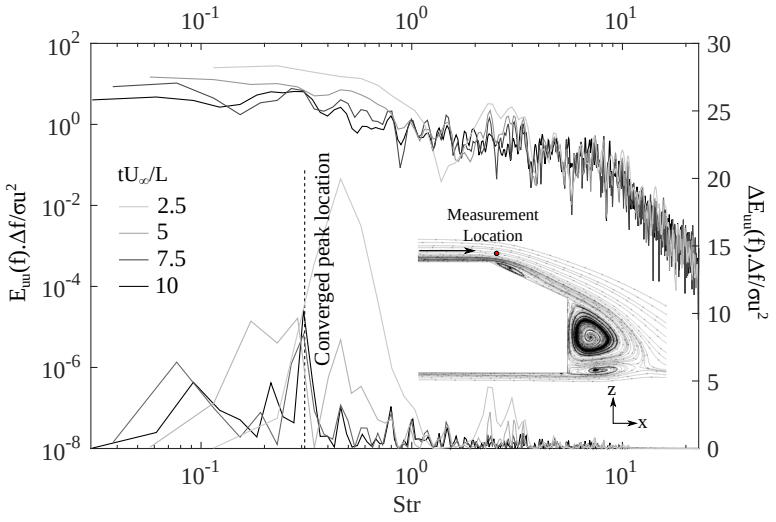

FIGURE 2.23: Convergence of the raw frequency spectrum (upper) and processed frequency spectrum (lower) throughout the temporal period, shown for a point velocity measurement over the backlight location in the straight-line condition

of similar magnitude increasing downstream. At location L1 the frequency associated with the dominant wake mechanism was identified as Str = 0.52.

These values were all recognised to fall within a similar range to those recorded in previous experimental and numerical studies, as listed in Table 2.4.

TABLE 2.4: Ahmed Body with 25° backlight angle wake Strouhal numbers

	Method	Location	Str
Zhang et. al [76]	Hot-wire	Backlight	0.23-0.31
		Trailing Face	0.51
Joseph et. al [73]	Hot-wire	Backlight	0.38-0.6
Thacker et. al [69]	Hot-wire	Backlight	0.27
Heft et. al [80]	Surface Pressure	Backlight	0.35
Krajnović and Davidson [58]	LES	Backlight	0.26
Minguez et. al [55]	LES	Backlight	0.27
		Trailing Face	0.42
Vino et. al [66] (30°)	Surface Pressure	Trailing Face	0.45

Respectively these frequencies were associated with transient flow mechanisms occurring within the wake. On the backlight surface, different interacting effects were identified to occur within the separation bubble region. The sequence of events which occurred at this location are shown in Fig. 2.25.

Spanwise vortices were observed to continually merge within the separated region before being ejected down the backlight surface. The mean flow was deflected upwards and downwards above this region dependent on the state of flow structures within the bubble

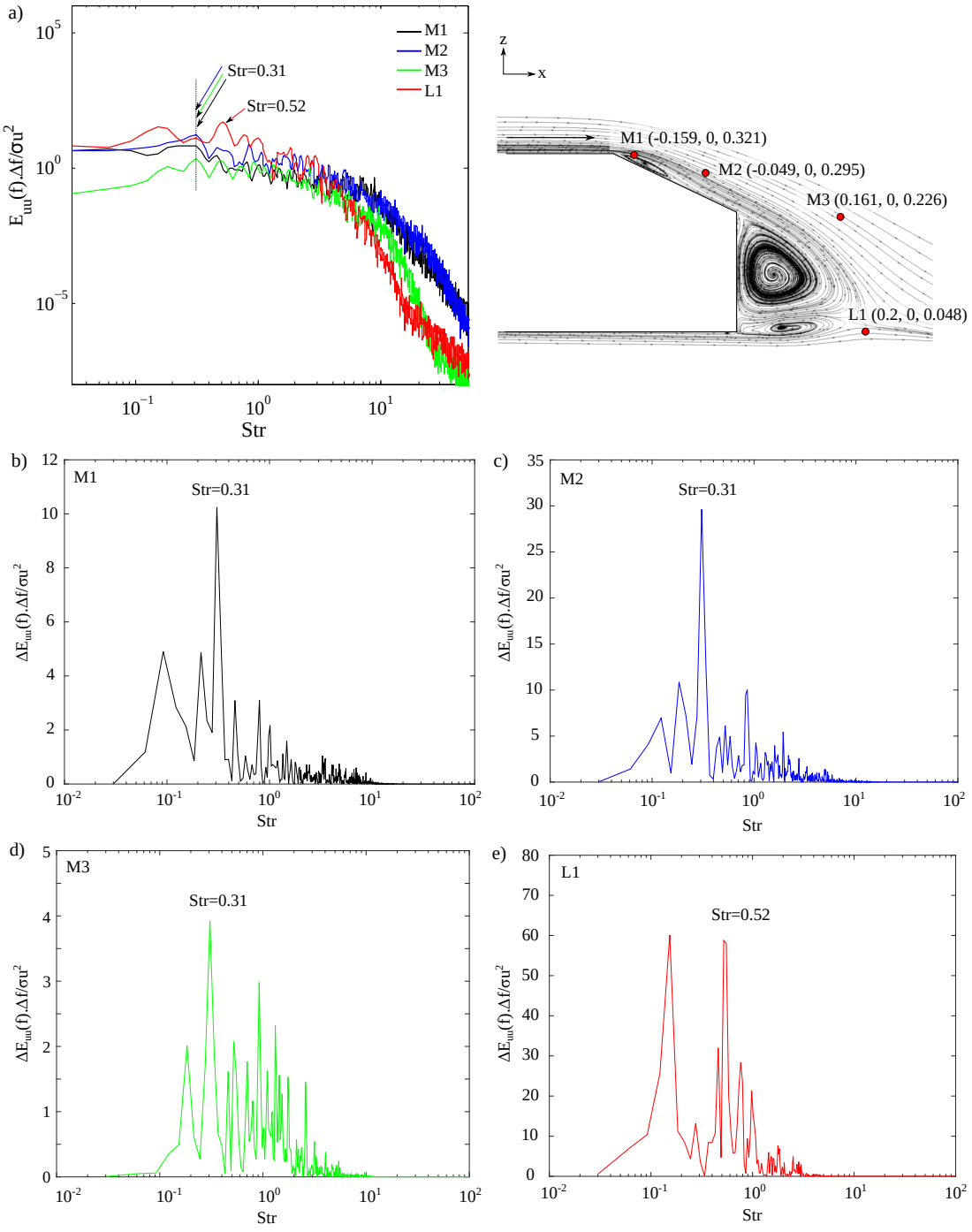

FIGURE 2.24: a) Raw frequency spectrum at indicated points along the centreline plane, with processed spectrum at the b) M1 location, c) M2 location, d) M3 location, and e) L1 location

region, which would explain the flapping motion attributed to this frequency by Thacker et. al [69].

The more common attribution of the specific frequency has been the periodic enlargement and contraction of the vortex merging region as was identified by Wang et. al [75] and Zhang et. al [76], and further supported by the observations of Kiya and Sasaki [123] for a separation bubble on a flat plate. The observed three-dimensional nature of this region due to the formation of alternating hairpin vortices, as opposed to a continuous structure across the span, resulted in the present findings supporting the expansion and contraction as more accurately descriptive.

The merged structures were observed to differ in size dependent on the stage within the transient cycle. Periodically a larger structure would form and result in the ejection of a large fluid structure from the separation bubble region, as shown in Fig. 2.25a). The flow which passed over the separation bubble would then be more immediately deflected downward as reattachment occurred between the vortex merging region and the ejected fluid parcel. The increased path curvature and decrease in pressure, resulted in local flow acceleration and thus explained the dominant frequency identified in the velocity signal. After this rapid contraction the region was observed to gradually extend further down the face over a longer period, shown in Fig. 2.25b) and c).

After extension down nearly the entire length face, the merging region began to again reduce in size, as shown in Fig. 2.25d). The propagation back up the face corresponded to the formation and ejection of larger merged vortices until again reaching the critical point shown in Fig. 2.25a).

Observing the separation bubble which occurred aft at the trailing face, this feature consisted of two recirculations, as is shown in Fig. 2.24 and 2.14, and was also identified by Ahmed et. al [40] in their initial study.

Str = 0.52 was identified to correspond to a periodic bursting mechanism within both the upper and lower recirculations, and this sequence is shown in Fig. 2.26. This was in general agreement with the presented results of Zhang et. al [76], observed through PIV images taken on the symmetry plane. The primary effect they noted was the periodic expansion and then emission of flow from the upper and lower recirculations in the wake. This occurred when the swirling motion resulted in a centrifugal force that exceeded the radial pressure gradient and a fluid parcel was ejected.

In the present case the expansion and emission of flow through a bursting-type mechanism was more significant for the lower recirculation. While the upper structure also periodically ejected flow, it was through a partial outer ejection while the central region

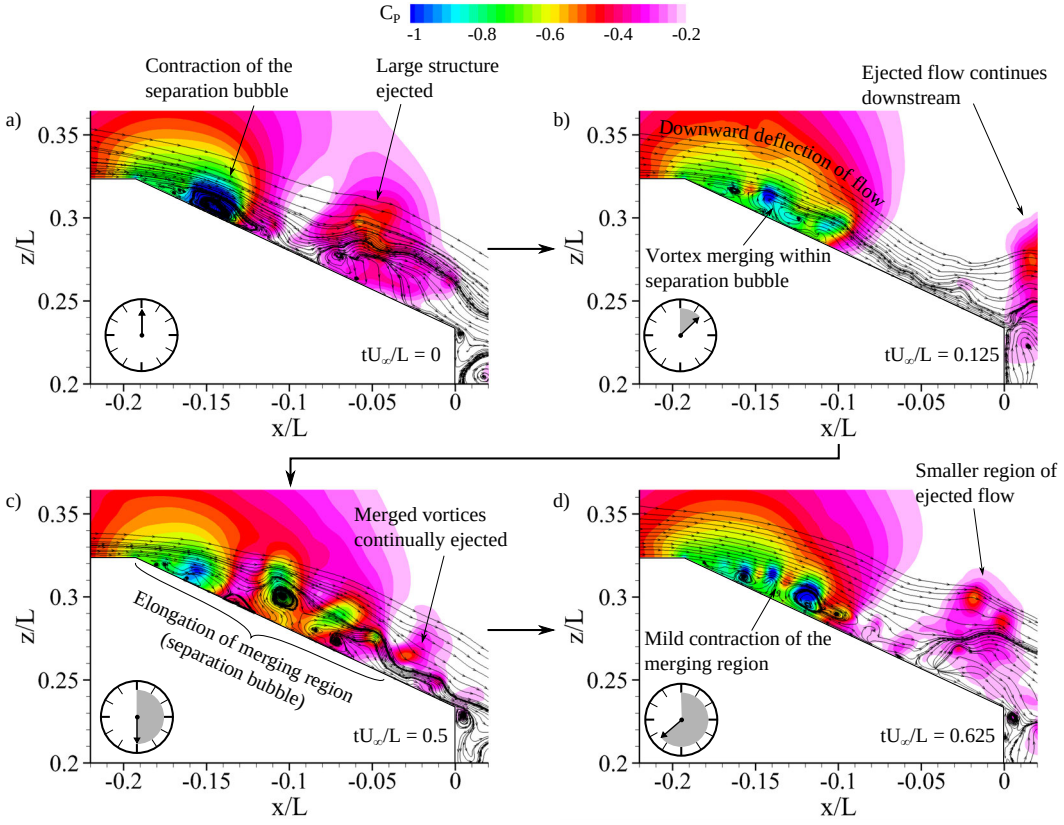

FIGURE 2.25: Transient sequence of the backlight separation bubble, showing instantaneous streamlines with contours of static pressure at y/L=0 for a) $tU_\infty/L = 0$ b) $tU_\infty/L = 0.125$ c) $tU_\infty/L = 0.5$ d) $tU_\infty/L = 0.625$

was largely sustained. The differences between the upper and lower structures were attributed to the different conditions from which they were formed. This was namely the presence of the angled backlight surface above the immediate wake, and the interaction of the ground with the lower recirculation.

The lower recirculation began formation through merging of the vortices in the location shown as region B in Fig. 2.26. Once the vortex reached a critical size it was projected outwards below the upper recirculation and continued to draw flow from underneath the body, passing into region D. The core pressure decreased and as the longitudinal extension exceeded that of the upper recirculation it drew more flow upwards from underneath the body. The expansion of the flow drawn from underneath was exacerbated by the constricting effect of the ground and resulted in the development of a high pressure region immediately adjacent to the lower recirculation. The lower recirculating structure then burst resulting in a spiralling outward motion of the flow which was propagated downstream.

The angle of the flow down the backlight resulted in greater mass flow entering the

upper recirculation with it also being notably larger. This flow would primarily remain at the outer radius with the centre being fed from the lower merging vortices in region B, in addition to drawing flow about either side of the spanwise orientated recirculation. The rotation of the large structure was observed to induce a counter-rotating vortical structure on the trailing face, show in region A which would be followed by the formation of yet another vortex, this time off the backlight surface, and these would then merge into the larger recirculation about the outer radius. Flow was observed to enter the upper recirulation both through direct tangential entry, in addition to the drawing in of smaller formed vortices.

In Fig. 2.26a) it can be observed that the upper recirculation periodically assumed an outwards spiral with the ejection of a small fluid parcel from the outer radius. This was then followed by a mild contraction as the structure reduced in size, coinciding with the bursting of the lower recirculation. Overall, this effect toward the upper recirculation was observed to be led by the more dominant lower mechanism. For the upper recirculation the flow was drawn downwards prior to this ejection and, in this instance, filled the void left by the burst lower recirculation, as shown in Fig. 2.26d).

The bursting was also observed to occur in a more three-dimensional manner than has been previously recognised. In addition to the emanation of a fluid parcel in the longitudinal axis, a concurrent lateral wake expansion resulted. In the present study this effect was observed to result in clear wake pulses when viewed from directly above. Where the effects can be observed as most significant in the lower region of the wake, as shown in Fig. 2.27.

2.11.4 Forebody Structure

A separated region also occurred due to the adverse pressure gradient over the curvature of the nose, with both the time-averaged and instantaneous surface flow structures shown in Fig. 2.28. The separation line $\mathrm{NBL_{UF}}$ extended laterally across the front of the body and ended at two stable focii ($\mathrm{SF_{FO}}$ and $\mathrm{SF_{FI}}$). The stable focii corresponded to the origin of the vortical structure forming across the separation bubble, as shown in Fig. 2.29. After formation at the focii, the vortical structure spiralled into the spanwise axis and drew flow into the centre of the separation bubble. In the time-averaged sense an arched vortex was identified to occur within the separation bubble, which surrounded a central region containing an unstable node. An illustration of the time-averaged flow structure and the corresponding critical points is shown in Fig. 2.30.

The true instantaneous structure shown in Fig. 2.28b) indicated the presence of small unsteady flow structures developing within the central region, while the location of $\mathrm{NBL_{UF}}$,

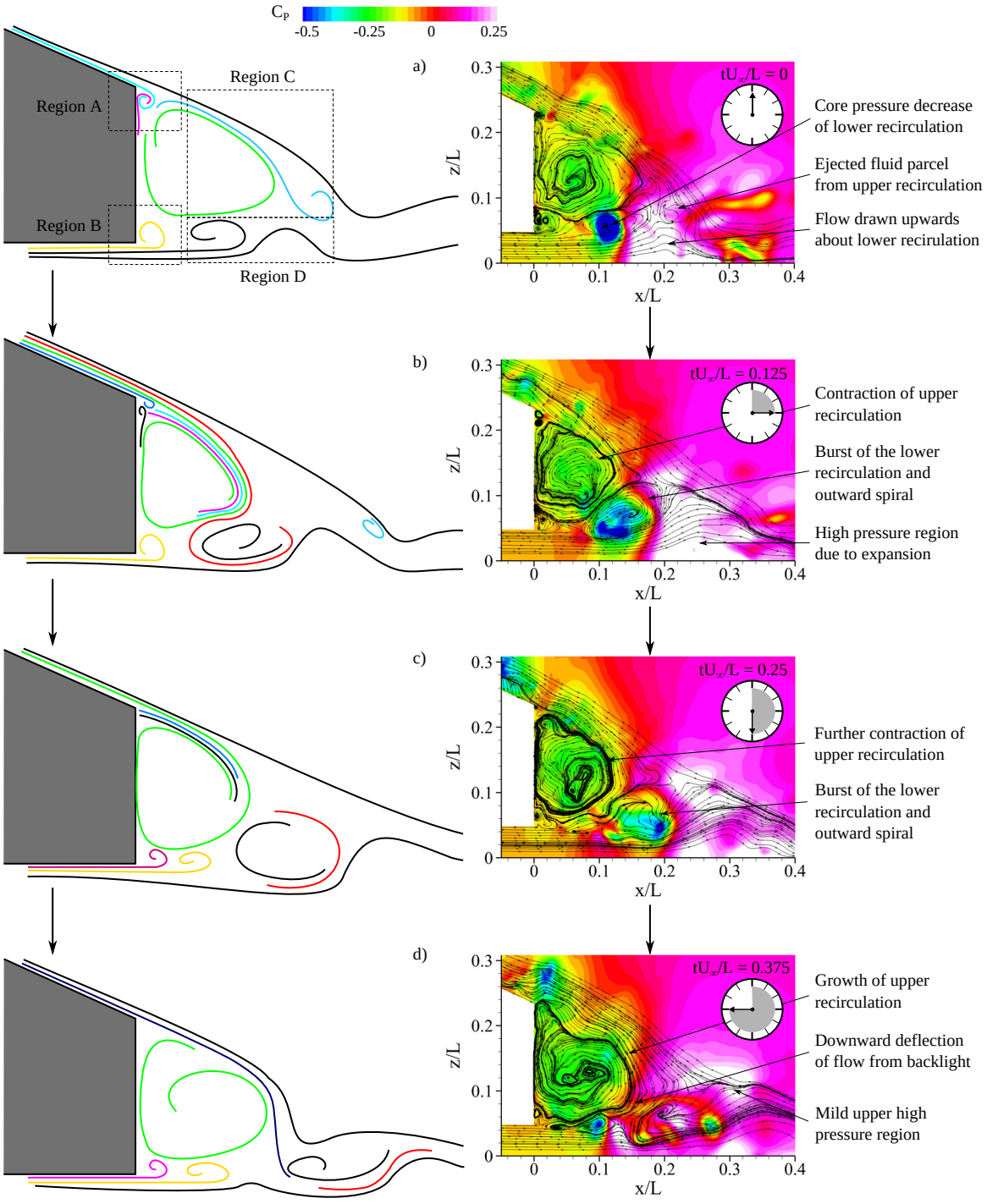

FIGURE 2.26: Transient sequence of the two recirculations within the rear separation bubble, showing instantaneous streamlines at y/L=0 for a) $tU_\infty/L = 0$ b) $tU_\infty/L = 0.025$ c) $tU_\infty/L = 0.05$ d) $tU_\infty/L = 0.075$

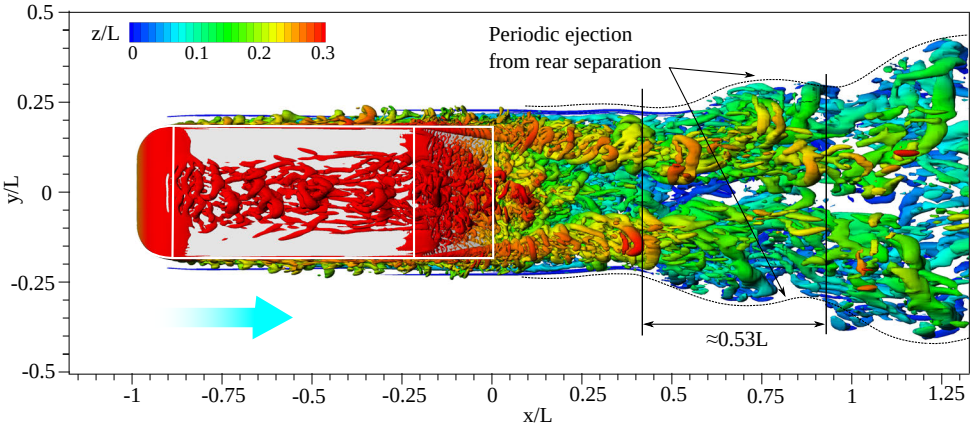

FIGURE 2.27: Isosurfaces of Q = 2×10^4 showing the pulses most evident in the lower wake structure due to the rear bursting mechanism

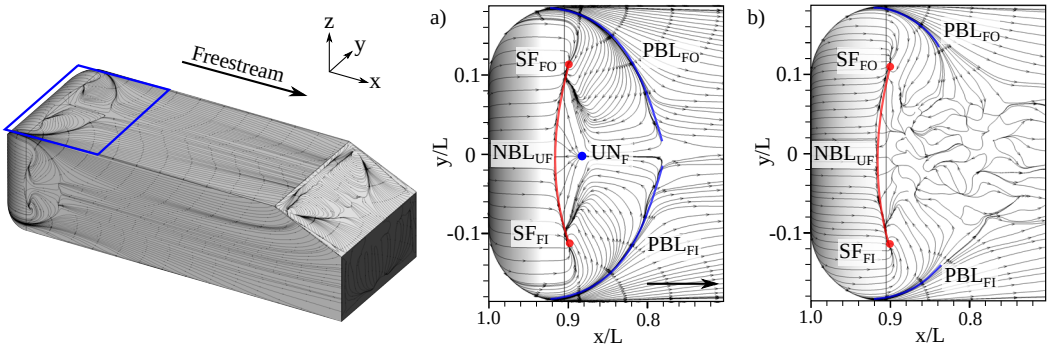

FIGURE 2.28: Surface streaklines indicating the time-averaged (a) and instantaneous (b) critical point structure observed for the forebody separated region

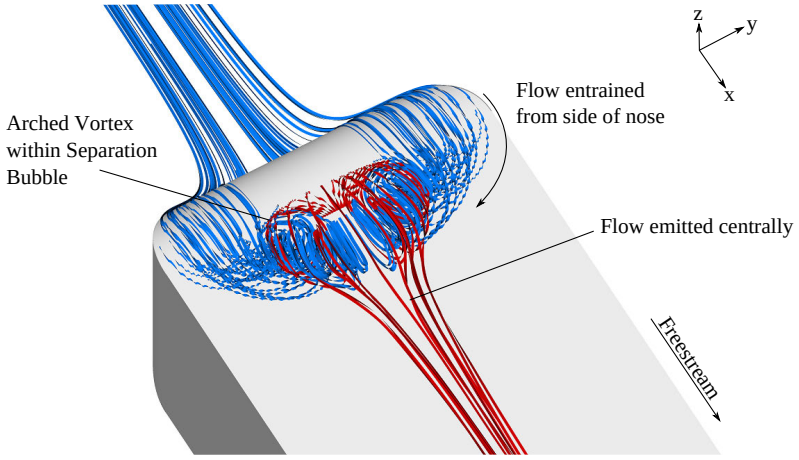

FIGURE 2.29: Streamlines indicating the time-averaged structure of the forebody separation region

SF_{FO} and SF_{FI} remain constant. The flow drawn into the arched vortex structure was noted to be emitted centrally and form merged hairpin vortices. These were observed to alternatively emanate from either side of the unstable node across the length of NBL_{UF} and propagate downstream, as is shown in Fig. 2.27. Downstream from the separated region the vortex was stretched longitudinally and detached from the surface to be drawn into the central downwash over the backlight.

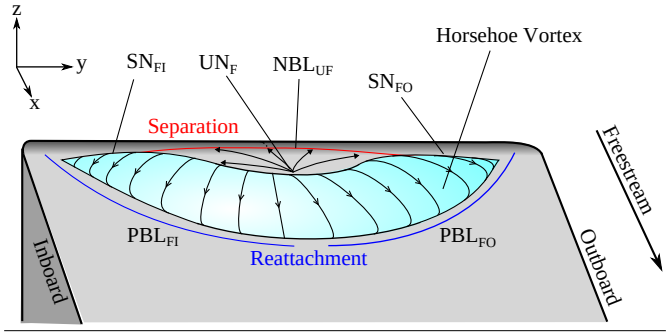

FIGURE 2.30: Diagram of the time-averaged forebody separation bubble structure observed

Spohn and Gillerion [77] observed a similar structure through surface flow visualisation at a Reynolds number of 9×10^4, as shown in Fig. 2.31a). Figure 2.31b) was taken from a plane 0.01L above the surface and identified counter-rotating longitudinal vortices originating from the focii. Although a considerably larger forebody separation was identified in comparison to the present work.

Sims-Williams and Dominy [10] used surface flow visualisation to investigate the same feature at $Re = 6.2 \times 10^5$ and observed reattachment x/L = -0.88. They also noted recordings of high turbulence up to x/L = -0.85 downstream. In the present work the mean location of reattachment was at x/L = -0.83 indicating a likely over-prediction of this length compared to the experimental studies of Spohn and Gillerion [77], and Sims-Williams and Dominy [10].

In terms of flow structure, Spohn and Gillerion [77] believed the central region of the forebody separation to contain Kelvin-Helmholtz type instabilities which linked the longitudinal structures forming on either side. However, the present study identified that any type of continuous structure across NBL_{UF} did not occur but rather vortices of a shorter span which alternatively emit from either side of UN_F.

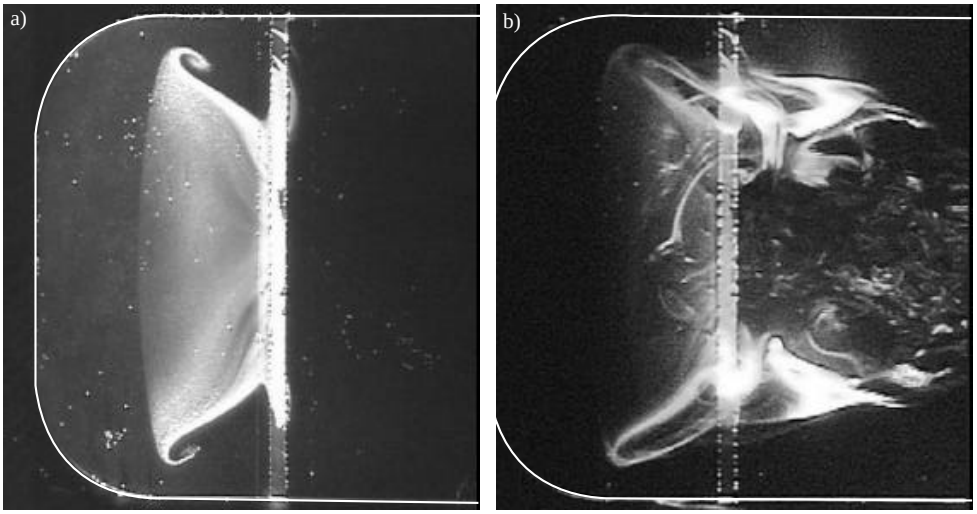

FIGURE 2.31: a) Surface flow visualisation of forebody separation bubble region, b) Flow visualisation 0.01L above the surface within the separation bubble from Spohn and Gillieron [77]

2.11.5 Aerodynamic Forces

Direct measurement of the aerodynamic drag acting on the body was not part of Lienhart and Becker's [63] study. Comparison was made between present numerical results and the experimental study of Joseph et. al [73] which included drag measurements and the effect of Reynolds number on drag coefficient. They used a closed test-section with a blockage ratio of 0.7%, which was lower than the 1.0% used in the present study, thus amounting to a mild discrepancy.

Across prior experimental (and numerical) studies there has been a wide range of reported drag coefficients, as shown in Fig. 2.32. All studies shown used a force-balance to attain the values shown and maximum reported experimental error is shown next to the data set. The calculated drag coefficient from the straight-line numerical simulation was 3.0% lower than the comparable experimental result of Joseph et. al [73] at the same Reynolds number. The proportional contribution of the viscous component to the total drag coefficient was 13.1%. This value was slightly below the 15% contribution reported in the initial findings of Ahmed et. al [40].

For all cases drag was considered to act in the freestream direction. This ensured the quantity was representative of the aerodynamic resistance encountered due to the motion of the body through the flow. The overall drag value recorded for Configuration A at a 4.3% blockage ratio was 25.9% higher than the value measured for Configuration B, which had a blockage ratio of only 1.0%. This result further emphasized the likely high sensitivity of this specific geometry to the blockage ratio. It must be reminded,

however, that Configuration A also differed due to the use of a stationary ground plane and support struts. Krajnović and Davidson [105] investigated the influence of ground plane motion for the same geometry and identified an increase in spanwise mass flux which led to an increase in drag for the case with a stationary ground. So directly comparing only these two results would be expected to give an exaggerated difference. Despite this, the magnitude exceeds what would be expected when both remain at blockage ratios commonly deemed to be adequate for the testing of vehicles.

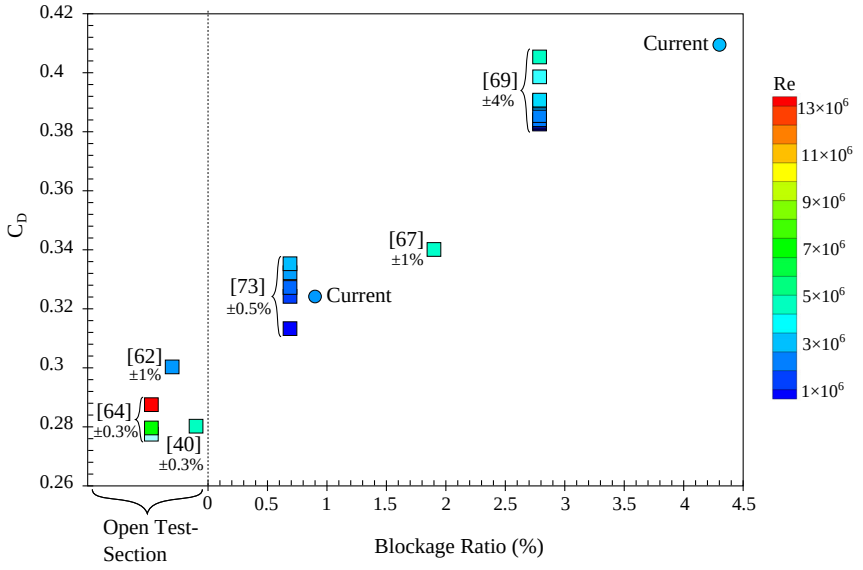

FIGURE 2.32: Drag coefficient comparison between present study, and past experimental results with reported maximum experimental error

Inherently the blockage ratio amongst experiments has differed, however, this parameter is rarely considered to have a substantial influence. The experiments of Thacker et. al [79] and Conan et. al [67] were conducted at blockage ratios of 2.8% and 1.9% respectively, and Fig. 2.32 shows that reported drag values were respectively 36.7% and 19.4% higher than the average coefficient of 0.285 for open test section experiments. This would indicate a potentially greater dependency on blockage ratio than is suggested by approximate methods such as Maskell theory [124] which predicts only a 1.7% increase in drag at a blockage ratio of 1.9% (at $\mathrm{Re} = 4.29 \times 10^6$) [67]. Direct comparison between experimental results is skewed due to nuances and thus these observations could be coincidentally exacerbated. However it must be noted that prior numerical studies at the 25° backlight angle have tended to over-predict the drag coefficient, and the high blockage ratio typically used is seldom identified as source of error [54, 55, 58, 65].

In the present study the LES results indicated a significant difference to occur in the pressure distribution over the upper surface due to the change in blockage ratio, as is shown in Fig. 2.33. The freestream acceleration due to blockage was evident in the

consistently lower pressure recorded along the length of the roof for the 4.3% blockage ratio. The suction peak was also 14.1% greater when compared to the straight-line case at a 1.0% blockage ratio. Thus the increased acceleration down the rear surface resulted in a more significant induced drag component at this location. This finding further contributed to the results obtained from the initial boundary sensitivity study and highlighted the care that should be taken when assessing the effect of blockage ratio for future numerical simulations and experiments.

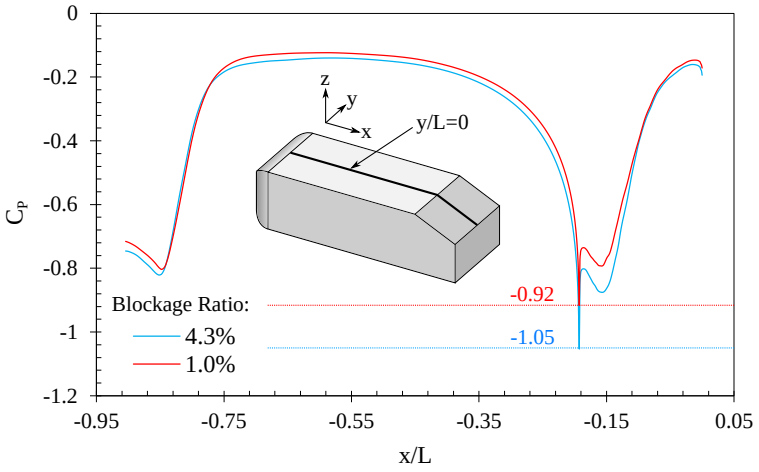

FIGURE 2.33: Change in pressure coefficient distribution over the upper surface for different blockage ratios

2.12 Summary

LES with a Smagorinsky-Lilly SGS model was demonstrated to be capable of modelling the complex flow structures developing around the 25° backlight angle Ahmed Body. Small discrepancies were noted to occur in the predicted length of the forebody separation and the shedding of the shear layer from the lower surface. The time-averaged flow structures developing in the wake were captured, particularly the dominant C-pillar vortex and the induced secondary structures, as well as the two large recirculations at the trailing face.

The numerical technique was also capable of capturing transient flow mechanisms which occurred at frequencies in agreement with prior experimental studies. Results demonstrated that the drag coefficient was able to be predicted within the expected range, but was sensitive to blockage effects. The results offered insight into a wide range of flow effects occurring around the bluff body and demonstrated the ability of the model to permit detailed analysis of both transient and time-averaged flow phenomena.

Chapter 3

The Effects of Yaw Angle

The yawed condition is often treated as a condition where a vehicle will exhibit similar aerodynamic characteristics to cornering [6, 13, 14]. In reality the cornering flow conditions are more variable and complex, however first developing an understanding of the aerodynamic effects of a constant flow angle allowed the two conditions to be distinguished. Experimentally the two conditions are unable to be compared due to the difficulty in replicating the true cornering condition (a new method to overcome this limitation is proposed in Chapter 6), however both can be achieved through numerical simulation and this allows comparison using a common method.

The flowfield developing around the 25° backlight angle Ahmed body in yaw has been a subject of limited investigation. It represents a much lesser known characteristic of an otherwise extensively investigated geometry. Prior investigation has been through experimental analysis and focussed on the aerodynamic forces and moments [64, 83], with more extensive flowfield analysis conducted for other configurations [83, 85, 86].

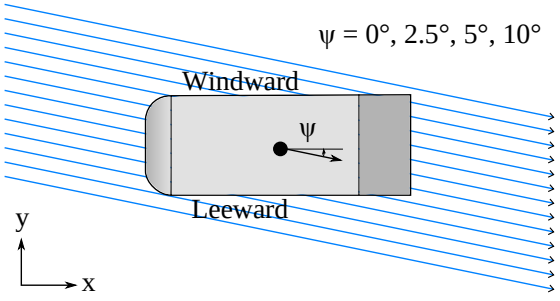

FIGURE 3.1: Diagram of yaw angles with respect to the Ahmed body

The condition investigated was representative of a true yawed condition, where the body can be considered as advancing through still air at the indicated yaw angle, shown in

Fig. 3.1. Three different angles (2.5°, 5°, and 10°) were analysed and compared to the results in the straight-line condition. The translational motion of the ground plane was zero relative to the freestream flow, and therefore passed below the body at an angle equal to that of yaw. The freestream velocity remained constant at 25 m/s while the yaw angle (ψ) increased. Thus the freestream x and y-velocity components varied according to $cos\Psi$ and $sin\Psi$ respectively.

The specific angles were selected as they are representative of isolated flow angles that relate to those experienced be a vehicle travelling through a corner. 10° was larger than the maximum flow angle that occurred for the corner radii investigated in Chapter 4, however it was less than the maximum total change in flow angle along the length of the body (for the smallest radius corner investigated, the total change from front to rear, $\Delta\Psi$, was 11.42°).

3.1 Force and Moment Coefficients

All aerodynamic force and moment coefficients were compared to time-averaged experimental results of Meile et. al [83]. In their work they reported all force and moment coefficients for the 25° backlight angle Ahmed body in the steady-state yawed condition at yaw angles up to 25°, with each 2.5° interval measured.

The experiments were conducted at a Reynolds number of 2.1×10^6 (30 m/s) at 0.2% turbulence intensity in a 3/4 open test-section with a fixed ground plane. The increased freestream flow velocity in comparison to the present simulations was expected to have only a minor effect due to the low Reynolds number sensitivity within this range. All force and moment measurements were taken using a force balance with a reported error of ±0.5%. Moment coefficients were measured about a position on the ground at x/L = -0.56. This point differed from the x/L = -0.5 position used throughout the present work — hence the inclusion of measured values at both locations.

The lift and drag coefficient values were compared, as shown in Fig. 3.2, where the most substantial difference was a 25.6% lower prediction of lift coefficient by the numerical model. This discrepancy was able to be largely attributed to the differences in boundary configuration between the experiments and numerical model. A fixed ground, as used in the experiment, has been shown to result in an increased prediction of lift due to the additional development of a boundary layer over the ground, and the resultant constricting effect of the flow passing underneath the model. Krajnović and Davidson [105] used LES to compare the fixed ground condition to the use of translational motion equal to that of the freestream velocity. They identified a 18.6% increase in lift coefficient prediction

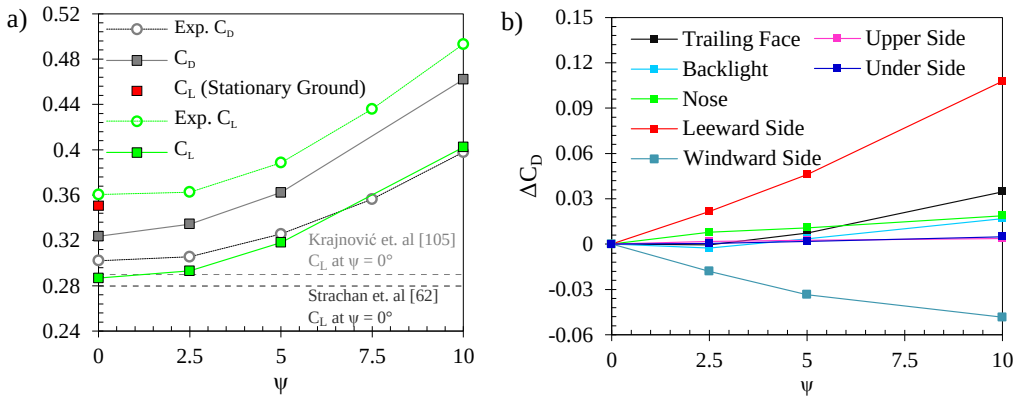

FIGURE 3.2: a) Lift and drag coefficient values for increasing yaw angle, compared to experimental results of Meile et. al [83] b) Change in drag coefficient contribution for individual surfaces of the body

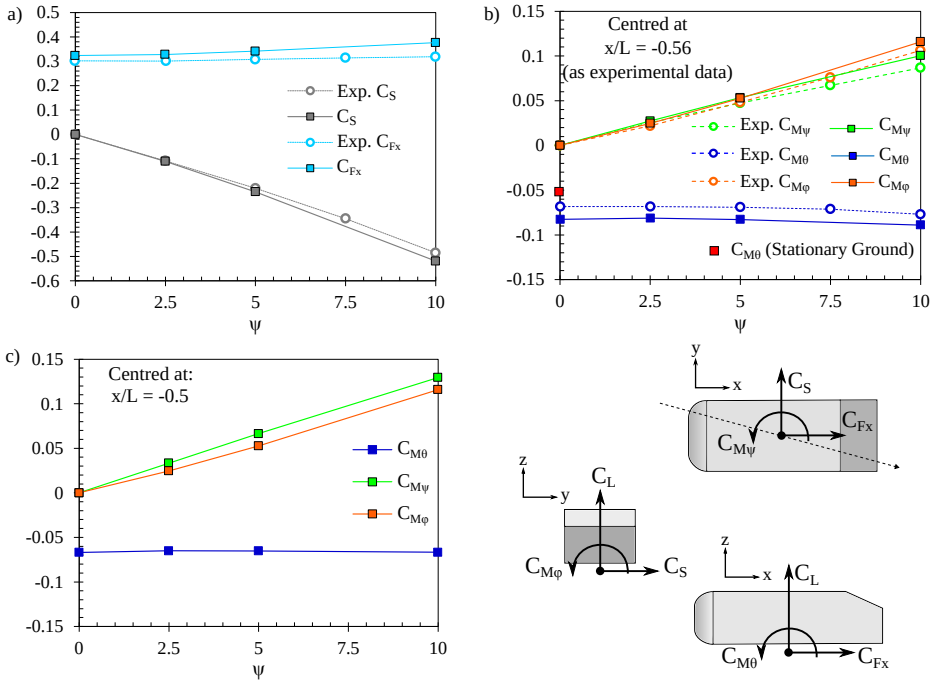

FIGURE 3.3: Force and moment coefficients compared to experimental results of Meile et. al [83]: a) Coefficient of side force and force in the x-direction b) Pitching moment, yawing moment, and rolling moment coefficient taken about x/L = -0.56, and c) Moment coefficients taken about x/L = -0.5

for the case adopting the fixed ground condition. This was attributed to reduced mass flux underneath the model in the freestream direction with increased spanwise flux. In the present work this same comparison was also made for the straight-line condition, as shown in Fig. 3.2. A similar result was observed where the lift coefficient increased due to the stationary ground condition, but by a more substantial 21.7%, and thus accommodated the majority of the discrepancy between the numerical and experimental results. The straight-line case where the relative motion of the ground was simulated was in agreement with experimental findings achieved in the presence of a moving ground by Strachan et. al [62], and the LES results of Krajnović and Davidson [105], as shown in Fig. 3.2.

Despite the initial offset in the measured value, the lift coefficient trend was observed to agree with experimental values. A 2.2%, 10.9%, and 40.2% increase occurred for flow angles of 2.5°, 5°, and 10°. The increase in lift was largely attributed to the longitudinal vortex development along the upper windward edge, which reduced upper surface pressure, as is discussed further in Section 3.4.

An increase in drag also occurred as yaw angle increased. At an angle of 10° there was a 42.8% increase in the drag coefficient, with 11.9% and 3.3% occurring for the 5° and 2.5° angles respectively. In all cases drag was considered to act in the freestream direction, which was consistent with all analysis conducted throughout this work. Due to this there was an increase in the effective frontal area as the angle increased. The change in drag was the product of an increase both the viscous and pressure components.

The viscous component was 21.8%, 26.2%, and 40.2% greater than the straight-line magnitude for the 2.5°, 5°, and 10° yaw angles respectively and there was a proportional increase in the local contribution for all surfaces with the exception of the leeward side. However, as the viscous component contributed only 12.8-15.4% of the total drag force, these changes affected the overall magnitude at the higher angles to a lesser extent. The proportional increase in the pressure component was 0.5%, 9.8%, and 43.1% for the 2.5°, 5°, and 10° yaw angles respectively, where a local increase over the leeward side was identified to be the most significant isolated effect.

Fig. 3.2b) indicates the proportional contribution of each surface toward the overall values. While the leeward side experienced the greatest increase, the windward side experienced the largest reduction. In the straight-line condition case the flow accelerated past the curved radii at the nose and over the sides of the body, which caused a reduction in the surface pressure over the sides. As yaw angle increased the area of the windward face normal to the flow direction increased proportional to $sin\Psi$ while the surface static pressure remained below ambient. This resulted in a negative drag force with yaw angle.

An increase in the drag coefficient contribution of the trailing face also occurred and was attributed to a more significant wake pressure deficit.

The coefficient of force in the x-direction increased with yaw angle, as is shown in Fig. 3.3, where a 16.3%, 5.5%, and 1.4% increase occurred at flow angles of 10°, 5°, and 2.5°. This was notably less significant than the increase in overall drag coefficient, thus indicating the side-force component having greater influence. Overall this prediction of the x-component was the most substantial difference between the experimental results and numerical simulation, with the experiments indicating only a 5.4% increase over the straight-line condition at a 10° angle of yaw. This is believed to be attributed to differences in the near-wake region. Comparison of the experimental results of Meile et. al [83] to those of Lienhart et. al [121], as shown in Fig. 3.4, reveal an increased velocity deficit extended further down the backlight face in addition to a taller near wake region. A separated region drawing from a comparatively decelerated backlight flow is postulated to have resulted in reduced near-wake circulation, where the change due to yaw angle would have had an overall smaller effect.

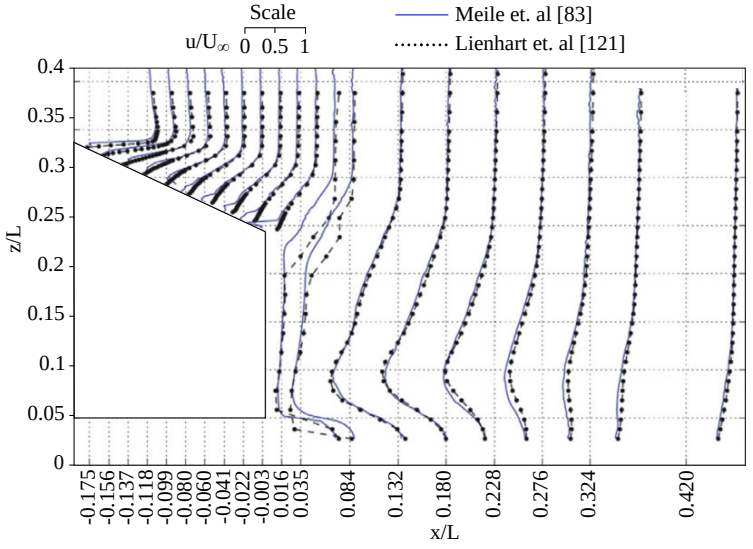

FIGURE 3.4: X-velocity profiles taken over the backlight and in the wake by Meile et. al [83], compared to the result of Lienhart et. al [121]. *Reprinted from [83] with permission from Elsevier*

A negative side force occurred due to the difference in surface pressure distribution over the sides of the body, as is illustrated in Fig. 3.5, with close agreement identified between the experimental and numerical results. The magnitude of this force exceeded that of the drag coefficient at 10° due to both the larger normal surface area, and also the acceleration of the flow over the leeward side. The pitching moment coefficient demonstrated a near-linear, but less substantial increase where a maximum 7.5% change occurred at a yaw angle of 10°. This increase in pitching moment was also attributed to

the occurrence of additional longitudinal vortices which passed over the upper surface and an increase in the backlight suction peak. The pitching moment for the straight-line condition, as simulated with a stationary ground, was -0.051. The experimental prediction fell between the stationary and translational ground conditions, and indicated the discrepancy could be partially attributed to the relative motion of the ground, but would likely have also been further affected by the presence of the experimental supports.

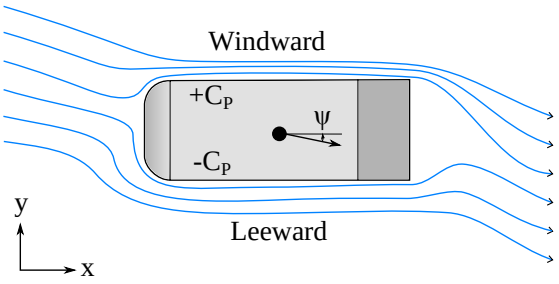

FIGURE 3.5: Diagram of the net surface pressure distribution change due to yaw angle

The change in yawing and rolling moment coefficient was more significant and agreed with the experimental trends identified by Meile et. al [83]. Values increased from initially being zero in the straight line condition to a maximum yawing moment coefficient of 0.10 and a rolling moment coefficient of 0.12 for the 10° yaw angle case. This moment exhibited a linear relationship with yaw angle and was primarily attributed to the pressure difference occurring near the windward and leeward sides of the nose. The increased flow angle about the leeward side resulted in greater suction would turn the body in the direction of the flow angle, while the positive rolling moment coefficient occurred due to the difference in pressure over the sides of the body.

3.2 Forebody Structure

An introduction to the flow structures which developed in the yawed condition and their corresponding locations is shown in Fig. 3.6. Within the yawed condition flowfield changes were dominated by variation in both the separated flow structures and longitudinal vortices, with these effects initiated at the front of the body.

Within the yawed condition the surface pressure distribution over the windward and leeward sides was notably affected in the forebody region due to the change in angle of the oncoming flow. On the windward side the flow angle aided toward the suppression of the side separation bubble due to a reduced adverse pressure gradient. This decreased

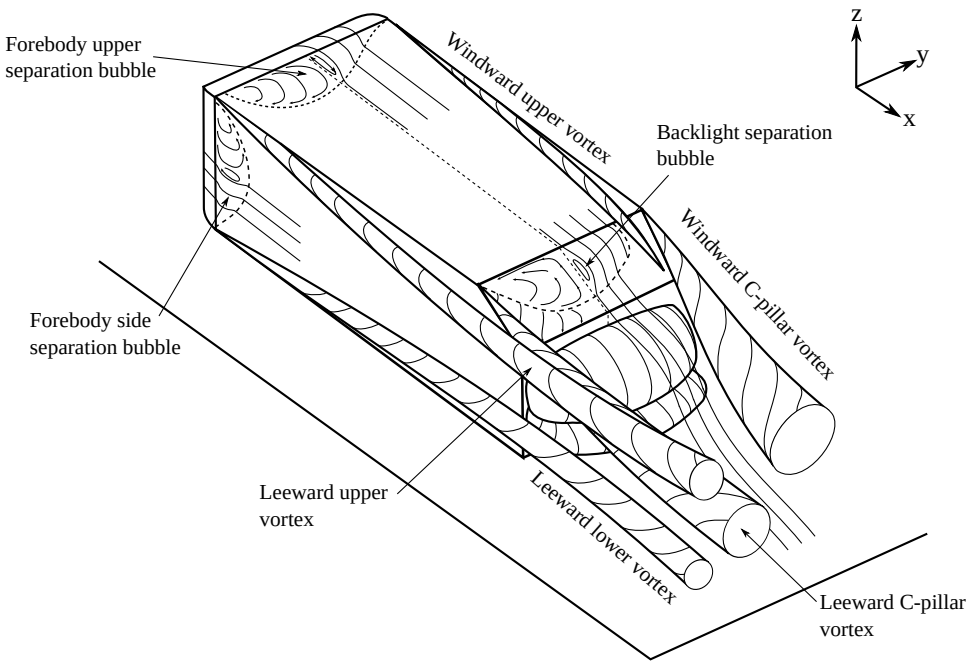

FIGURE 3.6: Diagram of the prominent time-averaged flow structures identified in the yawed condition

the separation length and resulted in an overall increase in the windward surface pressure distribution, particularly focussed toward the forebody region.

The suppression of the separated region on the windward side was progressive as the yaw angle increased. At a 10° yaw angle the flow remained completely attached, as is shown in Fig. 3.7d)ii) which resulted in the loss of vortices propagating along the windward side. At 2.5° and 5° yaw angles a narrowing of the separated region was observed to occur with a decrease in the length of NBL_W. SN_{UW} changed from a stable node structure to stable focus in Fig. 3.7b)ii) as the reduced separation bubble size resulted in the vortical structure being more aligned in the normal axis to the face.

On the opposing leeward side the opposite effect occurred. The adverse pressure gradient increased as the flow turned through a sharper angle. This resulted in an increase in the separation length, and additional changes to the flow structure. The leeward side separation line NBL_L, as shown in Fig. 3.7, extended further across the width of the face. Its vertical extension in the z-axis increased from 0.114L in the straight-line condition to 0.151L, 0.172L, and 0.210L at 2.5°, 5°, and 10° yaw angles. At a 10° yaw angle the line extended completely to the lower edge of the face, as the separated area also increased in width.

A central unstable node emerged in the centre and was encircled by the primary vortex. SF_{LL} shifted aft and remained in a similar position in the z-axis as NBL_L following a

continuous arc about the lower side. PBL_{UL} extended further toward the lower side as PBL_{LL} was observed to contract as the yaw angle increased. This corresponded to an increase in the size and strength of the lower longitudinal vortex which drew the flow from the separation bubble downward, and is discussed further in Section 3.4.

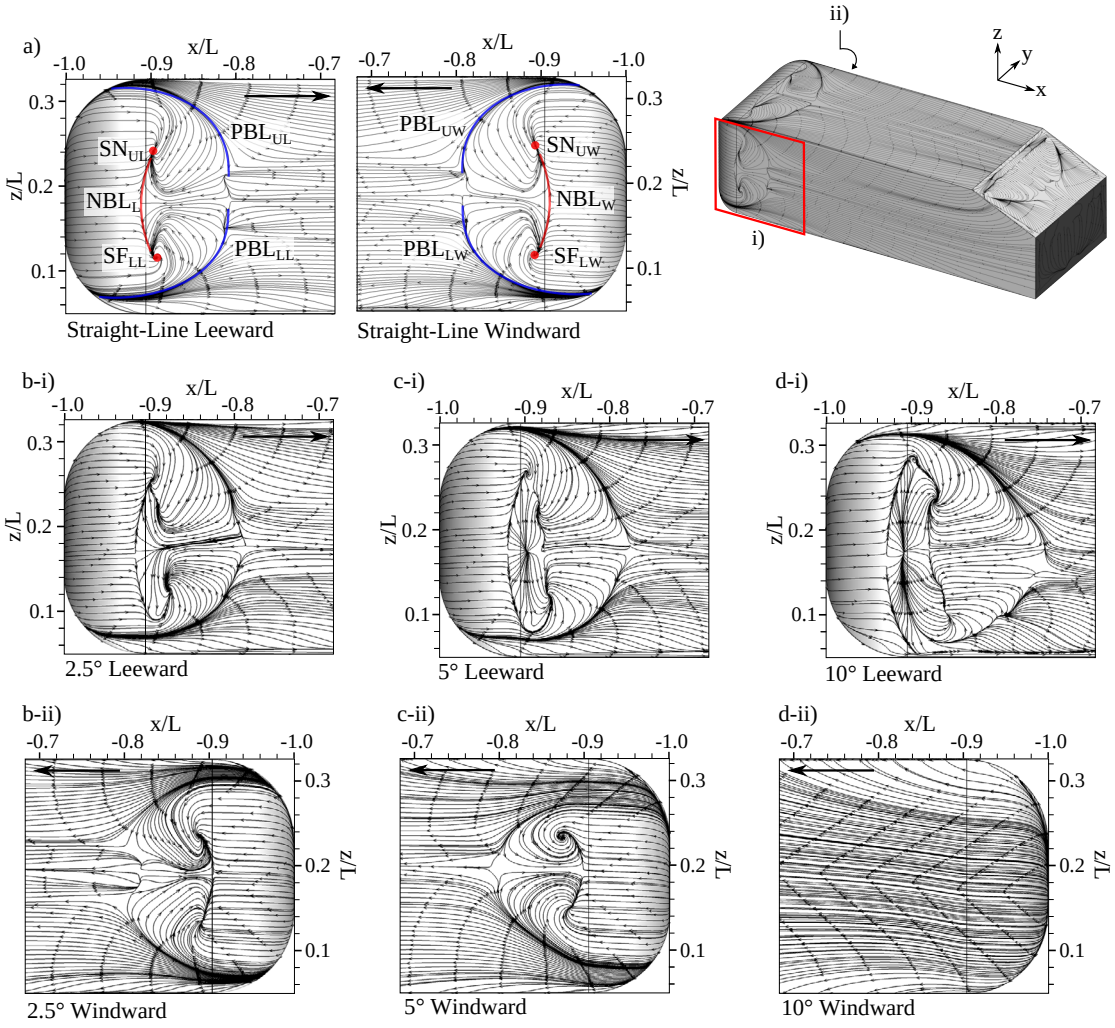

FIGURE 3.7: Surface streaklines over the sides of the forebody indicating locations of separation and reattachment for a) the straight-line condition, b) 2.5° angle of yaw, c) 5° angle of yaw, and d) 10° angle of yaw

The additional change in the surface pressure is shown in Fig. 3.8. The flow angle resulted in a leeward suction peak of greater magnitude, where a 44.8%, 24.7%, and 10.7% decrease in pressure occurred at this point for the 10°, 5°, and 2.5° angles, coupled with an extension of the pressure recovery region. From $x/L \approx -0.75$ to $x/L = 0$ the surface static pressure along $z/L = 0.18$ remained similar to the straight-line condition. The presence of the vortical structures emitted from the separation bubble were observed to regulate surface static pressure over the face. At a 10° yaw angle the suppression of

this separation on the windward side caused the greatest change with a abrupt increase in the surface static pressure.

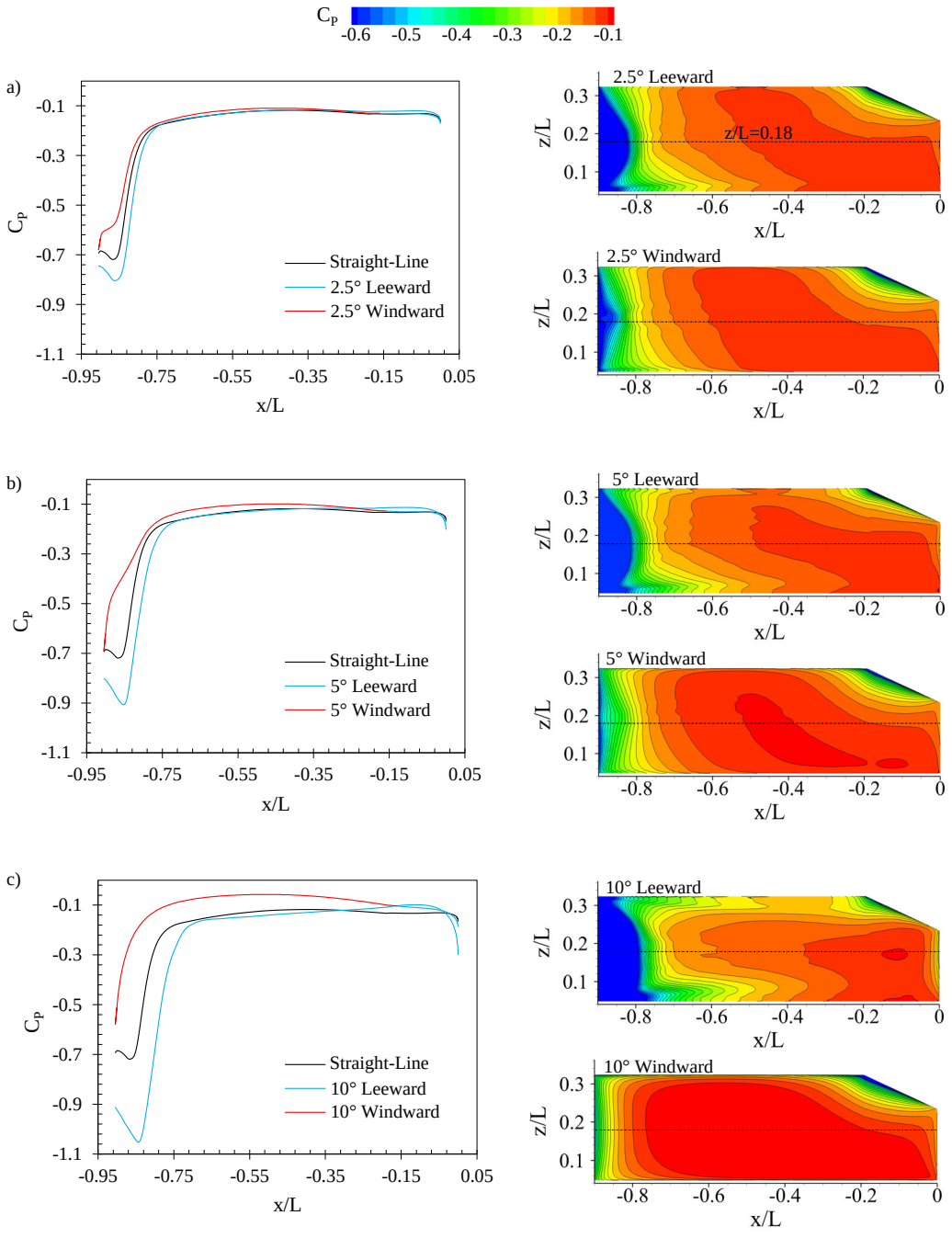

FIGURE 3.8: Pressure coefficient distribution over the sides of the body for a) 2.5° angle of yaw, b) 5° angle of yaw, and c) 10° angle of yaw

The pressure contours shown in Fig. 3.8 on the leeward side for the 5° and 10° yaw angles revealed evidence of a pressure distribution that indicated the formation of stronger longitudinal vortices over these sides, with a corresponding low pressure region occurring

along both the upper and lower edges. The surface static pressure gradient near the C-pillar can be observed as larger on the windward side. The low pressure region was observed to extend both further down the backlight and further back along the upper surface, as will be discussed further in Section 3.5.

The flow angle also resulted in the upper separation bubble being shifted toward the leeward side. As the yaw angle increased the stagnation point on the nose shifted toward the windward side and resulted in more flow entering the upper bubble from the windward side. At a 10° yaw angle shown in Fig. 3.9 the exiting flow from the separation bubble was entrained directly into the longitudinal vortex rolling off the upper edge and contributed to an increase in its size.

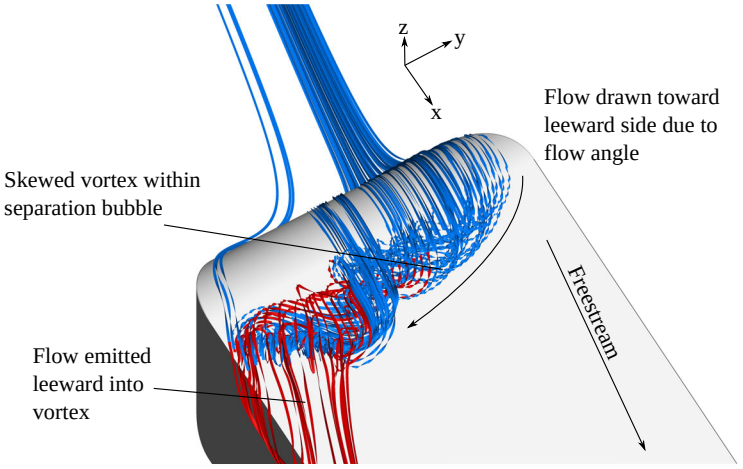

FIGURE 3.9: Streamlines indicating separation bubble flow structure over the forebody upper surface in the yawed condition

Examining the surface flow structure in detail, as shown in Fig. 3.10, highlighted the change in the separated flow regions which occurred downstream of the nose. On the upper surface in Fig. 3.10a) equal flow (in the time-averaged sense) was drawn into the structure about both the windward and leeward sides. For the 2.5° and 5° yaw angles SN_{FL} shifted toward the leeward side by 0.015L and 0.027L respectively and this corresponded to less flow entering the bubble about the leeward side. For the 10° yaw angle this feature was no longer visible with the leeward component of the arched vortical structure becoming less prominent.

UN_F corresponded to the location about which the emitted vortical structures would be alternately shed and propagate downstream. This central flow region was observed to also shift leeward with SN_{FL} remaining the feature which bound the structure at its leeward border. UN_F was positioned 0.011L, 0.023L, and 0.052L further leeward for the 2.5°, 5°, and 10° yaw angles when compared to the corresponding central straight-line position.

SN_{FW} was drawn into NBL_{UF} as this line extended across to the windward side. On this side The flow was observed to separate immediately adjacent to the vortical structure contained within the separated region, as opposed to over the divergent flow region containing UN_F.

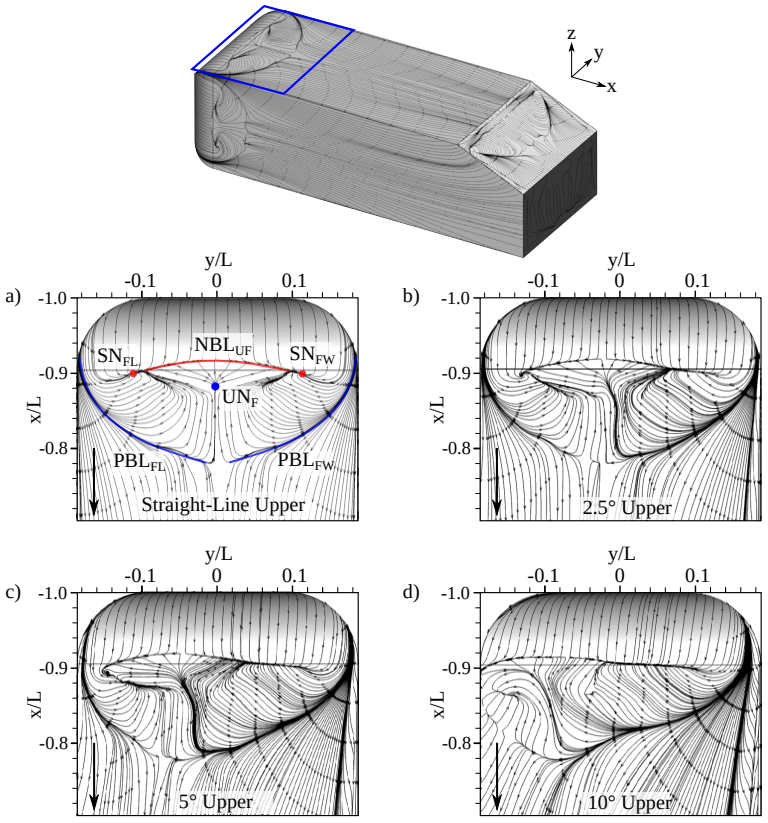

FIGURE 3.10: Surface streaklines in the forebody region over the upper side for the a) the straight-line case, b) 2.5° angle of yaw, c) 5° angle of yaw, and d) 10° angle of yaw

The instantaneous wake structure revealed more detail about the interactions occurring between the front and rear of the body, and is shown in Fig. 3.11. For a 5° yaw angle the vortical structures emitted from the forebody separation were observed to pass over the leeward C-pillar location which resulted in a brief increase in vertical displacement before being deflected downwards over the backlight surface. For the 10° yaw angle these structures can be observed to be drawn into the upper leeward vortex, shown in Fig. 3.11. The vortex continued downstream and resulted in increased vertical displacement of the leeward wake region.

The leeward separation bubble emitted vortices with an increased span which merged to form larger structures downstream. The increased strength of the upper leeward vortex deflected the structures downwards for the 10° yaw angle, causing an interaction with lower leeward vortex and a transient pulsing. Additionally, this vortex induced a counter-rotating vortex from the ground which increased proportional to yaw angle.

On the windward side the suppression of the forebody separation bubble can be observed to result in the absence of vortical structures along the windward side for the 10° yaw angle. For the 5° yaw angle case vortical structures were again emitted but occurred across a much shorter span which was in agreement with the reduction in the width of NBL_W.

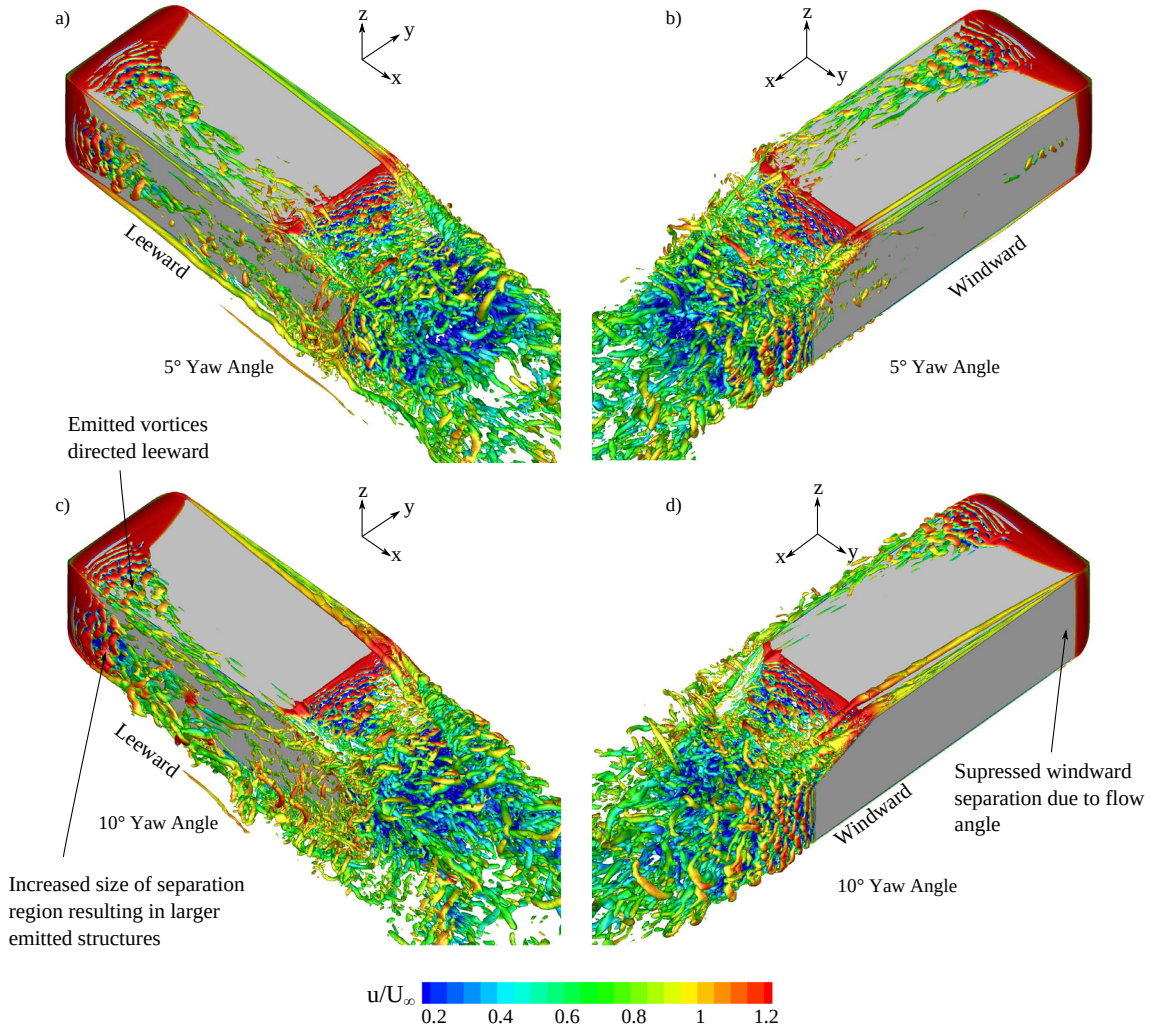

FIGURE 3.11: Isosurfaces of Q = 2×10^4 with contours of x-velocity for a 5° and 10° yaw angle

3.3 Mid Body

The changes that occurred over the forebody caused the time-averaged boundary layer thickness to vary when measured on the windward and leeward sides, as is shown in Fig. 3.12. The leeward boundary layer was 12.5 times thicker at the measured location than for the corresponding windward side. This occurred primarily through an extension

of the velocity deficit due to the interaction of the emitted vortical structures. For the 5° and 2.5° yaw angles the leeward boundary layer was 5.9 times, and 2.9 times thicker than the opposing side.

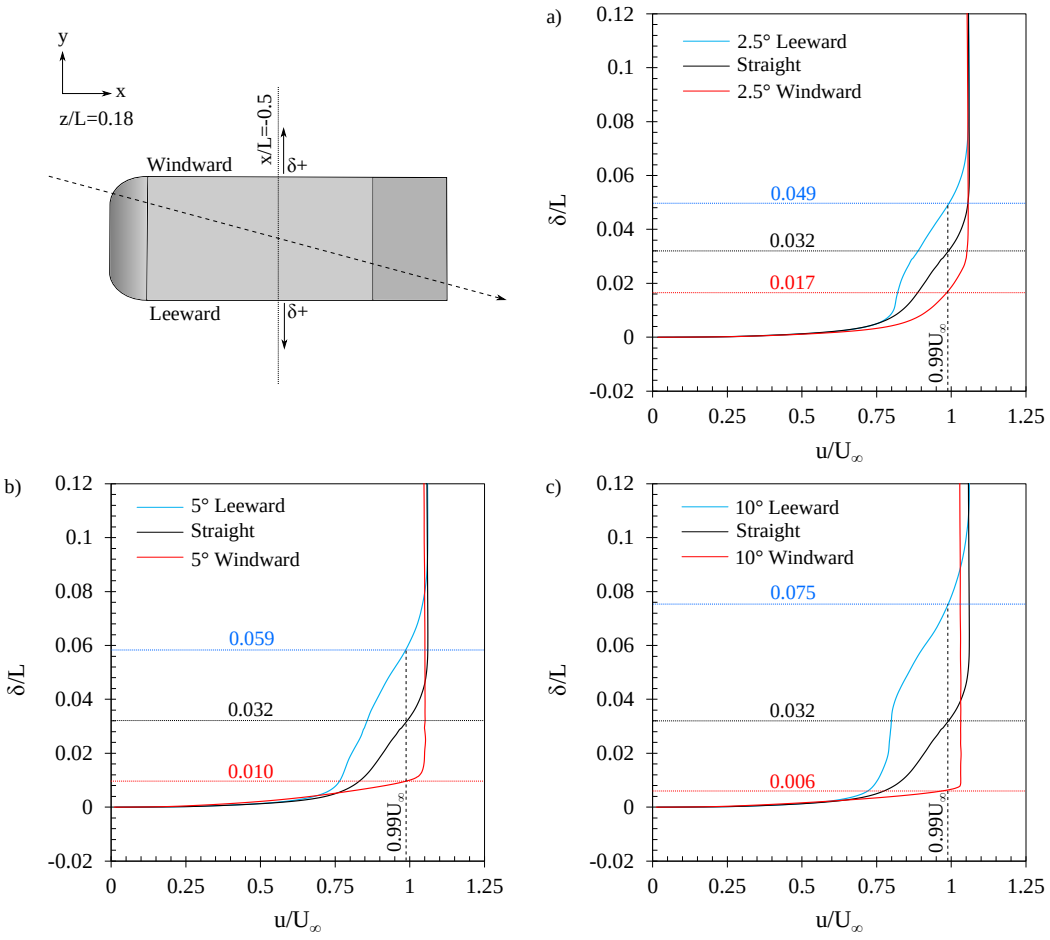

FIGURE 3.12: Time-averaged boundary-layer profile at z/L=0.18, x/L=0.5 for yawed cases compared to the straight-line condition for a a) 2.5° angle of yaw, b) 5° angle of yaw, and c) 10° angle of yaw

The pressure distribution was measured along the upper and backlight surfaces with profiles taken at y/L = 0.15 and y/L = -0.15, as shown in Fig. 3.13. The increase in the production of lift resulted from a local decrease in pressure which occurred over both surfaces. The formation of the longitudinal vortex, which passed over the upper surface and partially extended down the backlight, resulted in increased vortex-induced suction. For the 10° yaw angle case shown in Fig. 3.13c) the passage of this vortex above the surface caused a low pressure from x/L = 0.5 to the suction peak.

Increased C-pillar vortex strength combined with the additional longitudinal structure caused a windward suction peak 51.3% greater in magnitude for the 10° yaw angle, with the leeward suction peak also greater, albeit by a less significant 3.5%. For the 5°

yaw angle shown in Fig. 3.13b) the result is somewhat misrepresented due to the direct passage of the upper windward edge longitudinal vortex suppressing the suction peak, which was lower than the leeward side in this instance. However, in Fig. 3.13a) for the 2.5° case it was again observed that both the windward and leeward suction peaks were greater than the straight-line condition (by 4.4% and 25.7% respectively).

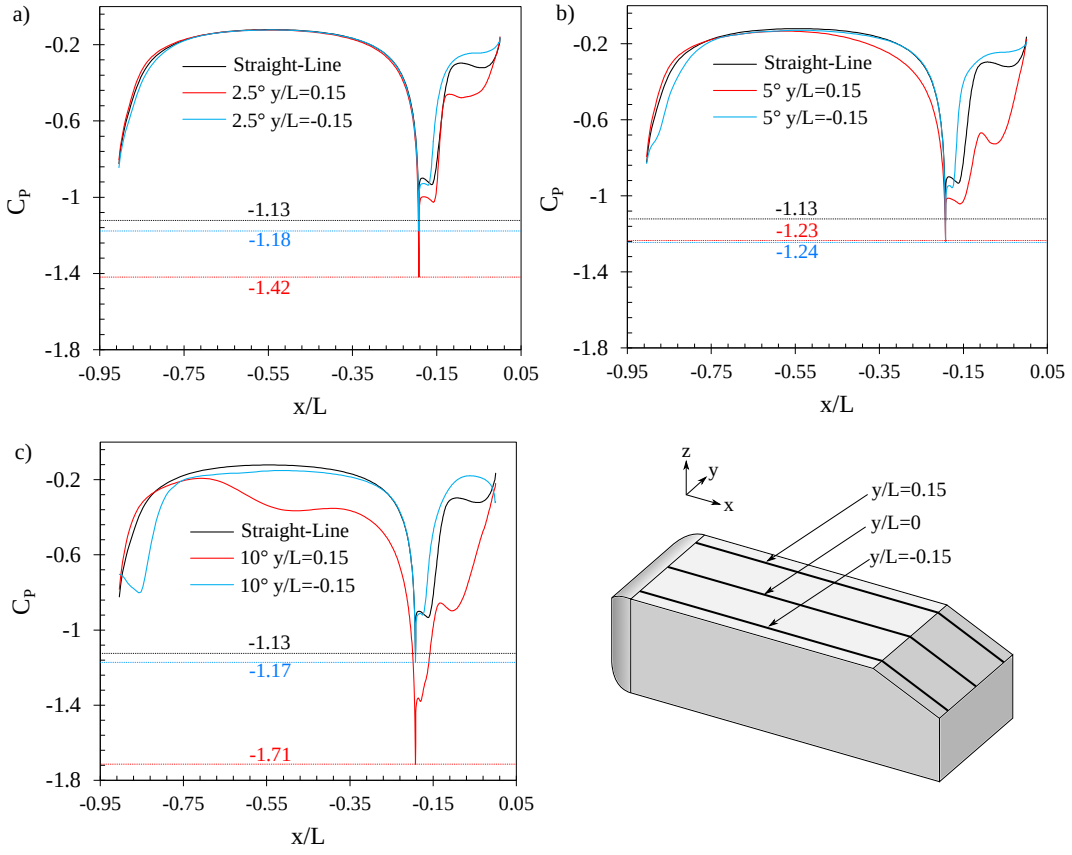

FIGURE 3.13: Pressure coefficient profile along upper side at y/L=0.15 and y/L=-0.15, compared to the straight-line condition at the same location for a a) 2.5° angle of yaw, b) 5° angle of yaw, and c) 10° angle of yaw

3.4 Longitudinal Vortex Structure

From these results it was established that the change in the longitudinal vortex structure was having a significant effect on the surface pressure distribution. The flow angle across the sharp edges of the body resulted in defined abrupt changes in surface pressure which caused the formation and detachment of the vortices shown in Fig. 3.14. The upper leeward, upper windward, and lower windward vortices all continued to increase in strength as the yaw angle increased and affected the aerodynamic forces and wake structure.

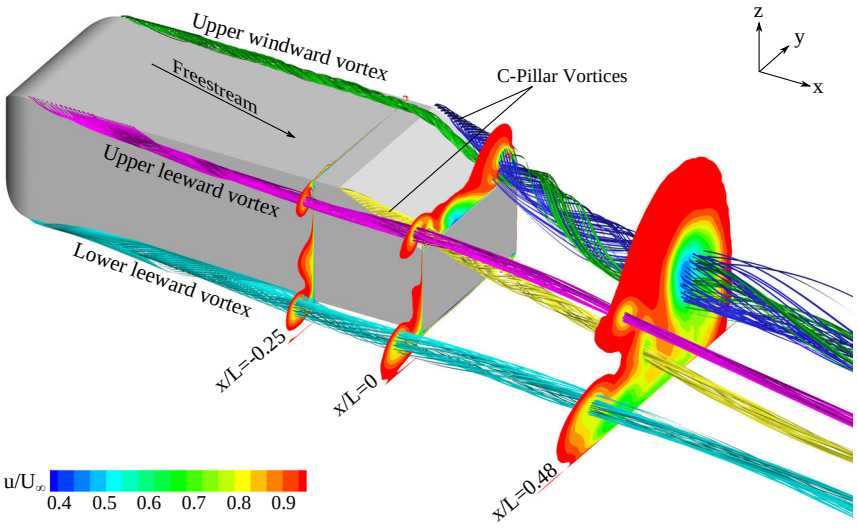

FIGURE 3.14: Locations of primary longitudinal vortices observed in the yawed condition and downstream measurement planes, with a 10° yaw angle shown

In the straight-line condition only minor vortex structures were noted to form near the upper edge along either side which merged with the C-pillar vortex at the start of the backlight surface. Examining the flow structure at x/L = -0.25, as shown in Fig. 3.15, highlighted the change in the longitudinal vortex structure developing along the length of the body, prior to the interaction with the backlight. Boundary layer growth on the lower surface resulted in the formation of vortices which rolled outwards from underneath the body, as is shown in Fig. 3.15. It can be observed that the lower leeward vortex became larger with an increased core deficit as the yaw angle increased. The flow angle resulted in a progressive absence of vortices on the windward side, most evident in Fig. 3.15d).

The time-averaged central velocity deficit on each side of the upper, windward, and leeward sides was due to the emission of vortices from forebody separation bubbles. As the yaw angle increased from Fig. 3.15b) to c) the upper surface deficit shifted leeward due to the flow angle, and at 10° the emitted vortices from the separation bubble were drawn directly into the upper leeward vortex which resulted in an increase in size as shown in Fig. 3.15d).

In Fig 3.16b) it can be observed that at a yaw angle of 2.5° the formation of the lower windward vortex was suppressed and a minor structure formed underneath the body, which assumed the opposite rotational sign. For 5° and 10° of yaw, two lower windward structures formed underneath the body due to the detachment of the initial vortex. At x/L = 0 the lower leeward vortex increased in size due to the flow angle and was also located further away from the surface.

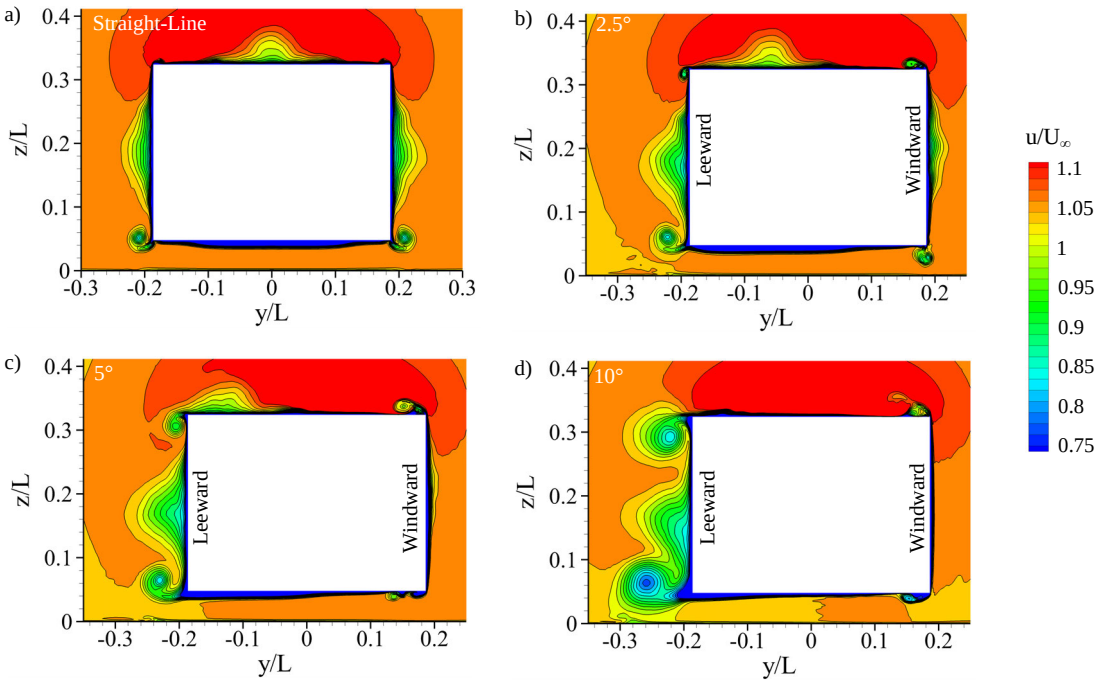

FIGURE 3.15: X-velocity contours at x/L=-0.25 for a) the straight-line case, b) 2.5° angle of yaw, c) 5° angle of yaw, and d) 10° angle of yaw

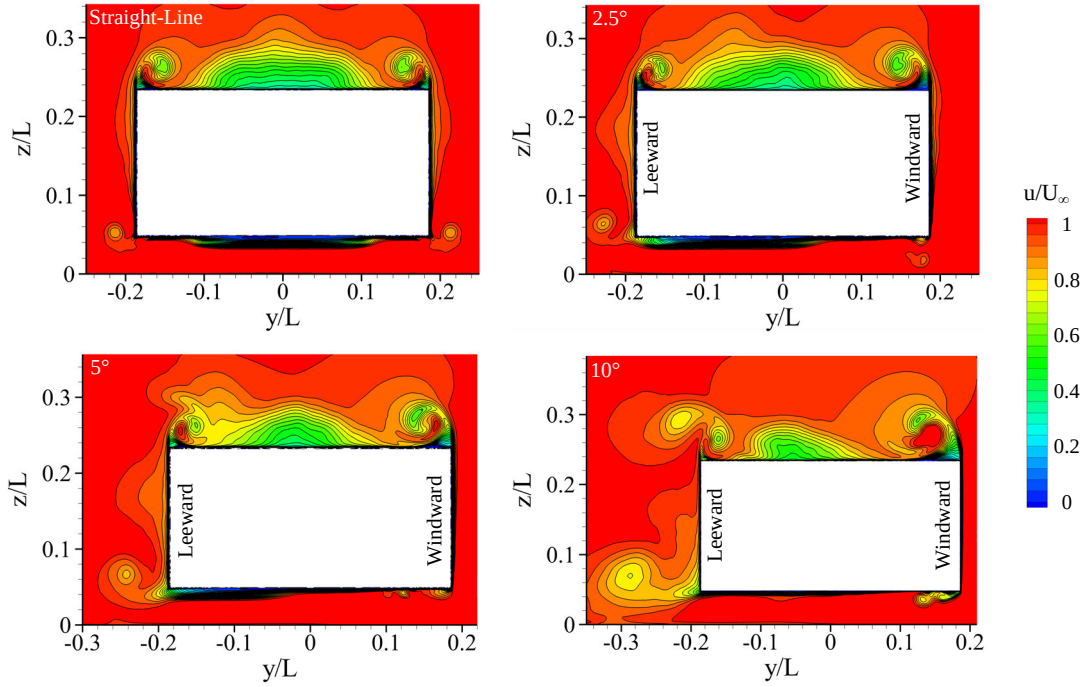

FIGURE 3.16: X-velocity contours at x/L = 0 for a) the straight-line case, b) 2.5° angle of yaw, c) 5° angle of yaw, and d) 10° angle of yaw

At x/L = 0.5 the time-averaged wake primarily consisted of two counter-rotating longitudinal vortex structures, as shown in Fig. 3.17. At yaw angles of 2.5° and 5° the trajectory of the upper leeward vortex resulted in an interaction with the stronger leeward C-pillar vortex where it failed to remain a separate coherent structure. The lower leeward vortex was also drawn into the wake and resulted in the skewed leeward wake structure observed in Fig. 3.17b) and c).

At a yaw angle of 10° the prominent longitudinal vortices remained distinctly separate. Differing from other cases, these did not merge with the central wake deficit and remained separate coherent structures.

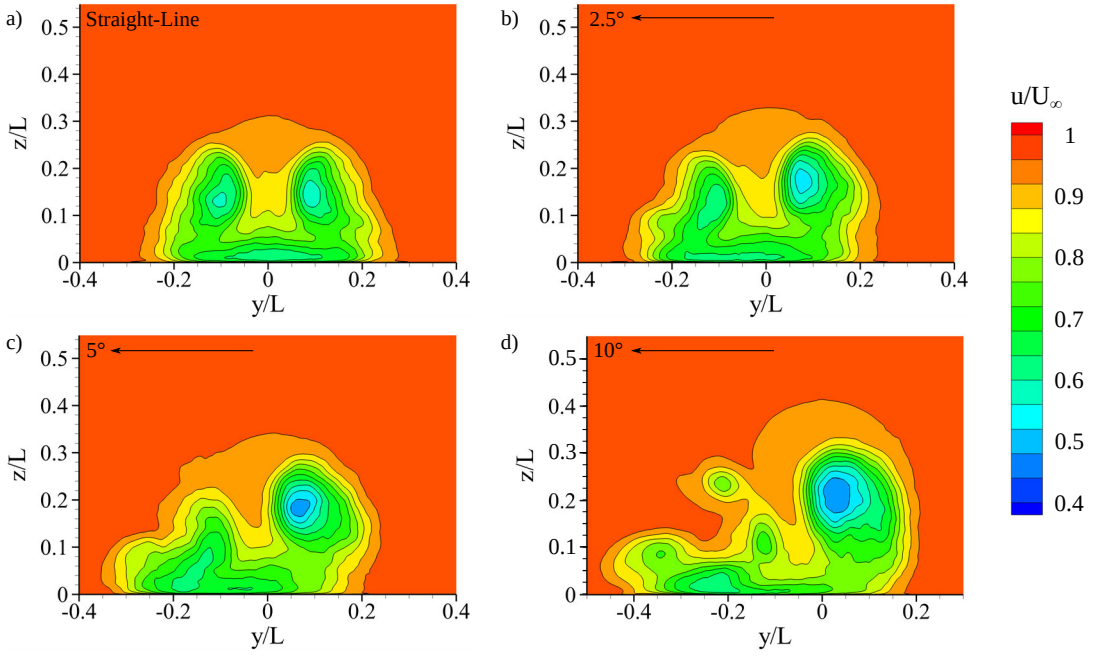

FIGURE 3.17: X-velocity contours at x/L=0.5 for a) the straight-line case, b) 2.5° angle of yaw, c) 5° angle of yaw, and d) 10° angle of yaw

3.5 C-Pillar Vortices

When measured at x/L = 0 vortex core locations were shifted leeward as yaw angle increased and the windward vortex increased its vertical displacement, as shown in Fig. 3.16. At a 10° yaw angle, the windward C-pillar vortex core was positioned -0.023L (positive leeward) in the y-axis and +0.021L higher in the positive z-direction, comparatively smaller displacements occurred for 5° (y = -0.012L, z = +0.008L) and 2.5° (y = -0.004L, z = +0.002L).

Smaller displacement occurred on the leeward side with this structure demonstrating a comparatively higher degree of independence. Only a -0.007L shift in the y-axis and +0.002L positive shift in the vertical axis occurred for the 10° yaw angle, with respectively smaller changes for the lower angles of yaw.

C-pillar circulation was measured over the backlight surface to gain a quantitative comparison of the effect of yaw angle toward the C-pillar vortices, as is shown in Fig. 3.18. The flow angle across the rear of the body increased the adverse pressure gradient and induced a stronger vortex, with the alternative scenario occurring on the leeward side. The windward side is shown in Fig. 3.18a) where an increase in circulation occurred with yaw angle. Between x/L = -0.1 and 0 the increase was an average of 82.1%, 51.9%, and 23.1% for yaw angles of 10°, 5°, and 2.5° respectively. For the leeward side shown in Fig. 3.18b) a less-consistent trend emerged where circulation was observed to decrease, but to a small extent. For a 10° yaw angle an average 10.8% decrease occurred, where a 12.6% and 10.7% reduction occurred for yaw angles of 5° and 2.5°.

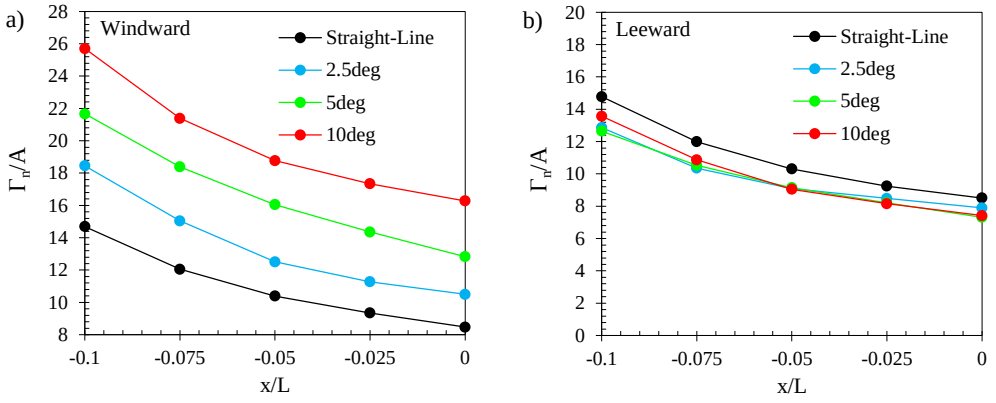

FIGURE 3.18: Circulation strength at C-Pillar locations for a) the windward location, and b) the leeward location

An increased pressure deficit was thus observed on the windward side and is shown in Fig. 3.19a). For a 10° yaw angle the pressure deficit was 132.1% greater than the straight-line condition. The larger magnitude effect toward the pressure deficit compared to circulation was further attributed to the windward increase in the acceleration of the flow down the backlight surface, as shown in Fig. 3.13. On the leeward side the pressure deficit was of a smaller magnitude as yaw angle increased. A 2.5° yaw angle resulted in a 21.2% static pressure increase, 5° resulted in 25.5%, with a maximum 39.7% change occurring for a 10° yaw angle. This similar change in leeward pressure deficit between a 2.5° and 5° yaw angle thus mirrored the circulation characteristics, and was attributed to the detrimental interaction of the counter-rotating upper leeward vortex.

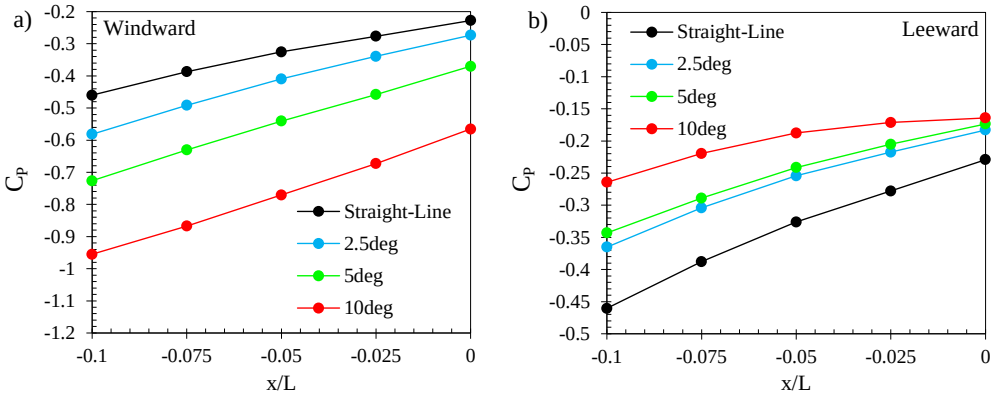

FIGURE 3.19: Pressure coefficient deficit at C-Pillar locations for a) the windward location, and b) the leeward location

A frequency analysis was conducted through measurement of velocity fluctuations at either upper corner of the backlight surface in the region of C-pillar vortex formation. In the straight-line condition spanwise vortex shedding off the initial backlight edge resulted in a clear dominant frequency Str = 17.5 due an induced pulsatile behaviour, as shown in Fig. 3.21. On the windward side, an increase in this frequency was observed which coincided with increased local acceleration of the flow. At yaw angles of 2.5° and 5° this same peak was measured as Str = 19.4 and 20.9 respectively. For the 10° yaw angle a range of peaks were identified to occur between Str = 4.9 and 27.4 and was attributed to increased interaction with the longitudinal vortices developing over the upper windward edge.

On the leeward side the development of the longitudinal vortex structure which bordered the separation bubble region resulted in the C-pillar vortex and the spanwise structures remaining separate, as is shown in Fig. 3.22. This effect resulted in a loss of the pulsatile vortex core characteristics and a broadband frequency distribution.

3.6 Backlight Structure

Examining the backlight flow structure in more detail, as shown in Fig. 3.22 and 3.21, the initial formation of spanwise vortices across the width of the face remained common with the straight-line condition. Vortices exhibited the same merging mechanism within the separation bubble region. In all instances they combined to form larger vortices, before the central part of the span raised off the surface to form a hairpin or arch-type shape followed by detachment of the legs from the surface. The vortex merging region was observed to narrow as the yaw angle increased due to the impingement by the longitudinal vortices. This narrowing resulted in the head of the merged vortex

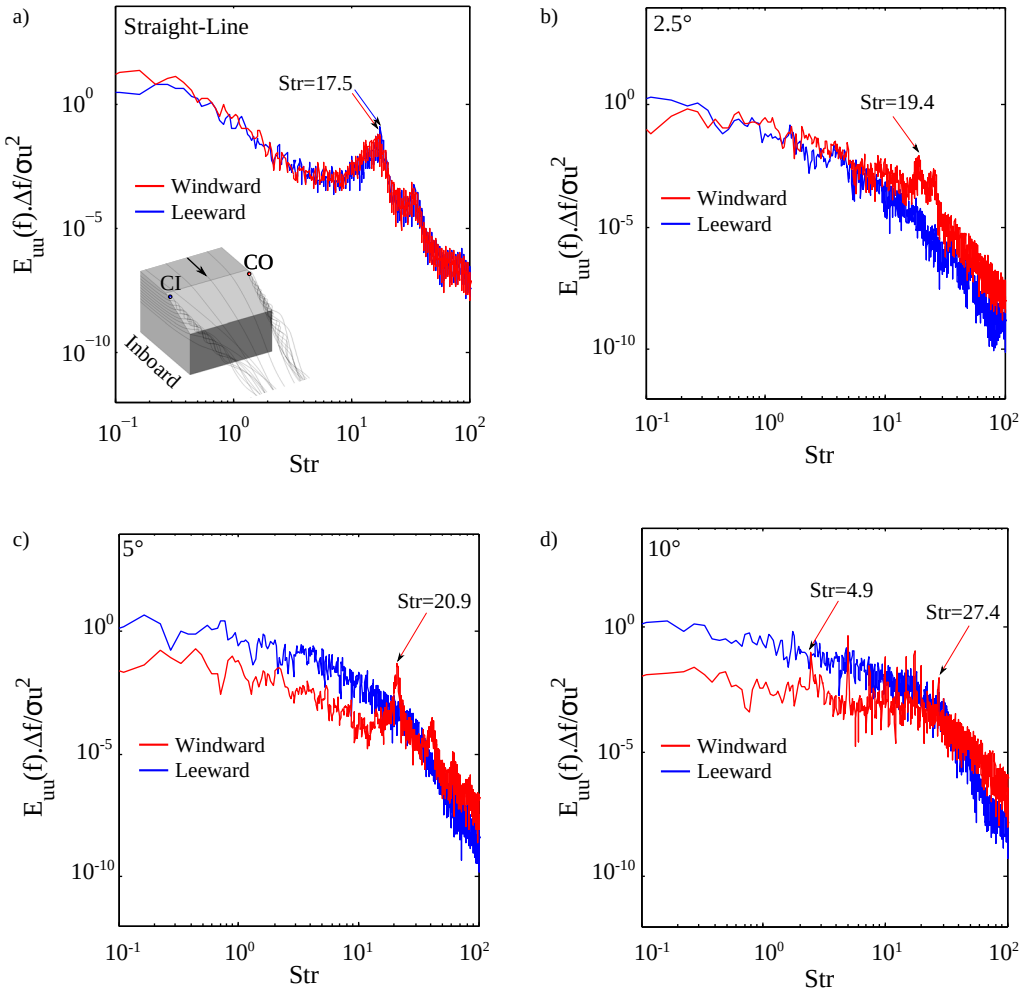

FIGURE 3.20: Power spectral density plot of velocity magnitude at the CI and CO location for a) the straight-line condition, b) 2.5° angle of yaw, c) 5° angle of yaw, and d) 10° angle of yaw

structures lifting higher off the backlight surface and into a region of higher velocity, which is most apparent in Fig. 3.22d).

On the leeward side, near the C-pillar, as shown in Fig. 3.22 the leeward leg of the merged vortices remained attached further down the face. This was attributed to the longitudinal vortical component induced by the flow angle across the upper region of the separation. This resulted in the absence of significant vortices forming between y/L≈0.12 and the primary C-pillar vortex. Furthermore the regular shedding of the shear layer was also observed to no longer interact with the C-pillar vortex. The resultant effect toward the vortex was the meandering-type motion shown in Fig. 3.22c) and d), as opposed to the rapid pulsing motion shown in Fig. 3.22a).

On the windward side the passage of the upper windward vortex was observed to suppress the vortex merging and resulted in small vortices retaining close proximity to the surface.

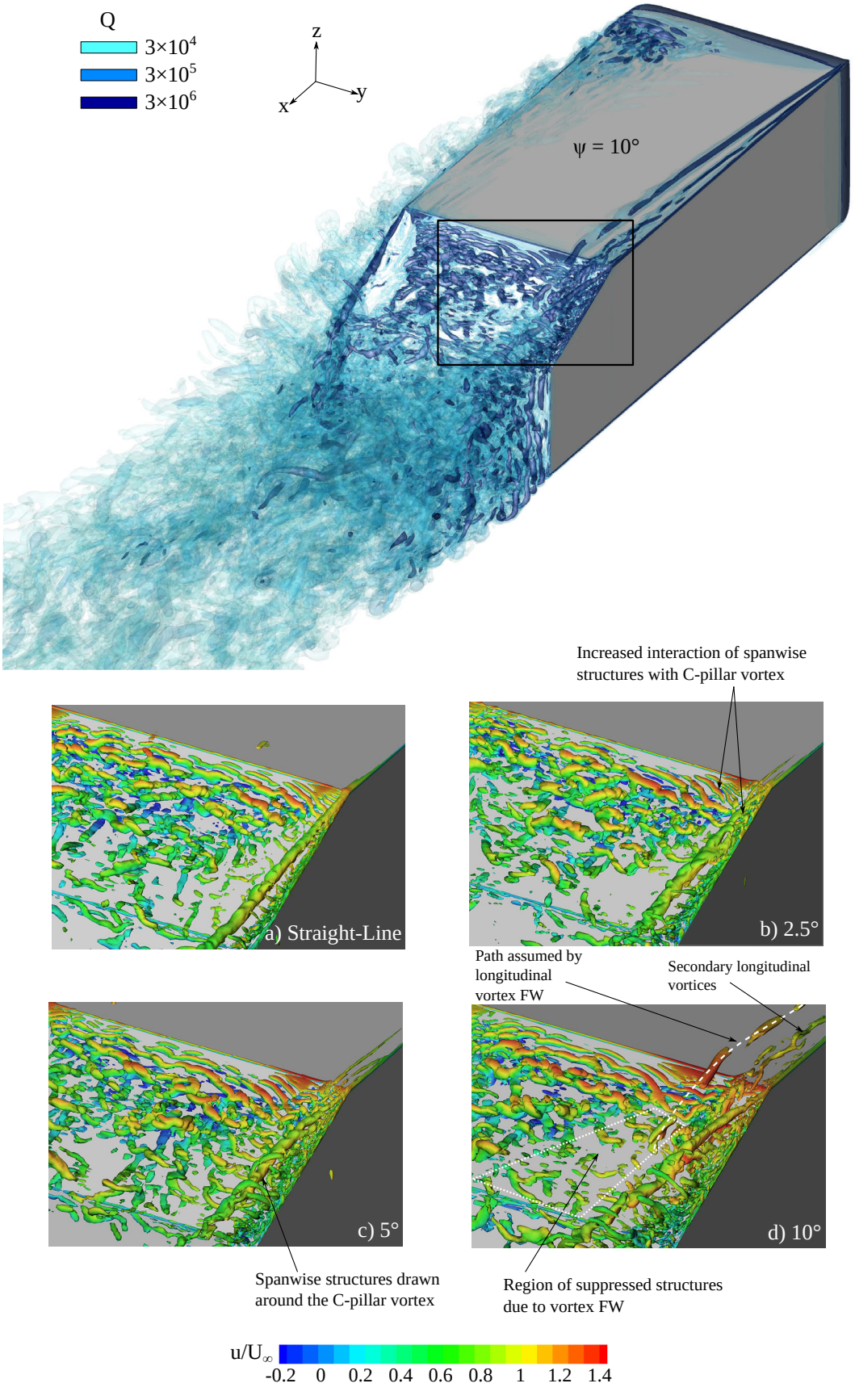

FIGURE 3.21: Instantaneous backlight flow structure on the windward side shown with isosurfaces of Q = 1.5×10^6 coloured according to instantaneous non-dimensional x-velocity for a) the straight-line case, b) 2.5° angle of yaw, c) 5° angle of yaw, and d) 10° angle of yaw

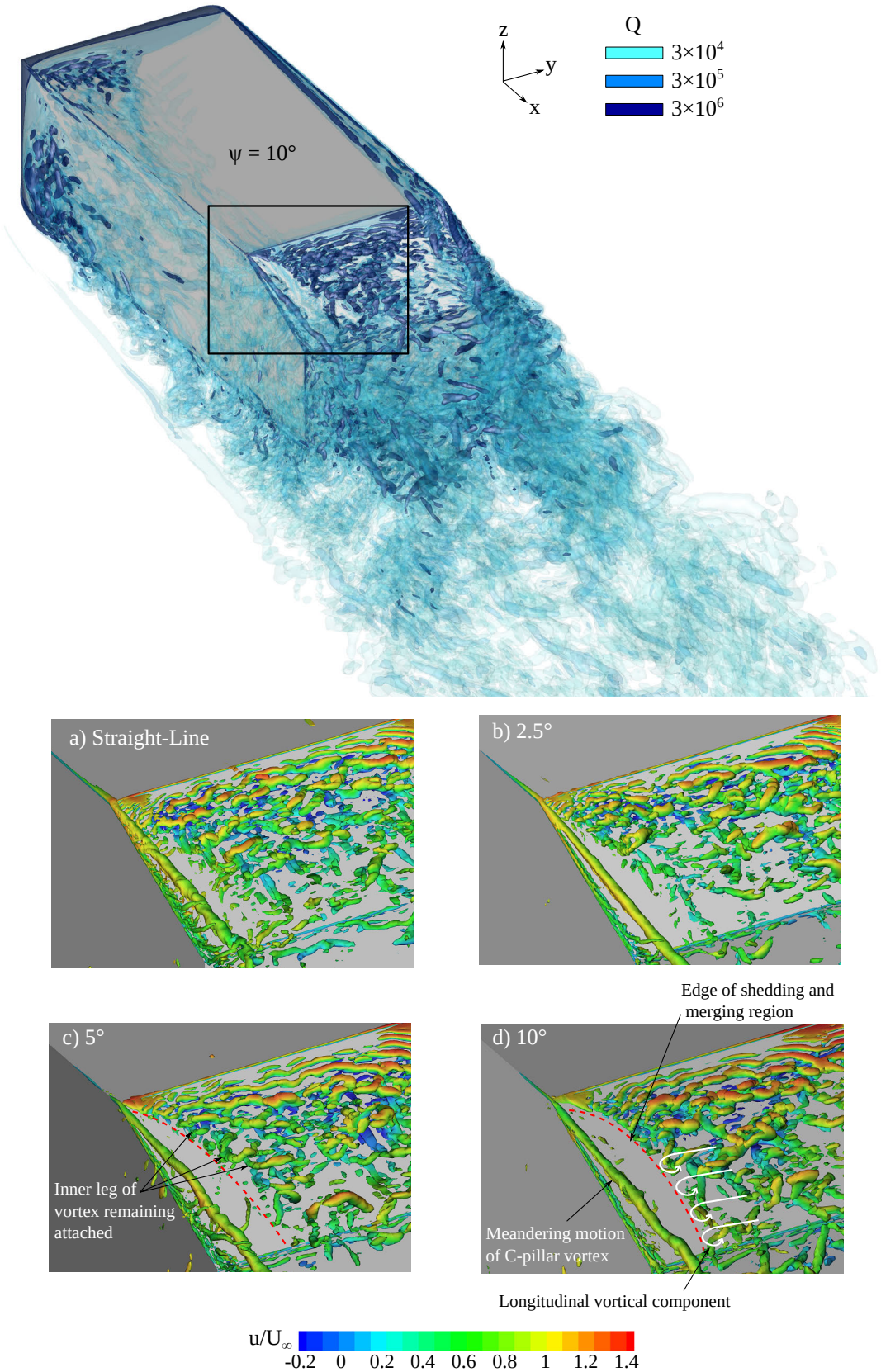

FIGURE 3.22: Instantaneous backlight flow structure on the leeward side shown with isosurfaces of Q = 1.5×10^6 coloured according to instantaneous non-dimensional x-velocity for a) the straight-line case, b) 2.5° angle of yaw, c) 5° angle of yaw, and d) 10° angle of yaw

The vortices were noted to have an increased span in the case of a 5° yaw angle but retained a narrow core diameter. At a yaw angle of 10° these were orientated irregularly with a shorter span. In addition to the primary FW vortex the formation of secondary smaller longitudinal vortices occurred further along the upper face. These were observed to pass underneath the primary vortex and merge with the larger structure.

Frequency analysis was conducted of velocity recorded at several locations on the symmetry plane to investigate the transient flow mechanisms which occurred in this region, with results shown in Fig. 3.23. Location M1 was positioned within the upper region of the separation bubble and an increase in the dominant frequency was observed to occur as yaw angle increased. The straight-line condition exhibited a peak where the maximum amplitude occurred at Str = 0.31. Nearby peaks in the distribution were attributed to the interaction of the forebody vortex shedding with Str = 0.28 recorded within the forebody separation bubble.

A graph of the primary bifurcation line corresponding to the location of flow reattachment down the backlight face is shown in Fig. 3.24 where the investigated yaw angles are compared to the straight-line condition. The increase in windward C-pillar circulation and the presence of the upper windward vortex were observed to result in earlier reattachment of the flow on the windward side and a reduction in the with of the separation bubble.

On the leeward side the separation length was also reduced despite a reduction in C-pillar circulation. For the 2.5° yaw angle leeward reattachment occurred 0.0015L earlier at y/L = -0.1 than at the corresponding windward location y/L = 0.1. However for the 10° yaw angle the windward separation length was 0.06L greater at y/L = -0.1 when compared to the corresponding leeward side. Of further note is how this separation length inversely correlated to the suction peak magnitude at the backlight edge, previously shown in Fig. 3.13, and highlighted the link between the production of lift and the backlight flow structure.

The time-averaged separation length of the backlight separation bubble was 0.151L, 0.144L, and 0.124L when measured on the symmetry plane for the yaw angles of 2.5°, 5°, and 10° respectively. In the straight-line condition this same length was 0.137L, however this was due to a central contraction of the separated region due to the interaction of the forebody vortices. Integrating above PBL_P to find the mean separated area identified the straight-line area to be equal to $0.042L^2$. For the 2.5°, 5°, and 10° yaw angles the size of this region was $0.037L^2$, $0.032L^2$, and $0.030L^2$. Thus the mean area occupied by the primary separation reduced as yaw angle increased.

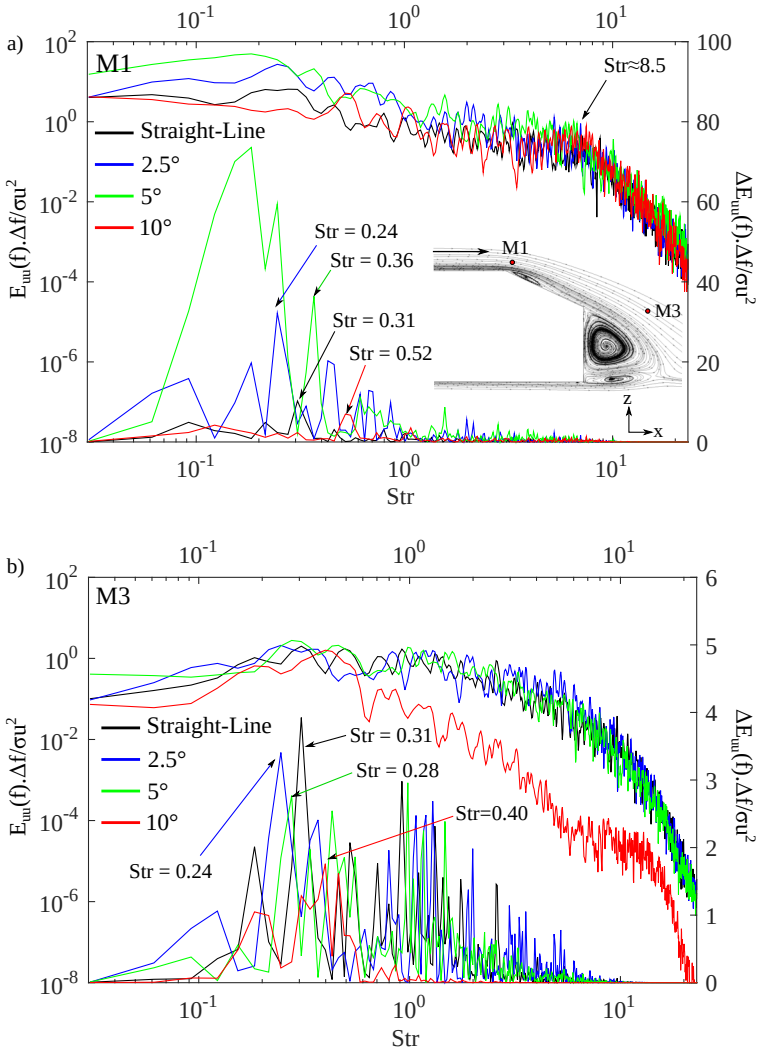

FIGURE 3.23: Raw (upper) and processed (lower) power spectral density plot of velocity magnitude for the three different yaw angles and the straight-line condition at location a) M1, and b) M3

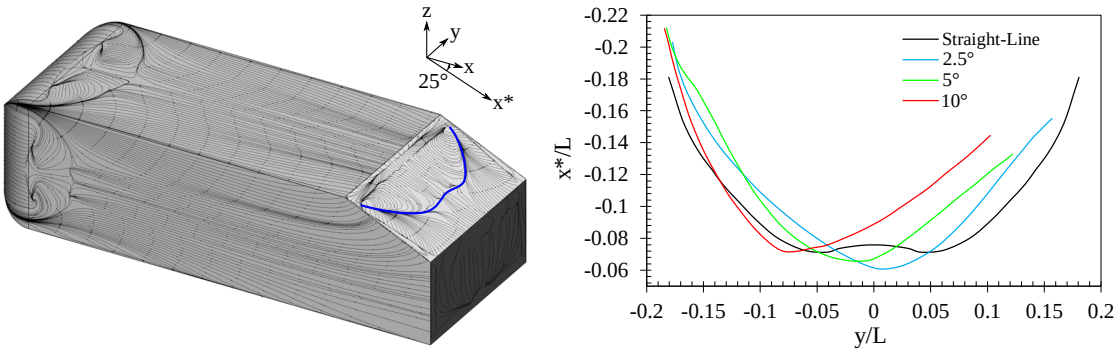

FIGURE 3.24: Mean reattachment line of the primary backlight separation bubble

The dominant frequency was identified to correspond to a periodic enlargement and contraction of the vortex merging region which occurred over the upper part of the backlight. The reduction in the length scale corresponded to a decreased time scale over which this occurred, and thus an increased Str. In addition, at a larger yaw angle the separation bubble increased its vertical displacement during this periodic enlargement, as opposed to the extension down the face which occurred in the straight-line condition.

Figure 3.23b) presents a spectral analysis of velocity measured at the M3 location further downstream. A similar trend was realised with an increased yaw angle observed to correspond to an increase in the dominant frequency recorded at this location, with the exception of the straight-line case. Where results indicated that the passage of flow structures from the forebody was responsible for the comparative increase.

Furthermore the spectrum for the 10° yaw angle became significantly differentiated from those observed for the other cases. The magnitude became similar to that observed near the C-pillar location and was attributed to the longitudinal vortices which damped the magnitude of the velocity fluctuations within the inertial subrange.

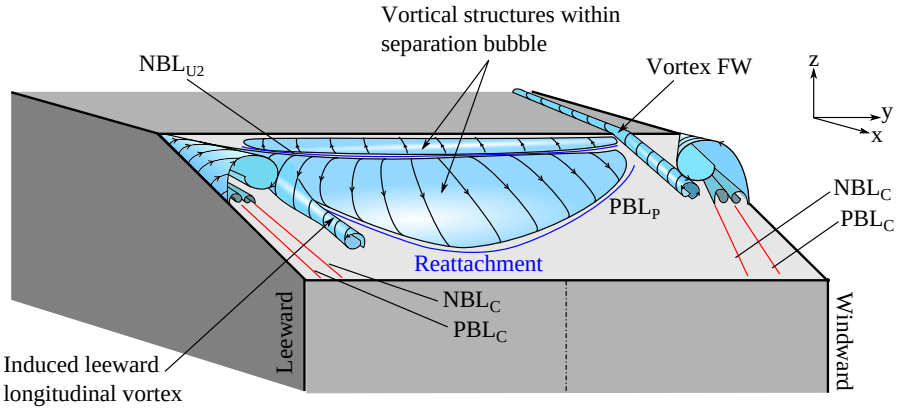

FIGURE 3.25: Separated flow structure over the backlight surface in the longitudinal and transverse axes in the yawed condition

Figure 3.25 gives an illustration of the prominent time-averaged flow features that were observed to occur in the backlight region for the Ahmed body in yaw. In addition to the windward and leeward C-pillar vortices an induced counter-rotating and co-rotating longitudinal vortex also occurred directly below the main structure.

Shear due to the flow angle across the upper region of the separation bubble resulted in the formation of a time-averaged longitudinal vortex which assumed a rotation in the opposite direction to that of the leeward C-pillar vortex and continued down the face.

3.6.1 Surface Flow Structure

Considering the time-averaged flow in more detail, the surface streaklines in the upper leeward and windward corners aided in further understanding the separated flow in the backlight region. In the straight-line condition a symmetrical surface flow structure was observed with positive and negative bifurcation lines indicating separation and reattachment locations respectively.

Within the separation bubble on the backlight there were two main vortex structures orientated across the span of the face. PBL_P indicated the reattachment location of the mean flow and the lower border of the primary separation bubble vortex. The counter-rotating secondary structure resulted in the observation of lines NBL_{U2} and PBL_U.

On the leeward side shown in Fig. 3.26b) and d) at yaw angles of 2.5° and 5°, NBL_{U2} was observed to continue to near the upper edge of the surface, intersecting the backlight edge at y/L = -0.178 and y/L = -0.16 respectively. At a yaw angle of 10° shown in Fig. 3.26f) NBL_{U2} was also shortened, but ended at a stable focus. The decreased the span of the induced counter-rotating structure, resulted in the primary vortex extending to the upper edge of the backlight.

In Fig. 3.26b) at $x^*/L \approx$ -0.17 PBL_P split to form a second bifurcation and this corresponded to the formation of a time-averaged longitudinal vortex which bordered the separation bubble on the leeward side, as shown in Fig. 3.25. At a 5° yaw angle PBL_P was shifted in the positive y-direction and then alternatively back in the opposite direction as the yaw angle increased to 10°. This was again observed to be the result of the front to rear interaction affecting separation length.

On the windward side shown in Fig. 3.26c), e) and g) a complete change in the surface structure occurred due to interaction of the induced upper windward vortex with the backlight separation and C-pillar vortex. At a yaw angle of 2.5° the upper windward vortex merged with the C-pillar vortex at x^*/L = -0.17, to minor effect. While at the 5° and 10° yaw angles, the vortex suppressed flow separation and reduced the width of the backlight separation bubble.

3.7 Rear Structure Interactions

Rear flow structures remained common with the straight-line condition, as shown in Fig. 3.27, however their interactions differed. The leeward C-pillar vortex became more isolated as the angle increased and the stronger windward C-pillar vortex drew flow from across the wake. At a 10° yaw angle the backlight separation bubble, upper recirculation,

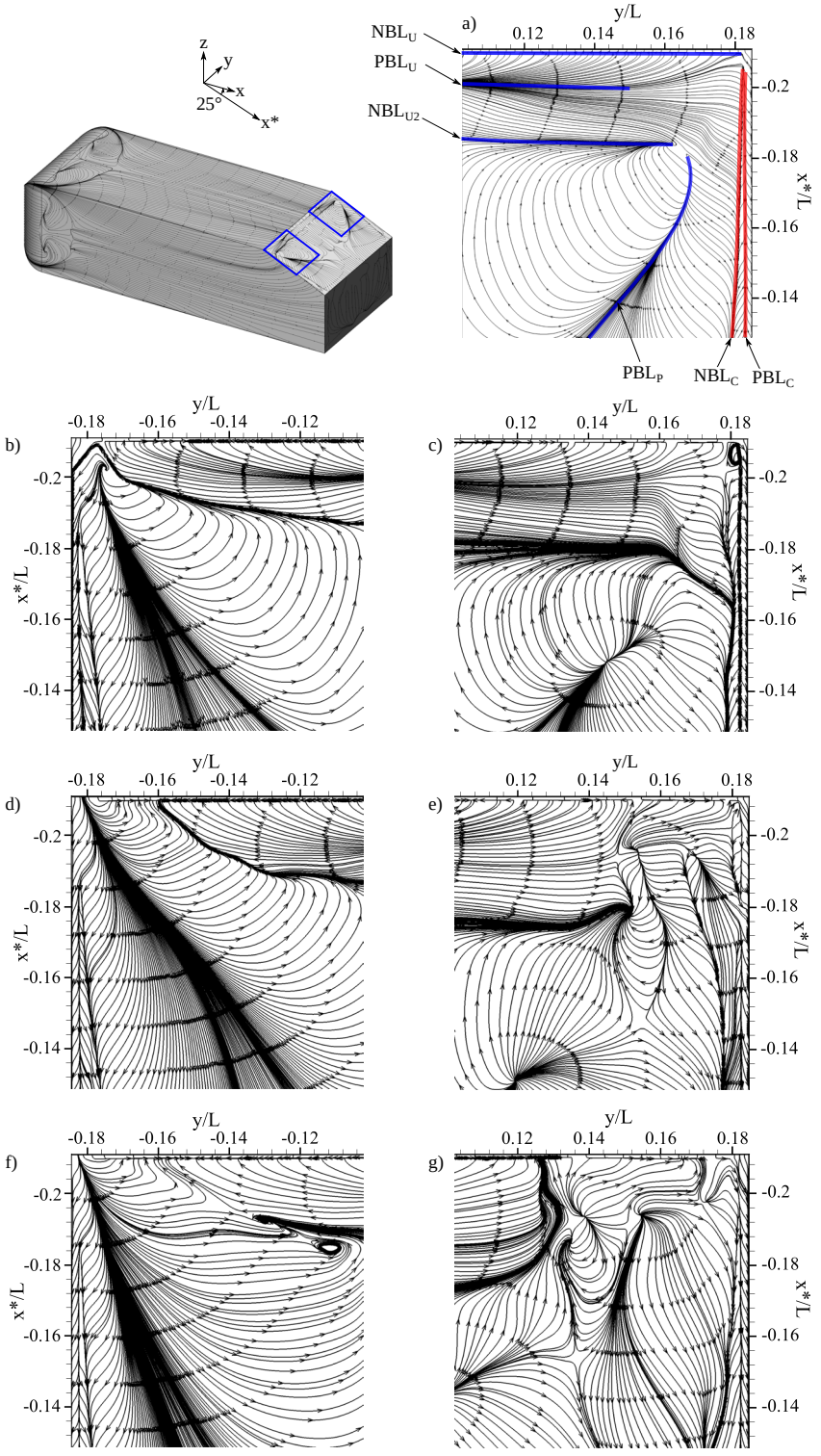

FIGURE 3.26: Surface flow structure and critical points occurring near the initiation of the C-pillar vortex for a) the straight-line case, b) 2.5° yaw leeward side, c) 2.5° yaw windward side, d) 5° yaw leeward side, e) 5° yaw windward side, f) 10° yaw leeward side, and g) 10° yaw windward side

and lower recirculation all emitted flow toward the windward side which was entrained around the C-pillar vortex. This increased the size of the windward longitudinal vortex in the wake and contributed to the significant disparity observed at x/L = 0.5, as shown in Fig. 3.17.

On the leeward side the lower recirculation passed into the centre of the upper recirculation, as can be observed in Fig. 3.27f), and was drawn windward through the centre. A vertical vortex structure was observed on the leeward side at the location of the flow transfer to the upper recirculation, which increased in prominence with yaw angle.

The entrained flow within the backlight separation bubble exited this region toward two separate locations. Aided by the presence of the additional upper windward vortex, the windward side was partially drawn directly into the C-pillar vortex. While on the leeward side flow was entrained into the spanwise-orientated upper wake recirculation, as occurred in the straight-line condition.

3.8 Trailing Face Structure

At the trailing face the upper and lower recirculations were contained within a low pressure region. Figure 3.28 compares the flow structure and static pressure distribution in the wake at y/L = 0.1 and y/L = -0.1 for each case. Corresponding graphs show a profile of normalised z-velocity. For the straight-line case, as shown in Fig. 3.28a) the wake structure was symmetric about either side, hence only one side is shown.

As the yaw angle increased the leeward separation bubble was observed to contract while the windward side extended mildly further downstream. The extension was skewed for the 5° and 10° yaw angles due to the angled path of the windward C-pillar vortex, where structures were drawn toward this feature. At a 5° yaw angle the rear separation only extended 0.6% further than the corresponding straight-line case and at 2.5°, by 2.0%.

On the leeward side the opposite effect was more consistent and measurable. At y/L = -0.1 the separated region length reduced by 15.4% and 33.0% for the 5° and 10° yaw angles. For the 2.5° yaw angle a minor change of only 0.2% was measured. As the region contracted, more of the flow leaving the backlight surface was drawn into the lower recirculation.

The extension of the rear separated region then had an effect on the vertical velocity component which occurred in the wake. On the leeward side an increased downwash angle occurred as the region contracted. When yaw angle increased the wake region became more concentrated below $z/L \approx 0.15$ at x/L = 0.2 and 0.3, which corresponded

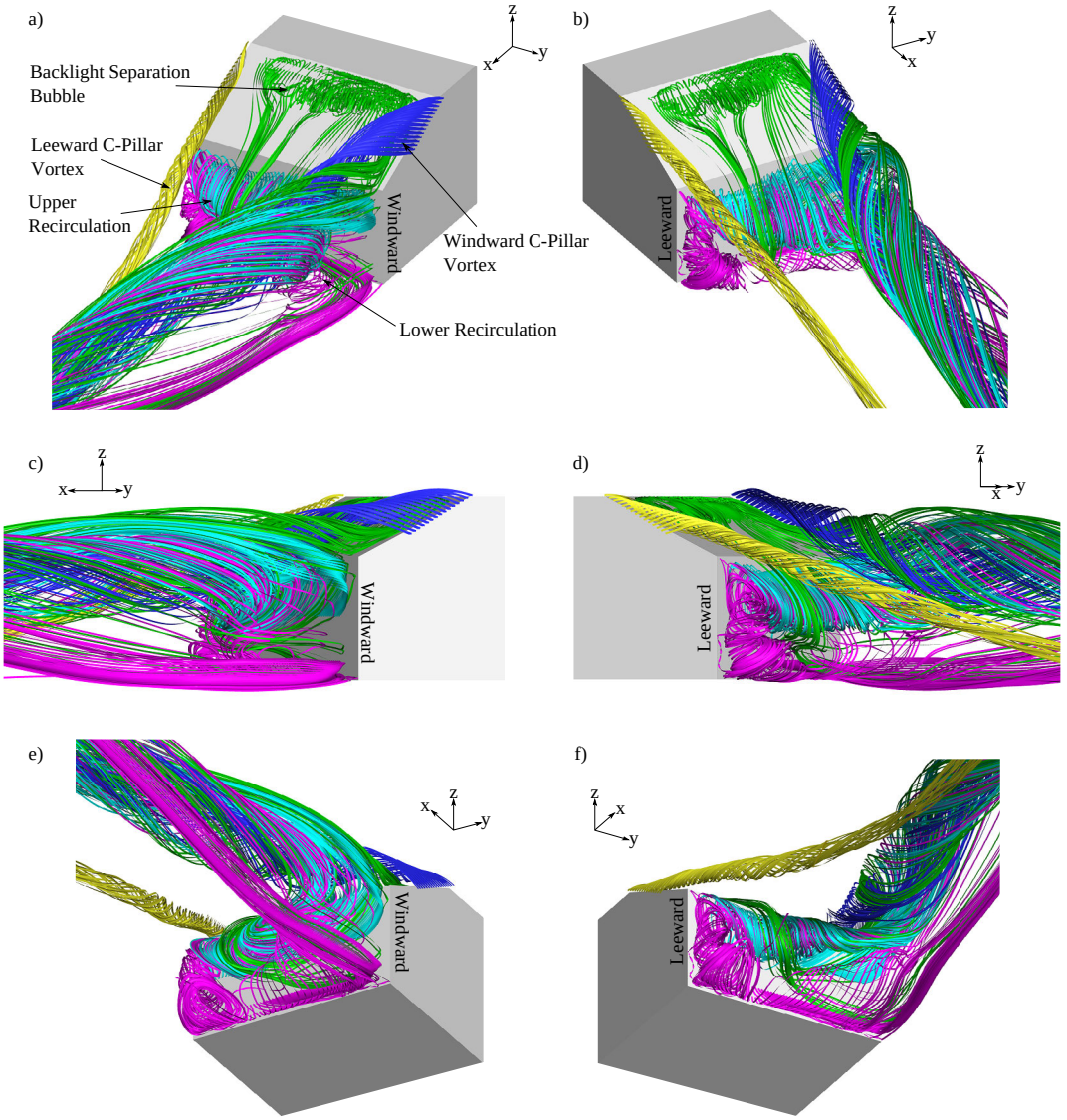

FIGURE 3.27: Streamlines released from within prominent rear flow structures for 10° yaw angle a) outboard upper isometric view b) inboard upper isometric view c) outboard side view d) inboard side view e) outboard lower isometric view f) inboard lower isometric view

to the observations in Fig. 3.17. On the windward side the vertical velocity component increased in comparison to the straight-line case. This effect became more pronounced at the downstream locations of x/L = 0.2 and 0.3 and occurred due to the C-pillar vortex.

A decrease in the dominant frequency was identified for all cases at a yaw angle in comparison to the straight-line condition, as shown in Fig. 3.29. An exception was the 5° yaw angle case where two separate peaks occurred, both at Str = 0.52 and 0.37. In the straight-line condition the transient wake sequence was identified to be the result of the upper and lower recirculation zones increasing in size as core pressure decreased

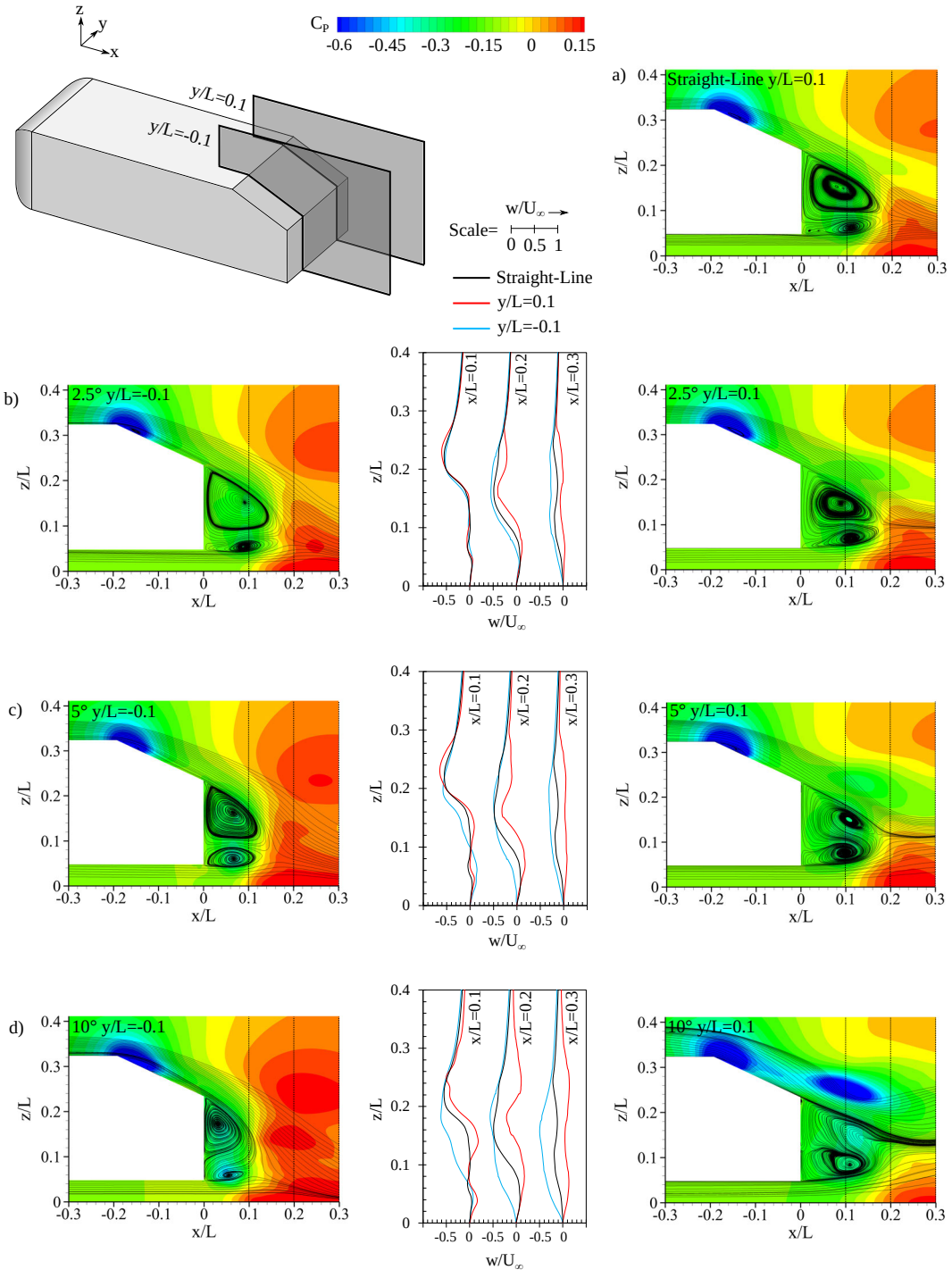

FIGURE 3.28: Wake streamlines and pressure coefficient distribution at y/L=0.1 and y/L=-0.1, with z-velocity profiles for a) the straight-line case, b) 2.5° angle of yaw, c) 5° angle of yaw, and d) 10° angle of yaw

until the structure burst which resulted in a quasi-periodic emission of flow at the rear of the body. The core pressure for the lower recirculation reached a lower value and exhibited a more significant size variation.

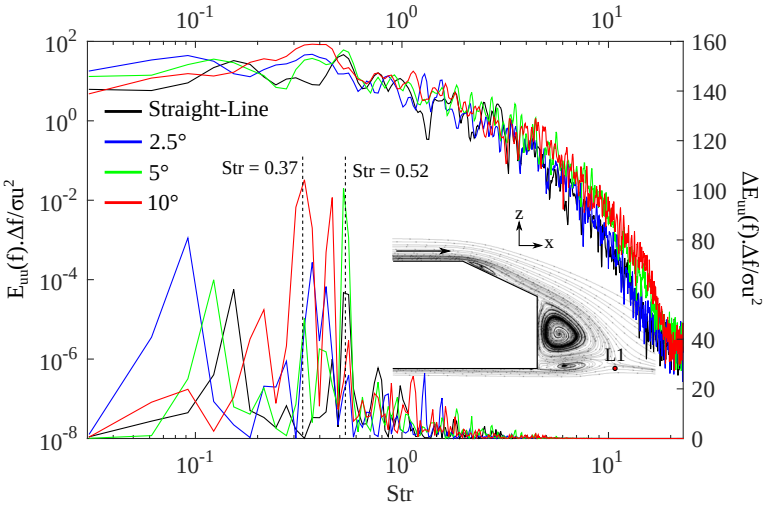

FIGURE 3.29: Raw (upper) and processed (lower) power spectral density plot of velocity magnitude for the three different yaw angles and the straight-line condition at location L1

With the leeward contraction of the separated region more flow from the backlight surface was diverted to the lower structure, as shown in Fig. 3.30. On the leeward side the upper and lower recirculations remained notably more distinguished and retained closer proximity to the face. The shear layer from the lower surface was deflected upwards with the extension of the lower recirculation until it burst and emitted a fluid parcel downstream, as shown in Fig. 3.30a) and b). Alternatively the opposite occurred in the case of the upper recirculation, shown in Fig. 3.30c) and d). The mean downwash angle can be observed as steeper on the leeward side and resulted in the upper recirculation deforming over the lower before emitting a fluid parcel downwards.

On the windward side the lower recirculation primarily drew flow from underneath the body and the bursting exited into the upper part of the wake toward the windward C-pillar vortex. The downwash angle thus remained more gentle. Due to the extension of the wake region the upper and lower recirculations were observed to consist of multiple vortices passing below the larger structure, as opposed to the leeward side where the roll up of the shear layer then immediately merged into the single prominent lower structure.

The same pulsatile wake mechanism as the straight-line condition was observed, however this became less pronounced as the yaw angle increased. Ultimately the separated flow structures evolving on the leeward side were attributed to a stabilising effect which restricted the transient mechanism, as shown in Fig. 3.31.

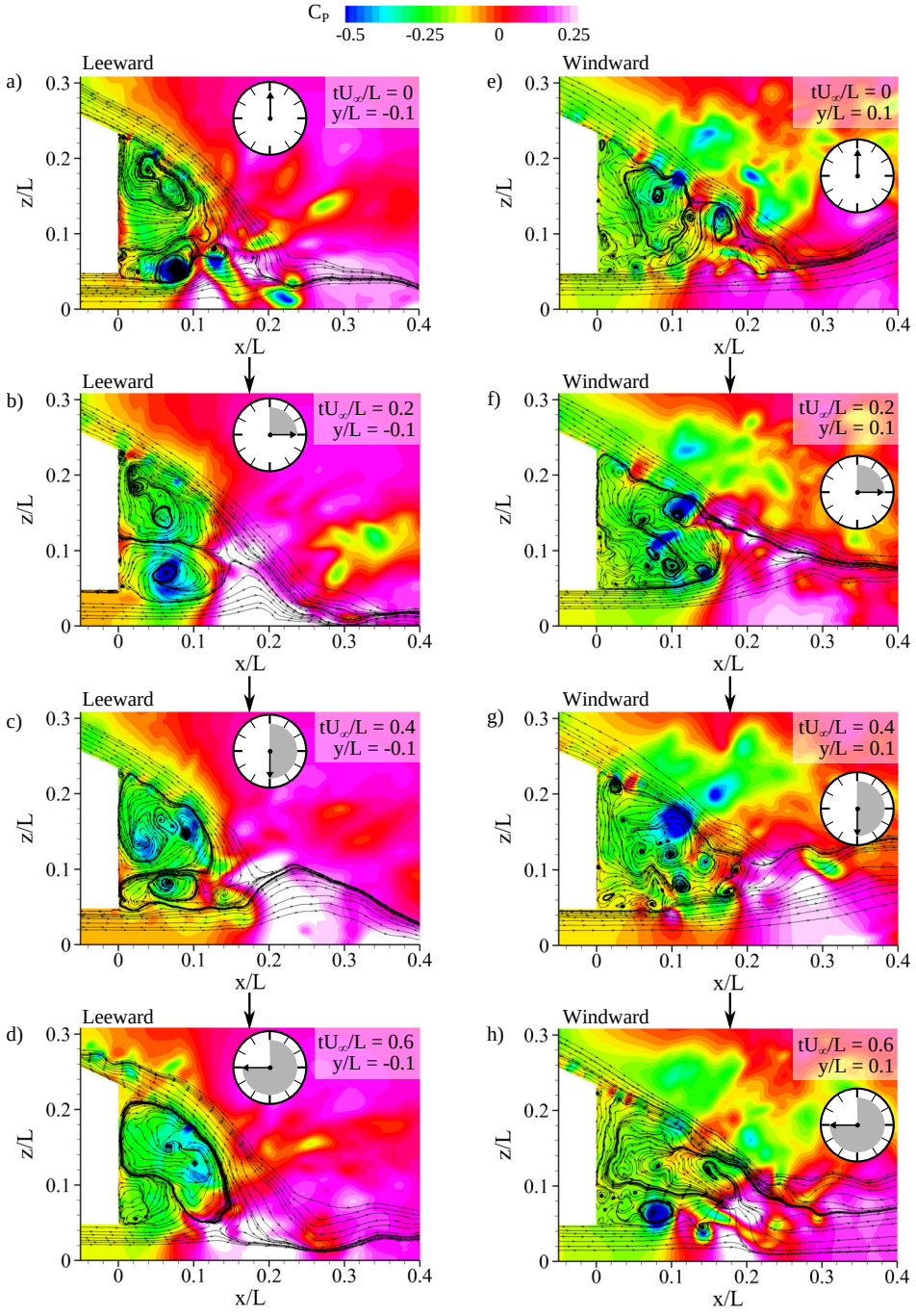

FIGURE 3.30: The transient motion of the wake structures stepping forward in time for a 5° yaw angle at y/L = -0.1 and y/L = 0.1

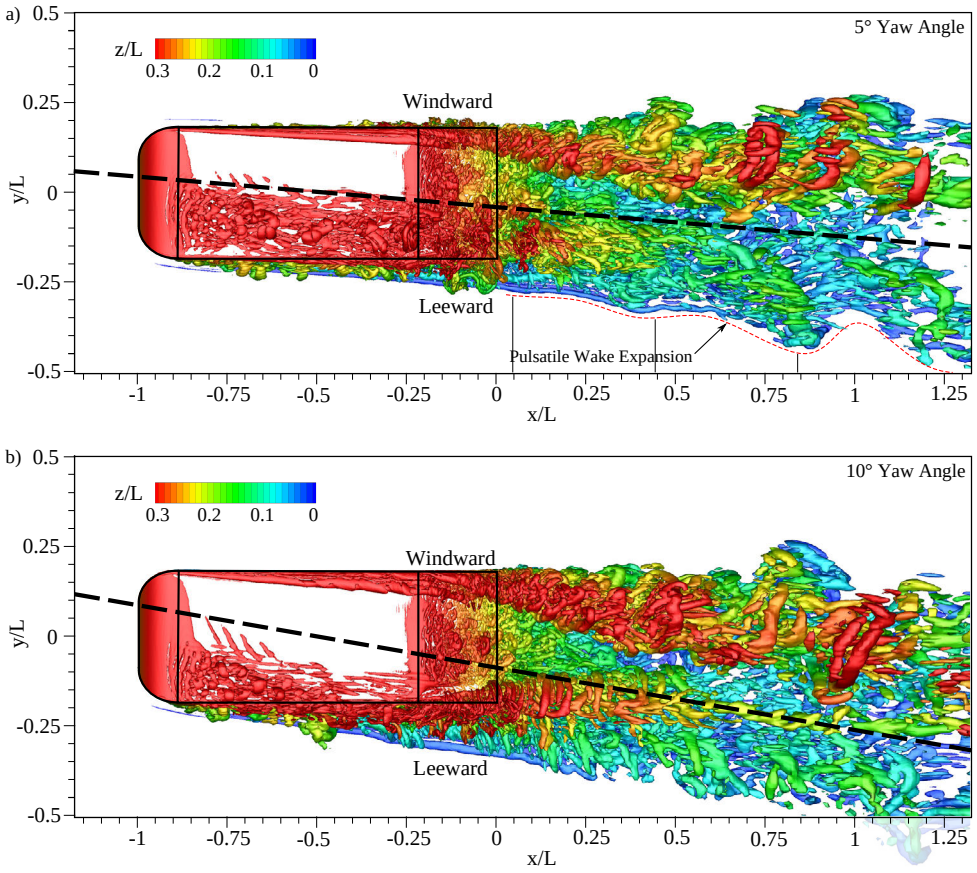

FIGURE 3.31: Top view of isosurfaces of Q = 3×10^4 coloured according to z/L for a) 5° yaw angle, and b) 10° yaw angle

3.9 Summary

The defined geometric features of the Ahmed body resulted in both the flow structures and the aerodynamic forces demonstrating a high sensitivity to yaw angle. At an angle of 10° the drag force increased by 42.8% over the straight-line condition. This was in addition to a 40.2% increase in lift, and a side force and yawing moment which acted in the direction of the flow angle.

The surface pressure gradient across the nose was the most influential effect toward the forces and moments acting on the body. This flow angle resulted in increased leeward suction, with the opposite effect occurring on the windward side. The upper forebody separation bubble shifted leeward and altered the interaction of the emitted vortices with downstream flow structures. The windward forebody separation was suppressed, while the leeward region increased in size in correspondence with a shift in the wake region. In this way the change in flow angle had a cumulative effect toward to the interactions which occurred along the length.

The windward C-pillar circulation and pressure deficit increased due to the angle of the flow across the rear of the body, and prominent longitudinal vortices were observed to form over the upper windward and leeward edges. In conjunction with the C-pillar vortex, the upper windward edge vortex reduced the size of the backlight separation bubble through suppression of the windward spanwise vortex merging. This confined the backlight vortices to a narrower region which resulted in a raised vortex head and an increased frequency of the periodic enlargement and contraction of the region.

While the results highlight largely detrimental aerodynamic effects to result from an increase in yaw angle, specific areas demonstrate potential for creative designs which could mitigate these changes through adapting and accommodating the change in angle. In the present context the results permit understanding of the sensitivities of the geometry to a change in flow angle and thus provide an initial platform for investigating the cornering condition.

Chapter 4

The Effects of Cornering

The investigation into cornering analysed three different constant radius turns. In this chapter the centre of the body remained aligned tangent to the curved path of its motion, such that the angle of the flow at the front and rear remained equal but opposite. As discussed in Chapter 1 the corner radii investigated were selected to be equivalent to corners that a modern vehicle could approach at speeds where the aerodynamic forces would remain considerable. The front and rear flow angles that the corner radii corresponded to is shown in Fig. 4.1 with the values shown in Table 4.1.

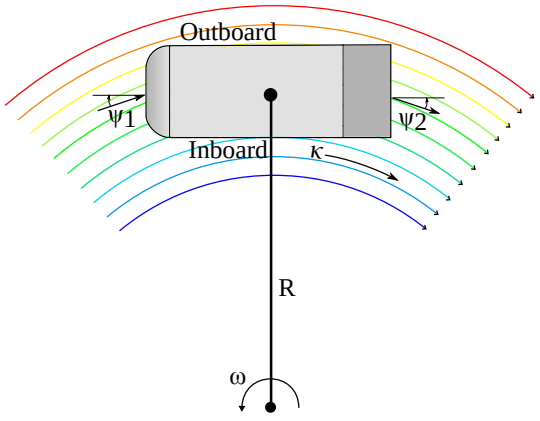

FIGURE 4.1: Diagram of flow angles, radius and curvature for analysis of corners

TABLE 4.1: Front and rear flow angles for within the cornering flow conditions

R	κ (L^{-1})	$\psi 1(^\circ)$	$\psi 2(^\circ)$
Straight-Line (∞)	0	0	0
20L	0.05	-1.43	1.43
10L	0.1	-2.86	2.86
5L	0.2	-5.71	5.71

Before conducting the simulations it was necessary to first address some common aerodynamic testing practices, and consider their applicability to the cornering conditions.

4.1 Aerodynamic scalability of cornering

A high percentage of automotive aerodynamic testing is conducted at reduced Reynolds numbers. Both budgetary and regulatory constraints will influence what is feasible. For experimental analysis most cars are of a bluff shape which typically requires a very large wind tunnel to test at full-scale (without a prohibitively high blockage ratio). Only a limited number of such facilities exist worldwide, and publicly available research is very rarely conducted in them. As a result, most testing, in typical university-scale wind tunnels, will normally be conducted at Reynolds numbers which are an order of magnitude below what occurs in reality, and it is thus important to understand the effects of this compromise when drawing conclusions.

For numerically modelling vehicle shapes the high Reynolds number and blockage effects can also increase the computational expense. Techniques such as Large-Eddy Simulation (LES) and Detached Eddy Simulation (DES) are the most widely utilised methods in recent studies. While these are well suited to the highly turbulent flowfield around a vehicle, the spatial and temporal discretization requirements are dependent on Reynolds number, which again can lead to a lower Reynolds number being favoured.

A practical consideration in the present work is whether the cornering condition can also be scaled. If we conduct testing at a reduced Reynolds number or reduced scale, does this translate to what is occurring in reality?

The significance of the cornering-specific effects occur according to the proportional change in the flowfield relative to the body, as is discussed and analysed in detail throughout the present work. So as with all other aerodynamic testing, by scaling relative to the body, similarity between flowfields can be achieved. A practical example illustrates this as is shown in Fig. 4.2, where the Reynolds number is calculated based on length with $\rho = 1.2kg/m^3$, and $\mu = 1.8 \times 10^{-5}kg/ms$. Figure 4.2a) is the original case and b) and c) are at 50% scale.

However, as we reduce the scale and maintain the same Reynolds number the centripetal (and hence centrifugal within the rotating reference frame) acceleration increases according to:

$$a_c = \frac{U^2}{R} \tag{4.1}$$

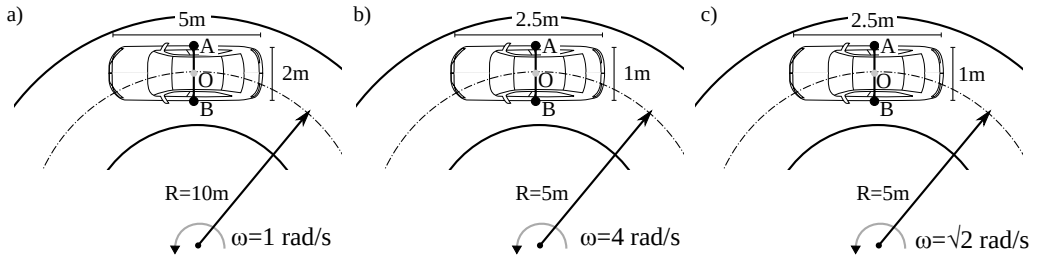

FIGURE 4.2: Equivalent cornering cases occurring at different scales and velocities

TABLE 4.2: Comparison of physical property variation within equivalent cornering cases

	a)	b)	c)
Re_O	3.33×10^6	3.33×10^6	1.18×10^6
$a_{cO}(m/s^2)$	10	80	10
Δa_{cAB}	20%	20%	20%
Δq_{AB}	20%	20%	20%

The combined effects of an increase in the velocity term and decrease in radius results in a 50% scale test at the same Reynolds number experiencing a centripetal acceleration magnitude which is 8 times greater, as is shown in Table 4.2. While this increase in acceleration introduces a practical issue for experimental testing, as will be discussed in Chapter 6, the proportional change in terms of aerodynamic properties remains identical. The same situation arises if we reduce the Reynolds number, and make the acceleration magnitude equivalent. The percentage change in the relative dynamic pressure across the body remains the same in all conditions, as well as the change in angle and curvature, and thus the cornering specific effects. As such, the cornering condition can also be scaled with Reynolds number.

4.2 Aerodynamic forces in the cornering condition

The drag coefficient value is typically the most important force parameter when designing the external shape of a passenger or commercial vehicle. However, as the freestream flow assumes a curvature relative to the body this value can no longer be calculated in the same manner. In the present study a method was sought where the coefficient could be calculated in a manner that is comparable to the straight-line calculation.

As the vehicle assumes a curved path, the assumption of drag acting in a direction aligned with the longitudinal axis of the vehicle becomes incorrect. Rather, the drag force is proportional to the moment acting on the body in the same circular path, resisting the

curved motion of the vehicle. Lift continues to act in the vertical direction, as its axis is parallel to the axis of rotation of the body, with all other force and moment conventions detailed in Fig. 4.3.

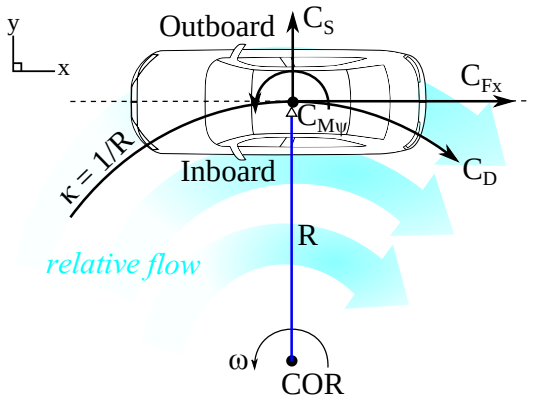

FIGURE 4.3: Direction of forces and moments in the cornering condition

Complete details of the method utilised for the calculation of drag, as suitable for the incompressible CFD simulations, can be found in Appendix A.

4.3 Coordinate System

When analysing the cornering condition, a further consideration is the most effective method for visualising results. Certain aspects of cornering simulations lend more favourably to analysis within a cylindrical coordinate system, while others are more suited to Cartesian.

The geometry of a vehicle remains defined and suited to the Cartesian system, this is to say that it remains an approximately rectangular shape, and symmetrical (in this instance). However, the path of its motion is curved, and the resistance to that motion (drag) also acts back in a curved path.

If all other aspects were also analysed in the cylindrical coordinate system some difficulties arise. Firstly, the present work specifically sought a geometry that had been the subject of thorough previous investigation. This was to allow comparison to a wide range of existing research. In building on these prior findings it became favourable to use the Cartesian system to allow direct comparison.

Secondly, the cylindrical coordinate system only becomes more suitable when considering further downstream locations. Imagining a plane of interrogation at a fixed angle through the near wake region as is shown in Fig. 4.4, it can be noted that it is at a

different proximity to the geometry from the inside to outside. In close proximity for a tight radius corner it could then lead to partial intersection. A profile would have to be interrogated at a constant radius (rather than constant x, y, or z) so would pass over different geometric features dependent on the corner radius. For these reasons the system becomes less practical for analysis near the surface, despite the preferential suitability to the freestream flow.

Due to these considerations, the Cartesian coordinate system was adopted consistently throughout all analyses of the Ahmed body across the different flow conditions.

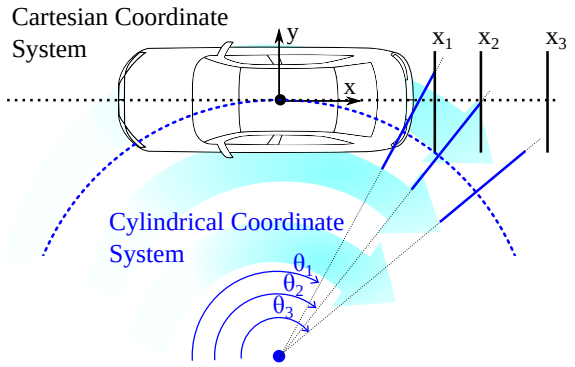

FIGURE 4.4: Comparison of Cylindrical and Cartesian coordinate systems and their applicability to cornering analysis

4.4 Side Surface Pressure Distribution

Within the rotating reference frame of a corner the vehicle itself is under acceleration, while the freestream flow does not experience any. When considering this motion with respect to the absolute reference frame, the centrifugal acceleration acting on the flow becomes proportional to the absolute velocity and radius. Therefore at the surface the flow is subject to acceleration which is proportional to the vehicle's. Assuming incompressible flow the change in pressure across two radial locations can be calculated according to the variation in radial location between the two considered locations:

$$\Delta p = \int_{R1}^{R2} \rho \omega^2 R \, dR \tag{4.2}$$

The pressure gradient between two locations thus becomes dependent on the difference between the square of the radius. For the Ahmed body geometry the radial distance between the inboard and outboard sides at x/L = 0.5 is equal to 0.372L. From this value the pressure coefficient difference due to acceleration, can be calculated for the corner radii, as shown in Table 4.3:

TABLE 4.3: Pressure difference across the sides of the body due to the acceleration within the cornering condition

R	κ (L^{-1})	ω (rad/s)	ΔC_P
Straight-Line (∞)	0	0	0
20L	0.05	1.20	0.036
10L	0.1	2.39	0.073
5L	0.2	4.79	0.145

Within the relative reference frame a radially orientated total pressure gradient occurs due to the increase in relative dynamic pressure. Inherently this static pressure gradient is then equal to the relative variation in dynamic pressure. In Fig. 4.5 the consistent offset in surface pressure which occurred between x/L = -0.7 and x/L = -0.1 can be observed to correspond closely to the calculated value. Thus due to the centrifugal acceleration within the rotating reference frame a radially orientated external force occurred which acted toward the centre of the corner. As a consequence of this effect the outboard side surface pressure distribution was consistently higher than that which occurred on the inboard side.

In addition to the effects attributed to acceleration, further localised differences were the product of a change in perception of the geometric shape by the freestream flow. When straight flow meets a curved surface a change in the velocity and pressure will occur dependent on its orientation. The cornering condition represents the opposite scenario where the flow is curved, rather than the surface. Changing to the frame of reference of the flow, the body will thus assume a perceived curved shape.

In this way it was observed that the flat outboard and inboard sides of the Ahmed body no longer exhibited their typical straight-line characteristics, but rather differences which reflected the differing flow angle along the length. This was most readily observed in the pressure distribution over the forebody where the effects occurred in relative isolation from further interaction.

For the cornering cases the change in flow angle resulted in an inboard shift of the stagnation point which occurred on the nose, and this caused the flow to turn through a greater angle over the outboard side of this feature. The suction peak was visible at x/L $\approx$ -0.87, and as the angle increased this became more significant. Conversely, on the inboard side the angle progressively reduced as the radius decreased and weakened the suction peak. Thus the cornering condition resulted in a progressive and consistent increase in the gradient across the forebody as corner radius decreased, acting in the opposite direction to the radial force.

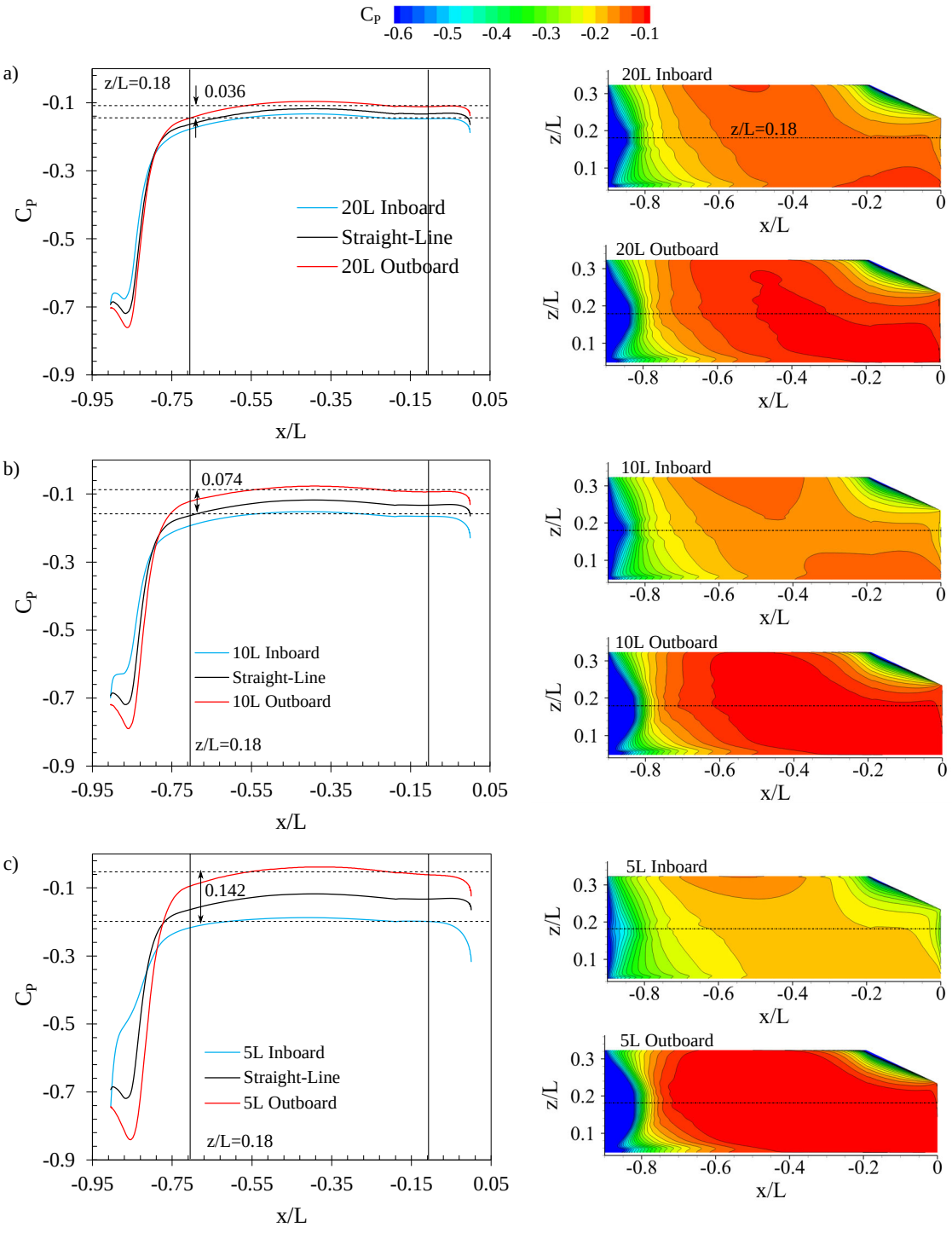

FIGURE 4.5: Pressure coefficient distribution over the sides of the body for a a) 20L radius corner b) 10L radius corner c) 5L radius corner

4.5 Forebody Flow Structure

The separated flow structures over the forebody were further affected due to this inherent change in the oncoming flow angle at the front. On the upper surface the oncoming flow angle skewed the forebody separation bubble which formed at the start of the face, where the outboard shift was observed to progressively increase as corner radius decreased.

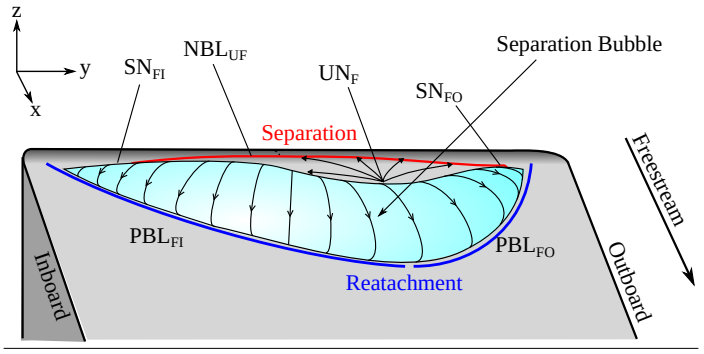

FIGURE 4.6: Forebody separation bubble with the corresponding location of critical surface points

On the upper surface the separation length reduced toward the inboard side and extended on the outboard side of the upper surface. The corresponding locations of the surface lines with respect to flow features is shown in Fig. 4.7.

Investigating the structure in further detail $\mathrm{NBL_{UF}}$ was shown to be split into two separate regions. As the unstable flow region was shifted outboard, the inboard part of the line extended across the width of the upper surface. The central region containing UN_F shifted outboard and for all cornering cases and the stable focus increased in size.

For the 5L radius corner the negative bifurcation followed a continuous arc and increased proximity to the outboard edge as the majority of the flow entrained within the vortex was drawn from the inboard side, as is shown in Fig. 4.8. The flow entered the separation bubble and spiralled toward the unstable node before being emitted downstream. The curved freestream path resulted in this emitted flow not being deflected further outboard, but rather remaining contained above the upper surface and propagating downstream.

Observing the instantaneous flow structure shown in Fig. 4.9 it can be observed that a vortex merging and spanwise splitting occurred in this region, which was consistent with the straight-line condition. The vortices formed alternatively at either side of the unstable node. After merging the centre of the span raised off the surface and were then stretched in the longitudinal axis as they continued downsteam toward the backlight. As the downstream path of these structures was deflected back inboard due to the curved

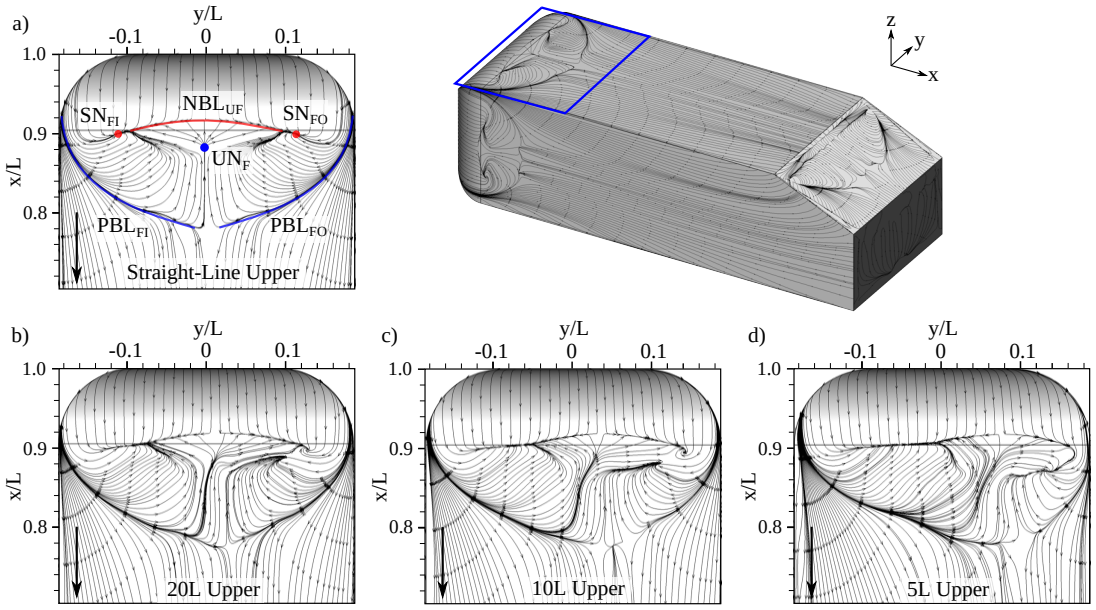

FIGURE 4.7: Surface streaklines indicating separated flow structure on the upper surface for a) the straight-line condition, b) 20L radius corner, c) 10L radius corner, and d) 5L radius corner

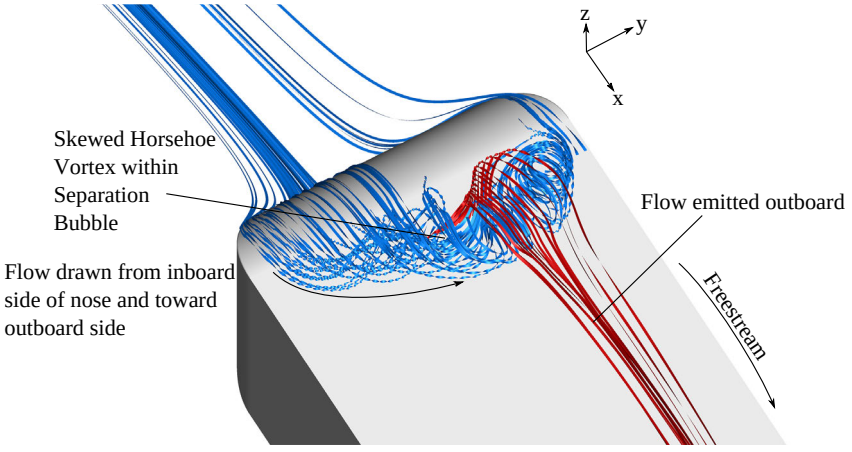

FIGURE 4.8: Streamlines indicating separation bubble flow structure over the forebody upper surface in the 5L radius cornering condition

flow, this led to an interaction with the separated region over the backlight even for the smallest radius case. The resultant energy transfer due to these structures is discussed in more detail in Section 4.8.

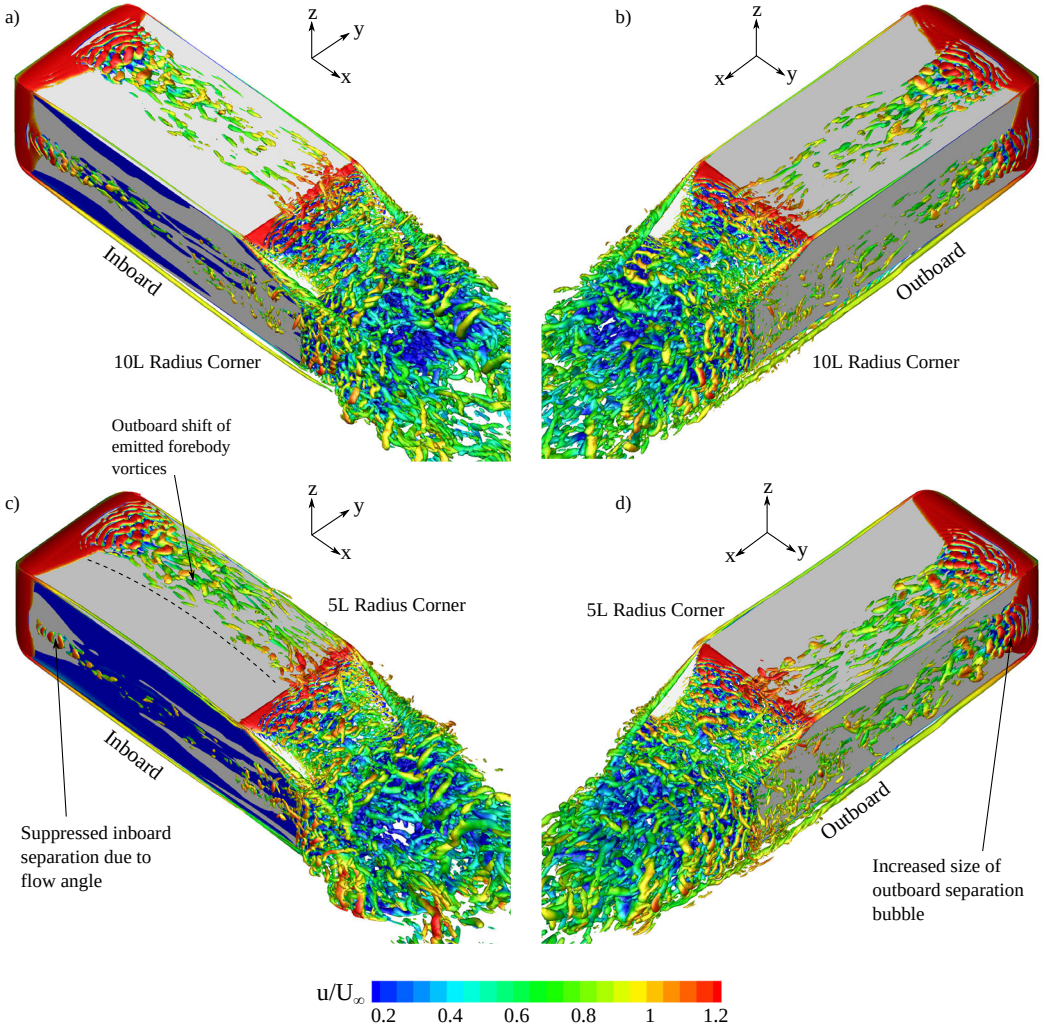

FIGURE 4.9: Q-criterion of 2×10^5 with x-velocity contours for the 10L radius corner observed from the a) inboard side, and b) outboard side, and for a 5L radius corner from the c) inboard side, and d) outboard side

The inboard and outboard faces experienced a respective decrease and increase in the length of the separation bubble as flow curvature increased. These changes were attributed to effects occurring at the surface which were the result of flow angle, as shown in Fig. 4.5. The outboard angle resulted in an increased adverse pressure gradient over the curved nose radius, while the inboard gradient reduced.

The most notable outboard effect was the development and increase in size of the flow region which contained the unstable node aft of NBL_O. This corresponded to the increased emission of flow from within the separation bubble, as shown in Fig. 4.9. The

defined unstable node was minimally visible in the straight-line condition, however it became pronounced for both the 10L and 5L radius corner cases, and corresponded to the emission of larger vortices.

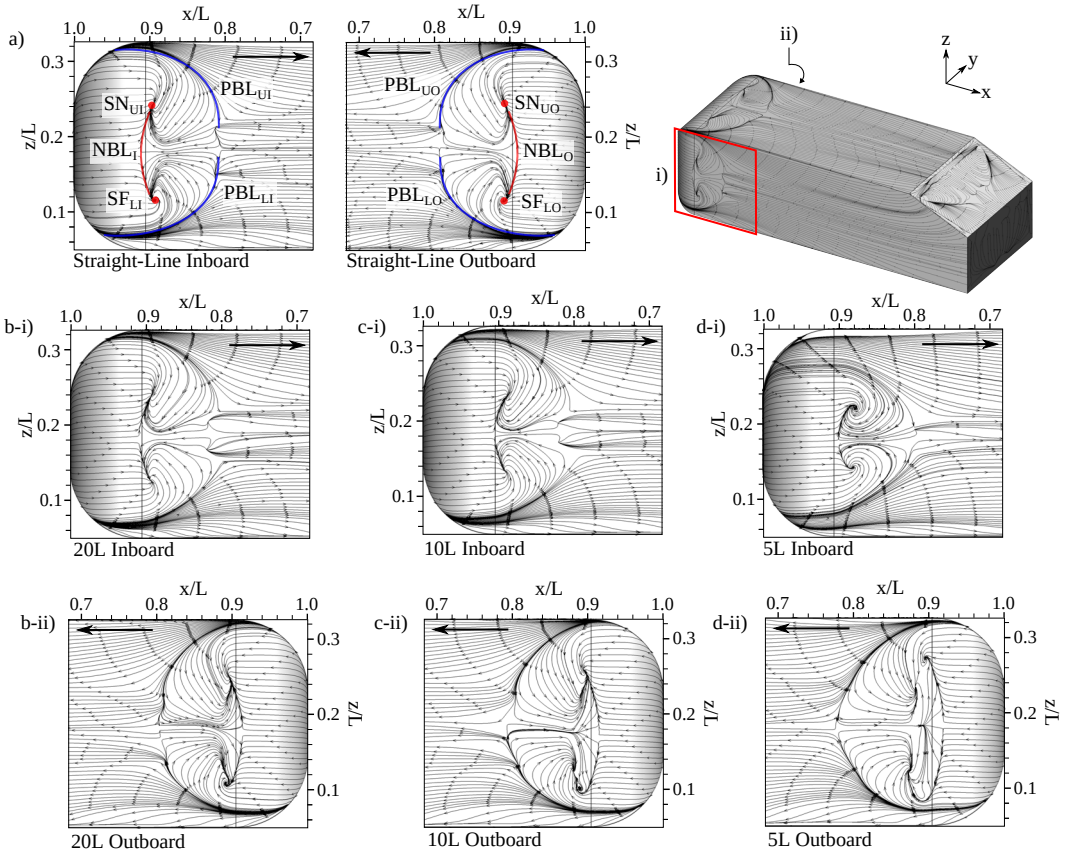

FIGURE 4.10: a) 20L radius corner b) 10L radius corner c) 5L radius corner

On the inboard side the location of the separation line NBL_I occurred further aft as the corner radius decreased. The location of the reattachment lines PBL_{UI} and PBL_{LI} remained similar, while the centrally contained region reduced to the near cessation of its existence. SN_{UI} and SF_{LI} increased in size to form two large stable focii due to the rotational component becoming orientated normal to the face. This same structure is similar to what has been observed in prior studies for geometries with a smooth curvature transition [120].

4.6 Mid Body

The increased emission of vortical structures from the separation region caused a thicker outboard time-averaged boundary layer to develop within a corner, as is shown in Fig. 4.11. For consistency the measurement shown does not accommodate for the change

in tangential freestream velocity across the width of the body and hence gives a conservative estimate. The inboard profile can be observed to return to a comparatively reduced freestream flow velocity, while the outboard was in a higher region.

For the 5L cornering case the outboard boundary layer, when measured at the centre of the face (z/L = 0.18, x/L = -0.5), was 205.6% thicker than the respective inboard location. For the 20L and 10L radius corners respectively smaller differences of 48.1% and 100% were observed. As a compounding effect the outboard increase in boundary layer thickness then resulted in a thicker shear layer separating at the trailing face, and C-pillar location.

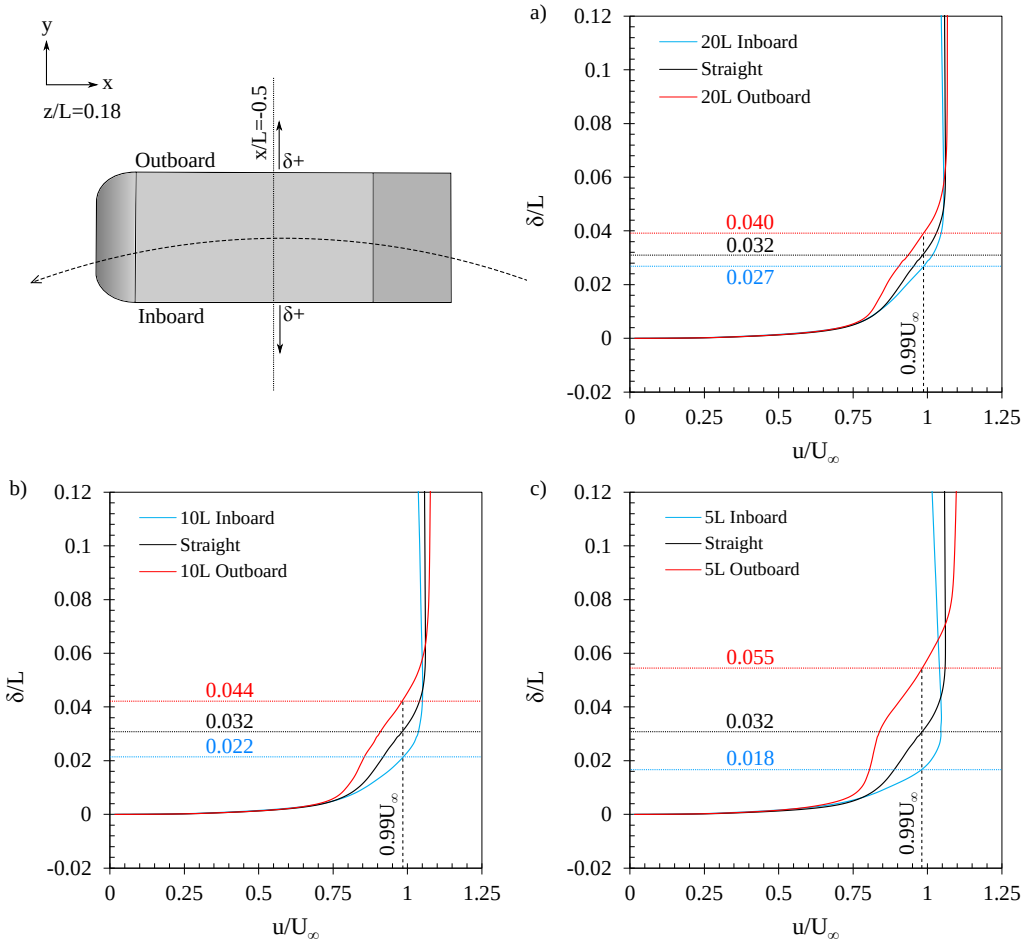

FIGURE 4.11: Time-averaged boundary-layer profile at z/L=0.18, x/L=-0.5 for cornering cases compared to the straight-line condition for a a) 20L radius corner, b) 10L radius corner, and c) 5L radius corner

To understand the mechanisms contributing toward the production of lift pressure coefficient profiles were taken along the upper face and backlight surfaces at y/L = -0.15 and y/L = 0.15. The suction peak occurring at the junction of the upper surface and the start of the backlight surface increased in magnitude at the outboard location when

within a corner. For the 20L, 10L and 5L radius corner cases the magnitude of this suction peak increased by 2.7%, 11.5%, and 35.4% respectively. In these instances it was also observed that the pressure recovery initiated earlier. The initial curvature in the profile for 5L, y/L = 0.15 was due to the forebody separation bubble being shifted outboard and becoming evident at that location. While the inflection occurring in the profile near the trailing face was the result of the passage of the C-pillar vortex across the face.

The inboard reduction in the suction peak was of a lower magnitude than the increase observed outboard. This reduction was also greater for the 20L and 10L radius corner cases, than the 5L radius, where 6.2%, 4.5%, and 1.8% reductions occurred respectively. Hence the decreased radius resulted in the return of the peak value to near the straight-line value rather than becoming further differentiated.

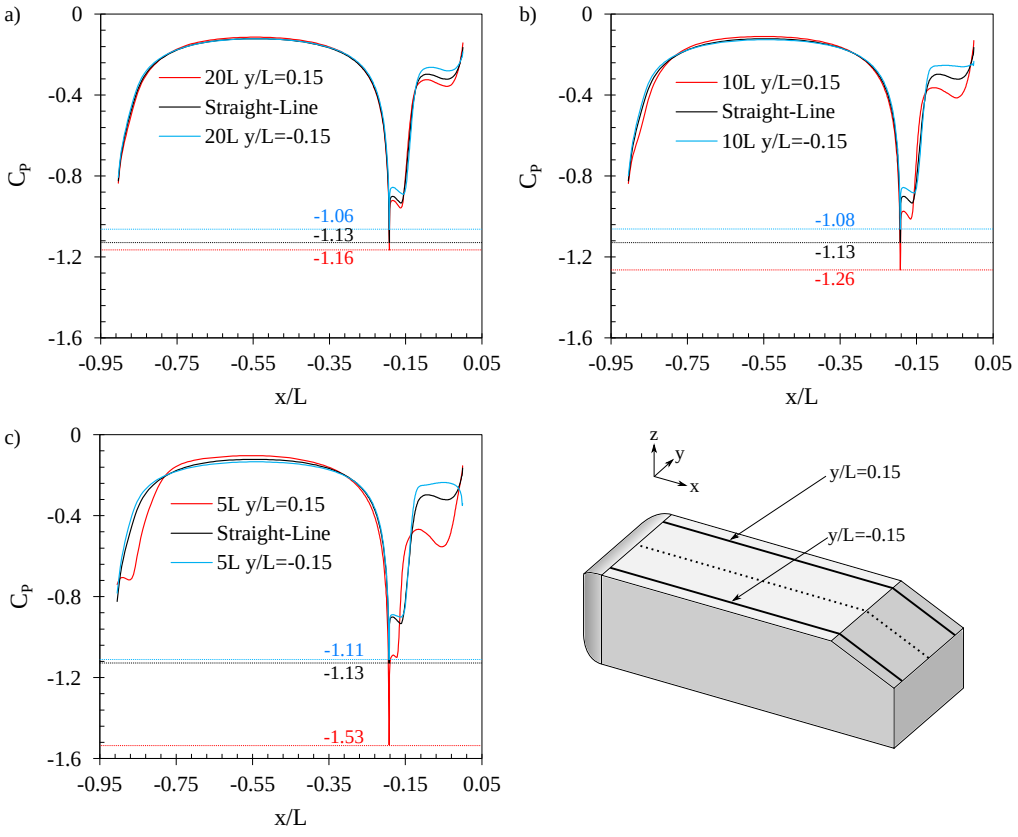

FIGURE 4.12: Pressure coefficient profile along upper side at y/L=0.15 and y/L=-0.15 for a a) 20L radius corner b) 10L radius corner c) 5L radius corner

4.7 Longitudinal Vortex Structure

Within the cornering condition the variation in the surface pressure distribution affected the formation of longitudinal vortices at the defined edges. The structure is summarised in diagrammatic form in Fig. 4.13.

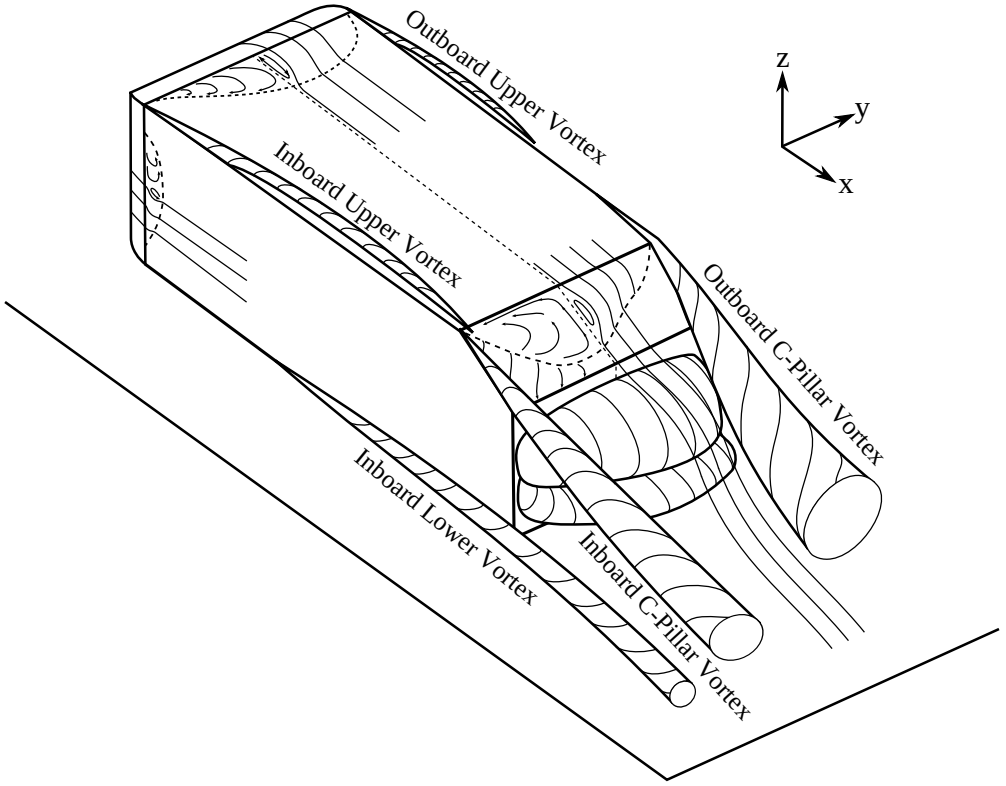

FIGURE 4.13: The longitudinal flow structures within the cornering condition

As the corner radius decreased the near wake structure became more asymmetric. Cumulative effects towards the downstream development of the C-pillar vortex increased the magnitude of this difference which is shown in Fig. 4.14.

The formation of a larger outboard vortex occurred at the trailing face for the cornering cases, as is shown in Fig. 4.15 due to the angle resulting in an increased pressure gradient. In addition to the primary structure, the lower longitudinal vortices also differed. The increased surface pressure over the outboard side caused the direction of the pressure gradient across the lower edge to reverse – resulting in the rearward formation of an additional vortex. This second counter-rotating vortex formed underneath the body, as shown in Fig. 4.15, causing rearward suction. The structure interacted with the shear layer from underneath the body – displacing the thickest region further to the inboard side.

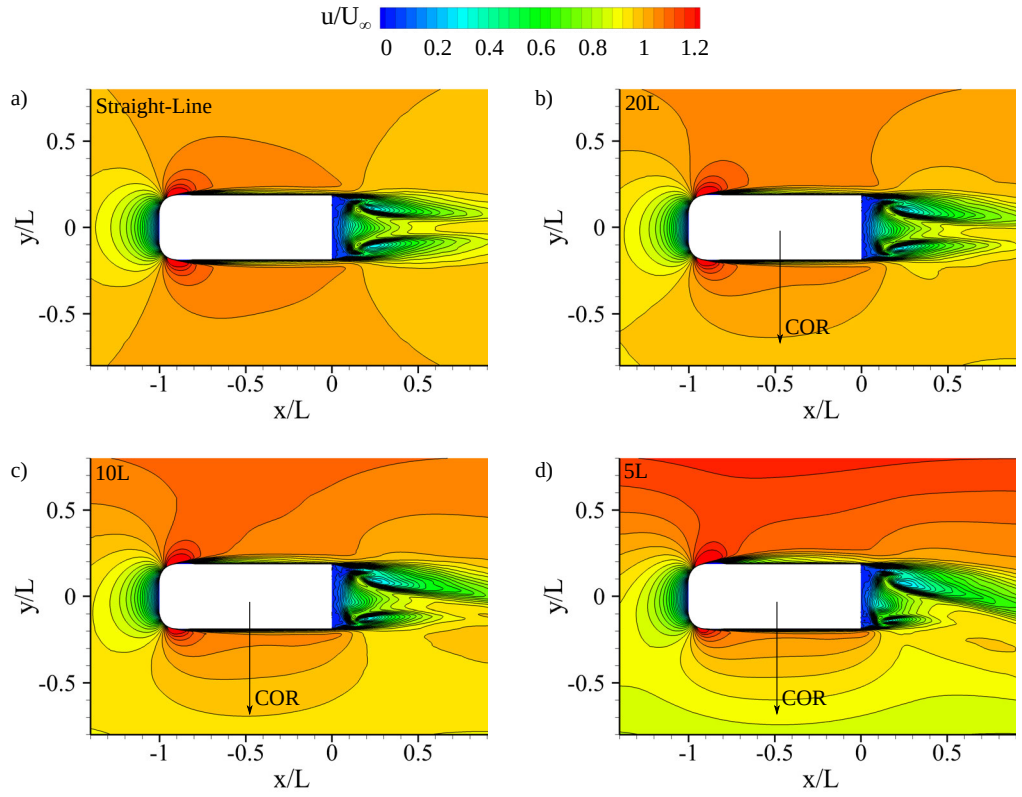

FIGURE 4.14: X-velocity contours at z/L=0.18 for a) the straight-line case, b) 20L radius corner, c) 10L radius corner, and d) 5L radius corner

On the inboard side the lower vortex increased its elevation above the ground, shown in Fig. 4.15c) and d), and was drawn toward the low pressure which occurred rearward on the inboard side. As a unique occurrence in the 5L radius corner, two co-rotating vortices were observed at x/L = 0 due to the separation of the initially formed longitudinal structure prior to the trailing face.

Downstream the wake asymmetry became more apparent, as is shown in Fig. 4.16. The inboard vortex reduced in size and the core velocity deficit was less significant. While the inboard C-pillar vortex was directed further downward as the corner radius decreased, thus being positioned close to the ground a much shorter distance downstream. This effect can be observed in Fig. 4.16d). In the 5L and (to a lesser extent) 10L radius corner cases the imbalance caused a collapse of the inboard wake structure, whereby the longitudinal rotation was reduced. The outboard C-pillar vortex alternatively had an increased vertical displacement as corner radius decreased, and further exacerbated the disparity across the wake.

Mean circulation strength and the integrated mean pressure deficit were measured on surfaces aligned along the C-pillar vortex tube as it passed over the backlight surface.

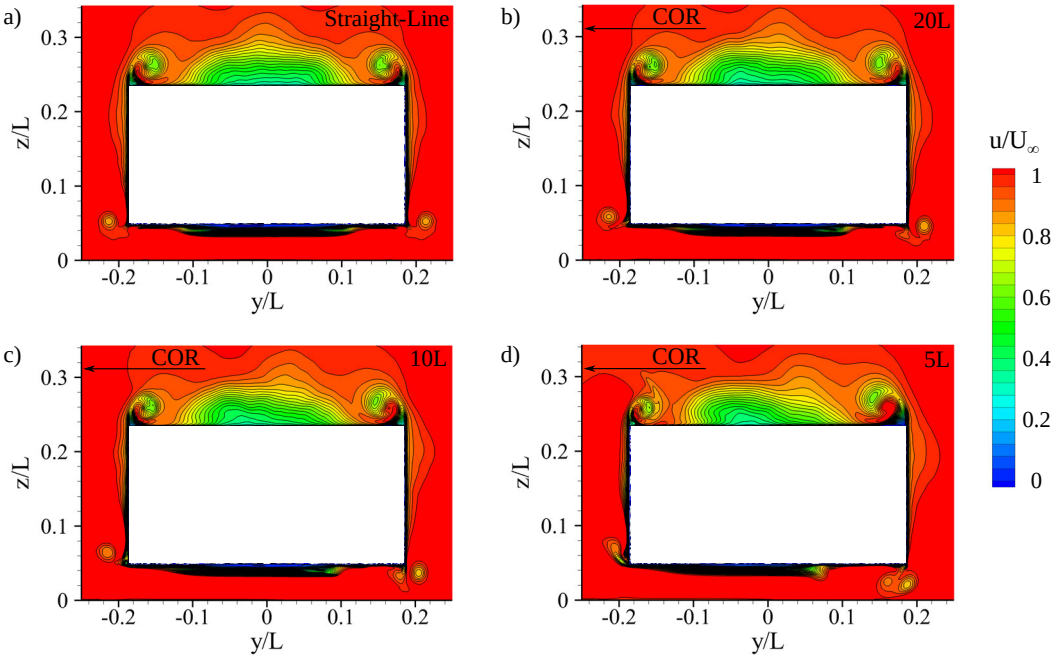

FIGURE 4.15: X-velocity contours at x/L=0 for a) the straight-line case, b) 20L radius corner, c) 10L radius corner, and d) 5L radius corner

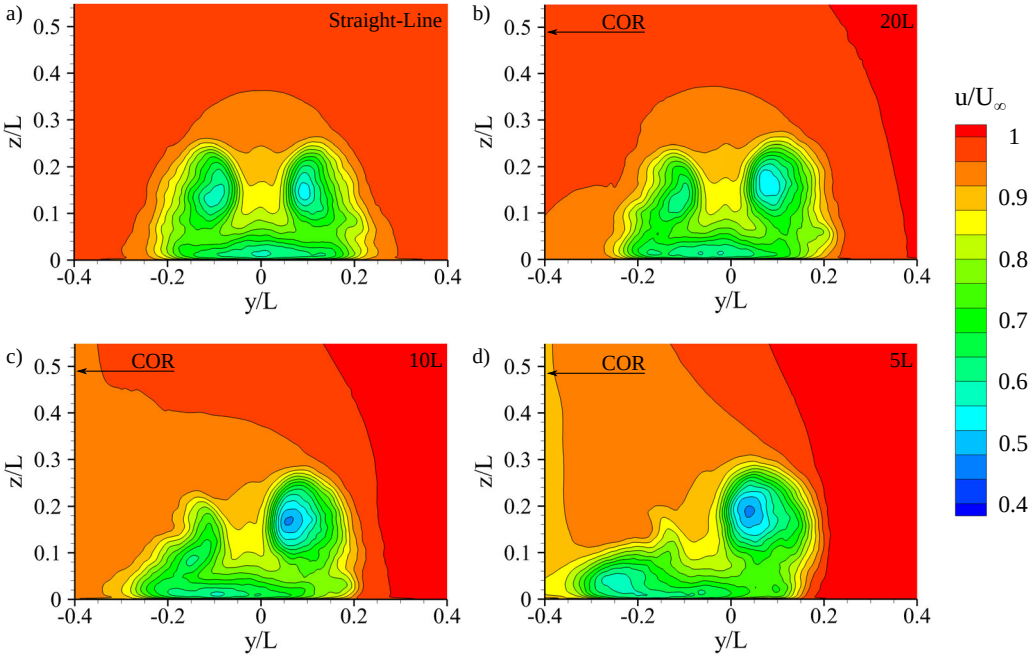

FIGURE 4.16: X-velocity contours at x/L=0.5 for a) the straight-line case, b) 20L radius corner, c) 10L radius corner, and d) 5L radius corner

Non-dimensional circulation strength is shown in Fig. 4.17 for the outboard and inboard locations.

An outboard increase in circulation occurred as the corner radius decreased. This difference in strength was greatest at x/L = -0.1, and reduced towards the trailing face. The rate of decay increased proportional to circulation strength and thus resulted in the smallest measured difference occurring at the furthest downstream location. The inboard trend opposed that of the outboard location, where a reduction in circulation strength occurred. This reduction occurred due to the decrease in pressure along the inboard side specifically attributed to a rearward expansion from the perceived curvature. This consistently reduced the pressure gradient across this location as corner radius decreased. At x/L = -0.1 for the 5L cornering case the circulation strength at the outboard location was 117.7% greater than inboard.

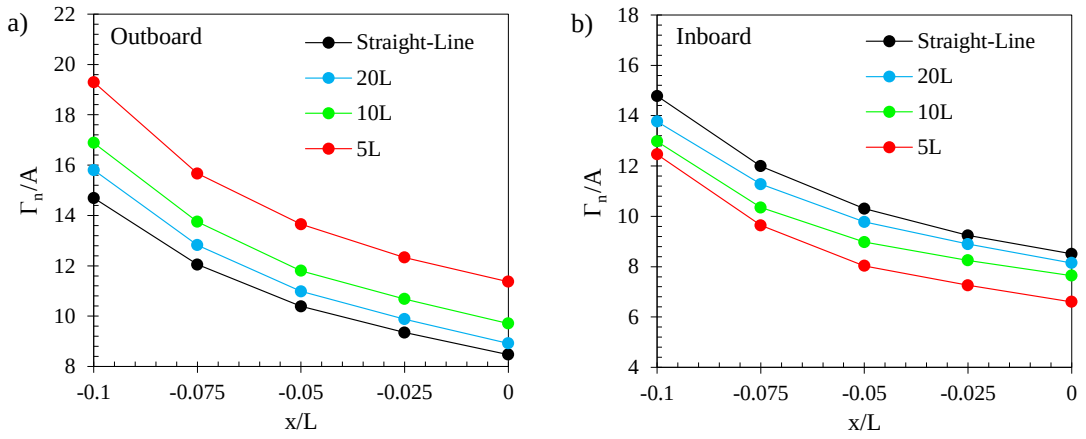

FIGURE 4.17: Circulation strength at C-Pillar locations for a) the outboard location, and b) the inboard location

The integrated pressure deficit at the C-pillar location was also greater at the outboard location as the corner radius decreased. The magnitude of the difference was more significant for the outboard location, while the inboard location approached the local static pressure as the reduced circulation strength alleviated the core deficit.

A frequency analysis of the velocity signal measured at the location of C-pillar vortex formation revealed a variation in the pulsatile characteristics. In the straight-line condition shown in Fig. 4.19a) Str = 17.5 occurs both inboard and outboard as the dominant frequency. As the corner radius decreased the inboard frequency reduced while the outboard increased. Prior inspection of the vortex structure identified the high frequency activity of the C-pillar vortex to be due to spanwise vortex shedding from the upper edge of the backlight. The outboard local acceleration shown in Fig. 4.12, was observed to

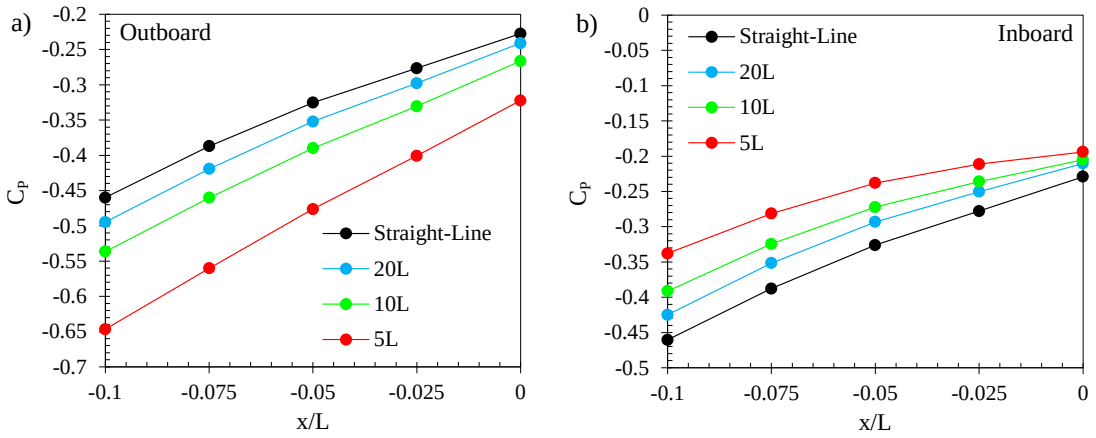

FIGURE 4.18: Pressure coefficient deficit at C-Pillar locations for a) the outboard location, and b) the inboard location

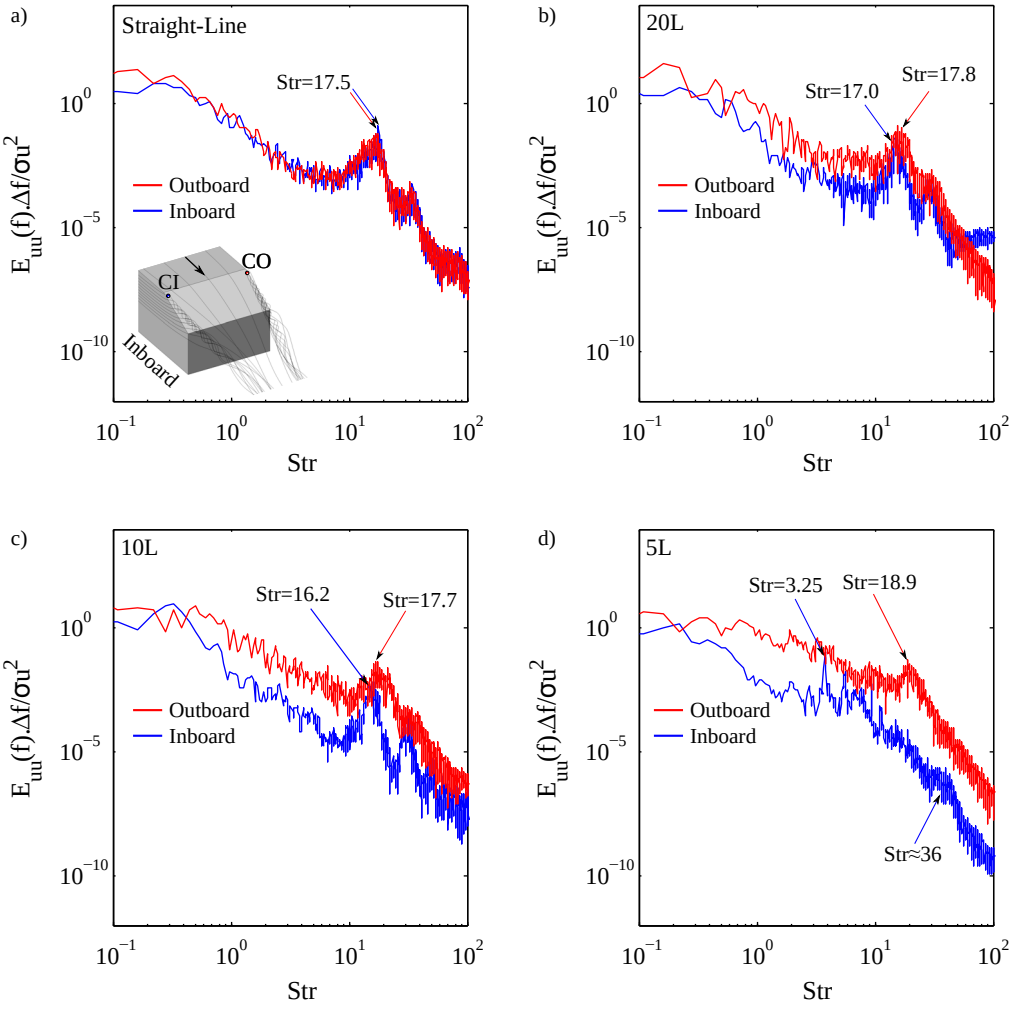

FIGURE 4.19: Power spectral density plot of velocity magnitude at the CI and CO location for a) the straight-line condition, b) a 20L radius corner, c) a 10L radius corner, and d) a 5L radius corner

affect a change in the dominant frequency, due to a correspondingly increased spanwise shedding.

For the 5L radius corner case shown in Fig. 4.19 the inboard spectrum differed from the straight-line condition, and that of the other cases. Due to the induced shear over the backlight separation bubble, a longitudinal vortical component was introduced to the inboard side of the separation bubble which resulted in the isolation of the C-pillar vortex from the spanwise shedding occurring over the upper edge, as shown in Fig. 4.20. Due to this a dominant peak of a far reduced frequency occurred at Str = 3.25 with a meandering type motion observed to result.

4.8 Backlight Structure

The instantaneous backlight flow structure is shown in Fig. 4.20 for the inboard side, with the outboard shown in Fig. 4.21.

Fundamentally the primary mechanism remained common with the straight-line condition, whereby the spanwise vortices which formed at the upper edge initially merged into larger structures. The decreased separation length on the outboard side resulted in the merging and raising mechanism occurring more rapidly. The reduced temporal period of this interaction produced smaller structures which detached from the surface more imminently, and proceeded to break down, as shown in Fig. 4.21.

Inboard structures were larger and the development of the hairpin vortices occurred further downstream allowing increased merging, and augmented growth before the centre of the vortex began to lift off the surface. The vortices were taller inboard and separated from the surface further downstream. The leg closest to the centre first detached almost immediately after the centre lifted from the surface, however the outside leg was observed to remain in contact with the surface further down the length of the backlight surface. The higher velocity of the central portion relative to the attached outer leg stretched the structure which also became longer before separating.

A frequency analysis was conducted at two wake locations along the centre z-x plane to assess the influence of cornering on the corresponding transient mechanisms, as shown in Fig. 4.22. Peaks were extracted through the subtraction of a polynomial curve fit to locate local maxima. At the M1 location, positioned in the mean shear layer off the upper surface, a dominant frequency was identified to occur at a Strouhal number of 0.25 for a 20L and 5L radius corner, and 0.28 for a 10L radius corner. As discussed in Chapter 2 the straight-line condition had a peak at Str = 0.31. A common roll-off of the spectrum occurred at Str $\approx$ 8.5 as lower magnitudes occurred in the higher

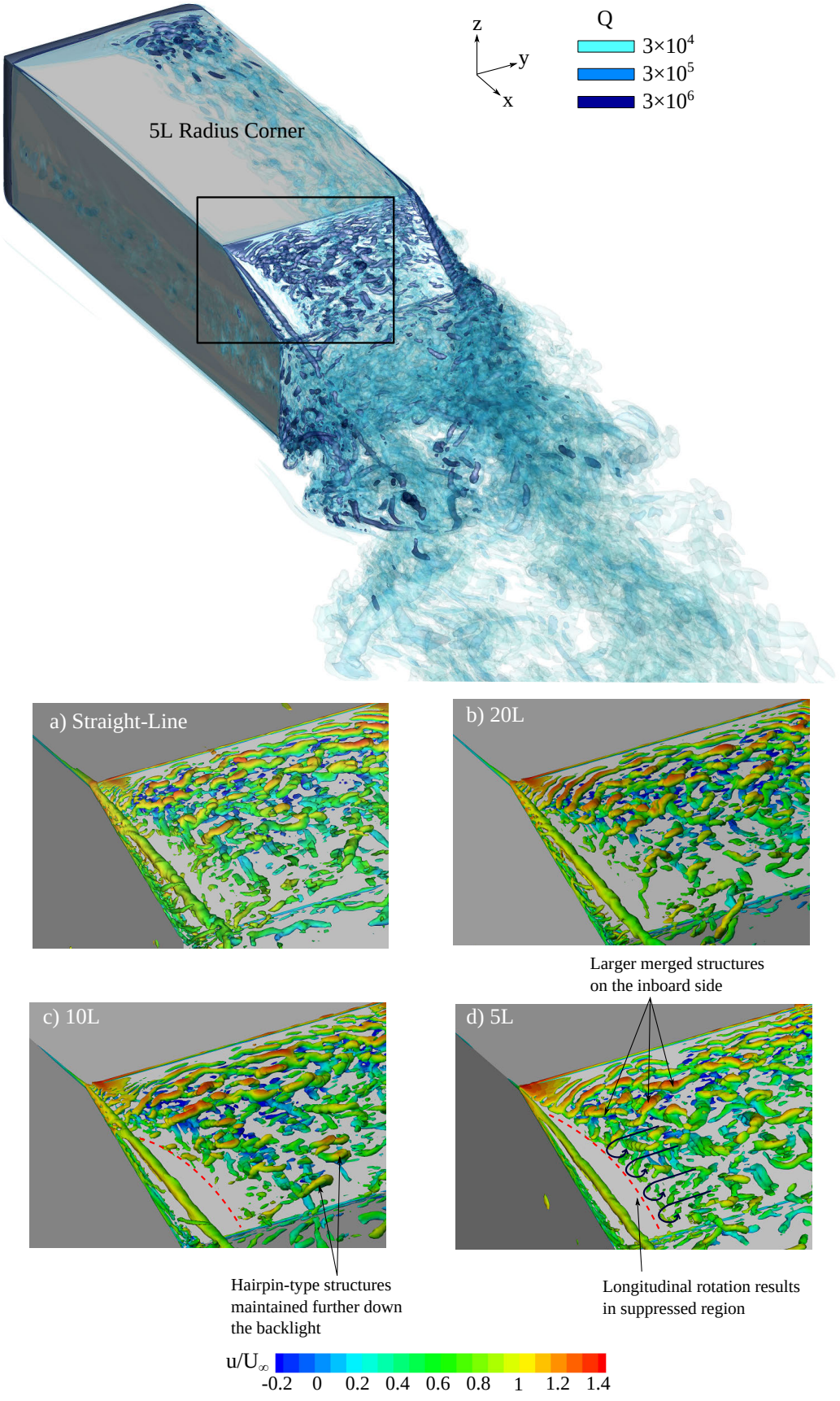

FIGURE 4.20: Instantaneous backlight flow structure on the inboard side shown with isosurfaces of Q = 1.5×10^6 coloured according to instantaneous non-dimensional x-velocity for a) the straight-line case, b) 20L radius corner c) 10L radius corner, and d) 5L radius corner

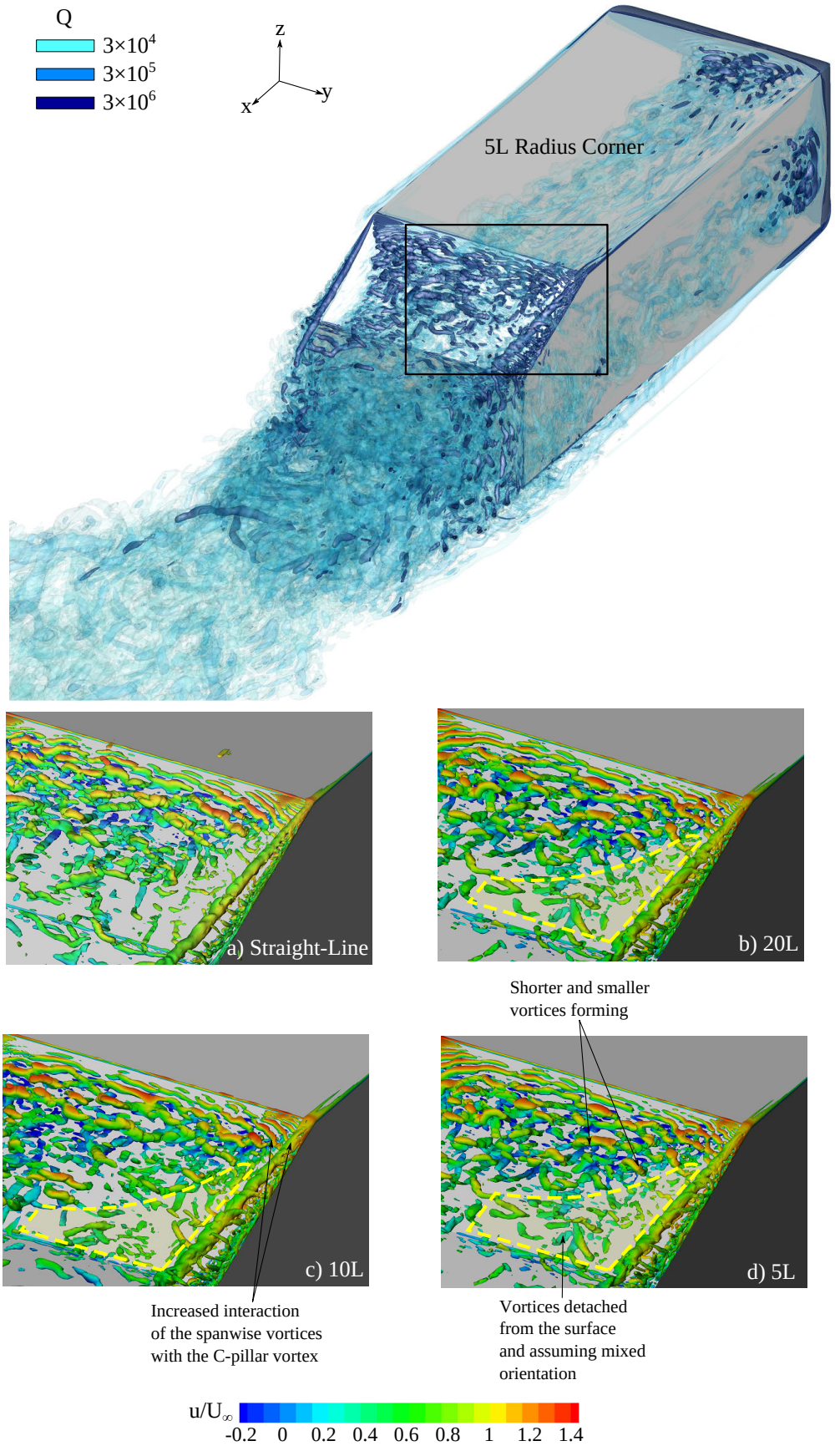

FIGURE 4.21: Instantaneous backlight flow structure on the outboard side shown with isosurfaces of Q = 1.5×10^6 coloured according to instantaneous non-dimensional x-velocity for a) the straight-line case, b) 20L radius corner c) 10L radius corner, and d) 5L radius corner

frequency range, similar to experimental results of Thacker et. al [69]. The dominant frequency was observed to correlate with the periodic enlargement and contraction of the separation bubble, as was discussed in detail in Chapter 2. This mechanism remained largely (but not completely) two-dimensional in the z-x plane, and thus was less affected due to the curved motion occurring within the x-y plane. The angle of the flow across the backlight face resulted in the minor differences in each instance. Of most significance in this instance was the differed interaction of the separated structures from the forebody (with a dominant frequency measured at Str = 0.28 in the straight-line condition) and the differences in this interaction due to the altered passage.

The measurement location M3 in Fig. 4.22b) exhibited a wide range of peaks and harmonics of similar magnitude throughout the low frequency range. A dominant frequency of occurred for the straight line condition at Str = 0.31. For the 20L, 10L and 5L radius corners this occurred at 0.28, 0.28 and 0.25. In this instance the dissimilarity of the wake structures meant the relative position differed. Thacker et. al [69] identified a region of high frequency activity occurring above the primary separation bubble due to shearing which propagated downstream into the wake. Due to the skew in the wake structure the M3 wake position was effectively shifted further into the outboard side of the wake as corner radius decreased. With the increased vertical displacement of the outboard wake, the M3 location was observed to occupy a region corresponding to a lower wake position with reduced frequency transient flow activity.

As the corner radius decreased the level of instability within the backlight separation bubble became greater toward the inboard side. It was observed that the C-pillar vortex and forebody vortices had a stabilising effect on the primary backlight separation bubble. Clipped contours in Fig. 4.23 highlight this shift in the peak RMS velocity value toward the inboard side (with surface skin friction coefficient used for identification of the separated region). This demonstrated that due to the larger inboard separation, the magnitude of the transient enlargement and contraction increased, however this occurred with the retention of a common frequency.

4.8.1 Surface Flow Structure

The surface streakline patterns allowed a more detailed investigation of the time-averaged separated flow structures which emerged in the backlight region. In the straight-line condition, shown in Fig. 4.24 symmetric reattachment occurred for the time-averaged separation bubble, where the feature extended equally down both sides of the face. The primary separation bubble extended furthest toward the central part of the face, reducing in length with proximity to the C-pillar vortex. The graph in Fig. 4.24 illustrates

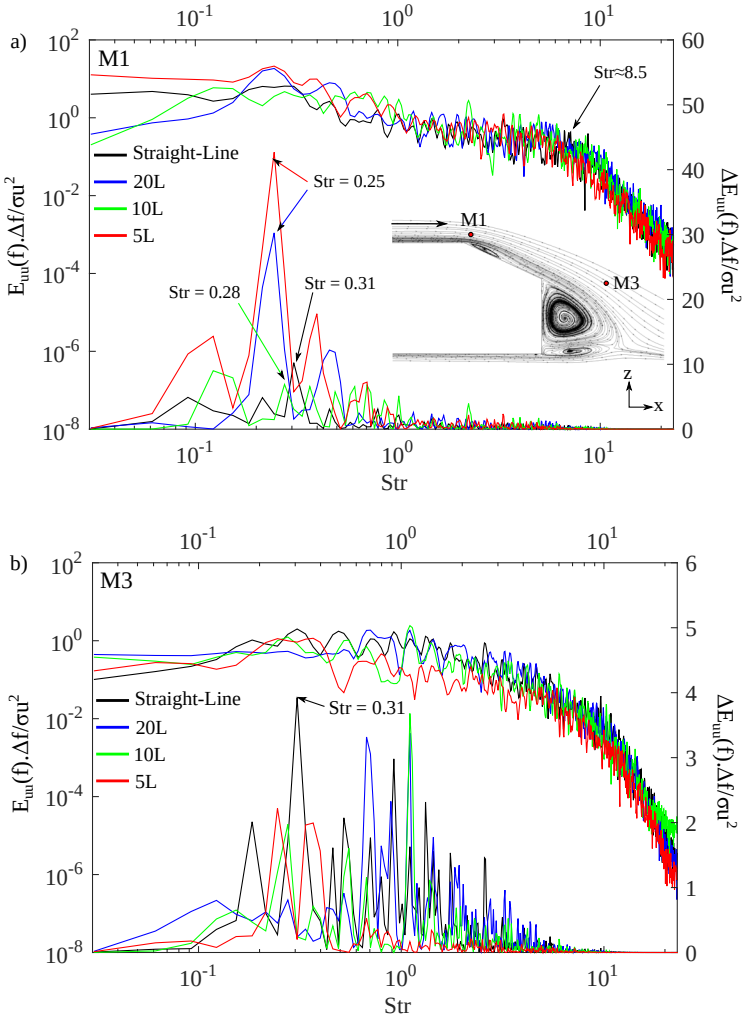

FIGURE 4.22: Raw (upper) and processed (lower) power spectral density plot of velocity magnitude for three different corner radii and the straight-line condition at location a) M1, and b) M3

how this primary reattachment length changed with corner radius. In the 10L radius corner case the increased outboard pressure deficit at the C-pillar location drew more flow across the face and resulted in the outboard half of the arched vortex structure being 18.2% wider. The reattachment length increased inboard but remained similar for all cornering cases while the width of the inboard circulation region continued to decrease. Rather than continuing to reattach further along the face, the separation bubble skewed towards the inboard side.

Integrating above the line shown in Fig. 4.24, a reduction in the separated area was measured to occur as corner radius decreased. In the straight-line condition the area between the positive bifurcation line and the upper edge of the backlight surface was $0.042L^2$, for the 5L radius corner case this separated region reduced by 12.0%, where

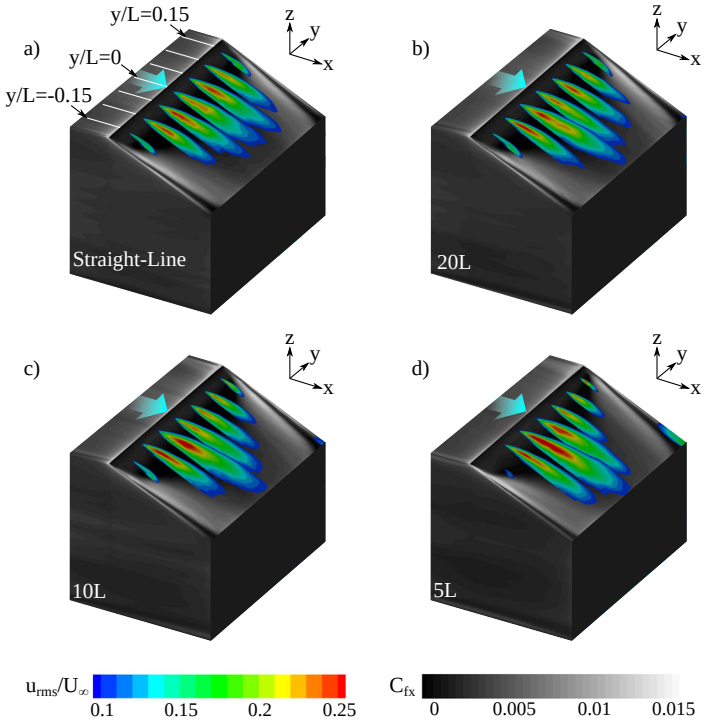

FIGURE 4.23: Root mean square of x-velocity contours across the backlight with skin friction coefficient in the x-direction shown on the surface for a a) 20L radius corner, b) 10L radius corner, and c) 5L radius corner

respectively smaller decreases of 10.4% and 6.2% occurred for the 10L and 20L radius corners.

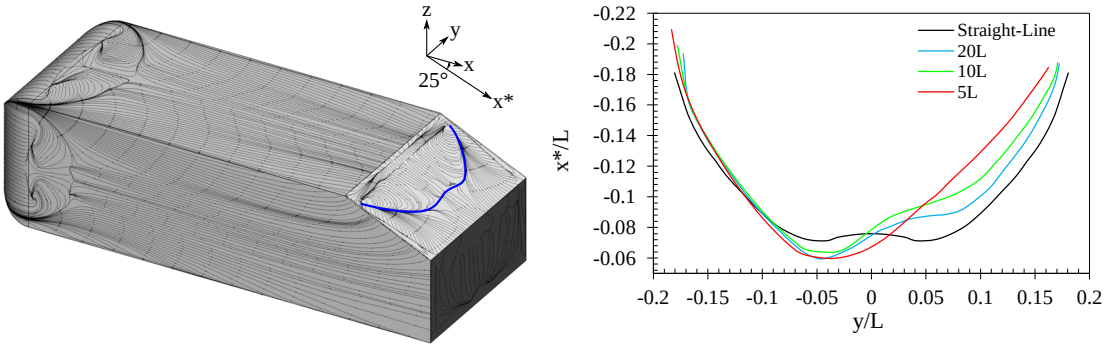

FIGURE 4.24: Mean reattachment line of the primary backlight separation bubble

A diagram of the observed cornering condition flow features is shown in Fig. 4.25 with the corresponding surface features. The separation bubble contained an arch type primary vortex with an induced counter-rotating spanwise structure near the upper edge. Due to the rear flow angle a longitudinal rotation occurred which bordered the separation bubble on the inboard side.

Primary flow structures initiated at the upper edge and over the sides of the backlight due to the sharp edges resulting in defined points of formation. The observed differences occurred near the upper corners of the backlight surface, at the junction of the edges, as is presented in Fig. 4.26.

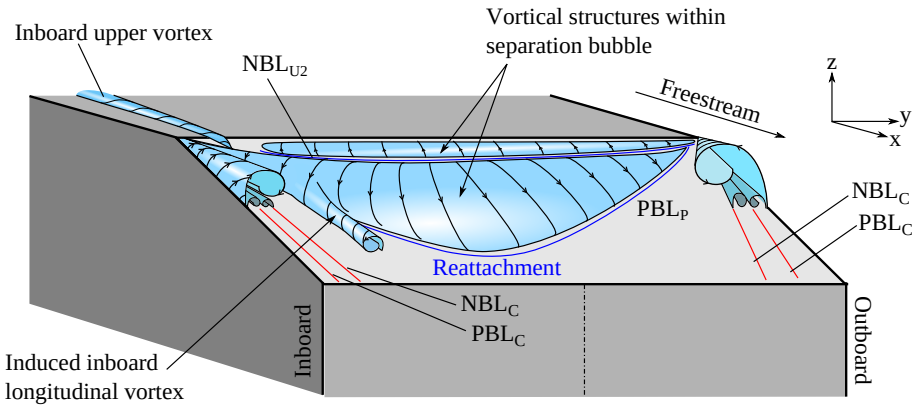

FIGURE 4.25: Separated flow structure over the backlight surface in the longitudinal and transverse axes in the cornering condition

As PBL$_P$ increased proximity to the inboard side the bifurcation line of reattachment extended to near the upper corner. A passage can be seen to emerge from the backlight edge into the main spanwise vortex structure within the separation bubble. This was due to the upper longitudinal vortex on the inboard side, which is shown in Fig. 4.25. As the corner radius decreased the forebody angle increased the size and strength of this vortex. Ultimately it burst due to the steep adverse pressure gradient over the backlight, however this resulted in a passage which increased the flow entering separation bubble on the inboard side.

As the height of this inboard side of the separation bubble grew larger, the rotational component of the vortex normal to the face increased. The upper region was drawn to the stable focus point at the end of NBL$_{U2}$, and a saddle point emerged at the junction between these zones. The point occurred further down the face as corner radius decreased. The focus drew more flow and the vortical structure was larger at the inboard side of the separated flow region. The induced secondary spanwise recirculation then extended further down the face on the inboard side, while on the outboard side the secondary recirculation narrowed.

On the outboard side the smaller longitudinal vortex structures forming below the primary C-pillar vortex through the 'gearwheel' mechanism increased their displacement across the face with the occurrence of a larger and stronger C-pillar vortex. NBL$_C$ corresponded to the separation location of the induced counter-rotating vortex and at

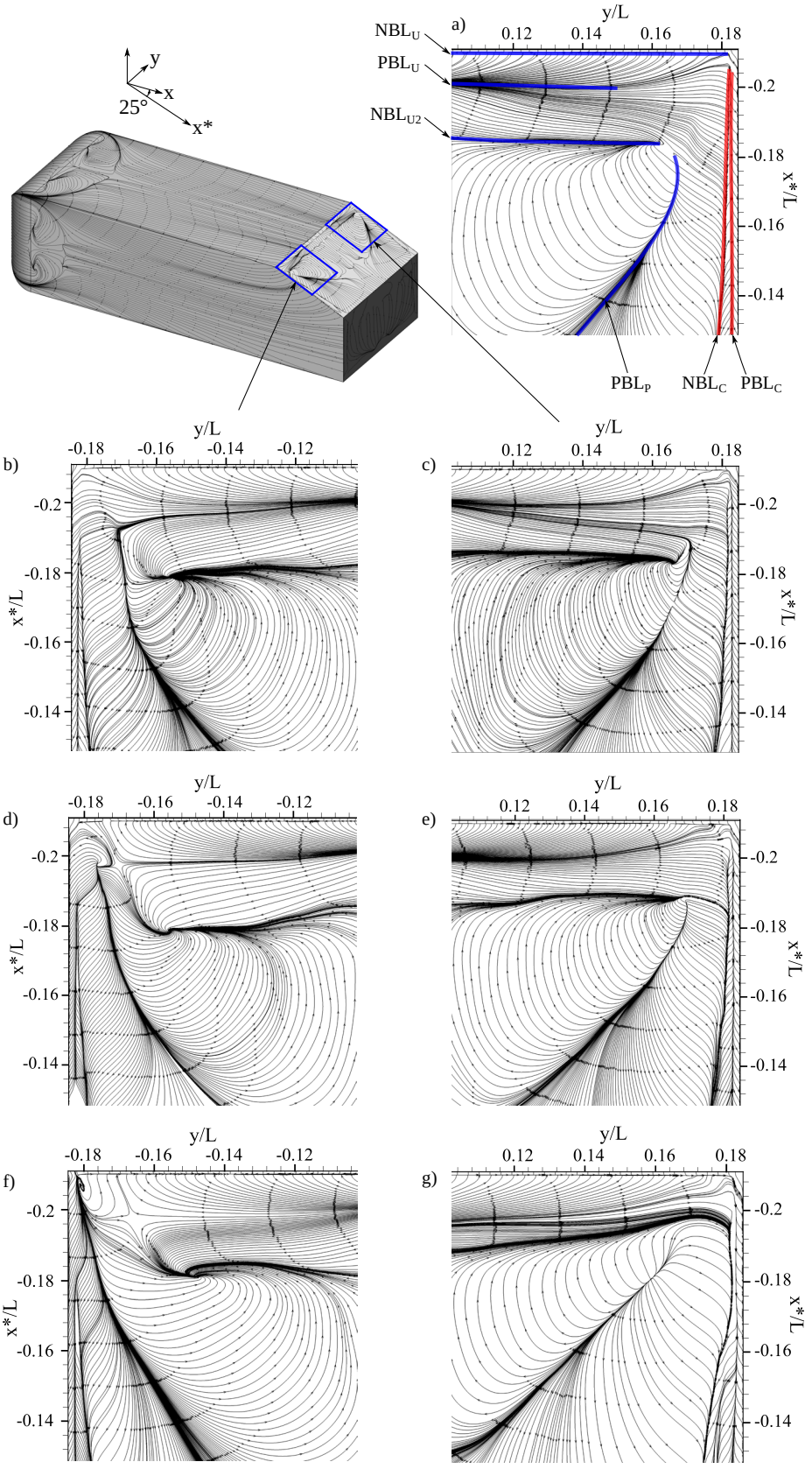

FIGURE 4.26: Surface flow structure and critical points occurring near the initiation of the C-pillar vortex for a) the straight-line case, b) the 20L radius corner case inboard side, c) the 20L radius corner case outboard side, d) the 10L radius corner case inboard side, e) the 10L radius corner case outboard side, f) the 5L radius corner case inboard side, and g) the 5L radius corner case outboard side

x*/L = -0.14 for the 5L radius corner this exhibited a 92.7% increase in the width (compared to the straight-line case) when measured from the edge. The distance between the side of the face and PBL_P increased by 6.5%, 39.2%, and 94.7% at x*/L = -0.14 as the corner radius respectively decreased from 20L to 5L. Due to the decreased vertical displacement of the separation bubble outboard, the initial normal rotation of the arch vortex was largely suppressed as the structure was immediately turned parallel to the face and also directed towards the geometric symmetry plane. This decreased height thus increased the freestream flow velocity and path curvature, resulting in the greater magnitude of the suction peak measured on the outboard side.

4.9 Rear Flow Interactions

Streamlines released from within the major separated flow features illustrated the differed interactions which occurred at the rear for the 5L radius corner, as shown in Fig. 4.27. Being the smallest radius corner the effects were most significant for the case shown.

The upper and lower recirculation interacted through flow transfer about the inboard side. This occurred where flow exited the lower recirculation, was turned into the vertical axis, and drawn into the centre of the upper recirculation. In the straight-line condition this interaction occurred on both sides, however for the 5L radius this became absent on the outboard side. The upper recirculation spiralled outboard and fed into the outboard C-pillar vortex as it merged downstream. Minimal flow from the upper recirculation was drawn to the inboard C-pillar vortex. Streamlines released at the inboard side in close proximity to the inboard C-pillar vortex were observed to travel completely across the width of the face to the outboard side. The inboard skew of the backlight separation bubble, resulted in the entrained flow exiting to the same side, and being drawn into the upper recirculation along with the shear layer off the backlight surface.

On the inboard side the lower recirculation partially exited near the lower corner and was turned in the longitudinal axis to merge with the C-pillar vortex downstream. However it was the increased strength of the outboard C-pillar vortex which resulted in the lower and upper recirculations, and most of the wake structure, being drawn across the rear face and into the outboard longitudinal vortex, significantly increasing the size of the observed downstream structure.

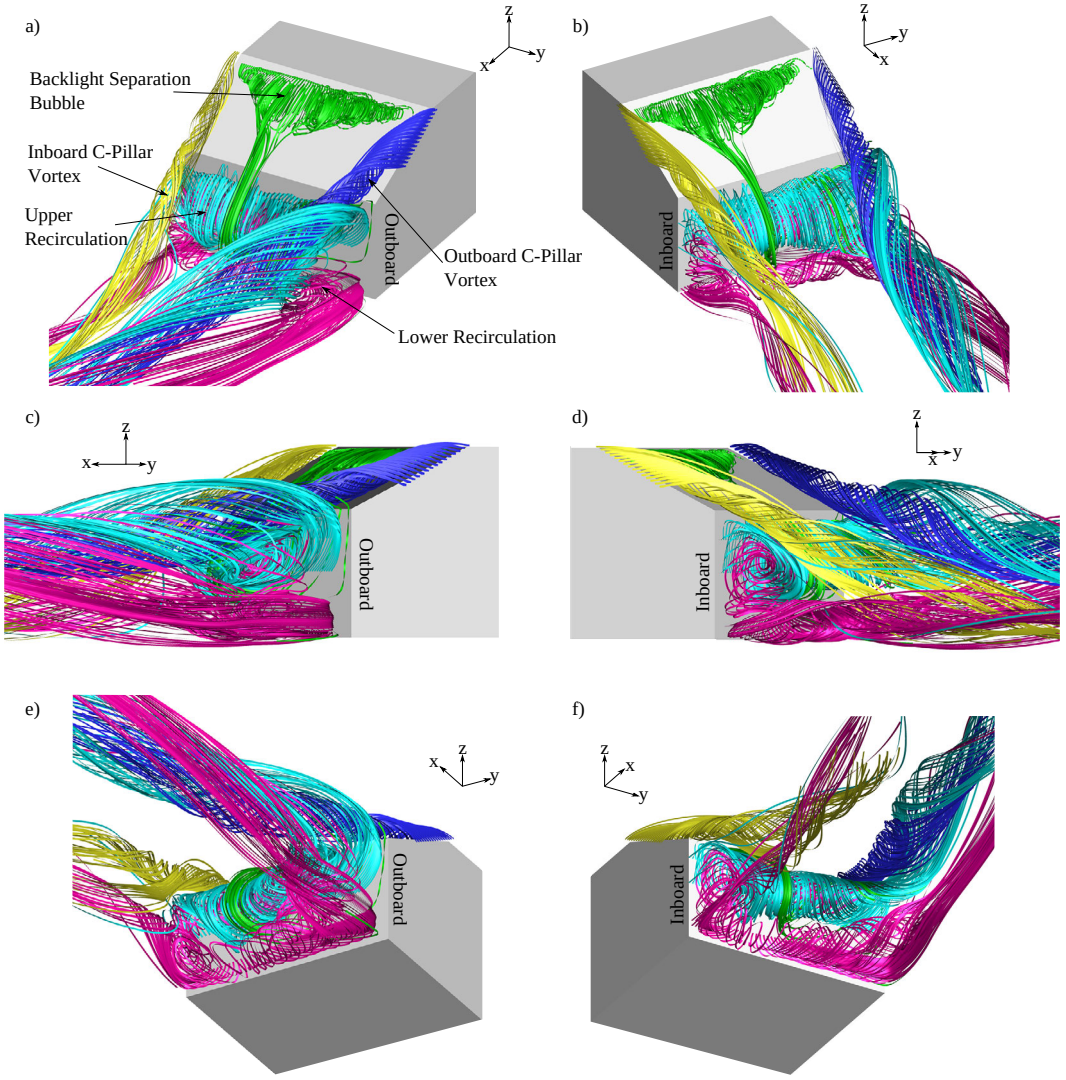

FIGURE 4.27: Streamlines released from within prominent rear flow structures for a 5L radius corner condition a) outboard upper isometric view b) inboard upper isometric view c) outboard side view d) inboard side view e) outboard lower isometric view f) inboard lower isometric view

4.10 Trailing Face Structure

The rear separation bubble in the straight-line condition at y/L = 0.1 is shown in Fig. 4.28a), and due to the symmetry of the body, the same flow structure was also observed at y/L = -0.1. For the cornering condition these are shown for each case at y/L = 0.1 and y/L = -0.1 in addition to profiles of the downstream z-velocity component.

The cornering condition was observed to result in an asymmetric time-averaged contraction of this feature at the trailing face. In most cases this was observed in the form of a mild outboard extension and larger inboard contraction. For the 10L radius corner a time-averaged elongation of 4.4% occurred on the outboard side (measured at y/L = 0.1)

and a decrease in the downwash angle, shown in Fig. 4.28b). While for the 5L radius corner an outboard contraction of 5.8% occurred — although this measurement was affected due to the angle of the C-pillar vortex across the rear of the body. For all corner radii a reduced downwash angle off the backlight surface occurred.

This difference at the inboard side of the separation bubble was more significant and for the 20L, 10L, and 5L radius cases as a contraction of 4.2%, 18.1%, and 31.1% occurred. In addition the time-averaged radial pressure gradient within both the upper and lower structures became more significant, and the inboard downwash angle thus became steeper.

At the location of L1 shown in Fig. 4.29 the trailing face separation bubble mechanism resulted in a dominant frequency of Str = 0.52 in the straight-line case. For the cornering conditions the corresponding peaks for the same mechanism were identified at 0.49, 0.46, and 0.40 for the 20L, 10L, and 5L radius corners respectively. The frequency reduction occurred due to a change in the quasi-periodic wake mechanism occurring within the separation structure at the trailing face. Due to the cornering condition the bursting mechanism became concentrated within the lower wake to the inboard side. In the absence of a strong longitudinal rotational component the pronounced bursting was also accompanied by a larger lateral expansion of the wake.

The sequence of wake motion within this region is shown in Fig. 4.30. The lower recirculation can be observed as dominant, particularly at the inboard location. Initially the lower structure formed through the merging of shear layer vortices off the lower surface of the body. This merging resulted in the formation of a single larger recirculation. The increase in the strength of the lower structure then caused a rapid expansion of the flow exiting from underneath the body, resulting in the decelerated high pressure region shown downstream.

As the size increased, the core pressure decreased and the lower recirculation began to draw flow from backlight surface. This flow from the backlight passed over the upper recirculation as shown in Fig. 4.30b) being drawn around and into the lower structure. This event coincided with the upper structure beginning an outward spiralling motion, initiating its burst.

At the next stage of the mechanism shown in Fig. 4.30c) the upper structure has burst completely while the lower has commenced an outward spiral. Flow is drawn down to the lower structure and then directed upwards at x/L = 0.2 due to the expansion of the flow passing underneath. The lower structure then bursts, as shown in Fig. 4.30d) with the downwash off the backlight surface, over the contracted near wake region, projecting

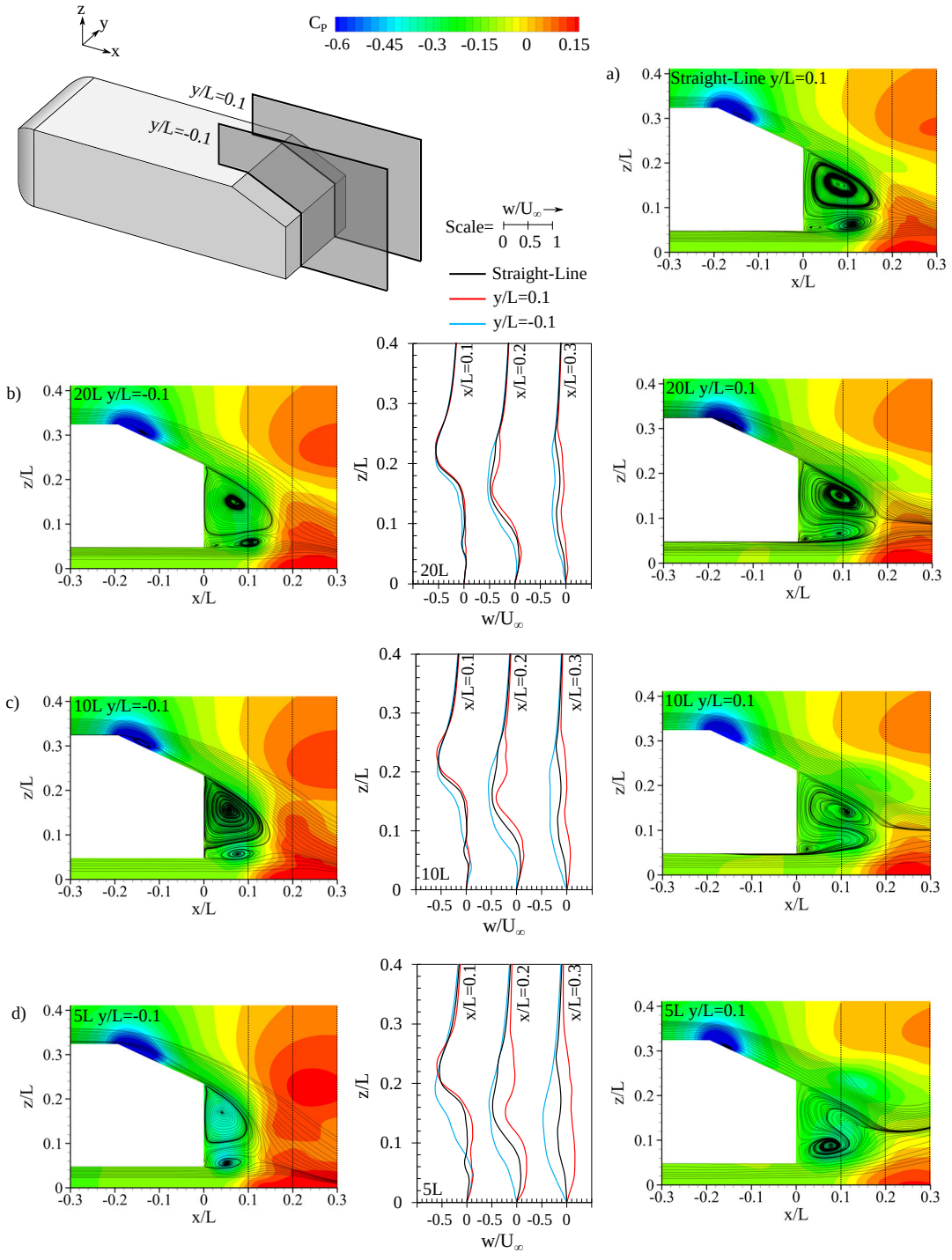

FIGURE 4.28: Wake streamlines and pressure coefficient distribution at y/L=0.1 and y/L=-0.1, with z-velocity profile for a) the straight-line condition b) 20L radius corner c) 10L radius corner d) 5L radius corner

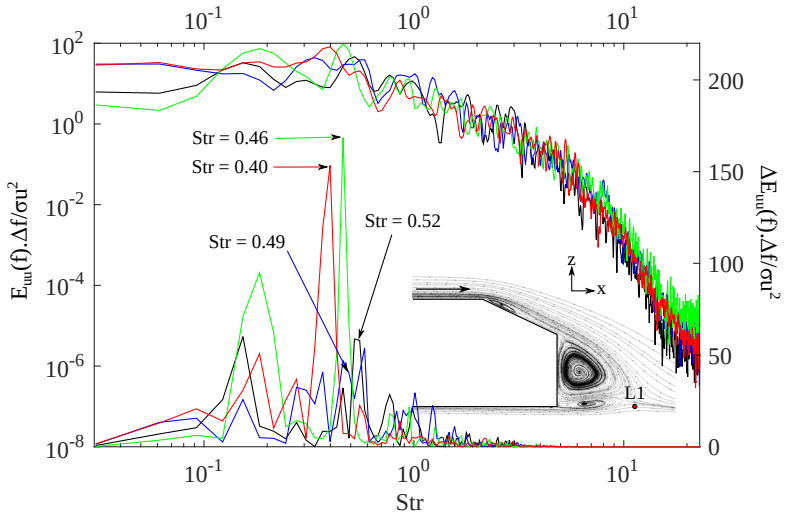

FIGURE 4.29: Raw (upper) and processed (lower) power spectral density plot of velocity magnitude for three different corner radii and the straight-line condition at location L1

the flow toward the ground plane. This resulted in the emission of a large fluid parcel which was observed to three-dimensionally expand within the wake region.

Similarly this same sequence of events occurred at the outboard side. However, the flow structures were drawn further downstream, particularly in the case of the lower recirculation, and become less coherent. The upwards downstream flow deflection was due to the angle of the C-pillar longitudinal vortex across the wake drawing the wake upwards. With the flow structures being larger in the absence of additional flow transfer, the core pressure was higher due to the reduced centrifugal forces. The burst of the upper recirculation can be observed in Fig. 4.30g), with the lower having burst prior to 4.30h). However the structures were observed to predominantly be drawn into and pass around the longitudinal C-pillar vortex to lesser effect.

The near-concurrency of the bursting mechanism of the upper and lower spanwise wake recirculations resulted in a more pronounced periodic enlargement and contraction of the wake, as shown in Fig. 4.31 for both the 10L and 5L radius corners. As corner radius decreased this became more concentrated toward the inboard side, and was coupled with an increased spanwise expansion.

Conversely the outboard side became comparatively more stable and assumed a regular curvature aligned with the freestream path. The differing effects on either side of the wake resulted in a tilt of structure, highlighted by the overlayed contours.

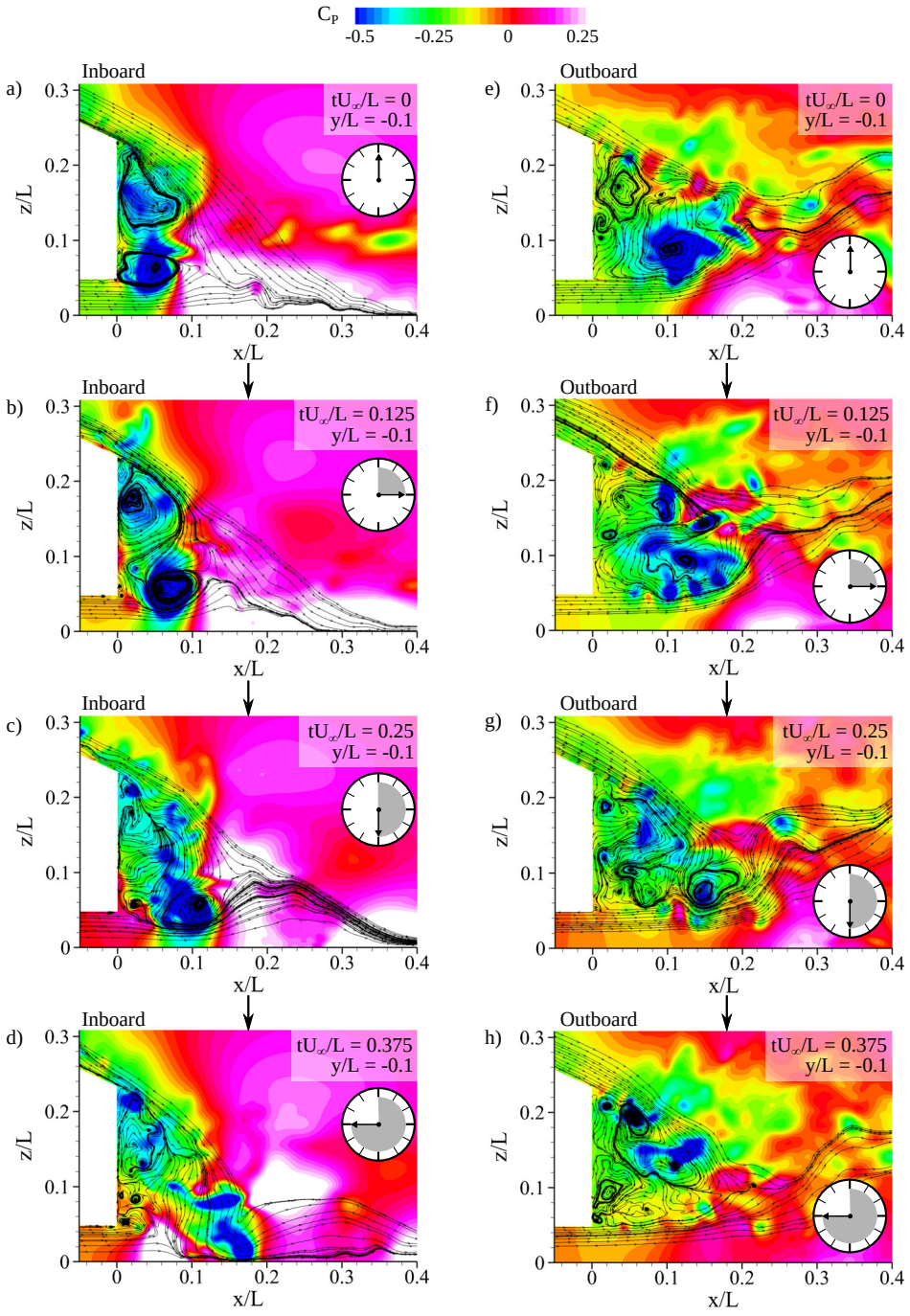

FIGURE 4.30: The transient motion of the wake structures stepping forward in time for a 5L radius corner at y/L=-0.1 and y/L=0.1

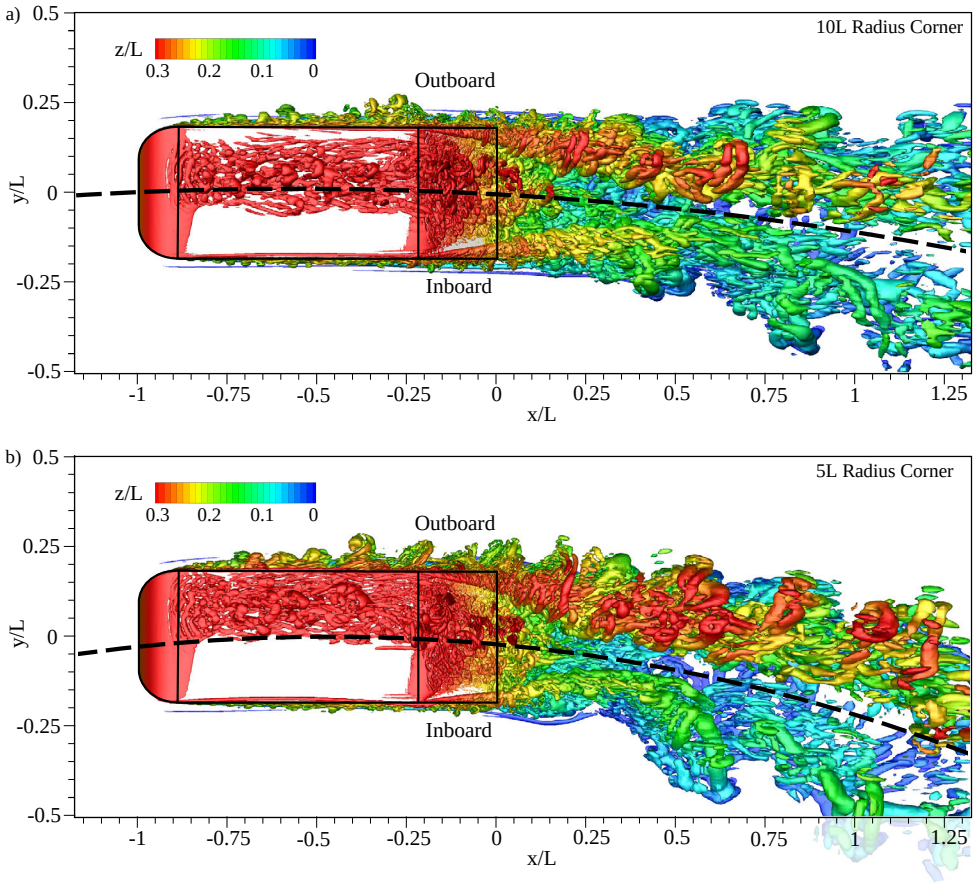

FIGURE 4.31: Isosurfaces of Q = 3×10^4 coloured according to z/L for a a) 5L radius corner, and b) 10L radius corner

4.11 Forces and Moments

For the application of these findings toward practical vehicle development it becomes of interest to analyse the aerodynamic forces and moments which result.

There was an increase in the aerodynamic drag coefficient as corner radius decreased and this followed a trend with an increasing gradient, as shown in Fig. 4.32a). The drag coefficient was 19.2% greater for the 5L radius corner when compared to the straight-line condition, and this difference was less for the respectively larger radius corners. The coefficient of force in the x-direction followed a similar trend, but was 3.4% less than the true drag coefficient for the smallest radii corner.

The maximum percentage increase in the viscous drag component was 8.3% and occurred for the 5L radius corner case, primarily due to the thicker outboard-side boundary-layer coupled with a rearward increase in wall-shear due to the flow angle. However, largely the overall increase in drag was attributed to the more dominant pressure component.

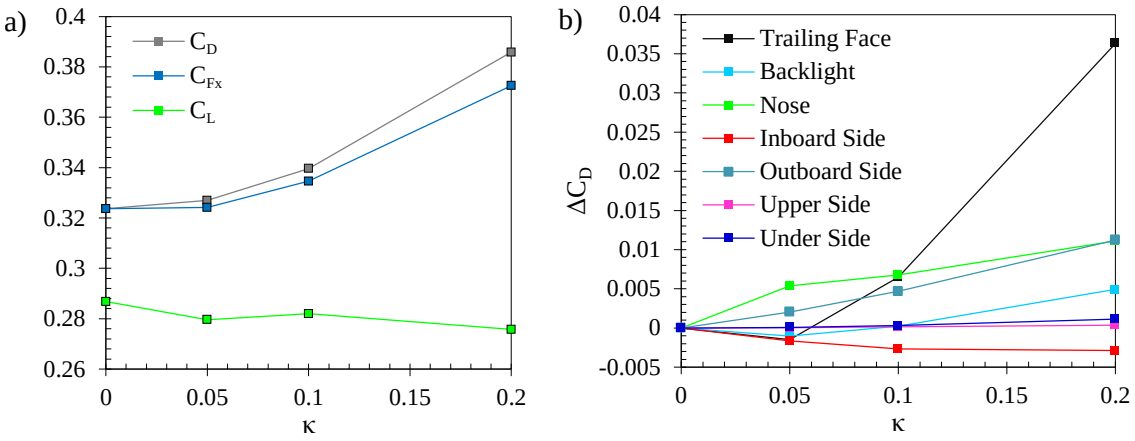

FIGURE 4.32: a) Cornering lift, drag, and force-coefficient in the x-direction b) Change in drag coefficient contribution for individual surfaces of the body

Figure 4.32b) details the change in drag coefficient contribution for each surface. The trailing face of the body was identified as having the greatest influence toward the net increase. This was due to the inboard contraction of the near wake structure, with a comparatively lesser outboard expansion. The contracted inboard recirculation had a decreased core pressure and resulted in the net surface pressure decrease, with an increased local drag component. A local increase also occurred for the backlight due to the reduction in the size of the separation bubble. This resulted in a decreased surface pressure due to a increase in flow acceleration, aided by the stronger outboard C-pillar vortex directed across the face.

The lift coefficient did not follow a similarly-consistent trend with corner radius, and the maximum reduction was 3.9% for the 5L radius corner. Lift was primarily generated due to the backlight angle and the resultant low pressure region which occurred at the upper edge. Despite the surface pressure reduction over the backlight, this was negated by the increased suction attributed to the outboard lower vortex, and resulted in a minor overall difference.

The aerodynamic side force and yawing moment were both attributed to the change in pressure distribution over the sides of the body, as is shown in Fig. 4.5. An inherent consequence of the flow curvature relative to the body, is that the two flat sides are affected in accordance with this change in perception. The angle of the flow approaching the nose resulted in a relative increase in the force which drew the nose outboard, and the rear inboard. This was in accordance with the change in flow angle along the length of the body. The net imbalance in the forces between the front and rear caused the increase in yawing moment observed in Fig. 4.33 where near-linear trend was again

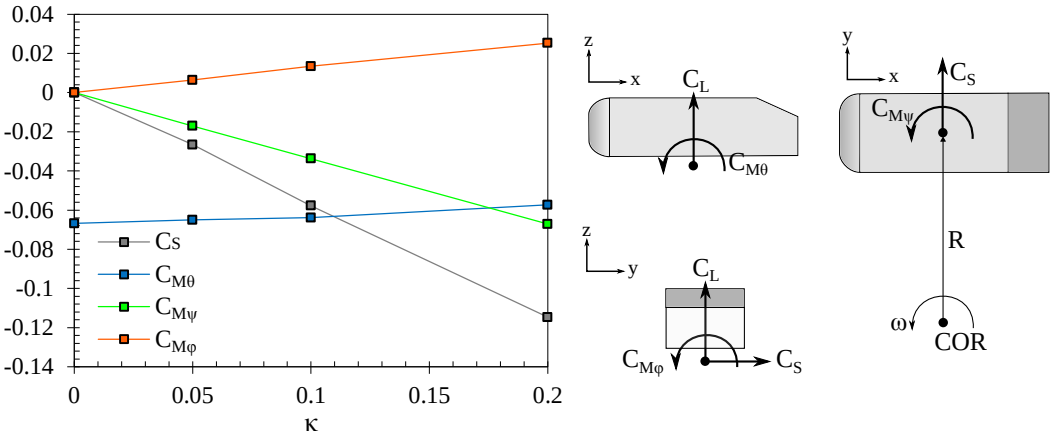

FIGURE 4.33: Cornering side force, pitching moment, yawing moment, and rolling moment coefficients

observed where the maximum coefficient was -0.07. This moment acted against the yaw rotation of the vehicle through the corner.

With the addition of the radially orientated pressure gradient due to the acceleration within the rotating reference frame a net side force occurred which increased as the corner radius decreased. This acted towards the centre of rotation, shown in Fig. 4.33. The magnitude of this force followed a near-linear trend as the curvature of the path increased and reached a maximum of -0.11.

Accordingly the rolling moment acted toward the centre of the corner due to the surface pressure distribution over the sides of the body. This reached a maximum value of 0.025 for the 5L radius corner case. Furthermore a decrease in the magnitude of the pitching moment occurred as corner radius decreased. The reduction was 2.8%, 4.4%, and 14.25% for the 20L, 10L, and 5L radius corners respectively. This was identified to occur due to the additional vortices developing along the underside, and the increased rearward suction reducing the nose-down pitching moment.

4.12 Summary

All separated flow regions demonstrated sensitivity to the variation in flow angle along the body. The inboard to outboard angle at which the flow approached the front of the body resulted in a positive outboard shift of the forebody separation bubble. This caused an imbalance in the structures forming within the bubble, notably with an extension of the contained inboard half of the vortex, and the outboard shift of the unstable node which corresponded to the location of the ejected vortices.

An inboard shift of the stagnation point resulted in increased flow curvature around the outboard side of the nose and a pressure gradient which would act to deflect the forebody outboard and damp the yaw rotation within a corner. Due to the centrifugal acceleration within the rotating reference frame, a radially surface pressure gradient occurred which was most apparent on the sides. The pressure over the inboard side was reduced, while the outboard surface distribution was increased relative to the straight-line condition. Due to the resultant distribution a net side-force acted toward the centre of the corner, in addition to a rolling moment coefficient which was directed inboard. In reality this external gradient would be opposed by a equal pressure gradient also affecting the internal flows and the net effect would need to be carefully evaluated in the assessment of a specific vehicle geometry.

The flow angle at the rear of the body further enhanced the pressure gradient across the outboard C-pillar location, and reduced the inboard gradient at the opposing edge. This then strengthened the outboard and weakened the inboard longitudinal C-pillar vortices. The resultant disparity in circulation strength suppressed the outboard size of the separation bubble and increased the inboard reattachment length. On the backlight surface the separation bubble was skewed toward the inboard side, and thus the emitted hairpin-type vortices were accordingly concentrated in the same direction.

In the wake region of the cornering Ahmed body an asymmetric extension of the two recirculation regions occurred in the form of an inboard contraction and outboard extension. In addition, this altered the transient bursting mechanism which occurred at this location. The upper and lower recirculations burst near concurrently, particularly for the 5L radius cornering case, with the inboard ejection of fluid being stronger and directed downwards due to the steep downwash angle off the backlight. This led to a more pronounced periodic expansion and contraction of the wake region, in addition to a reduction in the frequency at which this occurred.

The differences in the cornering condition wake region resulted in a 19.2% increase in aerodynamic drag for a 5L radius corner in comparison to the straight-line condition, with an increasing gradient observed in the trend relating the drag to the curvature of the body's path.

Results thus demonstrated the occurrence of a range of flow effects specific to the cornering condition, and also highlighted the importance of analysis within this condition — particularly for applications where the cornering performance is most critical.

Chapter 5

The Effects of Yaw Angle and Cornering

Yaw and cornering are often regarded to exhibit similarity in their aerodynamic characteristics for automotive applications [6, 13, 14]. However, to the best knowledge of the author, there is yet to be a published study that has reliably assessed the validity of this assumption. In this chapter, the results presented in Chapters 3 and 4 are compared and highlight the differences and similarities which occur between the conditions.

In addition, the yaw sensitivity of the Ahmed body is assessed within the cornering condition. For a 10L radius corner the body is positioned at three different angles of yaw while retaining the path curvature that occurs within a corner. For practical applications this angle within a corner can differ due to a variety of factors, and will inevitably vary during typical driving scenarios. In this way the findings from both the cornering and yawed conditions were combined to further understand the overall implications toward current-day testing techniques, and the application of cornering aerodynamics in real-world scenarios.

The predominant flow structures have been shown to differ between the cornering and yawed conditions, as detailed in Fig. 5.1. In the yawed condition the angle of the flow across the body remained constant, and resulted in flow structures being directed toward the leeward side. Figure 5.2 shows how the upper forebody separation bubble was shifted toward this side, with the emitted vortical structures being entrained into the upper leeward longitudinal vortex. These additional leeward longitudinal vortices formed off the upper and lower surfaces due to the flow angle and were accompanied by a larger leeward separation bubble. The changes contributed to a shift in the wake structure and an increased overall width. The body had a mild straightening effect on

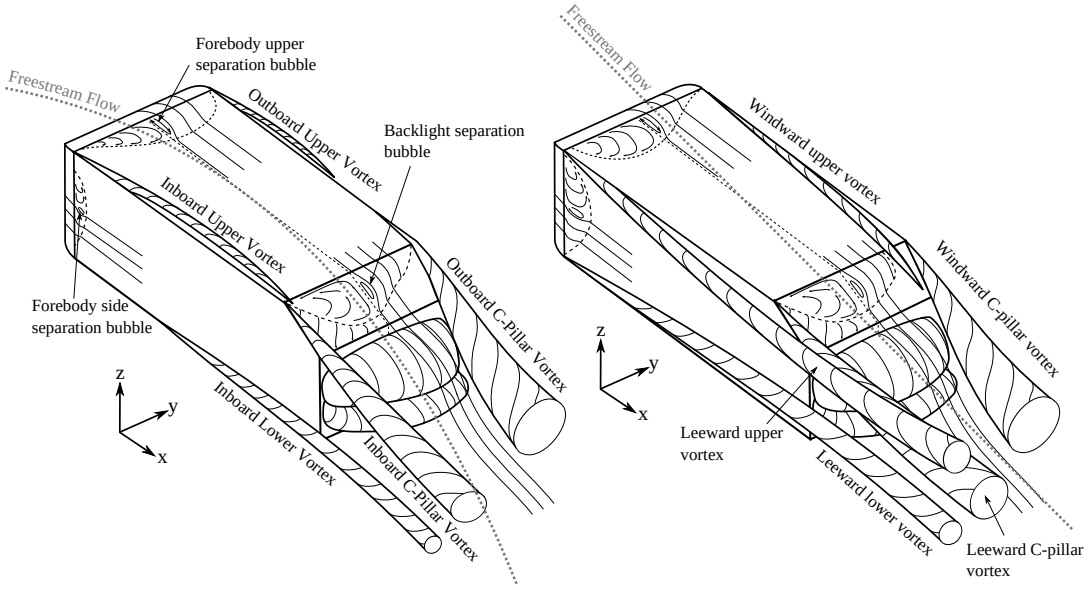

FIGURE 5.1: Diagram of the predominant time-averaged wake structures in the cornering (left) and yawed (right) conditions

the flow however the wake structure downstream was primarily aligned in the direction of the freestream flow.

In the cornering condition the angle at which the flow approached the front of the body was different to that which occurred at the rear, due to the continuous change in flow angle along the length. The body was also positioned within a rotating reference frame which resulted in acceleration due to the curved path and local variation in the freestream velocity. The forebody flow angle resulted in a similar shift of the forebody separated structures, however this shift occurred in the opposite direction. On the outboard side, the initial separated region increased in size and the flow angle resulted in the emitted vortices being directed back toward the surface at the rear, as opposed to being further displaced from the surface in the yawed condition.

The periodic bursting mechanism of the large rear spanwise structures was far more pronounced in the cornering condition. Increased circulation of the lower structure on the inboard side resulted in this becoming the dominant feature and caused the lateral expansions observed in Fig. 5.2b). The wake then followed a curved path downstream.

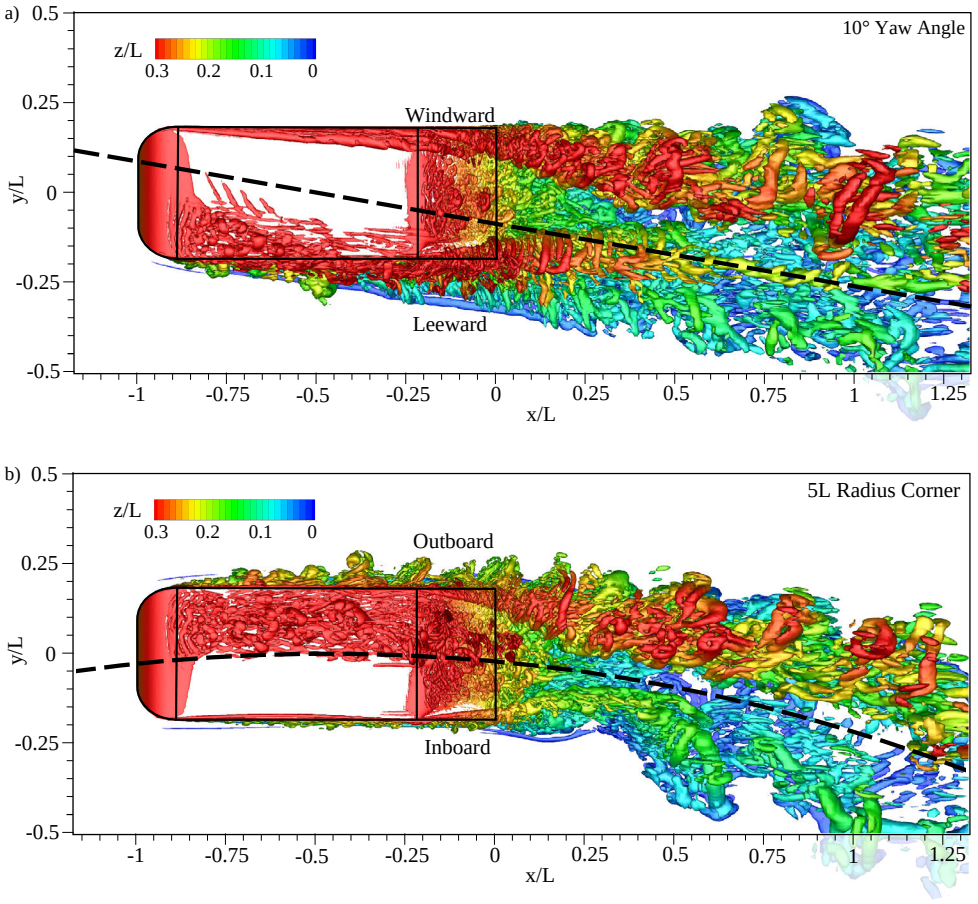

FIGURE 5.2: Isosurfaces of instantaneous $Q = 3 \times 10^4$ with contours of z-displacement, comparing the flow structures for a a) 10° yaw angle, and b) 5L radius corner

5.1 Comparison of Aerodynamic Forces and Moments

Initial observations of the two flowfields identified weak correlation between the two conditions for the considered geometry, with substantially differing flow structures. Comparison based purely on numerical values and trends identified the aerodynamic force and moment coefficients as being most similar between the two conditions when the angle of the flow at the rear was orientated in a common direction, as shown in Fig. 5.3. The rolling moment and side force, due to flow asymmetry, acted in the same direction, however, the yawing moment acted in opposite directions and again highlighted a fundamental difference between these two conditions.

The rate of change of the different aerodynamic forces and moments could also not be equated. The yawed condition experienced a significant increase in both lift and drag, with maximum changes of 40.25% and 42.8% occurring for a 10° yaw angle, while for the cornering condition the drag increase was far more substantial than that of lift.

The drag coefficient was 19.2% greater for the 5L radius corner when compared to the straight line condition, and lift *reduced* by 3.9%.

For the yawed condition the pitching moment only experienced a mild reduction, whereas a more substantial decrease occurred due to cornering. The maximum decrease in this parameter for the yawed condition occurred for the 2.5° yaw angle (2.68%), while for a 10° yaw angle the value was only 0.24% less than the straight-line condition. For the 5L radius corner a more significant 14.25% reduction in pitching moment was measured, with a progressive decrease in the value as corner radius decreased.

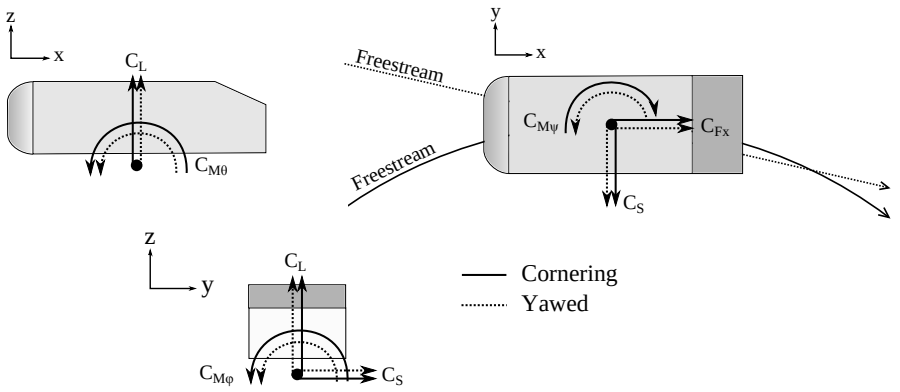

FIGURE 5.3: Comparison between the direction of action for the aerodynamic forces and moments within the cornering and yawed conditions

A numerical comparison was conducted based on the magnitude of force and moment coefficients. The values were compared based on the magnitude of the difference from the straight-line condition, and expressed as a fraction of the overall range. For any given coefficient C_a the ΔC value was calculated based on:

$$\Delta C_{a,max} = |C_{a,max} - C_{a,min}| \tag{5.1}$$

$$\Delta C_{a,val} = |C_a - C_{a,straight}| \tag{5.2}$$

$$\Delta C_a = \frac{\Delta C_a}{\Delta C_{a,max}} \tag{5.3}$$

With the minimum and maximum values were calculated based on the coefficient values for both the cornering and yawed conditions. The straight-line value of each coefficient was assigned a value of zero, and the maximum difference was given a value of one. This comparison thus neglected the change in direction for the yawing moment and lift coefficients.

For each force and moment coefficient both data sets were considered, with a second order polynomial curve fit used to identify the line of best fit:

$$K_2x^2 + K_1x + K_0 \tag{5.4}$$

Where the drag coefficient was omitted due to the difference in the calculation of this parameter for the yawed and cornering condition, as detailed in Appendix A

Based on achieving a maximum coefficient of determination for the entire data set, the polynomial coefficients and the ratio between yaw and curvature were evaluated to find the value that corresponded to the closest correlation between the two data sets. The final coefficients for the respective polynomial curves are shown in Table 5.1 which resulted in a maximum R^2 value of 0.832. The coefficient deltas and the polynomial curve

TABLE 5.1: Polynomial curve coefficients as fitted to force and moment coefficient data for the cornering and yawed cases

Coefficient	K_2	K_1	K_0
C_L	0.121	-0.239	0.205
C_{Fx}	-0.020	1.299	-0.658
C_S	0.060	0.392	0.041
$C_{M\theta}$	-0.202	2.104	-0.409
$C_{M\psi}$	-0.005	1.048	0.006
$C_{M\phi}$	0.060	0.387	0.060

fits are shown in graphical form in Fig. 5.4. From the analysed radii and yaw angles the closest correlation between the two data sets occurred when the ratio between curvature and yaw angle was equal to:

$$\frac{\psi}{\kappa} = 25.12°\text{L} \tag{5.5}$$

This indicated that, in the specific case of the 25° backlight Ahmed body, a 5L radius corner resulted in force and moment magnitude changes that were most similar to those for a 5.02° yaw angle.

The result further emphasised the weak correlation between the two conditions for this specific geometry. The values for the 10° yaw angle also skewed results due to the absence of a similar cornering condition. Such a comparison would be better suited to an experimental analysis (given the development of a suitable facility) where a large number of different yaw angles and corner radii could be used to obtain a larger data set of greater significance, however the results indicate the unlikely identification of common characteristics.

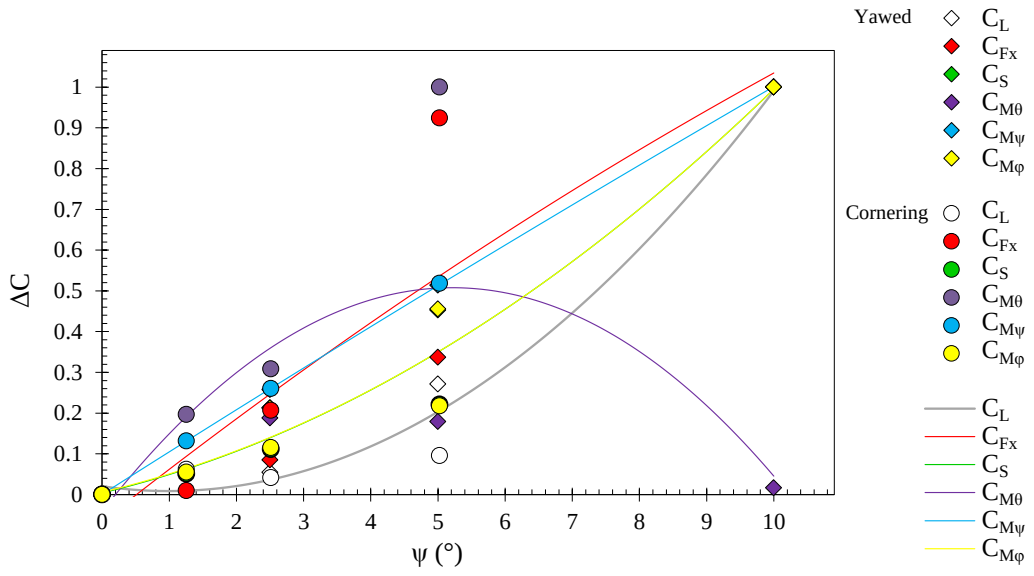

FIGURE 5.4: Polynomial curve fits for the aerodynamic force and moment coefficients in the cornering and yawed conditions

5.2 Comparison of Aerodynamic Characteristics

The 5° yaw angle case and a 5L radius corner were directly compared to aid towards further understanding the cause of this dissimilarity. The time-averaged surface pressure coefficient for 5° yaw angle was subtracted from the 5L radius corner using the common grid point distribution over the surface, as shown in Fig. 5.5.

The pressure distribution differed substantially over the forebody, and was due to the flow angle being in the opposite direction in this region. The inboard side in the cornering condition thus had a higher pressure distribution compared to the leeward side in the yawed condition, while the outboard side pressure distribution was lower compared to that of the windward. The difference on the upper surface was due to the separation bubble, and the contained low pressure region, also being skewed in the opposite direction.

Despite the opposing angle of the flow, this region was identified to be the location of greatest similarity between the two conditions, as in this region the flow was dominated by effects primarily attributed to the flow angle and was not subject to further cumulative changes acting along the length.

Observing the surface pressure profiles shown in Fig. 5.6, qualitative similarity was noted for the section between x/L = 0.9 and 0.8. In this region the difference between the two sides was more significant for the 5° yaw angle, with a 7.8% higher magnitude of the suction peak on the leeward side, in comparison to the 5L radius corner's outboard

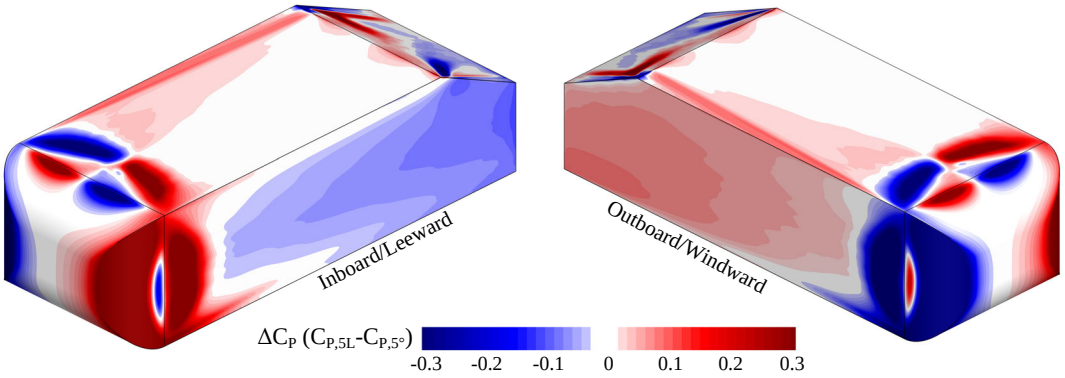

FIGURE 5.5: Pressure coefficient delta between the 5L radius cornering and 5° yaw angle conditions

profile. A comparatively higher pressure distribution was also observed for the windward side when compared to the inboard side in the cornering condition.

From x/L = -0.8 up to the trailing face of the body, a fundamental difference between the two conditions was apparent due to the change in pressure distribution along the sides of the body. The acceleration due to the curved motion with a non-inertial reference frame resulted in a pressure gradient acting across the boundary layer and contributed to the apparent increase in pressure along the outboard side and decrease on the inboard.

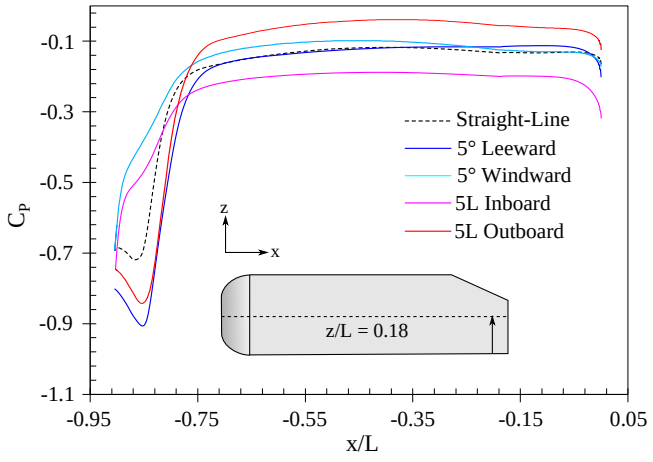

FIGURE 5.6: Comparison of pressure coefficient profiles along the side surfaces at z/L = 0.18

This effect was evident in Fig. 5.5 and 5.6 and resulted in a lower surface pressure over the inboard side when compared to the leeward, with the opposite occurring outboard. For the cornering condition the pressure gradient along the sides opposed the difference which occurred at the nose, and resulted in a comparatively smaller net side force than

the yawed condition. The side force for the 5° yaw angle was 2.05 times larger than that for the 5L radius corner.

There were also observed differences in the surface pressure distribution at the rear. The presence of the upper windward longitudinal vortex in the yawed condition was observed to result in cumulative effects toward the backlight region. In the absence of this structure within the cornering condition, comparatively higher pressure occurred along the outboard side on both the upper surface and the backlight, as shown in Fig. 5.7a).

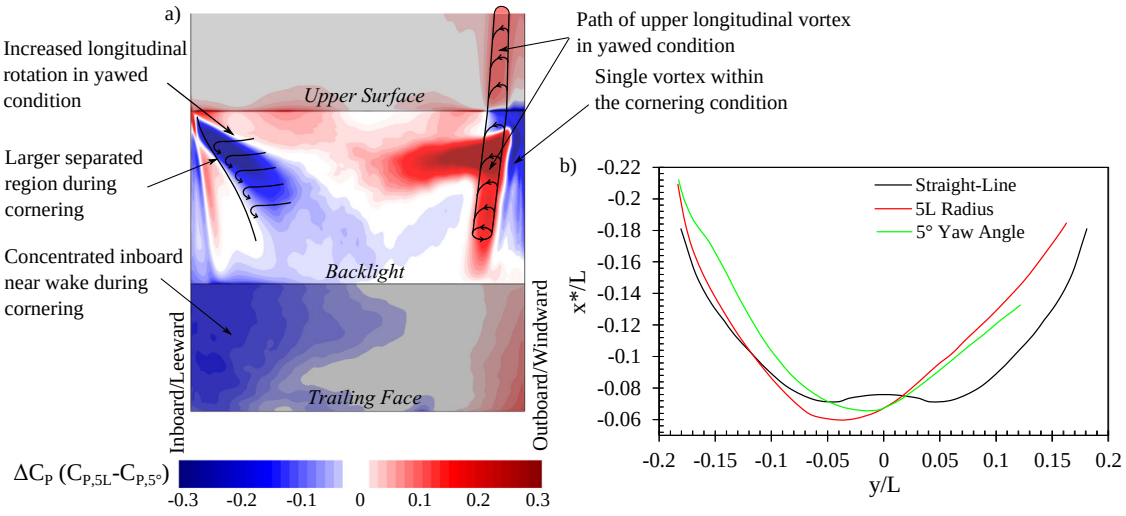

FIGURE 5.7: a) Pressure coefficient difference over the backlight surface between the 5° yaw angle and 5L radius cornering condition, and b) location of reattachment for separation bubble

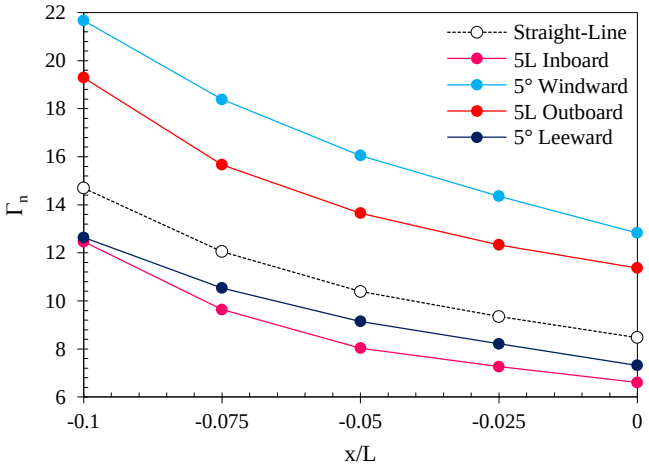

FIGURE 5.8: Comparison of C-Pillar circulation strength over the backlight surface

In the yawed condition this longitudinal vortex passed near the windward C-pillar vortex, and resulted in an average 51.9% increase in circulation, as shown in Fig. 5.8. For the

cornering condition the change in pressure distribution along the sides of the body contributed to the formation of a comparatively stronger but only single longitudinal structure on the outboard side with a overall smaller increase in circulation of 43.7%. Furthermore, on the inboard side a mildly weaker and comparatively smaller vortex formed in comparison to the leeward side in yaw.

In Fig. 5.7b) it can be observed that for the cornering condition between y/L = -0.17 and 0 the inboard backlight separation length was 16.1% longer than that which occurred on the leeward side in the yawed condition. The low pressure region for the cornering condition occurred due to the larger size of the separation bubble on this side. While in the yawed condition the longitudinal rotation along the leeward edge promoted the earlier reattachment.

On the outboard side separation length was reduced by an average of 15.0% for the 5L radius corner, and 11.9% on the windward side for the yawed condition when compared to the straight-line result. In both cases the reduction was associated with the occurrence of a stronger C-pillar vortex. The presence of the additional longitudinal vortex in the yawed condition resulted in decreased width of the primary separation bubble and the bifurcation line corresponding to the point of reattachment to over the backlight face did not extend beyond y/L = 0.122.

At the trailing face, the cornering condition resulted in a reduction in the surface pressure, which led to a 2.7 times more significant increase in the force component aligned with the x-direction. This coefficient for the 5L radius corner increased by 15.1% over the straight-line condition, while the 5° yaw angle resulted in a smaller 5.5%.

This difference in trailing face surface pressure was concentrated toward the inboard side, and was attributed to the increased circulation of the near wake in addition to the gradient induced by flow acceleration within the rotating reference frame. Thus the inboard region in the cornering condition was further contracted by 2.7% with a decreased core pressure and resulted in lower pressure at the surface.

5.3 Yaw Sensitivity within the Cornering Condition

As was explained in Chapter 1 the practical scenario of a vehicle travelling through a corner can be affected by a wide variety of factors. From an engineering and vehicle design perspective it then becomes of interest to understand how the aerodynamic effects will change when a vehicle is at different angles while still assuming a curved path. The scenario of the angle of the flow at the front being equal and opposite to that at the

rear is only representative of one specific condition. While the yawed and cornering conditions are different, their effects will often be combined in real-world scenarios.

To assess the sensitivities of the Ahmed body within the cornering condition, the 10L radius corner was additionally investigated at two further angles as shown in Fig. 5.9 and Table 5.2, where the body was at an angle of yaw with respect to the tangential flow direction at its centre. The positive angle would be representative of a high-speed, large lateral load corner which would result in a significant tyre slip angle. The negative angle would be representative of a low-speed manoeuvre, where the angle at the front exceeds that of the rear.

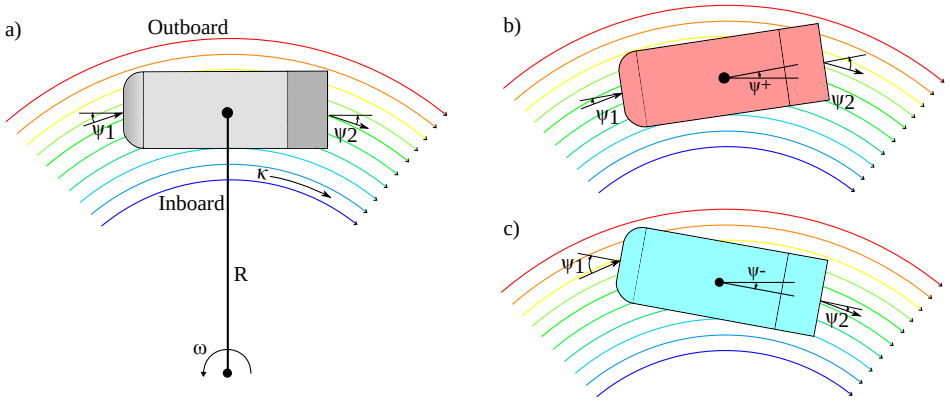

FIGURE 5.9: Diagram of flow angles, radius and curvature for analysis of different yaw angle within a the cornering condition

For these conditions the flow angle continued to exhibit variability along the length of the body due to the curvature, however the $\psi = 1.43°$ condition represented a scenario where the rear angle was greater than that at the front of the body and ψ = -1.43° had a greater flow angle at the front of the body in comparison to the rear. The specific angles were selected based on the centre of rotation shifting 0.25L fore and aft, as located perpendicular to the longitudinal axis of the body.

TABLE 5.2: Front and rear flow angles at different angles of yaw within the 10L radius cornering flow conditions

Radius	$\psi(°)$	Curvature (L^{-1})	$\psi1(°)$	$\psi2(°)$
10L	-1.43	0.1	-4.29	1.43
10L	0	0.1	-2.86	2.86
10L	1.43	0.1	-1.43	4.29

5.4 Forces and Moments

The aerodynamic forces and moments for the respective conditions are shown in Fig. 5.10 with the straight-line condition also shown for reference. The aerodynamic drag and force coefficient in the x-direction increased as the centre of the body was no longer aligned tangent with the curved path of the flow, as shown in Fig. 5.10a). A 3.4% increase in drag coefficient occurred for ψ = -1.43° and a larger 7.8% occurred for ψ = 1.43°. The increase in drag coefficient with a positive change in body angle was expected due to the dominance of the rear wake structure towards the production of drag, and ψ = 1.43° resulted in a change largely attributed to decreased surface pressure over the trailing face. While for ψ = -1.43° a similarly low surface pressure remained over the trailing face, which was comparable to *psi* = 0°, with the increase in the drag contribution of the nose surface resulting in the net gain. These respective changes demonstrated that the condition ψ = 0° could be regarded as giving the most conservative drag prediction within the cornering condition for a geometry of this type.

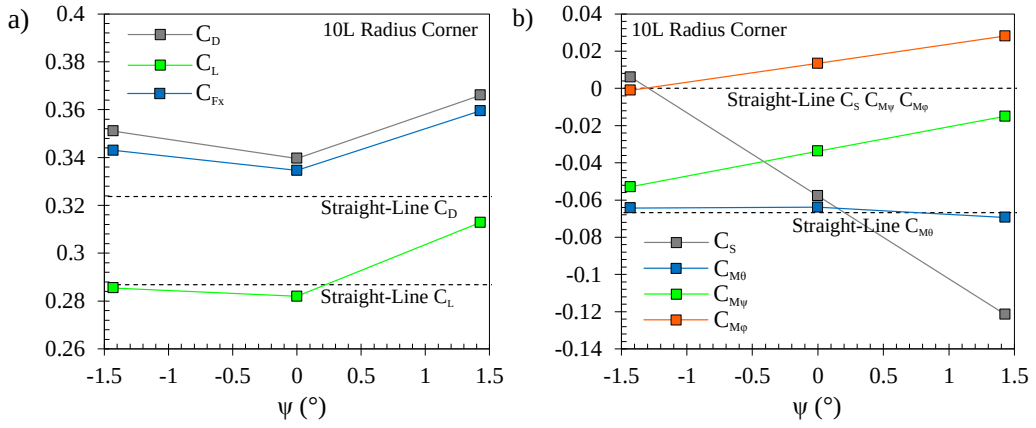

FIGURE 5.10: a) Coefficient of lift, drag and force in the x-direction, and b) coefficient of side-force, pitching moment, yawing moment, and rolling moment for different body angles through a 10L radius corner

A 10.9% increase in the lift coefficient occurred for the case where ψ = 1.43°. This was observed to occur due to a similar mechanism as that for the yawed condition, discussed in Chapter 3; reduced pressure occurred over the upper surface and backlight due to the formation of a longitudinal vortex from the upper outboard side. This change in lift coefficient was equal to that observed for a 5° constant angle of yaw, and thus highlighted an increased level of sensitivity, where the same change occurred for a much smaller angular increment. For ψ = -1.43° a smaller 1.22% increase in lift occurred relative the 0° 10L radius corner, with the value being close to that of the straight-line condition.

The side force was a significant difference with the change in the angle of the body, and this was due to the pressure gradient acting across the sides over the forebody. For the positive increase in angle this coefficient was greater than twice that for $\psi = 0°$, and for the negative increase in angle the net side force was largely mitigated, with only a small force acting in the opposite direction. Despite the loss of the side-force, the yawing moment for ψ = -1.43° was greatest at -0.053 and acted in a direction that would turn the nose outboard and damp the yawing moment of the vehicle; this was consistent with the direction identified to occur for all corner radii. The yawing moment reduced as the angle increased, demonstrating a linear trend. The moment for $\psi = 1.43°$ was 55.5% lower in comparison to the tangentially aligned cornering case.

Changes in the rolling and pitching moments were the result of flow effects over the backlight surface and sides. The rolling moment increased as the angle of the body increased in line with the change in side force. Compared to the 10L radius corner at a 0° angle, the moment increased by 109.3% for a positive 1.43° increase in angle, and decreased by 108.1% for the negative angle change. The pitching moment was affected by increased suction over the outboard side of the backlight at the increased angle of yaw. This was attributed to the upper vortex developing over the aft section of the side and increased the nose-down pitching moment by 8.5%.

5.5 Surface Effects

Surface pressure profiles were taken at y/L = 0.15 and -0.15 for each case and are shown in Fig 5.11. For the positive increase in angle ($\psi = 1.43°$), shown in Fig 5.11c), a 10.32% increase in the outboard suction peak occurred in comparison to the reference case. This increase was attributed to both a stronger C-pillar vortex in addition to the outboard upper longitudinal vortex structure over the rearward portion of the body, as is shown in Fig. 5.12a). With the cross-flow angle remaining in the negative y-direction over 75% of the total length, the rearward structure exhibited increased similarity to the constant yaw condition. While the outboard suction peak increased, the inboard experienced only a mild comparative reduction of 1.9%. For the negative angle the inboard and outboard suction peaks both increased, albeit to a smaller extent, being 2.8% and 0.8% respectively.

As the angle increased the low pressure region occurring along the upper edge of the backlight became greater while the inboard side experienced a comparatively smaller change.

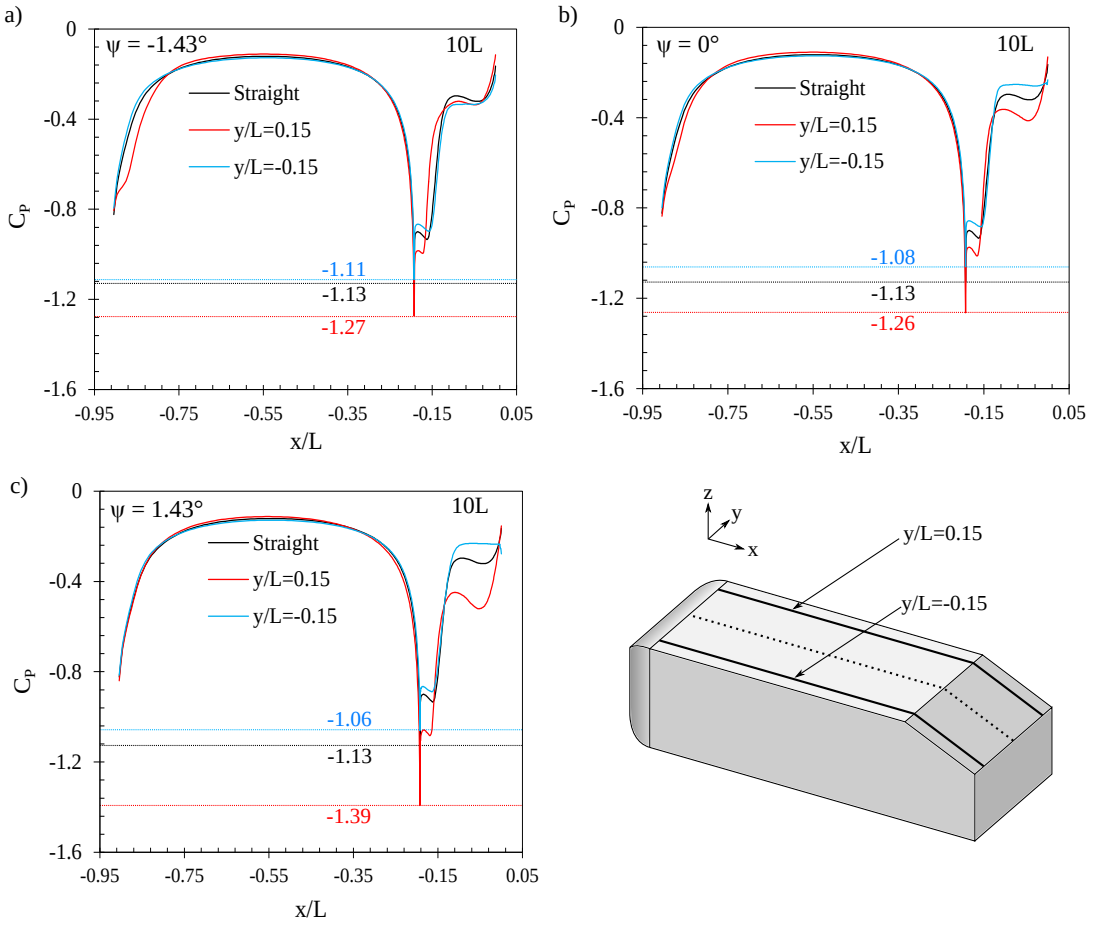

FIGURE 5.11: Pressure coefficient profiles along the upper and backlight surfaces at y/L = 0.15 and -0.15 for a 10L radius corner at a a) -1.43° angle, b) 0° angle, and c)1.43° angle

In Fig. 5.12b) the cross-flow angle was greatest over the front of the body and resulted in the forebody separation bubble being skewed by the largest amount toward the outboard side. In Fig. 5.12a) the front angle decreased while the rear angle increased, and thus the forebody separation bubble became more closely aligned to the centre of the face.

In the case of the ψ = -1.43° the outboard skew of the forebody separation bubble resulted in the emitted structures being shifted toward the outboard side, as shown in Fig. 5.12b). Their interaction resulted in the mild increase in suction peak over the outboard side, while the reduced flow angle at the rear results in a comparatively stronger inboard C-pillar vortex.

The side force and yawing moment occurred due to the variation in the pressure distribution over the sides of the body. Profiles taken along the respective sides at z/L = 0.18 are shown in Fig. 5.13 with the straight-line condition included for reference. ψ = -1.43° is shown in Fig. 5.13a) where a 7.8% increase in the magnitude of the outboard suction

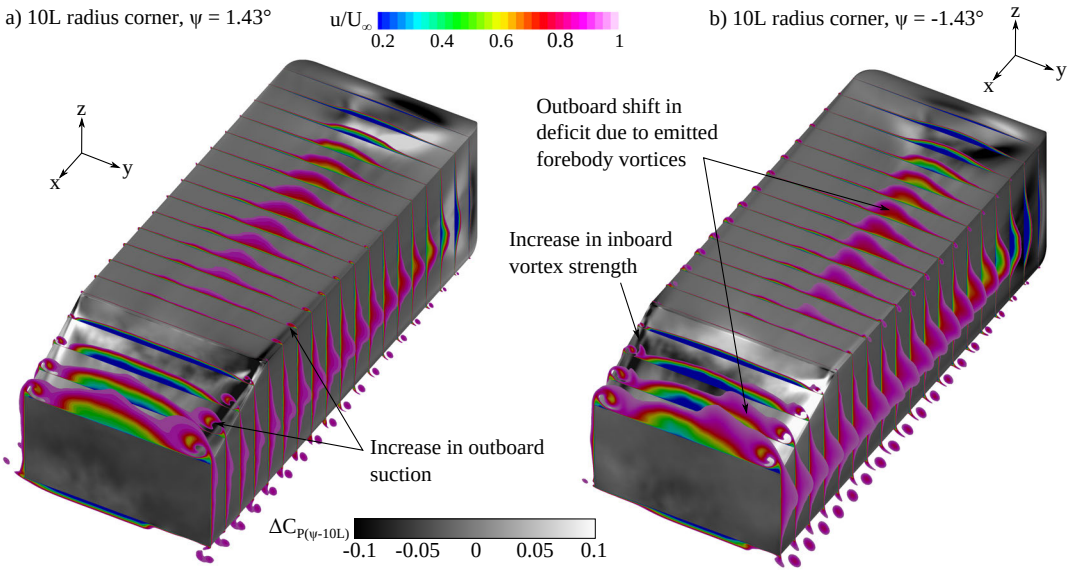

FIGURE 5.12: Clipped contours of x-velocity with surface pressure coefficient delta compared to the 10L radius, 0° yaw angle case for a a) 1.43° angle, and b) -1.43° angle

peak aft of the nose resulted due to the increase in the angle turned by the flow about this location. Similar to the cornering and yaw cases presented in Chapters 3 and 4 this was also associated with an increase in the separation length and the creation of larger vortical structures. The smaller outboard angle for the case shown in Fig. 5.13c) where $\psi = 1.43°$ resulted in a 6.6% reduction when compared to the case aligned tangentially with the flow curvature shown in Fig. 5.13b). On the inboard side the separation was further suppressed as flow angle increased, and resulted in a loss of the prominent peak occurring along that side, as it was milder and shifted forward.

Downstream of x/L $\approx$ 0.75 the acceleration of the body due to the rotating reference frame resulted in an increased surface static pressure on the outboard side, with an inboard decrease. The magnitude of this difference remained similar in all cases. This remained consistently unique to the cornering condition due to the radially orientated pressure gradient; for the yawed cases this same effect was not observed.

The consistency of the rearward pressure distribution combined with the change that occurred over the forebody explained the aerodynamic force coefficient effects. For ψ = -1.43° as shown in Fig. 5.13a) the outboard acceleration past the nose is mitigated by the milder pressure increase over the rearward section of the body and results in the loss of the side force. However, this front to rear surface pressure imbalance increased the yawing moment acting about the centre of the body. As the body angle increased in Fig. 5.13b) and c) the reduction in the forebody outboard suction peak resulted in an increase in the side force acting toward the centre of the corner. Furthermore the loss of

this suction resulted in the reduction of the imbalance in the pressure distribution and a reduction in the the moment about the centre of the body.

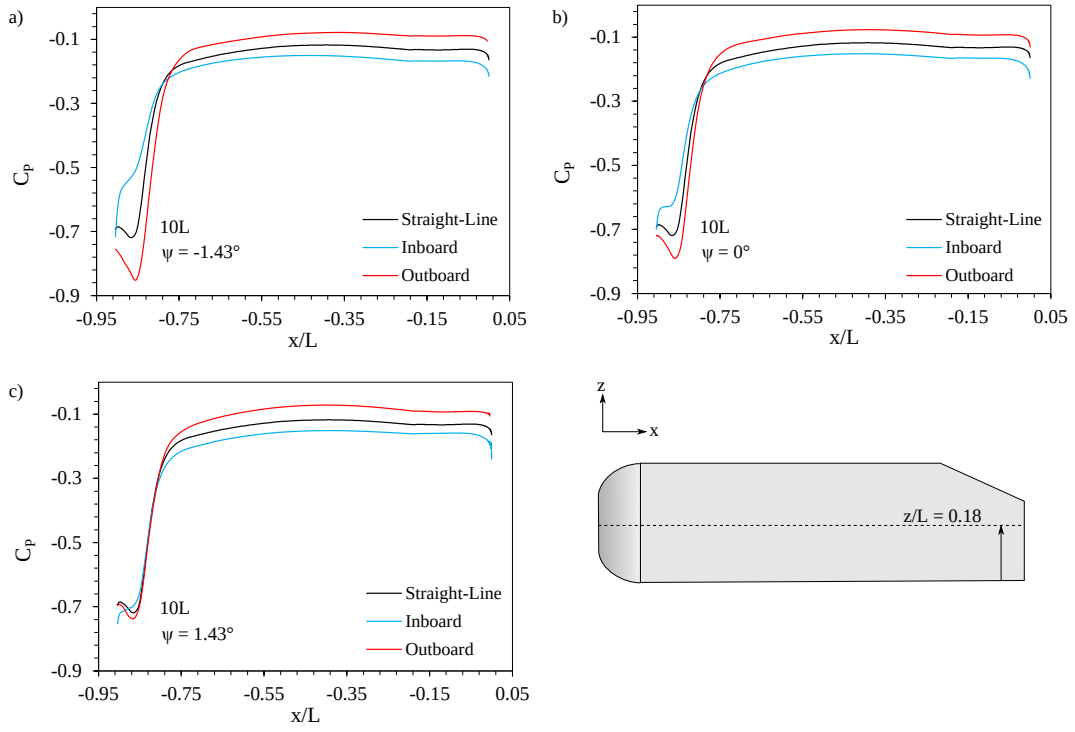

FIGURE 5.13: Pressure coefficient profile along the sides of the body at z/L = 0.18 for a 10L radius corner at a a) -1.43° angle, b) 0° angle, and c)1.43° angle

5.6 Rear Flow Structures

The most significant effect toward the primary separation bubble over the backlight was attributed to the interaction of the forebody, with the central separation length being the most significant variation, as shown in Fig. 5.14. For the ψ = -1.43° case the emitted vortical structures pass toward the outboard side and result in the greatest central extension of this region and a total 3.4% increase in the integrated area below the positive bifurcation line corresponding to the reattachment point. At ψ = 0° the discontinuity in the profile is due to these being shifted inboard and partially interacting, while the combination of the inboard propagation of the forebody vortices over the backlight and the strength of the outboard vortex result in the ψ = 1.43° case having the shortest separation length and a 2.8% reduction in the total area contained within the bifurcation.

The separation bubble which formed at the trailing face also demonstrated sensitivity to the cornering yaw angle and further affected the direction of the flow down the

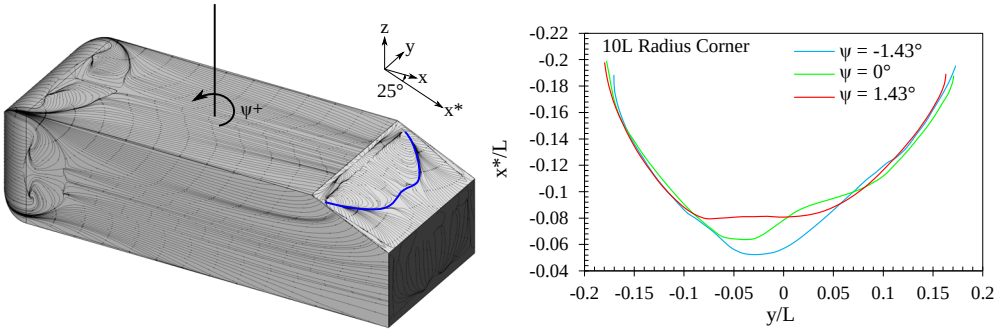

FIGURE 5.14: Primary bifurcation line corresponding to location of reattachment for the backlight separation bubble for different angles of yaw within a 10L radius corner

backlight face and the angle of the flow into the wake. At the outboard location shown in Fig. 5.15b), d), and f) the most significant change occurred toward the lower recirculation within the dual structure. At ψ = -1.43° two structures can be observed in the time-averaged flowfield, and as the angle increased these were observed to merge into one stronger recirculation.

The two separate time-averaged structures occurred due to a longitudinal extension of the lower part of the rear separation bubble. This resulted in spanwise vortex merging occurring and propagating to the second location before reaching a critical bursting point. For the increased angle shown in Fig. 5.15f) the contraction of the lower wake resulted in a single time-averaged lower recirculation whereby the roll up of the lower shear layer directly merged with the main feature.

At the inboard location shown in Fig. 5.15a), c), and e) the rear bubble was observed to contract as the angle of the flow which passed the rear of the body increased. This remained consistent with the findings for a constant yaw angle and the different corner radii. For ψ = -1.43° the separation bubble extended 6.8% further from the trailing face, while for ψ = 1.43° this was further contracted by 1.4%. With the contraction of the inboard side, the mean pressure within the recirculation reduced and resulted in the increased production of drag attributed to the lower surface pressure on the trailing face.

5.7 Longitudinal Wake Structure

The near wake structure remained asymmetrical in all instances where the outboard longitudinal vortex structure was the dominant feature, as shown in Fig. 5.16. The lateral shift of the separation bubble resulted in the emission of the hairpin-type vortical

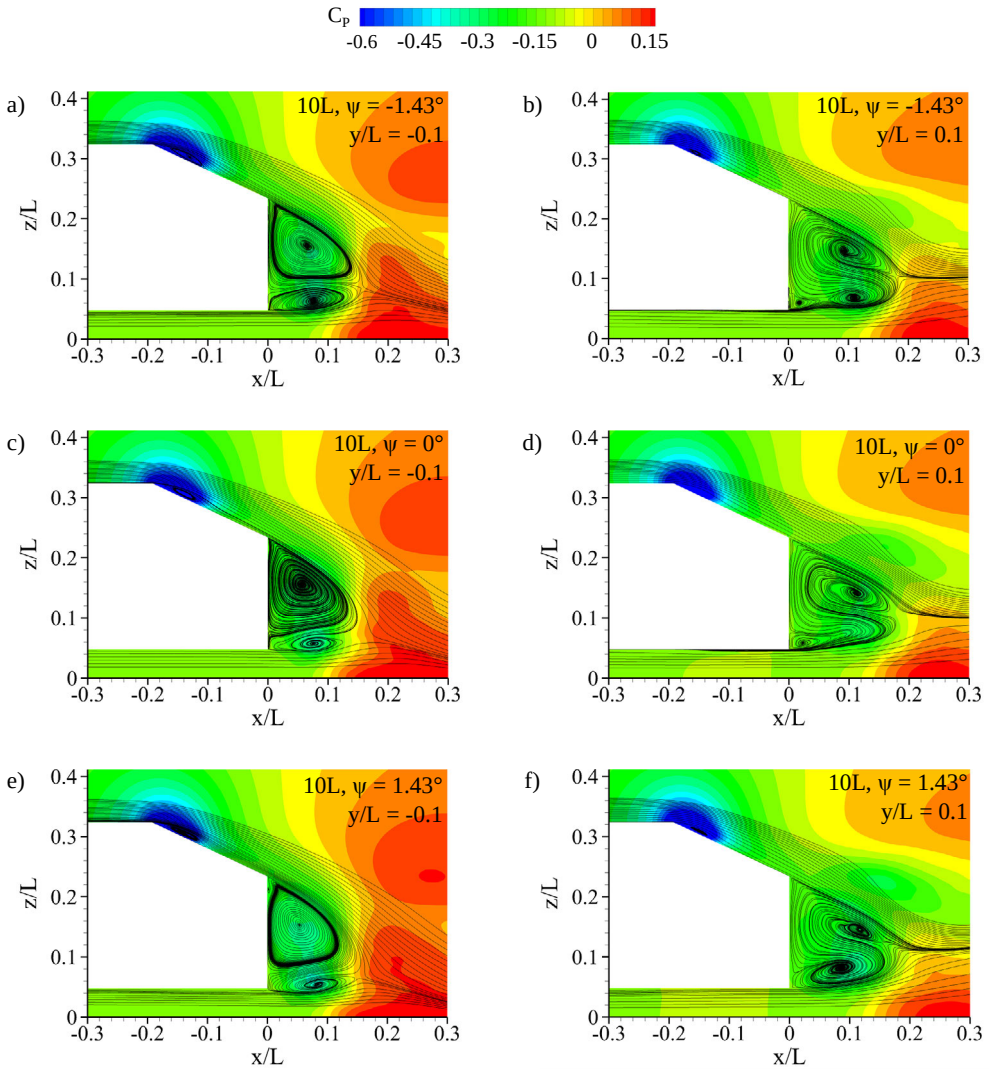

FIGURE 5.15: Pressure coefficient contours with streamlines indicating rear separated structure for a 10L radius corner at different angles of yaw

structures being shifted toward the outboard side of the wake for $\psi = -1.43°$, as shown in Fig. 5.18a). As a result these were observed to be partially drawn into the outboard C-pillar vortex

As the flow angle increased at the rear, the increased strength of the outboard C-pillar vortex drew more flow across the rear of the body and resulted in the larger outboard structure. The inboard longitudinal structure was directed progressively more downwards due to the contraction of the rear separation and resulted in a collapse of the inboard wake similar to that observed for a decrease in corner radius.

As observed on the horizontal plane at z/L = 0.18 the outboard longitudinal vortex continued further downstream within the upper part of the wake region. These wake effects remained progressive, as findings remained within a range that occurred due to a

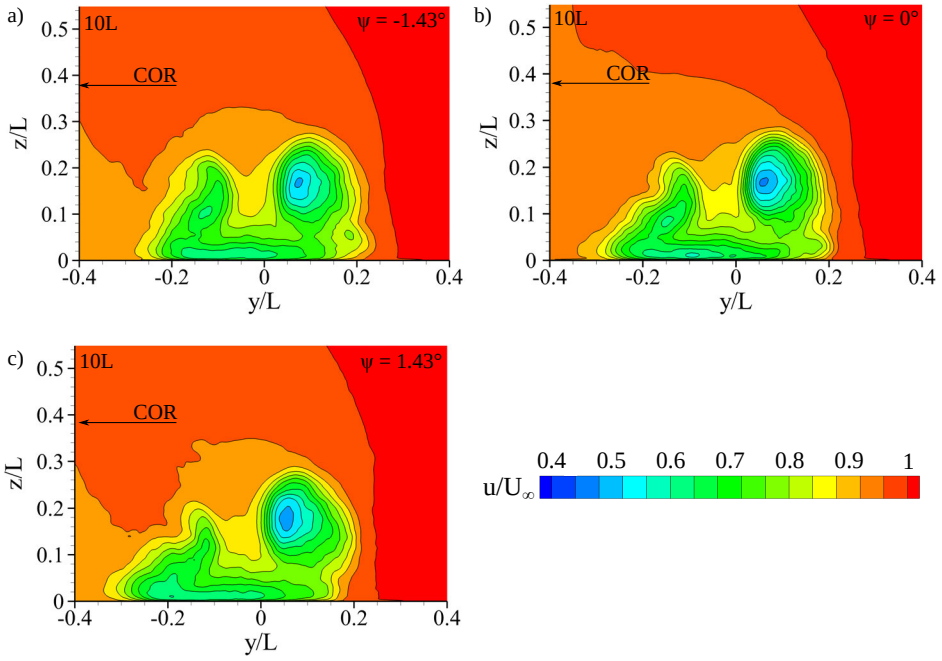

FIGURE 5.16: X-velocity contours at x/L=0.5 for a 10L radius corner at a a) -1.43° angle, b) 0° angle, and c)1.43° angle

similar change associated with an increase in yaw angle (detailed in Chapter 3), or the respective angle change associated with a decrease in corner radius shown in Chapter 4.

As the body angle increased the periodic bursting mechanism within the wake was observed to increase in magnitude and resulted in the periodic lateral expansion most notable in the inboard wake. For the yawed condition this effect was suppressed by the separation of the flow over the corresponding leeward side, and its interaction with the wake. As such, the effect was observed to be specific to the cornering condition. Comparing Fig. 5.18a) and b) the lateral expansion associated with the bursting was reduced at the decreased angle of ψ = -1.43°, and became more pronounced for ψ = 1.43°. This change was consistent with the contraction of the lower recirculation and the mean pressure reduction. With a lower core pressure the centrifugal force also increased and thus the bursting mechanism was more pronounced on the inboard side.

5.8 Summary

The yawed and cornering conditions were identified to result in significantly different aerodynamic effects for the Ahmed body at a 25° backlight angle. A direct comparison based on force and moment coefficient magnitudes further emphasised the dissimilarity of the two conditions. The yawing moment and lift coefficient exhibited directly opposing

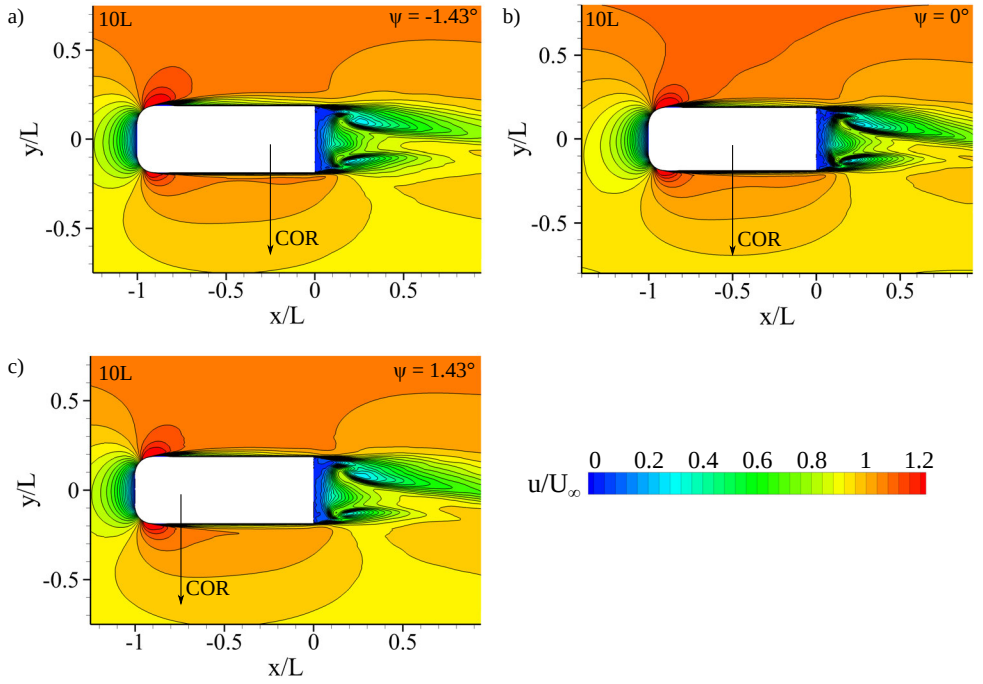

FIGURE 5.17: X-velocity contours at z/L = 0.18 for a 10L radius corner at a a) -1.43° angle, b) 0° angle, and c)1.43° angle

trends, with all parameters demonstrating variation in their equivalent rates of change. Comparison of the 5° yaw angle and 5L radius corner identified the longitudinal vortices to be the key flow features to cause the difference between the two conditions, and resulted in a surface pressure distribution that became increasingly differentiated toward the rear. Ultimately, the inherent difference in angle at different locations along the body, in addition to the acceleration within the rotating reference frame, resulted in cumulative effects that made the yawed and cornering conditions fundamentally different.

Investigation into yaw sensitivity within the cornering condition identified a heightened degree of variability when compared to an increase in yaw angle within the straight-line condition. The pressure gradient across the sides, which was attributed to the acceleration within the reference frame, remained constant, however most local effects reflected the different flow angle from front to rear and the respective change within each condition. Both an increase and decrease in the relative angle of yaw resulted in an higher coefficient of drag, and of the force in the x-direction. As the yaw angle increased the rearward flow structures demonstrated more similarity with the straight-line yawed condition due to the formation of longitudinal vortices along the edges. For the positive angular increase of 1.43° a 10.9% greater lift coefficient occurred in comparison to the condition aligned tangentially. This value coincidentally was equal to the difference observed between the 5° yaw angle and the straight-line condition, but occurred for

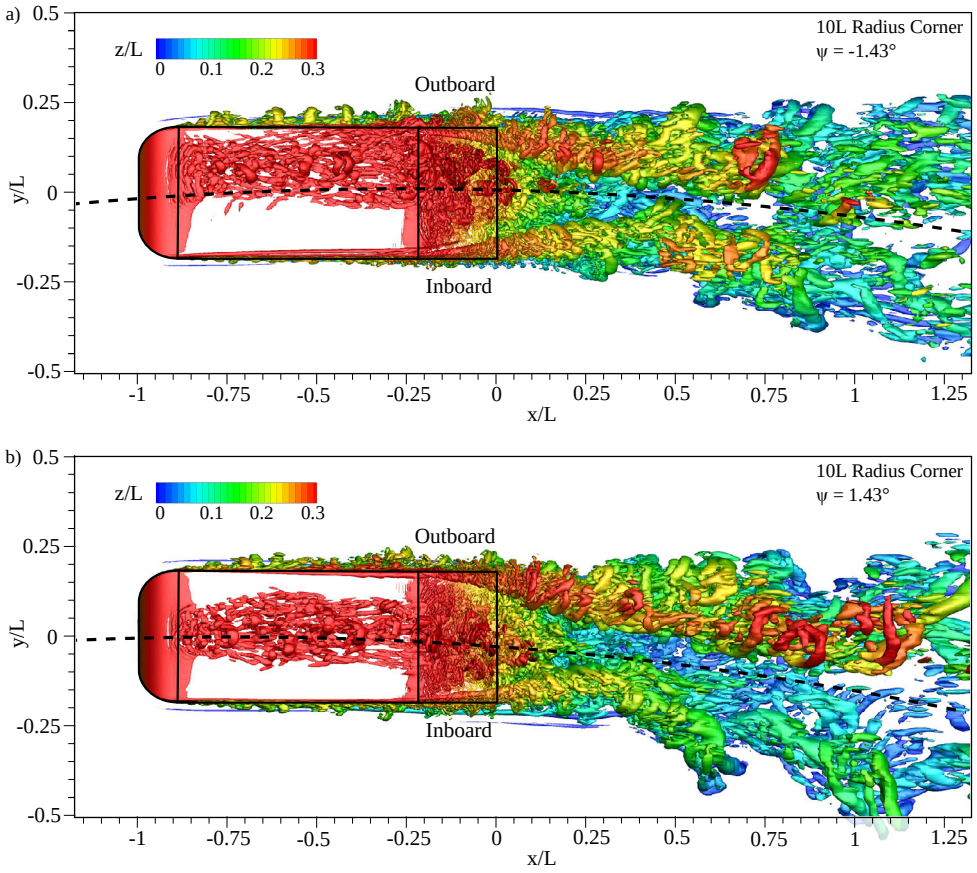

FIGURE 5.18: $Q = 3 \times 10^4$ coloured according to z/L for a 10L radius corner with a a) negative change in yaw angle, and b) positive change in yaw angle

a far smaller angular increment. While only a 0.5% reduction occurred in the other direction.

For practical development of a specific vehicle this highlights the importance of using the dynamic characteristics to inform any analysis within this condition. The cumulative changes which occurred over the body were demonstrated to differ significantly dependent on the yaw angle while travelling in a curved path.

Chapter 6

An Experimental Method for Continuous Curved Flow

Attempts to experimentally recreate the cornering condition have not, to date, detailed a successful method capable of recreating all aspects [6, 25, 26, 29, 31, 32]. As was discussed in Chapter 1, induced curvature of the flow within an inertial reference frame results in the flow itself undergoing acceleration, where a static pressure gradient will occur to balance this effect. Only by creating an experimental method which places the model in a rotating non-inertial reference frame can the correct conditions be replicated.

A proof-of-concept of a new design was constructed in order to establish the viability of developing such an experimental rig. The concept was developed with the aid of CFD simulation, and this data was used to supplement experimental results and aid in visual representation of the aerodynamic function achieved by each component. As with any wind tunnel, correct flow conditions within the test-section was ultimately the most critical outcome. Thus both investigation and analysis primarily focussed on the flow conditions achieved within this region.

The open-circuit design consisted of both a stator and rotor component, distinguished in Fig. 6.1. A bellmouth, axial fan, and straight cylindrical tunnel section were positioned on a stationary external frame with a span that exceeded the swept region of the rotor. The rotor component consisted of a variably profiled tunnel section which delivered flow to a turning vane cascade. This turned the flow into the horizontal plane to then pass through a diffuser and contraction prior to reaching the test-section. A constant radius test-section continued to an open outlet positioned at the exit.

The proof-of-concept sought to achieve a mean 750 mm radius corner and utilised an octagonal cross section with maximum test-section dimensions of 250×336 mm. As

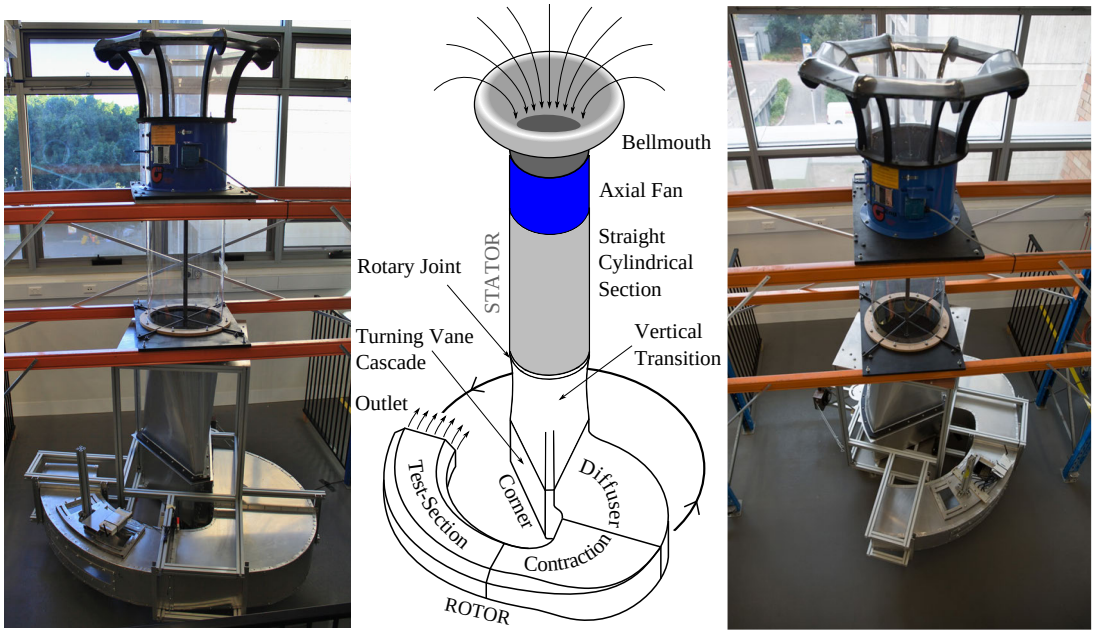

FIGURE 6.1: Photographs and diagram of wind tunnel indicating key aerodynamic components

designed, the experiment is mechanically capable of achieving an angular velocity of 13.3 rad/s which corresponds to a mean tangential velocity of 10 m/s in the test section. Dimensions are normalised according to the height of the test-section (H), and the mean test section velocity ($U_{\infty,m}$).

6.1 Concept

Dependent on any wind tunnel's alignment with respect to the Earth's axis of rotation, the flow would wish to naturally follow a very slight curvature, so slight it would be completely immeasurable. This occurs due to the Coriolis Effect [125] which dictates that any object in motion within a non-inertial reference frame will naturally deflect in a direction which is dependent on one's location within that reference frame. This effect is obviously so small that it can be completely neglected in the construction of a regular wind tunnel. The present design differs in that the test-section is positioned within a rotating non-inertial reference frame to enhance this effect.

To explain the basic principle behind the design it becomes simpler to regard an isolated particle. If a single fluid particle travelling at a constant velocity enters a rotating reference frame at the centre of rotation (and we change our frame of reference with the particle), the initial velocity of the particle will remain unchanged – despite the change in reference frame. Within a rotating reference frame the relative dynamic pressure

(q_{rel}) will increase proportional to:

$$q_{rel} = \frac{1}{2}\rho(\omega R)^2 \tag{6.1}$$

As the displacement of the particle from the centre increases, its relative velocity, and relative dynamic and total pressure (within the rotating reference frame) will increase according to Eqn. 6.1. If left unimpeded the particle will assume a spiralling outwards path due to its acceleration within this frame. An anti-clockwise rotation causes the particle to be observed to deflect to the right within the rotating reference frame as shown in Fig. 6.2. Noting the equal time increments labelled 1 to 5, it can be observed that the distance travelled in each interval will increase as the particle travels further from the centre. If one was to remain in the absolute reference frame the particle is simply following the normal straight path outwards from the centre, and its initial velocity would remain unchanged — it is only due to the acceleration of the reference frame that this relative acceleration is observed.

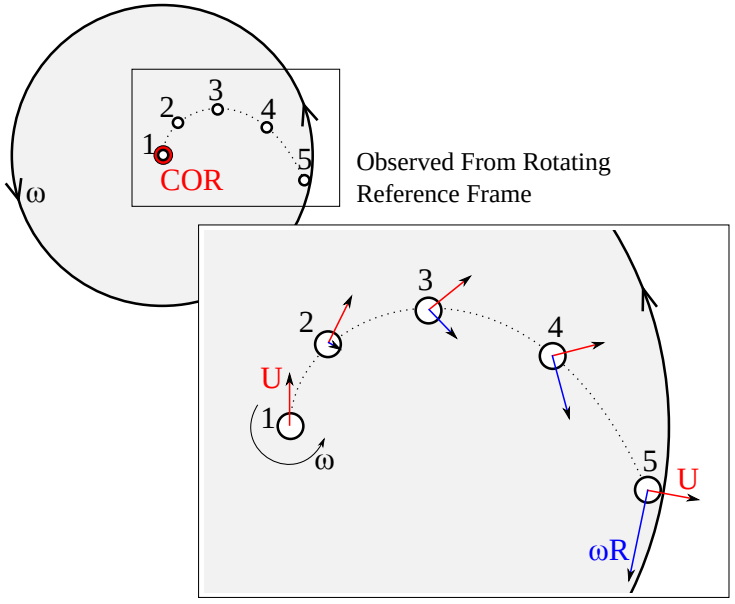

FIGURE 6.2: The motion of a fluid particle entering at the centre of a rotating reference frame, with a constant velocity defined in the absolute reference frame

If the same event was to occur again but this time the particle is decelerated as its radial displacement increases, its path would change. In the absolute reference frame as the velocity reaches zero, one observes the particle stopping at a finite distance. Within the rotating reference frame there would be an increasing ωR velocity component due to radial displacement, but at the same time the initial velocity component U would reducing to zero. At time interval 5, shown in Fig. 6.3, the unimpeded particle would follow a constant radius arc, maintaining a constant radial displacement from the centre

of rotation. Once the radius of the particle's path is fixed, the relative total pressure ceases to increase along a streamline. Assuming a Bernoulli relation static pressure will remain constant given the constant absolute velocity and thus absence of acceleration.

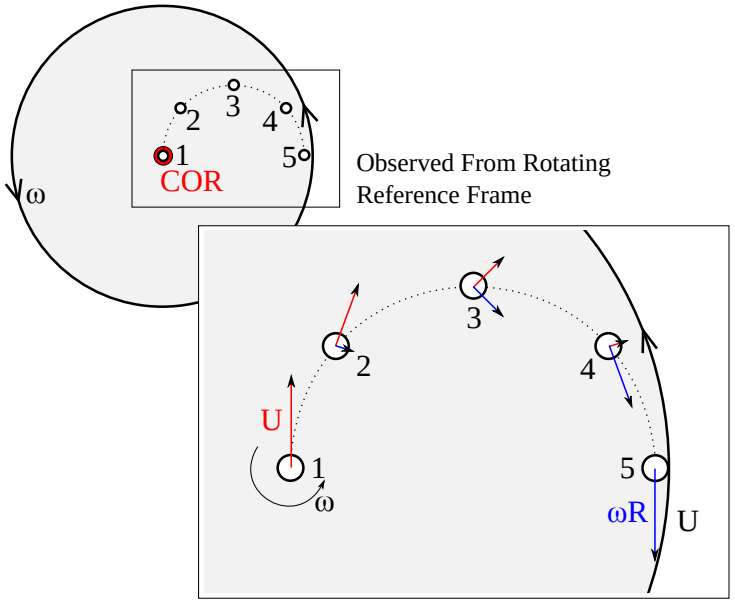

FIGURE 6.3: The motion of a fluid particle entering at the centre of a rotating reference frame and decelerating to zero while increasing radial displacement

The logical extension then becomes if volume of air can be affected in the same manner — such that it is decelerated to a zero absolute velocity at a given radial position. Assuming the volume had radial width this would result in the relative dynamic pressure (and hence a relative velocity increase) across the volume, while static pressure remained constant. In simple terms this method would create a volume of stationary flow for the object being aerodynamically evaluated to pass through, and in this way it would be an exact replication of what occurs in reality but created within a controlled system.

The same concept of passing the model through stationary air was used before the first wind tunnel was constructed, through the use of the whirling arm [126] which was discussed in Chapter 1. The design continuously spun a model in a circular path through the air, however, this meant the model was continuously travelling through its own wake, and prior investigations have detailed unsuccessful attempts to overcome this limitation [31, 32]. The new experimental design permits the same flow conditions to be achieved irrespective of the number of rotations undergone by the wind tunnel model.

Furthermore, acceleration and deceleration of flow is already an almost universal feature on wind tunnels. The challenge was developing a way that could combine these elements into a design that enabled the correct flow condition to be sustained. Such a method

would then offer potential for detailed investigation of a wide variety of flow phenomena, as well as development within the cornering flow conditions.

6.2 Computational Analysis

The achievement of the correct flowfield was dependent on being able to maintain attached flow with low viscous losses. CFD was utilised for design iterations of the proof-of-concept to ensure these conditions were achieved, and also permitted informative flow visualisation. The method allowed considerable efficiency gains in comparison to the physical construction of multiple different tunnel sections when assessing different parameters. The final design became a compromise between indicated flow quality from the computational analysis and manufacturability.

The volume of simulations necessitated an approach which allowed results to be obtained with a short time-frame. Reynolds Averaged Navier Stokes (RANS) simulations were favoured over the LES method adopted in the previous Chapters. The k-ω SST turbulence model [82] was used with a low-Re wall adaption which was suitable given the considered Reynolds numbers [98]. Partial simulations were also intermittently used, considering only components downstream of the turning vanes, and permitted further reduction in computational expense.

An overview of the boundary conditions of the model is shown in Fig. 6.4 with a detailed view of the unstructured computational grid. The inlet was modelled at the location of the fan with a constant velocity of 2.22 m/s which corresponded to a test-section Reynolds number of 7.85×10^5, based on test-section height. The inlet and downstream straight cylindrical tunnel section were modelled as a separate volume zone with a stationary reference frame and non-slip walls.

Lower tunnel sections were modelled as a rotating reference frame with a constant angular velocity of 6.28 rad/s. Honeycomb screens positioned at both the start and end of the transition were modelled as a zero planar velocity porous regions. All lower internal walls were modelled as non-slip boundaries, while the outlet was specified as a zero static pressure outlet. This outlet simplification did not account for external disturbances created by the tunnel due to its motion through the surrounding air. Initial isolated simulations of the outlet with an external disturbance indicated that the length of the test section ensured external effects would likely only have a small impact on the flow quality, however it is acknowledged that the outlet condition was not accurately representative of reality.

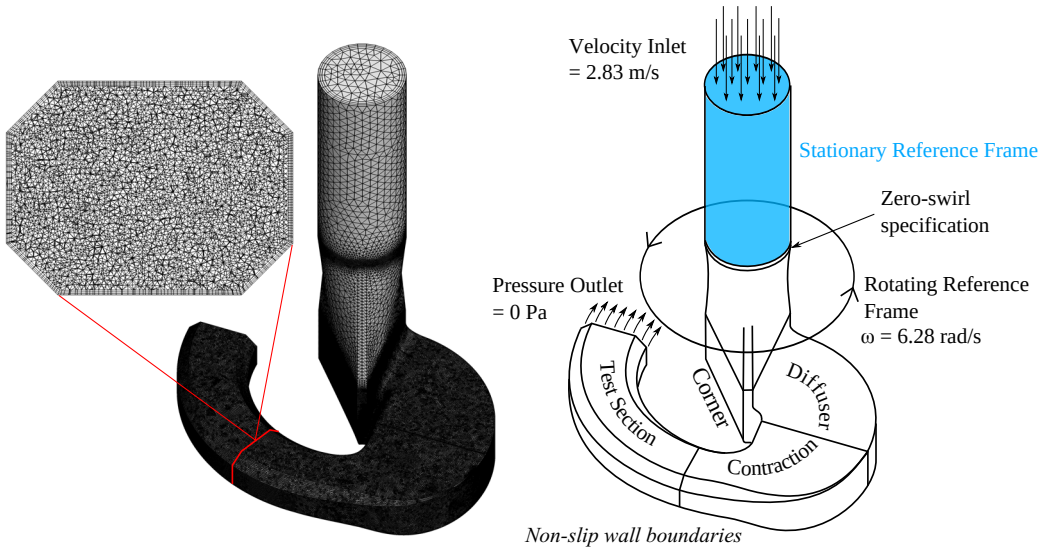

FIGURE 6.4: Detail of the grid and overview of the boundary conditions used in the numerical model

A pressure-based implicit coupled solver was utilized to achieve steady-state simulations. Compressibility effects at the simulated Mach numbers were deemed negligible and permitted the assumption of incompressible flow. Simulations were run using a second-order node-based upwinding discretization scheme across 64 processors. Three point velocity monitors were placed downstream of the trailing edge of the centre turning vane, at the start of the contraction nozzle, and at the test-section entrance. Convergence was deemed to be met when velocity values ceased to change by more than 0.005% over 1000 continued iterations, and this was achieved after 9000 iterations.

The geometric complexity of the corner region due to the presence of the turning vanes, and the necessity of using an efficient meshing procedure that could adapt to design changes, favoured the adoption of an unstructured tetrahedral meshing procedure, as is shown in Fig. 6.4. Cells were focussed in the region of the turning vanes, the contraction nozzle, and the test section — with these regions identified as most critical to the overall performance. Different grid densities were evaluated at several stages throughout development due to the large variations in geometric configurations, with mesh sizes ranging from 3.9×10^6 to 3.0×10^7. The grid adopted for the constructed concept consisted of 1.8×10^7 cells and was used for all full tunnel simulation results that are referred to.

6.3 Final Design Configuration

6.3.1 Axial Fan

As the angular velocity of the rotor increased, the flow velocity was required to increase to ensure flow within the test section remained correctly calibrated as stationary in the absolute reference frame. In the absence of any losses throughout the circuit, the rotation of the lower tunnel section would be theoretically sufficient to induce the correct relative dynamic pressure required, however, in reality the system losses required the energy input of a fan.

An axial fan was positioned at the inlet and directed air downwards. As the fan was upstream of the test section the tunnel assumed a blowing-type configuration. The position of the fan was critical and influenced the overall design of the tunnel. If the fan were to be positioned at any location where the whole fan assembly was rotating at a distance from the central axis this would compromise the quality of the inlet flow to the fan, and would increase the rotating mass. Positioning the fan in the centre allowed the component to be static which ensured it operated in a steady flow environment.

A 450 mm (1.8H) diameter aerofoil profiled fan was selected, driven by a 0.75 kW AC electric motor with the fan speed controlled by a variable frequency drive. This specification gave a fan to test-section area ratio of 2.12. The inlet to the axial fan was smoothed with the use of an elliptically profiled bellmouth with an upstream safety screen to prevent the entry of any foreign objects. Downstream of the fan the flow passed along a straight tunnel section 3.1H in length until reaching the rotary joint at the intersection of the stator and rotor components.

6.3.2 Rotary Joint

A simple overlapped circular joint with a felt seal connected the stator section to the rotor. A central shaft was positioned between the two components which stabilised any effects due to rotor imbalance, and ensured accurate alignment between the two components. The shaft was supported within the stator section, and ended at the rotary joint, sitting in a plain bearing connected by four slender arms to the rotor, as is shown in Fig. 6.5.

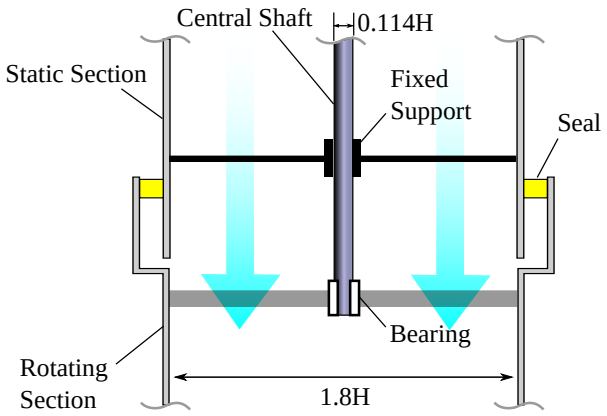

FIGURE 6.5: Diagram of the rotary joint and central shaft configuration

6.3.3 Vertical Transition

As discussed in previous sections, the desired relative velocity distribution was proportional to ωR, where R was the distance from the centre of rotation. As ω remained constant, the relative outer mass flux was required to exceed the inner. Therefore the correct proportional volumetric flow distribution needed to be achieved prior to entry into the horizontal plane.

To achieve this a vertical tunnel section was used to transition from a circular cross-sectional shape to a circular segment, as is illustrated in Fig. 6.6. The circular segment subtended 38.2° and had an inner radius of 0.3H and an outer radius of 2.7H. The tunnel section maintained a near-constant cross-sectional area along its length and honeycomb flow straightening screens were placed at both the inlet and outlet of the section. The inclusion of these screens was intended to induce swirl in the flow which matched to the angular velocity of the rotor and to aid in the prevention of vortex formation. The screens had a 3.2 mm nominal aperture and were 25 mm in thickness, made from 0.3 mm aluminium.

6.3.4 Corner and Turning Vanes

The flow was required to turn through a 90 degree bend into the horizontal plane, and also assume a curved path into the diffuser. A seven vane cascade was used with a profile that was developed from the turning vane design proposed by Gelder [127] — which has been used in a number of established wind tunnels.

The final vanes were variable profile which was used to achieve the correct velocity distribution upon entry to the diffuser section. A necessity for the variable profile was

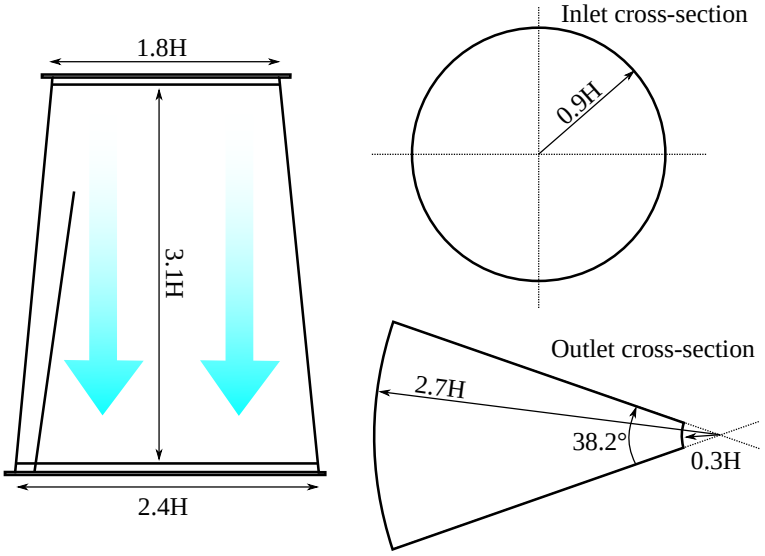

FIGURE 6.6: Dimensions and cross-sectional shape change in the vertical transition section

that they were required to achieve the correct expansion/contraction ratio from the inner to outer side and accommodate the perceived flow direction due to the curvature in the vertical axis. The difference between the inner and outer profile is shown in Fig. 6.7.

The turning vane spacing and the design of the inner profile was such that the flow was expanded to cause a deceleration relative to the mean velocity at the inner side. On this side an additional splitter vane with a span of 0.64H was used to prevent separation over the suction surface of the turning vane — more elegant future solutions are discussed in Section 6.7. On the outboard side the opposite effect caused local flow acceleration, as is shown in Fig. 6.8. The inner half of turning vane cascade thus functioned as an expanding corner (a feature occasionally used on wind tunnels to reduce circuit length [128]) while the outer half was a contracting corner, with the ratio varying linearly along the span. The final configuration of the vanes is shown in Fig. 6.8. A vertical spacing of 0.125H corresponded to a mean gap-to-chord ratio of 0.25, with an angular spacing of 4.8°.

A difficulty which affected all components in the rotor section was the occurrence of non-uniform pressure losses due to the local Reynolds number variation. A 30% larger chord at the outboard side was necessary to ensure adequate support of across the cascade, but resulted in proportionally higher outboard losses due to chord length, and a locally increased Reynolds number. Attempts to increase chord length at the inboard location were restricted due to protrusion into downstream sections.

To turn the flow in the vertical axis, curved vertical vanes were positioned across the span of the section, as shown in Fig. 6.7. These were positioned at the intervals shown

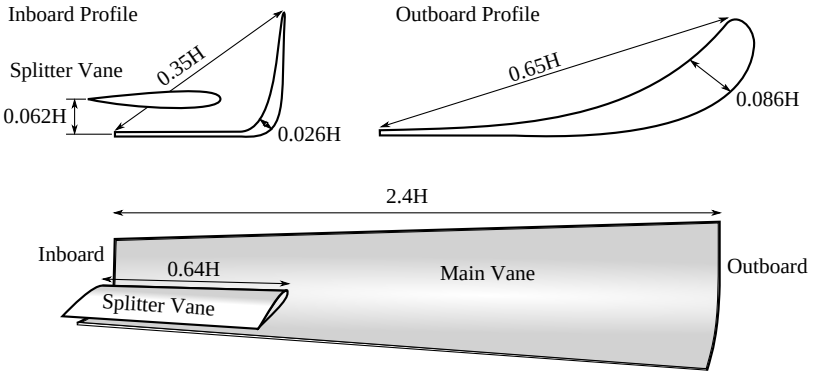

FIGURE 6.7: Cross-sectional profile of turning vanes and dimensional details

and prevented any flow separation occurring on the inner wall of the diffuser. Due to their curvature the vanes also had a suction and pressure side, which were the outer and inner sides respectively. In the same way that minor adjustments in the trailing edge positions of the horizontally aligned vanes could be used to correct any vertical flow inconsistency, adjustments in trailing edge position of the vertical vanes was also able to be used to correct the horizontal velocity distribution within the test-section.

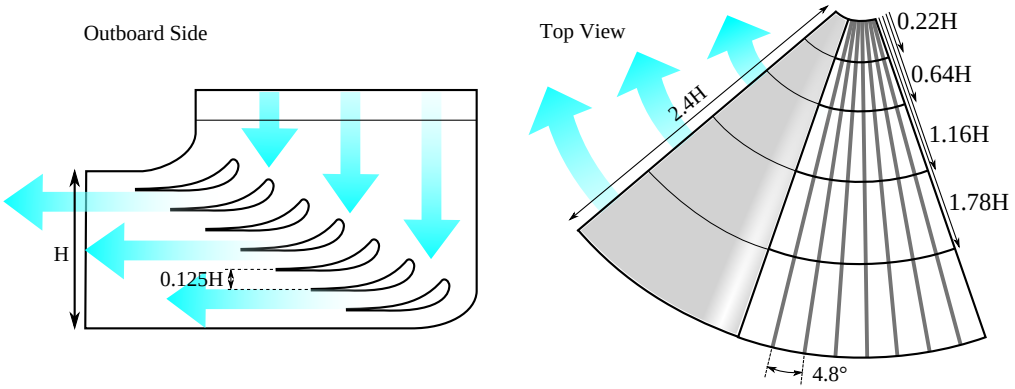

FIGURE 6.8: Turning vane configuration

6.3.5 Diffuser

Once entering the plane normal to the axis of rotation, it became necessary to understand the effects described in Section 6.1. While visually not resembling a diffuser, this section performs the same function within a rotating reference frame due to a deceleration of the flow within the absolute reference frame and a static pressure rise. CFD results taken from a partial simulations show this effect most clearly, as shown in Fig. 6.9. It can be observed that relative velocity remained constant while the absolute velocity was reduced, and resulted in an increase in the static pressure coefficient.

A 2.4×1H constant cross-sectional area was maintained with an expansion angle of 0.44° along the outboard side to allow for boundary layer growth, with the inner boundary layer growth deemed negligible. The mean radius of the circular arc followed by the section was 1.5H.

Furthermore the static pressure profile across the span can be observed to reverse in direction along the section. As the flow enters the diffuser section a reduced outer static pressure in comparison to the inner is due to the relative acceleration and deceleration of the flow. The perceived section curvature within the absolute reference frame is in the opposite direction to the physical curvature of the walls, and this occurs due to the angular velocity of the system exceeding the angular velocity along this section (about R = 0). This reversal in the curvature ultimately results in the outer static pressure exceeding the inner.

6.3.6 Contraction

A contraction nozzle was used to accelerate the flow in the relative reference frame into the test section. In the absolute reference frame the flow was accelerated to zero. This effect is shown in the CFD results in Fig. 6.10.

The contraction wall curvature was optimised through CFD analysis, as is shown in Fig. 6.10. A two-dimensional nozzle was used which retained a constant height where initial iterations of the wall curvatures were based on a matched cubics profile [129].

The distorted shape of the nozzle resulted in complications due to the inner side being comparatively only 33.6% the length of the outer profile (in the final design). Numerical simulation results indicated a tendency for separation to occur at the start of the inner side due to the steep pressure gradient. Smoothing the inside profile to a more gentle curvature aided in maintaining attached flow. Typically a shorter contraction would be desirable for flow quality in the test section due to the development of a thinner boundary layer [24], however due to the differing lengths of the two sides of the nozzle, the inner side determined the required nozzle length, and resulted an outer profile which would be longer than necessary under typical circumstances.

A secondary issue identified in numerical analyses was the formation of vortices within the contraction nozzle. Due to the non-uniformity of the flow across the nozzle these were predicted to form asymmetrically and create a secondary recirculation across upper and lower surfaces. These were able to be suppressed with the development of corner chamfers along the nozzle and resulted in a partially octagonal profile for the test section.

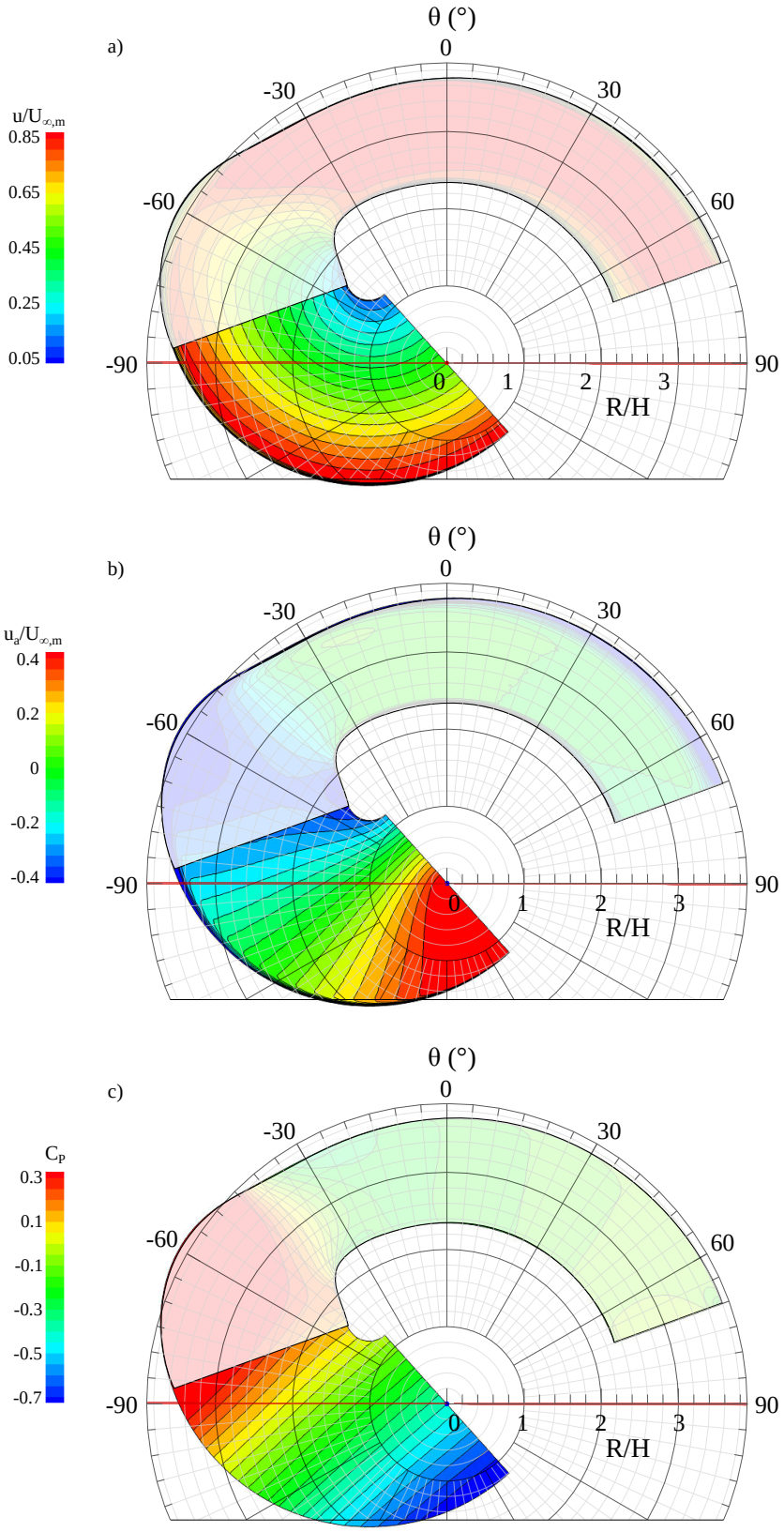

FIGURE 6.9: Computational analysis results of diffuser section indicatig a) relative velocity distribution, b) absolute radial velocity distribution, and c) static pressure distribution

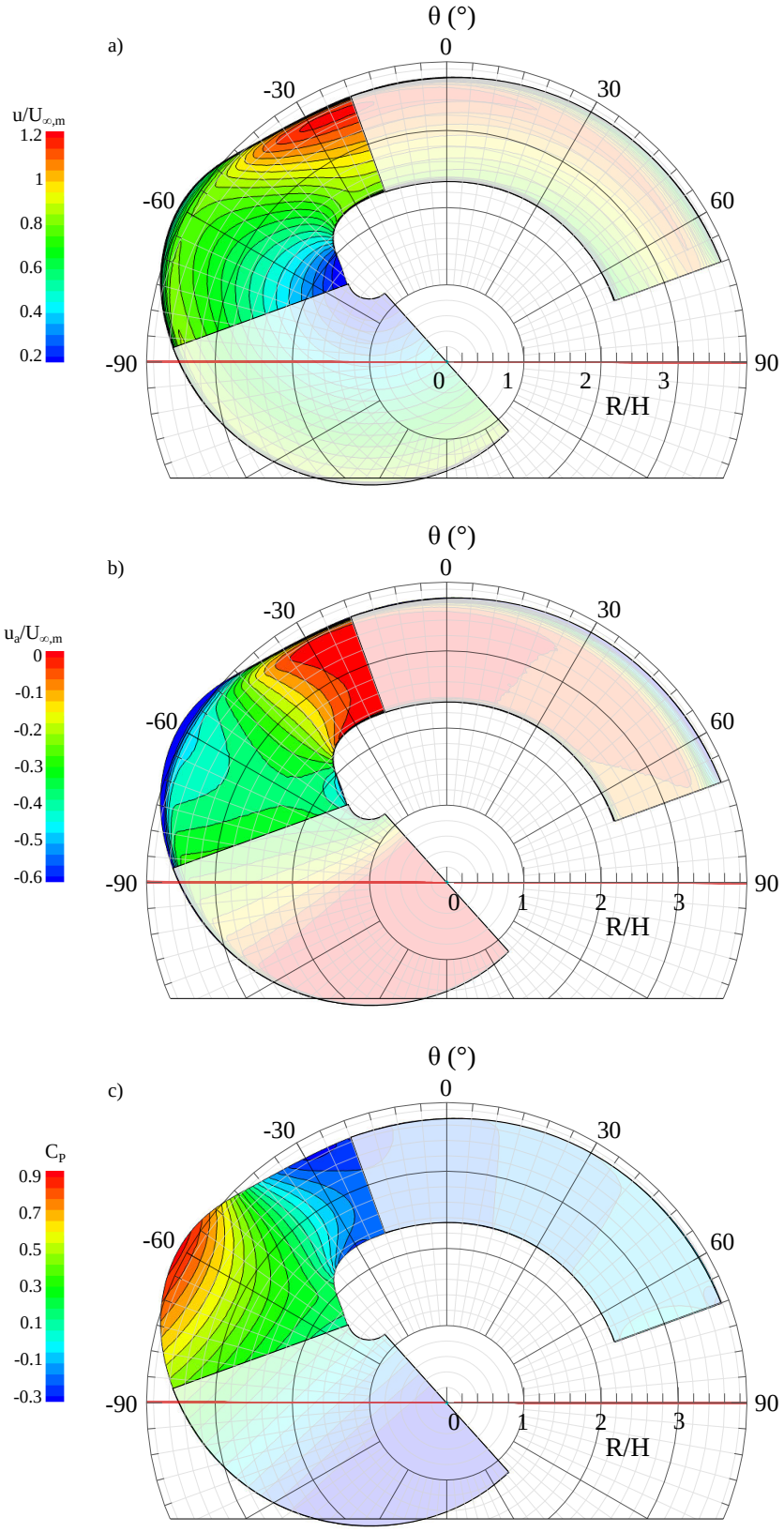

FIGURE 6.10: Computational analysis of contraction section indicating a) relative velocity distribution, b) absolute radial velocity distribution, and c) static pressure distribution

The final design was a contraction ratio of 2:1, and thus did not offer a significant turbulence intensity reduction within the test section. Higher contraction ratios were investigated but resulted in packaging issues (given the present configuration) and demonstrated a greater propensity for flow separation on the inner side.

6.3.7 Test Section

The test section utilized an octagonal profile with chamfers that were a continuation of the profile at the contraction exit, shown in Fig. 6.11. 1.34×1H dimensions with the chamfers gave a cross sectional area of 1.2H^2. A mean radius of 3H was maintained along the section as the flow followed a continuous circular arc. The width of the section resulted in the inner wall assuming a radius of 2.33H, with the outer at 3.67H. Due to the tangential velocity distribution this resulted in an anticipated 0.36 $\text{u}/\text{U}_{\infty,m}$ increase from the inner to outer wall, with an inner curvature of 0.43H^{-1}, and an outer curvature of 0.27H^{-1}.

The arc length of the mean radius was 4.71H which gave a mean test-section length of the same value. This is longer than typical designs, with respect to the cross-sectional area, and the additional length was intended to minimise any disturbances within the test-section due to the outlet being positioned immediately downstream.

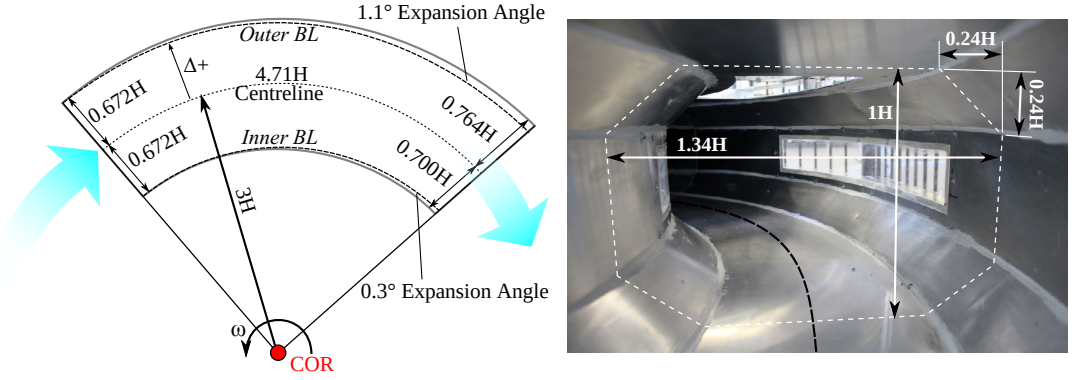

FIGURE 6.11: Test section dimensions with expansion angle to accommodate boundary layer growth, with photo of internal geometry

Numerical simulation results, as shown in Fig. 6.12, indicated the correct radial variation in the relative tangential velocity distribution, with a linear increase in this parameter from the inner to outer wall. This distribution was observed to remain consistent along the length of the section, but was subject to the influence of boundary layer growth.

A mild static pressure gradient was predicted from the inner to outer side and was attributed to two effects. The first was that the boundary layer was subject to a centrifugal acceleration due to its rotation with the tunnel, which caused a static pressure gradient at the surface — similar to the mechanism described in Chapter 4. Secondly, an inherent characteristic of the design is that any increase or decrease in flow velocity, with respect to zero in the absolute frame, will result in the initiation of a pressure gradient associated with flow curvature in the absolute reference frame. If the flow velocity is higher than the product of the angular velocity and radius, then a static pressure gradient occurs which increases towards the outer side, while the opposite occurs for a decelerated flowfield. Maintaining an accurate test-section velocity and pressure distribution thus becomes dependent on correctly accommodating the boundary layer growth in the shape of the walls.

The increased length of the outer side meant non-uniform boundary layer growth on the inner and outer sides, as shown in Fig. 6.12. Downstream of the contraction this layer continued to increase and was predicted as thickest on the vertical outer wall. Based on this initial estimate the outer side expanded at a 1.1°, while the inner at 0.3°, as is shown in Fig. 6.11. Experimental results indicated that this was an over-estimate and a more conservative expansion angle would have been ideal, highlighting one limitation of the numerical model toward prediction of physical experimental characteristics.

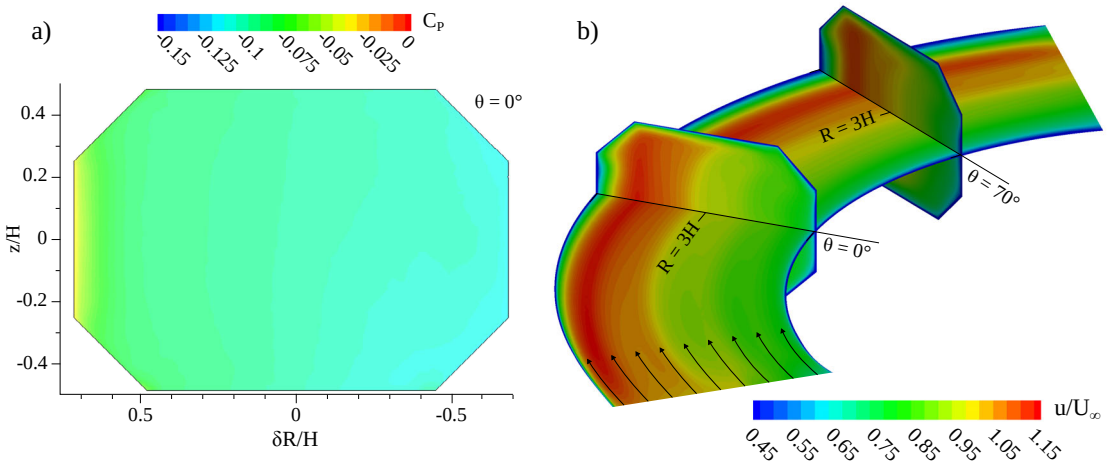

FIGURE 6.12: a) Test section static pressure distribution at $\theta = 0°$ and b) relative tangential velocity contours along z/H = 0 and $\theta = 0°$ and 70° from computational analysis

6.3.8 Outlet

When correctly calibrated the air in the test section is stationary in the absolute reference frame, and thus stationary relative to the external environment. Positioning the outlet

at the end of the test section meant the tunnel was filling it's own wake, returning stationary air to the surrounding room. However, in reality the motion of the experiment itself resulted in additional effects, as discussed in Section 6.6.

With the complete circulation of the rotor the flow was deflected radially outwards. Once exiting the test-section the flow would spiral outwards as observed in the rotating reference frame. Return circuit designs, that overcome the problems caused by the outlet position, are possible but were not pursued at this stage, due to unnecessary additional complexity for the proof-of-concept.

6.3.9 Construction Considerations

Hypothetically the entire tunnel could be rotated to achieve the same flow conditions. However, a practical consideration for the design was to reduce the rotor mass, and hence the fan and the straight tunnel section were fixed to a stationary frame positioned above the rotor component. A further function of the stationary frame was to stabilise the rotor using the central shaft.

All rotor tunnel sections were constructed from sheet aluminium. The curvature provided additional stiffness which allowed the predominant use of thin sheet (¡1.6 mm) even for large sections. The straight cylindrical section was constructed from perspex while the bellmouth was utilised clear vinyl stretched over a wooden frame. Perspex windows were manufactured above the test section and also along the inner and outer walls to allow both physical and optical access. Mounting points for instrumentation were also included above the test section.

A three-phase 1.5 kW AC motor and gearbox were used to drive the rotor as shown in Fig. 6.13, where the speed was controlled through the use of a variable frequency drive. The motor and gearbox were attached to a base-plate that was bolted directly to the ground, with a bearing housing to support the rotor fastened to the upper face of the gearbox.

The rotor was statically balanced prior to operation. To achieve this the entire rotor was aligned horizontally and supported using a central shaft. A balancing arm was positioned directly opposite the determined centre of imbalance and additional mass was then attached to the arm until the rotor component spun freely. This method proved effective within the given context and was sufficient to result in negligible vibration of the experimental rig during operation.

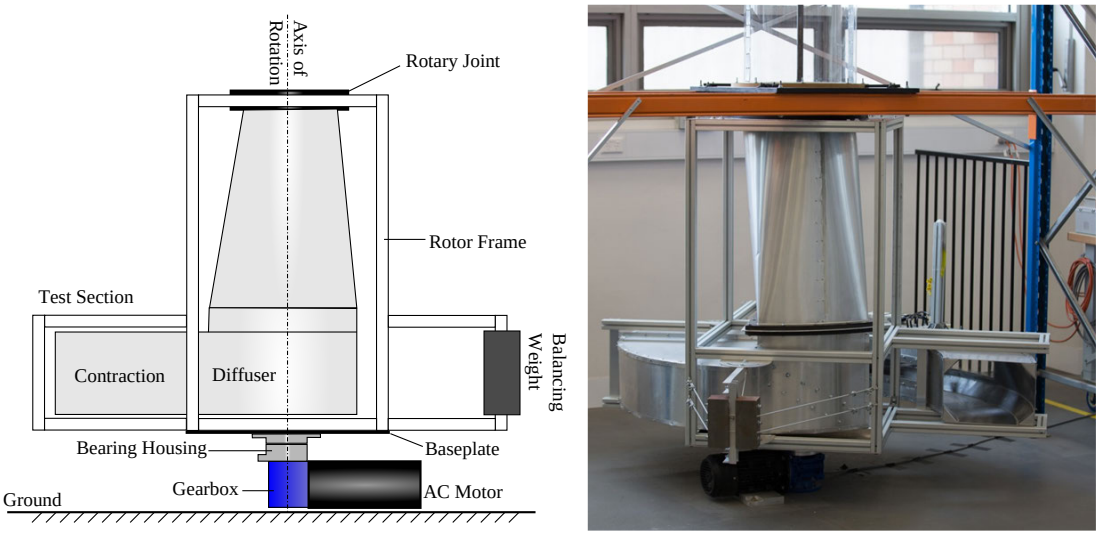

FIGURE 6.13: Diagram of the basic mechanical layout of the rotor section

6.4 Instrumentation

The rotation of the test section introduced additional considerations when selecting suitable instrumentation to investigate the flow within the test-section. The maximum design speed resulted in acceleration up to 163.1 m/s^2, however the maximum acceleration reached during the present experimental program was limited to 56.6 m/s^2. It was therefore necessary to ensure all equipment was operable under high acceleration.

6.4.1 Traverse System

A lightweight manual traversing system was secured in two curved rails which were external to the test section. The traverse used a vertical support strut which could be manually adjusted within an extruded channel to position probes as required. Accuracy was estimated based on physical measurement of probe position compared to indicated position. Vertical location (z) was estimated as accurate to ±2 mm, radial position (R) to ±3 mm, and angular position along the test section (θ) was accurate to within ±0.15°.

6.4.2 Rotor angular velocity

A rotary incremental encoder (British Encoder 755/HV - 068647) with 720 pulses per rotation was attached directly to the motor to monitor the angular velocity. As the gearbox had a 10:1 reduction ratio the encoder produced 7200 pulses per single rotation of the rotor section of the tunnel. Readings were recorded as averaged values over a

period of 0.1 s and angular velocity was remained within $\pm 0.02 rad/s$ of the reported value for all experiments.

6.4.3 Hot-wire measurements

A Dantec Dynamics Multichannel CTA system (54N82) was used for flow velocity and turbulence intensity measurements. The system was secured to the rotor section of the tunnel and measurements were taken by means of a four-probe rake mounted to the traverse, as shown in Fig. 6.14. A tungsten wire at a temperature of 250°C was utilised.

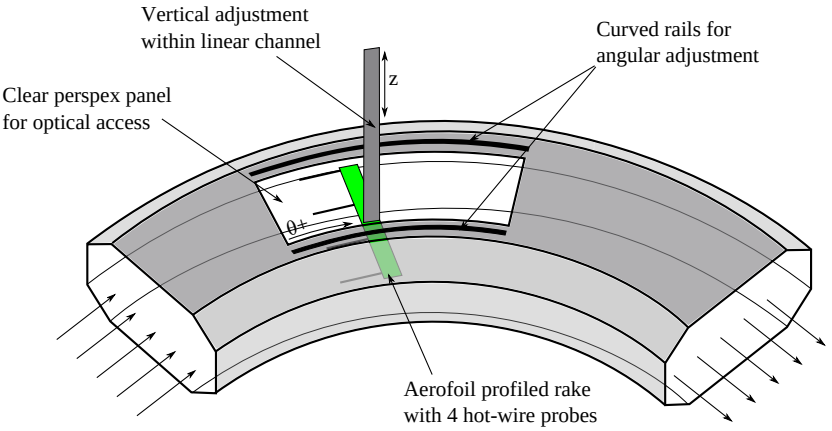

FIGURE 6.14: Diagram of hot-wire anemometer rake positioned within the test section

A four-channel 24 bit signal acquisition module (NI 9234) was used to record voltage outputs, and this was positioned in a National Instruments Wireless carrier (NI WLS-9163) which sent data via a WiFi connection to an external PC. All equipment was mounted externally above the test-section as shown in Fig. 6.15. Data was averaged over a 10 s sampling period at 12.8 kHz producing 1.28×10^5 samples with each measurement. Longer samples (60 s) were taken for frequency analysis to enable a more detailed examination of the turbulent properties, and are noted accordingly.

A TSI incorporated automatic calibrator was used with an MKS Instruments Baratron Manometer (220DD) to calibrate the hot-wire probes. A 40 point calibration from 2.5 to 35 m/s was conducted of each sensor using a x^{10} distribution which weighted calibration points toward lower velocities, as shown in Fig. 6.16. A King's law curve fit [130] was identified as superior to a polynomial fit within the low velocity range and was favoured in this instance. This resulted in R^2 values ranging from 0.9996 to 1.000. Probes were recalibrated every 24 hours during testing. The maximum absolute calibration error was 0.067 m/s for all probes within the considered velocity range.

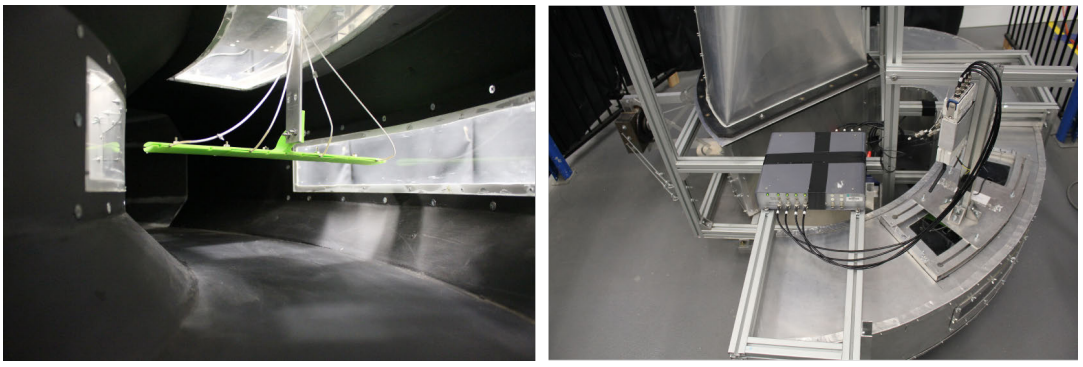

FIGURE 6.15: Position of hot-wire rake within test section and data acquisition system mounted externally

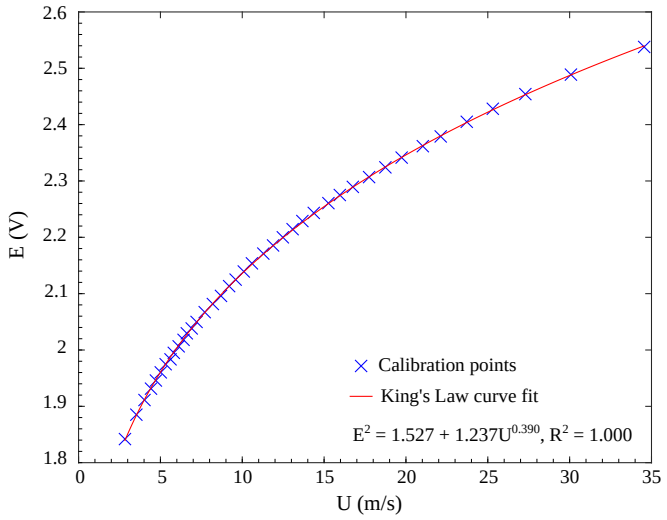

FIGURE 6.16: Example hot-wire calibration plot with King's law curve fit

Temperature was also recorded during experiments to an accuracy of $\pm 0.1K$ and a voltage correction was used to account for this effect. This was calculated using the manufacturer-provided guidelines [131]:

$$E_{corr} = \left(\frac{T_w - T_0}{T_w - T_a}\right)^{0.5} E_a \tag{6.2}$$

Turbulence intensity was calculated with respect to the theoretical freestream velocity according to $U_\infty = \omega R$ to ensure the parameter accommodated the designed freestream variability. It must be noted that this differs from standard practice where turbulence intensity will be measured according to a constant freestream velocity or dynamic pressure [24], but was deemed more appropriate for the given circumstances.

$$TI(\%) = \left(\frac{U_{RMSD}}{U_\infty}\right) \times 100 \tag{6.3}$$

6.4.4 Static rake measurements

Static pressure measurements were captured through a static rake consisting of four ports connected to digital low differential pressure LDE transducer by First Sensor AG. The pressure sensors were mounted externally to the test section, as shown in Fig. 6.17. A four-channel 24 bit signal acquisition module (NI 9219) was used to record voltage outputs, and this was again positioned in a National Instruments Wireless carrier. Differential pressure measurements between a reference value and the test section were taken at a frequency of 100 Hz. 10 s and 60 s samples were evaluated with less than 0.06% difference between subsequently performed measurements, and thus all measurements were averaged over the shorter period.

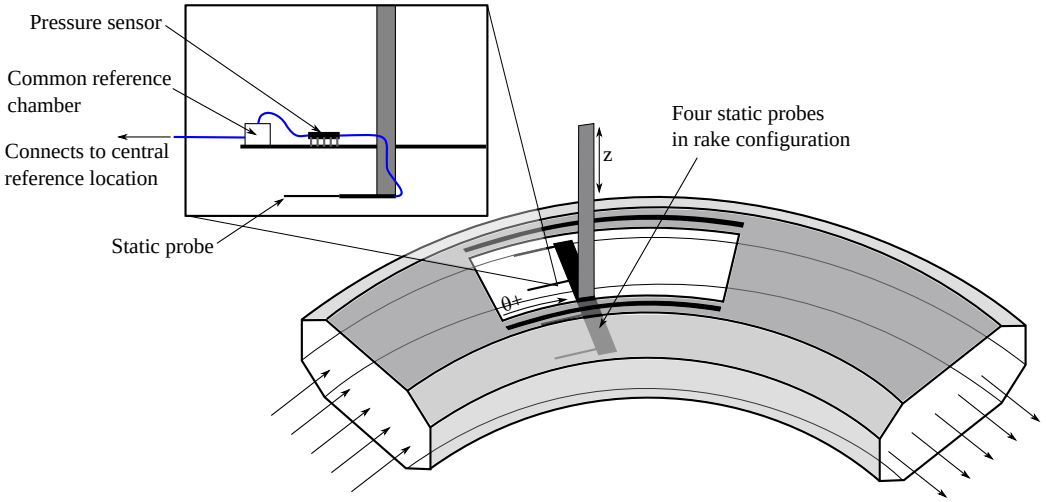

FIGURE 6.17: Diagram of static pressure rake and reference chamber positioned on the experimental rig

Sensors were individually calibrated also using an MKS Instruments Baratron Manometer. A 40 point distribution of pressures up to 100 pa with an x^{10} distribution. An ordinary linear least-squares fit was used to determine the relation between voltage and pressure, with an initial zero-offset value. The maximum absolute error was 0.015 Pa within the recorded range.

Pressure readings were compensated according to the change in absolute pressure, in line with the manufacturer specifications [132]:

$$p_{eff} = p_{sensor}\left(\frac{101.325 \times 10^3}{P_{abs}}\right) \tag{6.4}$$

Where P_{eff} is the true measured pressure value and $\mathrm{P_{abs}}$ was within $\pm 0.6Pa$.

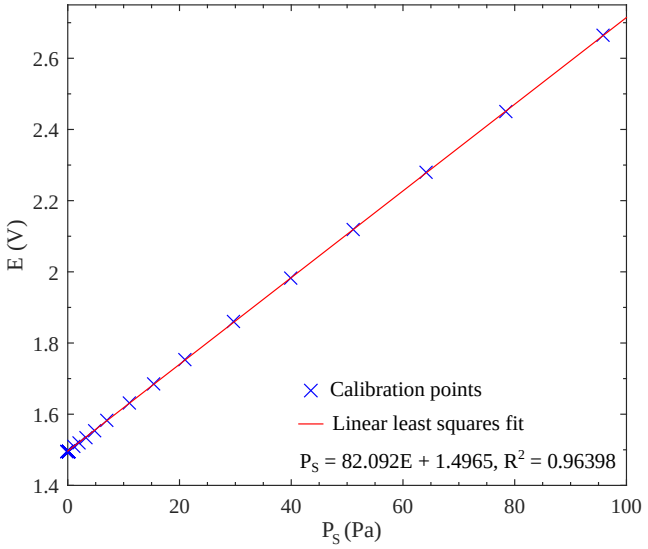

FIGURE 6.18: Example hot-wire calibration plot with King's law curve fit

The reference pressure measurement was taken at the centre of rotation of the experimental rig in order to measure the ambient value of the room. This probe was connected via tubing to a sealed plenum mounted on the traverse, where the reference ports on the pressure sensors were also connected. Thus the flow within the tubing and plenum experienced a pressure gradient due to centrifugal acceleration. Due to this effect a correction was necessary to ensure pressures were a gauge measurement with respect to the ambient conditions. Compressibility effects were assumed to be negligible and thus the difference in pressure across the radial displacement under acceleration was taken as proportional to the product of the flow density and acceleration.

The temperature and barometric pressure was recorded during experiments and ρ was calculated assuming air as an ideal gas.

Centripetal acceleration was equal to:

$$a_c = \omega^2 R \tag{6.5}$$

Thus the difference in pressure between two radial locations became:

$$\Delta p_R = \int_{R1}^{R2} \rho \omega^2 R \, dR \tag{6.6}$$

Where R_1 was the inner radius. As the reference static pressure was taken in the central axis where R = 0 mm, and z = -135 mm, R_1 remained constant at zero, and the pressure

measured at any radial location was corrected according to:

$$\Delta p_R = \frac{\rho \omega^2 R_2^2}{2} \tag{6.7}$$

Where R_2 was the radial position of the probe within the test-section.

In the same way a correction was also applied due to vertical displacement where the acceleration due to gravity was assumed constant at 9.79672 m/s^2[133] based on the measured value at the geographic location of the experiment. This vertical axis correction was applied according to:

$$\Delta p_z = \rho g \Delta z \tag{6.8}$$

6.5 Uncertainty

All quantitative results presented were repeated three times with the mean value shown in figures. Due to the number of samples recorded at each location not being sufficient to confidently conduct a statistical interpretation of the error, an estimate was calculated based on an Nth-order uncertainty analysis described by Moffat [134] for a single sample measurement data set.

The Nth-order uncertainty was calculated according to the root-sum-square (RSS) of all the uncertainty components within the system used for measurement.

$$\delta X_{i,N} = \sqrt{(\delta X_{i,1})^2 + (RSS\ \delta X_{i,fixed})^2} \tag{6.9}$$

Where $\delta X_{i,fixed}$ for each source was calculated based on the effect toward the result RT to give a sensitivity coefficient:

$$\delta(RT)_{X,i} = \frac{\partial(RT)}{\partial X_i} \delta X \tag{6.10}$$

Values were normalised according to the respective parameter of which the error was associated. As both pressure and velocity are reported as mean values, the typically-incorporated RMS error associated with the process unsteadiness (turbulence intensity) was reported as a separate value. The uncertainty interval only provided an estimate based on the quantifiable sources, but allowed an approximate 95% confidence interval to be established for each measured flow parameter. Full details of the calculated uncertainties is shown in Appendix B.

The velocity uncertainty was dependent on both radial position, angular velocity and freestream velocity. The confidence interval normalised according to the mean freestream value is shown in Table 6.1.

TABLE 6.1: 95% confidence interval for hot-wire velocity measurement in terms of $\pm U_{\infty,m}$

		$\delta R/H$						
ω (rad/s)	$U_{\infty,m}$ (m/s)	-0.54	-0.36	-0.18	0	0.18	0.36	0.54
4.71	3.53	0.0271	0.0281	0.0291	0.0301	0.0312	0.0323	0.0334
6.28	4.71	0.0209	0.0217	0.0225	0.0233	0.0242	0.0250	0.0259
6.28	3.2	0.0303	0.0312	0.0323	0.0334	0.0345	0.0356	0.0368
6.28	7.2	0.0173	0.0182	0.0191	0.0201	0.0210	0.0220	0.0229
7.85	5.89	0.0186	0.0194	0.0202	0.0211	0.0219	0.0228	0.0237
0	4.71	0.0206	0.0214	0.0222	0.0230	0.0239	0.0247	0.0256

The static pressure also incorporated an additional uncertainty term that was dependent on vertical displacement due to the correction applied in this axis, however this made less than 0.05% difference to the total confidence interval width, so is not shown for brevity. Results for the different flow conditions assessed are shown in Table 6.2 Turbulence intensity uncertainty was dependent on the magnitude of the root-mean-

TABLE 6.2: 95% confidence interval for static pressure measurement in terms of $\pm C_P$

		$\delta R/H$						
ω (rad/s)	$U_{\infty,m}$ (m/s)	-0.54	-0.36	-0.18	0	0.18	0.36	0.54
4.71	3.53	0.0158	0.0182	0.0212	0.0248	0.0292	0.0345	0.0408
6.28	4.71	0.0257	0.0282	0.0310	0.0342	0.0379	0.0422	0.0472
6.28	3.2	0.0189	0.0239	0.0301	0.0376	0.0465	0.0570	0.0693
6.28	7.2	0.0131	0.0143	0.0156	0.0171	0.0187	0.0205	0.0227
7.85	5.89	0.0175	0.0196	0.0221	0.0249	0.0283	0.0323	0.0371
0	4.71	0.0066	0.0071	0.0076	0.0081	0.0086	0.0091	0.0096

square derivative (RMSD), and thus demonstrated the greatest variability throughout the test-section. Consistency with respect to the vertical and angular displacements fell within an absolute value of 0.025, thus the results shown in Table 6.3 are for z/H = 0, $\theta = 10°$. For visual clarity error bars are not indicated in all figures throughout the present chapter, and in these instances the reader is encouraged to refer back to the appropriate table.

6.6 Results

Successful operation of the experiment was predicated on the achievement of stationary flow within the absolute reference frame while maintaining constant static pressure.

TABLE 6.3: 95% confidence interval for turbulence intensity measurement in terms of ±%

		$\delta R/H$						
ω (rad/s)	$U_{\infty,m}$ (m/s)	-0.54	-0.36	-0.18	0	0.18	0.36	0.54
4.71	3.53	0.348	0.380	0.390	0.337	0.326	0.324	0.405
6.28	4.71	0.273	0.323	0.337	0.253	0.236	0.235	0.365
6.28	3.2	0.435	0.467	0.472	0.410	0.395	0.402	0.494
6.28	7.2	0.598	0.627	0.633	0.577	0.563	0.561	0.650
7.85	5.89	0.408	0.449	0.461	0.387	0.370	0.373	0.483
0	4.71	0.356	0.387	0.396	0.345	0.335	0.335	0.413

Achieving these flow conditions within a rotating test-section would establish that the experiment is capable of correctly recreating the cornering conditions in a repeatable and continuous way. As all instrumentation was positioned within the rotating reference frame of the test-section, all velocity measurements were relative. The correct measured velocity was thus the product of the angular velocity of the test-section, and the radius at which the measurement was taken. The sought velocity profile should increase linearly with radius, and be achieved while a constant static pressure is maintained.

6.6.1 Flow Visualisation

Smoke flow visualisation was used as a qualitative technique to confirm the relative curvature of the flow within the test section. This was achieved through the use of incense positioned along a horizontal rake at $\theta = 5°$, z/H = 0. The positioning of the incense resulted in a split longitudinal wake structure which demonstrated a tendency to diverge. This was a mild hindrance, however the position was favourable over adopting a vertical alignment which resulted in a Von Kármaán street type mechanism. The temperature also resulted in buoyancy which caused the smoke streams to rise in the vertical axis within the test-section.

The method proved effective at low Reynolds numbers and the image shown in Fig. 6.19 was conducted at 1.57 rad/s which corresponded to $U_{\infty,m} = 1.18$ m/s. δR/H is a dimension introduced as equivalent to R/H but centred at the middle of the test section to aid in identification of the inner and outer sides of the test-section for all results. This visualisation confirmed the flow to assume a relative curvature with respect to the test-section. The curved path of the smoke lines was maintained along the length of the test-section and did not indicate any specific regions of flow misalignment.

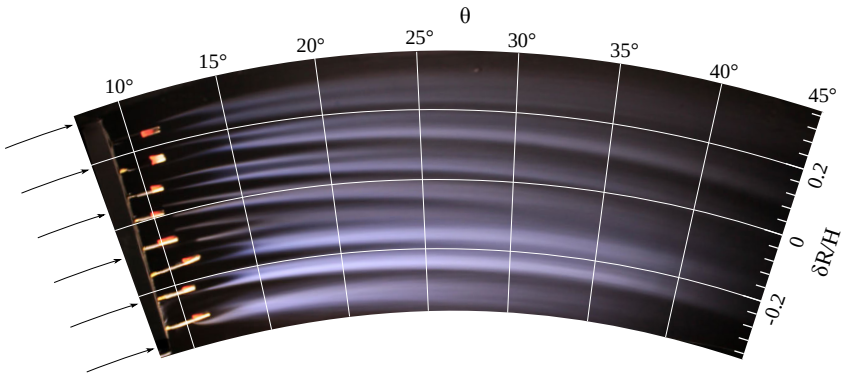

FIGURE 6.19: Smoke flow visualisation used for confirmation of flow curvature within the test section

6.6.2 Flow Consistency

Quantitative results were taken at seven point locations across the width of the test-section, allowing the extraction of horizontal flow profiles. These profiles were taken at nine vertical locations resulting in a three-dimensional distribution of point measurements throughout the test-section, as shown in Fig. 6.20.

The centre of the test-section was located at z/H = 0 and $\delta R/H = 0$, where z was aligned positive in the vertical direction and δR was positive as directed radially outward, and this remained constant for each angular position. Due to the octagonal shape of the test-section only three measurement were taken at z/H = -0.3, -0.4, 0.3, and 0.4 as the section narrowed.

Analysis was conducted using the same cylindrical co-ordinate system that has been introduced in this chapter where $\theta = 0$ corresponded to a position 20° downstream of the contraction nozzle exit. Vertically aligned cross-sectional planes were analysed at both $\theta = 0°$ and 10° as these spanned a region where it was designed to be most appropriate for positioning a model.

6.6.2.1 Cross-Sectional Planes

Cross-sectional velocity and static pressure distributions are shown in Fig. 6.21 with turbulence intensity distribution shown in 6.22. It can be observed that velocity measurements correlated with the theoretically ideal distribution and demonstrated an increase in the relative tangential velocity as the radius increased. These measurements remained in close accordance with the ωR relation in curved flow, as shown in Fig. 6.21a) and b).

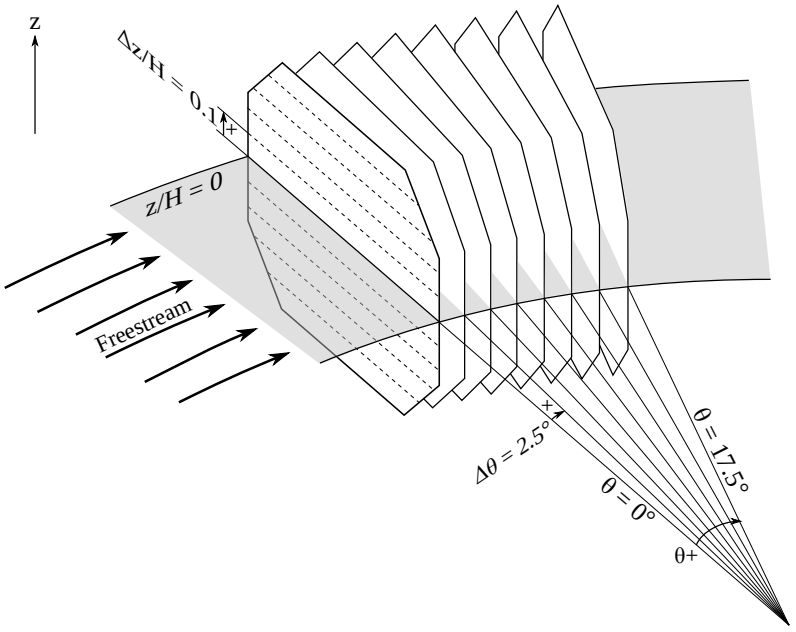

FIGURE 6.20: Diagram of test-section flow measurement profile locations

A coefficient of determination (R^2) value was used to quantitatively assess the fit of each experimental profile taken between z/H = -0.2 and 0.2. For the upstream plane taken at $\theta = 0°$, as shown in Fig. 6.21a), the mean value taken across these five profiles was $R^2_{mean} = 0.928$, where a maximum value of $R^2 = 0.948$ was measured for z/H = 0.2 and a minimum of $R^2 = 0.911$ for z/H = -0.2, which indicated a superior match to the theoretical velocity distribution in the upper region of the test-section. For the downstream plane measured at $\theta = 10°$, as shown in Fig. 6.21b), the experimental data matched the theoretical distribution more closely with $R^2_{mean} = 0.952$, where a maximum $R^2 = 0.973$ was measured at z/H = 0.2, and minimum of $R^2 = 0.931$ at z/H = 0.

A consistent discrepancy was a decelerated flow region measured at the outermost radial location (δR/H = 0.54). The correct relative velocity should continue to increase between δR/H = 0.36 and 0.54 by 0.06 $u/U_{\infty,m}$, however the opposite trend occurred in this instance. Considering all the profiles shown in Fig. 6.21 a common deceleration can be observed. The maximum value was -0.026 $u/U_{\infty,m}$, and this same value occurred at two separate locations (z/H = 0, $\theta = 0°$, and z/H = -0.1, $\theta = 10°$).

The static pressure coefficient remained close to the ambient value measured at the central reference port, and this was due to the outlet being positioned directly downstream. The ideal experimental condition sought a constant static pressure distribution, irrespective of the absolute value, so the consistency was of greater concern. Figures 6.21c) and d) show the static pressure distribution where the solid line indicates the mean value.

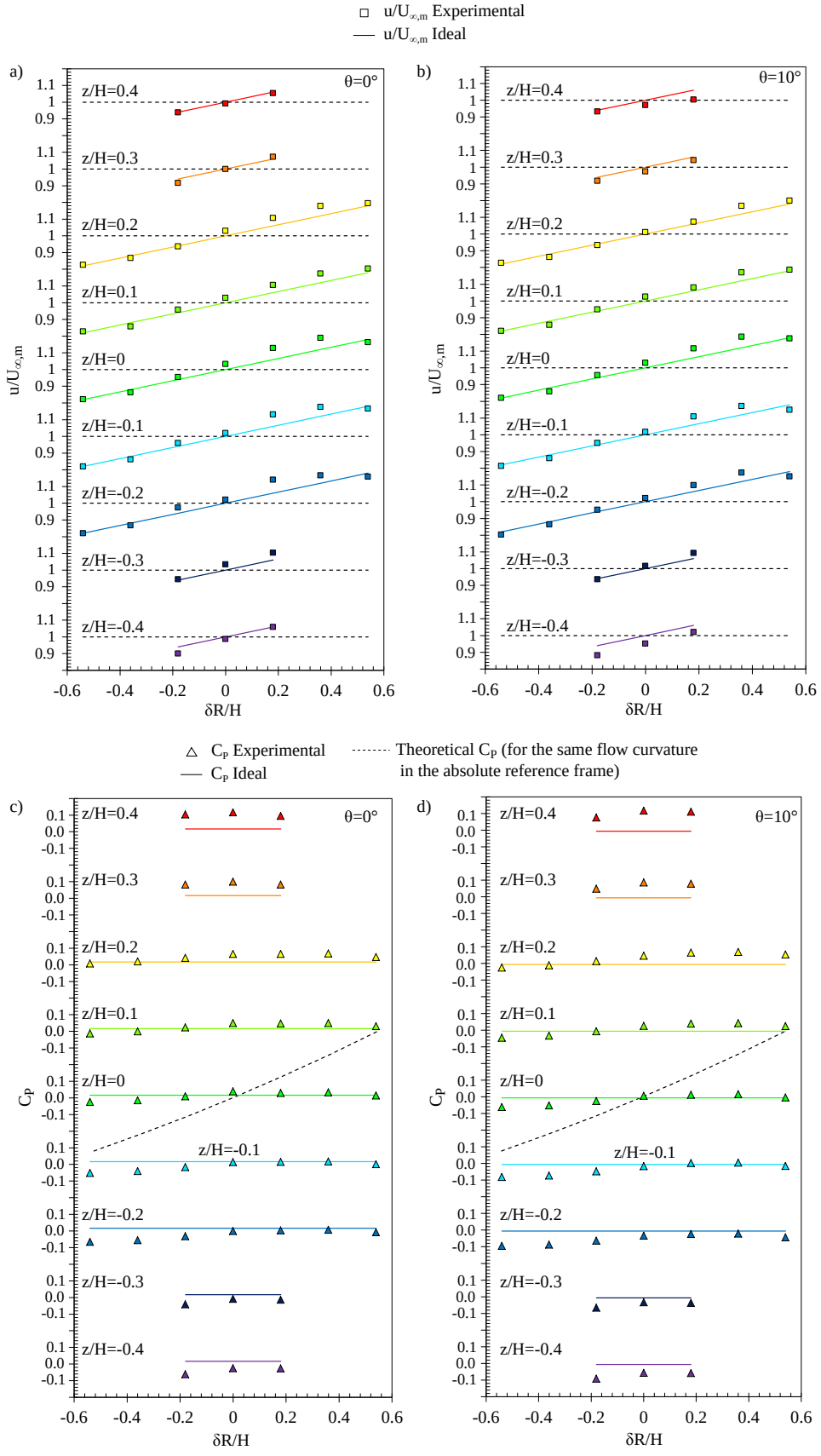

FIGURE 6.21: a) Velocity profiles taken at $\theta = 0°$ b) Velocity profiles taken at $\theta = 10°$ c) Static pressure profiles taken at $\theta = 0°$ d) Static pressure profiles taken at $\theta = 10°$

For comparison purposes the theoretical variation in static pressure for a rotating flow in the absolute reference frame, subject to the effects of centrifugal acceleration, is also shown.

The distribution across the test-section demonstrated a good level of consistency, however specific trends were observed to occur in both the vertical and radial axes. In the vertical axis the static pressure was observed to decrease in the lower part of the test-section, and increase near the top. For the upstream plane measured at $\theta = 0°$, as shown in Fig. 6.21c) the mean pressure coefficient at z/H = 0.4 was 0.14 higher than at z/H = -0.4 with a near linear trend exhibited between these locations, a similar value of 0.18 was measured for the same comparison at $\theta = 10°$.

This difference was attributed to flow effects due to the external shape of the tunnel itself. The lower side of the experimental rig remained flat, while the upper external surface was where all instrumentation was mounted, as shown in Fig. 6.15. A higher static pressure was thus believed to occur at the upper location as this flow was required to exit into the wake region of the instrumentation, and therefore would need to overcome a comparatively higher level of resistance when compared to the flow exiting in the lower half.

A second gradient was observed in the radial direction across the test-section, although this was to a smaller extent. For all profiles a decreased static pressure was measured at the three innermost locations ($\delta R/H$ = -0.54 to -0.18). This was common on both the upstream and downstream planes and the mean disparity between the inner and outer side was 0.05 at $\theta = 0°$, and 0.06 for $\theta = 10°$. The pressure coefficient profile was observed to inversely correlate with the turbulence intensity, shown in Fig. 6.22.

The turbulence intensity was notably higher than typical values achieved in automotive wind tunnels [24, 38, 135, 136] however was incidentally within a range observed for on-road driving conditions [1, 137], with results shown in Fig. 6.22. An increased turbulence intensity was expected due to the deliberate omission of both turbulence screens or a flow straightening screen downstream of the turning vane cascade. The implications of including these features for future development is discussed in Section 6.7.

The mean value across all measurements at the reference angular velocity ($\omega = 6.28 rad/s$) was 2.61% with a maximum recorded value of 5.25% and a minimum of 1.10%. The highest turbulence intensities were measured in the lower part of the test-section at z/H = -0.4 with this being the only location where local values exceeded 5%. At this height mean intensities of 4.35% and 4.80% were measured for $\theta = 0°$ and 10° respectively. A milder increase occurred toward the upper surface where mean values of 3.06% and 3.02% were measured on the upstream and downstream planes. The lowest

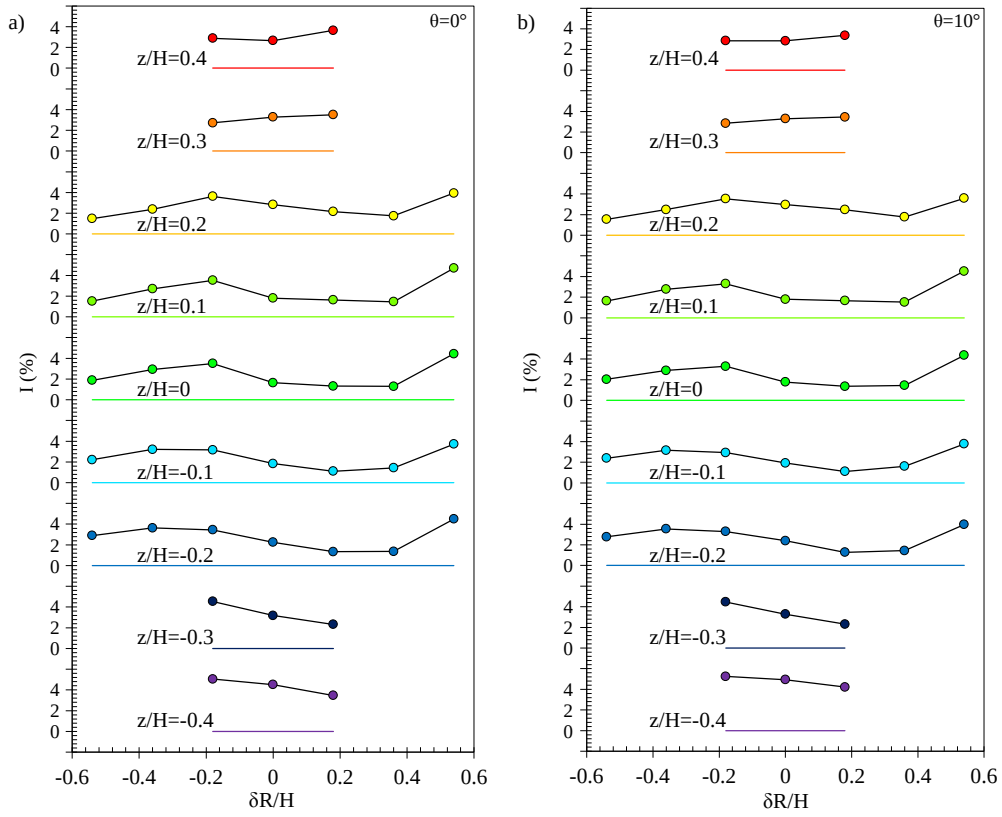

FIGURE 6.22: a) Turbulence intensity profiles taken at $\theta = 0°$ b) Turbulence intensity profiles taken at $\theta = 10°$

intensities were concentrated centrally and slightly toward the outer side. These were recorded at δR/H = 0 and 0.18 between z/H = 0.1 and -0.1.

Centrally, between z/H = -0.2 and 0.2, the turbulence demonstrated consistency in the z-axis, which can be observed in both Fig. 6.22a) and b). For each radial position similar values were measured across these heights, and at the outer measurement location (δR/H = 0.54) a consistent increase occurred. This occurred due to the vertical vanes positioned across the cascade an is discussed further in Subsection 6.6.3.

6.6.2.2 Horizontal Plane

The same parameters were also surveyed on a horizontal plane at constant vertical location (z/H = 0) along the test-section, as shown in Fig. 6.23, to ensure flow consistency within both axes. The velocity distribution was consistent from $\theta = 0°$ to 17.5°. The maximum variation in velocity at any radial position was 0.027 $u/U_{\infty,m}$. Consistent with the results recorded for cross-sectional planes, a decrease in velocity at outer measurement location was observed and remained the most notable discrepancy with the theoretical distribution.

The planar mean coefficient of determination was $R^2_{mean} = 0.928$, where a maximum value of $R^2 = 0.939$ and minimum of $R^2 = 0.912$ occurred at $\theta = 15°$ and $0°$ respectively. This further indicated a consistently good agreement between the experimental results and the theoretical velocity distribution throughout the test-section.

The static pressure exhibited a similar trend and was consistent along the length of the surveyed region shown in Fig. 6.23b). A gradient was observed where the value consistently decreased toward the outlet location. The mean pressure coefficient for the profile at $\theta = 0°$ was 0.012 and this value consistently decreased for each radial profile to reach a minimum of -0.036 at $\theta = 17.5°$. The result was attributed to the high turbulence intensity being responsible for greater than expected losses occurring along the test-section.

The turbulence intensity also remained consistent at each radial location across the surveyed angular positions, as shown in Fig. 6.23c). The outer measurement location at $\delta R/H = 0.54$ remained the highest recorded value across the span, and a milder increase at $\delta R/H$ = -0.18 was present. An increase in the uniformity of the turbulence intensity occurred for each angular increment and was attributed to mixing within the test section. The variance of each horizontal profile was taken to assess the turbulent uniformity and between $\theta = 0°$ and 17.5°, and reduced from 1.47 to 1.12 with a consistent incremental decline for each downstream angular position.

6.6.3 Turbulence Analysis

Due to the high turbulence intensity, further analysis was conducted to assess likely features responsible for the disturbances measured in the test-section. CFD simulation conducted throughout the design period permitted comparative analysis of the turbulent characteristics between the experiment and numerical simulation.

Figure 6.24 indicates the turbulence intensity prediction relative to U_∞ based on the turbulent kinetic energy transport variable. The planes demonstrate a qualitatively similar distribution to the experimental results with increased turbulence intensity toward each of the sides. A higher region spanned the majority of the inner half ($\delta R/H < -0.2$) where the intensity remained above 2%, similarly there was an increase toward the outer side of the test section (where $\delta R/H > 0.5$) which reached a higher magnitude at the boundary. Two vertical bands of low turbulence intensity were centred at $\delta R/H \approx 0.3$ and $\delta R/H \approx -0.1$. The consistency in the vertical axis was in agreement with the experimental results, in addition to the respective increases toward the upper and lower surfaces.

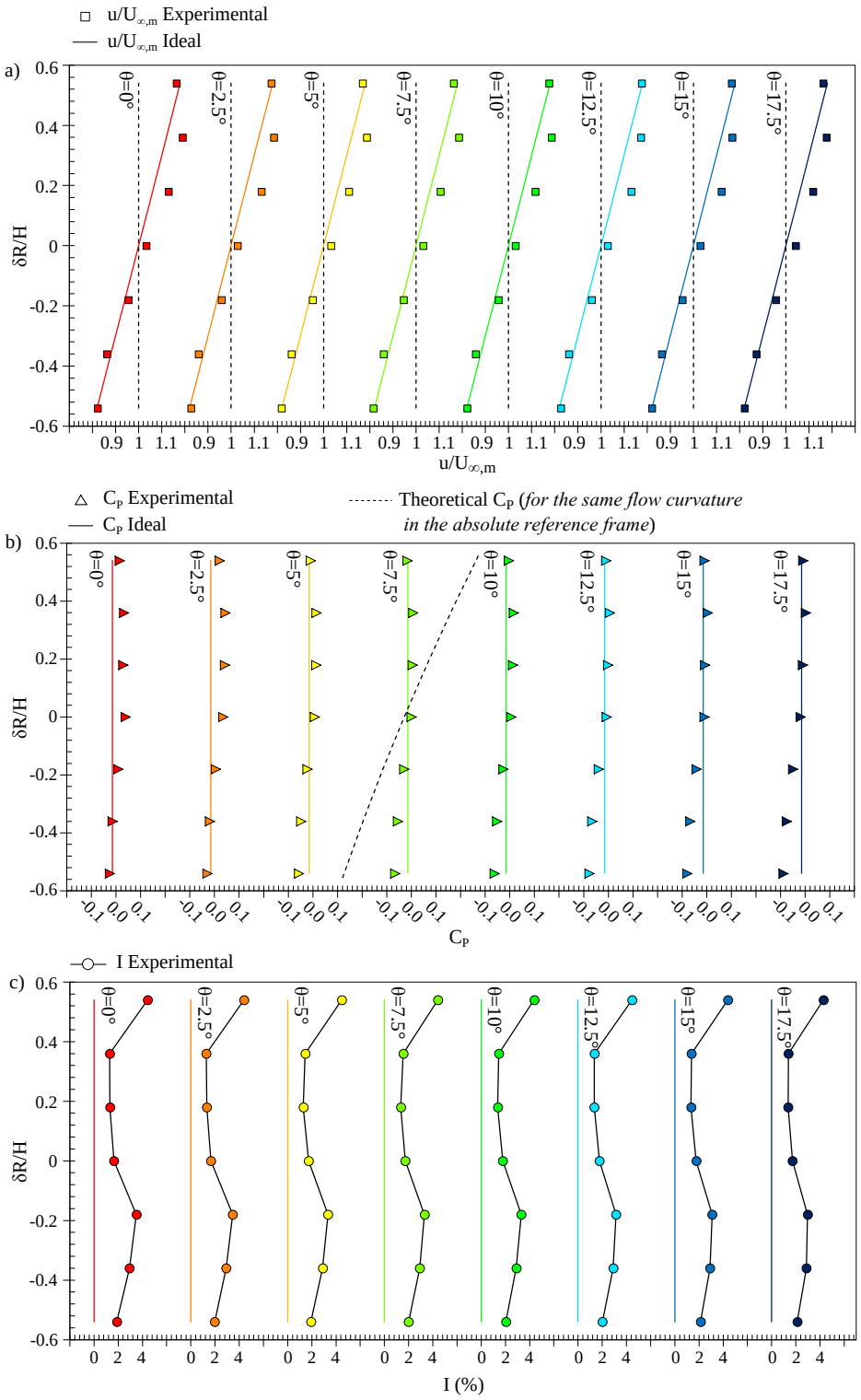

FIGURE 6.23: Test-section profiles taken at z/H = 0 for a) velocity, b) static pressure, and c) turbulence intensity

A noted discrepancy however, was the prediction at the location $\delta R/\mathrm{H}$ = -0.54, which was the experimental measurement of closest proximity to the inner wall. For this location at $\theta = 0°$ the measured average was 2.00%, and 2.08% at $\theta = 10°$. Differing from this prediction the numerical model indicated a continued rise toward the boundary with the average intensity exceeding 3.5%.

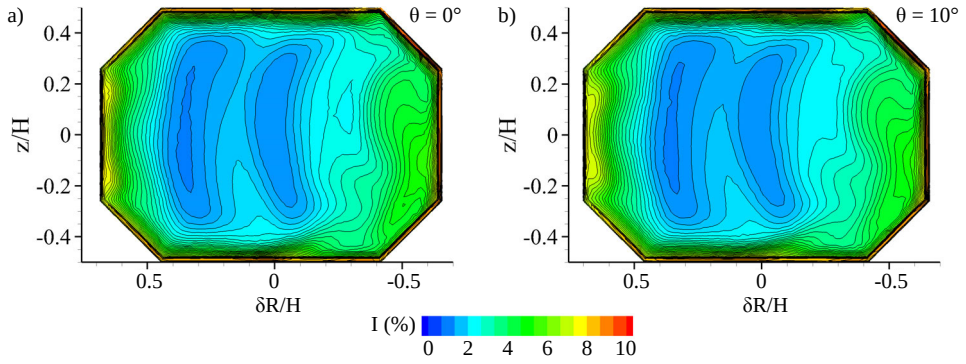

FIGURE 6.24: Numerical model turbulence intensity distribution within test section at a) $\theta = 0°$ b) $\theta = 10°$

Figure 6.25 shows the turbulent kinetic energy proportional to the mean test-section velocity. This demonstrated the vertical profiles of increased turbulence to correspond to the locations of the vertical curved turning vanes arranged across the cascade. Regions of increased turbulent kinetic energy were identified to occur on the inner side of the vanes and continue downstream into the test section. As the curvature of these vanes increased, the production increased, with the exception of the innermost vane.

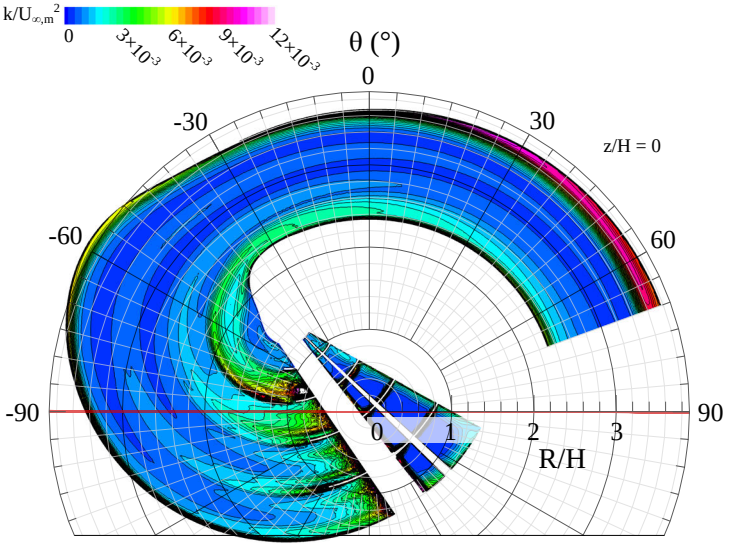

FIGURE 6.25: Numerical model turbulent kinetic energy distribution at z/H = 0

As the flow enters the cascade it remained aligned with the rotation of the tunnel section due to the use of flow-straightening screens. As such it can be thought of as the swirl matching the tunnel rotation. When passing over the turning vanes, flow swirl is required to be re-introduced, which requires the vertical curved vanes to provide adequate support in that second axis. At the intersection of the suction surface of the turning vanes with the pressure surface of the vertical vane, the gradient resulted in the formation of longitudinal vortices, as shown in Fig. 6.26. On suction side of the vertical vane this difference in pressure was more mild.

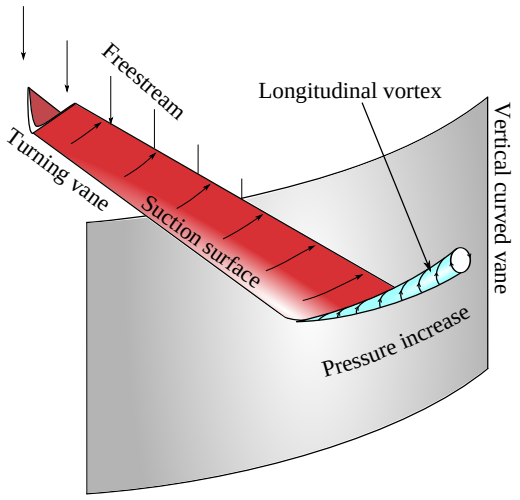

FIGURE 6.26: Location of formation of longitudinal vortices generated by the turning vanes at the intersection with vertical vanes

Numerical analysis indicated that this vortex formation resulted in the majority of the turbulence production and explained the regions of vertical consistency corresponding to the vertical vane position. The increased magnitude which occurred at the vane second from the inner wall was due to the additional presence of the splitter vanes and the increased curvature at this location. The indicated reduction at the innermost location was a result of both reduced mass flux and lower Reynolds number. Although it must be noted that the computational prediction towards the inner side of the test-section was not in agreement with experimental results, indicating flow behaviour may not have been accurately represented at this location.

The outer increase in turbulence intensity was identified to be the result of boundary layer growth within the contraction nozzle, and then continued to develop downstream into the test section. The region of highest turbulent kinetic energy was identified toward the test-section outlet. This discrepancy was anticipated due to the disparity in the respective lengths of either side of the nozzle, but would represent a region that could be improved through boundary layer control.

Analysis also sought to determine the presence of any frequencies corresponding to regular periodic transient motions. Figure 6.27 shows the frequency spectrum for measurements taken at z/H = 0, θ = 10° with the same seven radial locations shown. Measurements were taken over a period of 60 s where the sampling frequency remained at 12.8 kHz.

All but two measurement locations indicated predominantly isotropic turbulent characteristics, with an increased magnitude relative to the intensity recorded at that location. However, in the case of both δR/H = -0.54 and δR/H = -0.18 a dominant peak was observed that was centred about Str ≈ 0.6 (based on test-section heigh H) which indicated a regular mechanism. In both cases this peak occupied a similar range of frequencies however the maximum magnitude for δR/H = -0.18 was Str = 0.66, and at δR/H = -0.54 this occured at Str = 0.53. Despite the frequency band being consistent at both these locations a similar peak was not observed for the measurement taken between these two points (δR/H = -0.36). This indicated two isolated but similar flow mechanisms, as opposed to a spanwise orientated transient motion.

The local Reynolds number based on turning vane chord length ranged from 2.6×10^4 at the outer wall to 1.4×10^4 at the inner wall due to the relative increase and decrease in turning vane chord length. Adjusting the non-dimensional frequency relative to chord length, as opposed to tunnel height, gave Str ≈ 0.21 which would fall into a range typical of a von Kármán street mechanism resulting from trailing edge separation over an aerofoil at low Reynolds numbers [138]. The over-expansion of the flow at the inner side was suspected to have resulted in some trailing edge separation despite the support of the splitter vane. While the absence of this dominant frequency at δR/H = -0.36 could be explained by the intersection of the vertical vane suppressing this separation.

6.6.4 Reynolds Number

$U_{\infty,m}$ = 3.53 m/s and 5.89 m/s were also investigated to identify any effects attributed to operating the tunnel at the correspondingly lower and higher Reynolds numbers, as shown in Fig. 6.28. These corresponded to operating the tunnel at ±25% of the reference speed detailed throughout the previous sections. A complete horizontal plane at z/H = 0 and vertical plane at θ = 10° were investigated at both freestream velocities.

Consistent flow properties were identified to remain throughout the investigated planes within the test-section with a representative profile for each freestream condition shown in Fig. 6.28. A mean coefficient of determination was used to assess the overall fit of the velocity data to the theoretical value (ωR) where R^2_{mean} = 0.901 for $U_{\infty,m}$ = 3.53 m/s, and R^2_{mean} = 0.928 for $U_{\infty,m}$ = 5.89 m/s, which indicated improved overall correlation

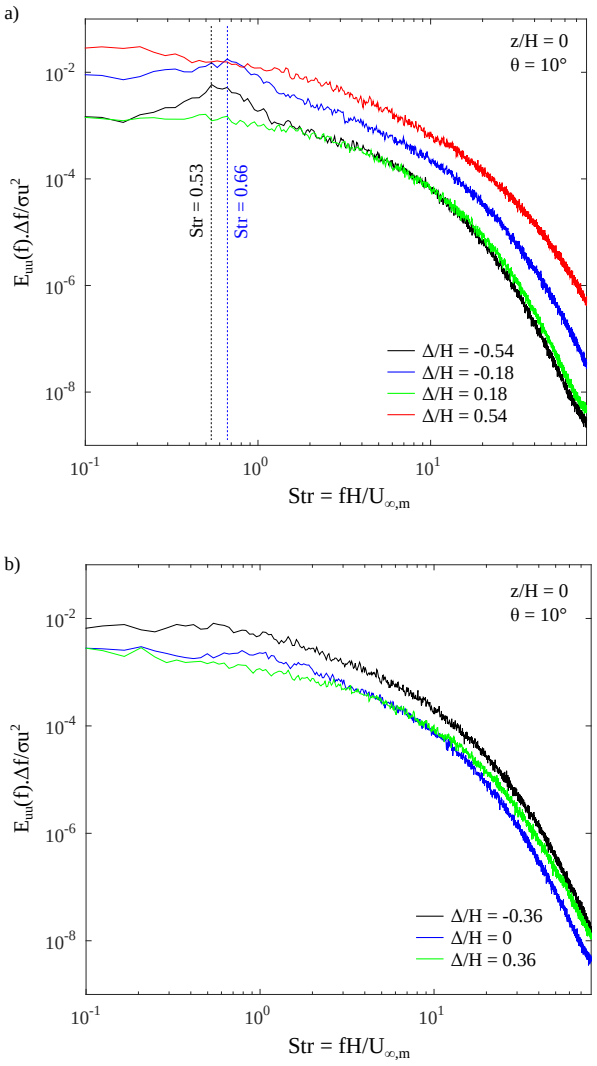

FIGURE 6.27: Velocity and static pressure coefficient profiles taken at constant angle within test section

between the theoretical and experimental velocity distribution for an increased Reynolds number. A linear least-squares fit was used to measure the gradient of each profile, and compare it to the theoretical value of $0.333\frac{U_{\infty,m}}{\delta R/H}$. The gradient was observed to exceed the theoretical value in all instances, but to a lesser extent as Re increased. The primary cause for this improved correlation, however, was the decrease in velocity at $\delta R/H = 0.54$ as Reynolds number increases, indicating the likely occurrence of Reynolds number dependent boundary layer effects.

At $U_{\infty,m} = 5.89$ m/s an increase in the test-section static pressure occurred with a mildly increased gradient across the test section, which can be observed in Fig. 6.28b). While at $U_{\infty,m} = 3.53$ m/s the identified gradient was smaller. The variability of the static

pressure within the test-section again correlated inversely with the region of higher turbulence intensity. This parameter was comparably lower at the reduced Re with a mean value of 2.52%, compared to 2.61% at $U_{\infty,m} = 4.71$ m/s, and 2.75% at $U_{\infty,m} = 5.89$ m/s. Thus the results demonstrated a reduced turbulence intensity to correlate with improved test-section flow quality.

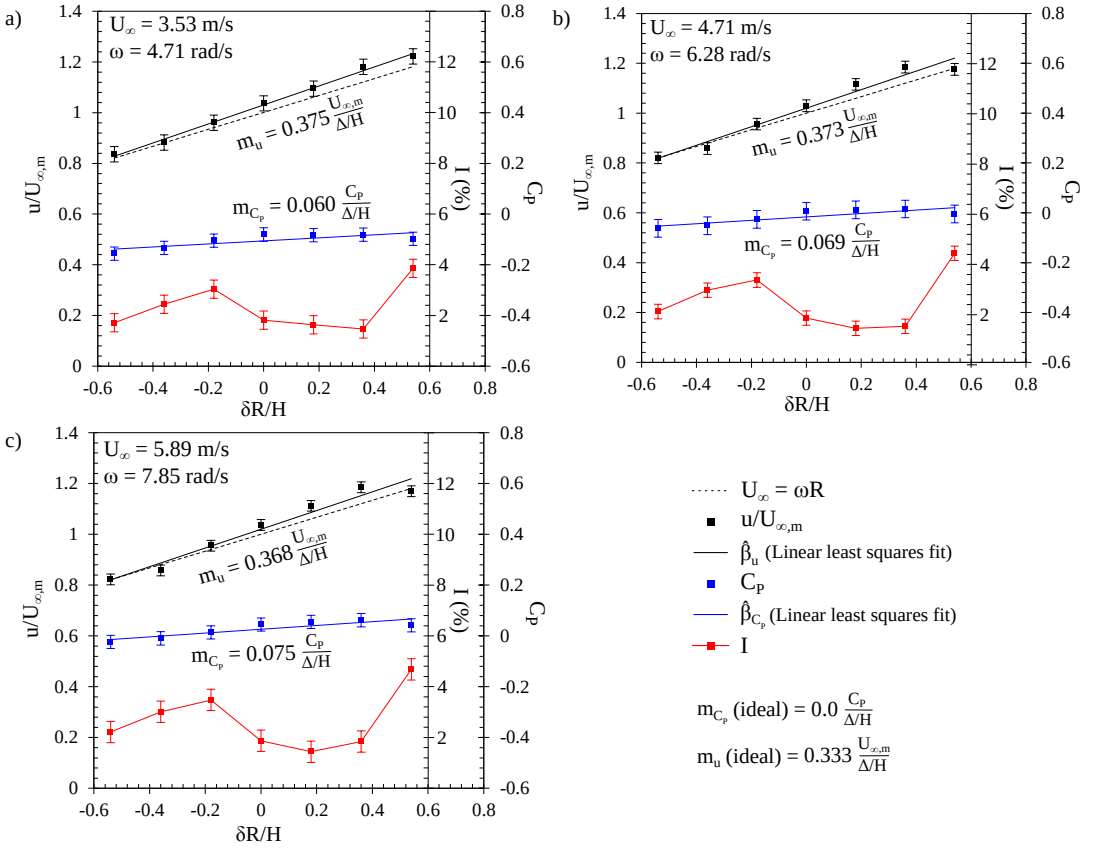

FIGURE 6.28: Velocity, static pressure, and turbulence intensity at z/H = 0, $\theta = 10°$ for a) $\omega = 4.71$rad/s, $U_{\infty,m} = 3.53$m/s, b) $\omega = 6.28$rad/s, $U_{\infty,m} = 4.71$m/s, c) $\omega = 7.85$rad/s, $U_{\infty,m} = 5.89$m/s

6.6.5 Angular Velocity

The rotation of the lower tunnel sections and test section presented the most significant challenge from a mechanical design perspective, and inherently make the present type of wind tunnel more difficult to scale than conventional designs. When operating correctly only one freestream velocity is suitable for any given angular velocity. This is because the velocity of the flow must remain at zero within the absolute reference frame to create the correct relative flow conditions without the flow being under acceleration itself. In this section the flow velocity and angular velocity were deliberately modified to result in flow

that was in motion within the absolute reference frame, thus deliberately introducing positive flow curvature.

Figure 6.29a) shows the aerodynamic characteristics at z/H = 0 and $\theta = 10°$ when the experimental rig is operating at $\omega = 6.28$ rad/s and $U_{\infty,m} = 4.71$ m/s, indicating the flow conditions for when the experiment is operating as designed.

In Fig. 6.29b) the mean freestream velocity remained at $U_{\infty,m} = 4.71$ m/s while the rotor was stationary. This caused an incorrect velocity profile to occur across the test-section. In this case the gradient between the inner and outer measurements was 79.7% that of the theoretically ideal flowfield. Across the central part of the profile between δR/H = -0.36 and δR/H = 0.18 the velocity remained near constant with a maximum change of only $0.033U_\infty$ across these four measured locations. The same condition was analysed along the test-section from $\theta = 0°$ to 17.5° where a further effect was the deceleration of flow by a mean value of 0.028 $U_{\infty,m}$ for each angular increment measured downstream.

To balance the induced flow rotation within the test-section a more significant static pressure gradient occurred. This resulted in a minimum static pressure occurring on the inner side, and maximum on the outer, where the difference between these locations was a pressure coefficient of 0.753. Thus the gradient in static pressure significantly exceeded that of dynamic pressure.

The mean turbulence intensity was 3.74%, which was higher than the value of 2.61% for the calibrated condition shown in Fig. 6.29a). The intensity was more consistent throughout the test section, and was attributed to increased mixing of the flow. With the variance being 0.39 for the stationary rotor, compared to 1.14 for the calibrated condition shown in Fig. 6.29a).

Figure 6.29c) and d) show representative profiles for conditions where the freestream velocity is higher and lower than the designed value with respect to the angular velocity. The conditions were achieved through increasing the fan speed and turning the fan off.

Increased freestream velocity resulted in a more significant gradient across the test-section (0.483 $U_{\infty,m}$/H as compared to 0.373 $U_{\infty,m}$/H for the calibrated condition) and demonstrated reduced linearity across the width.

In Fig. 6.29c) an increasing gradient in static pressure occurred on the inner side, but remained constant on the outer side. The net result was an increased mean gradient of $0.133\frac{C_P}{\delta R/H}$ from the inner to outer side. The increase in freestream velocity with respect to angular velocity resulted in curvature being introduced to the flow with the associated static pressure gradient, albeit to a more minor extent than occurred in Fig. 6.29b).

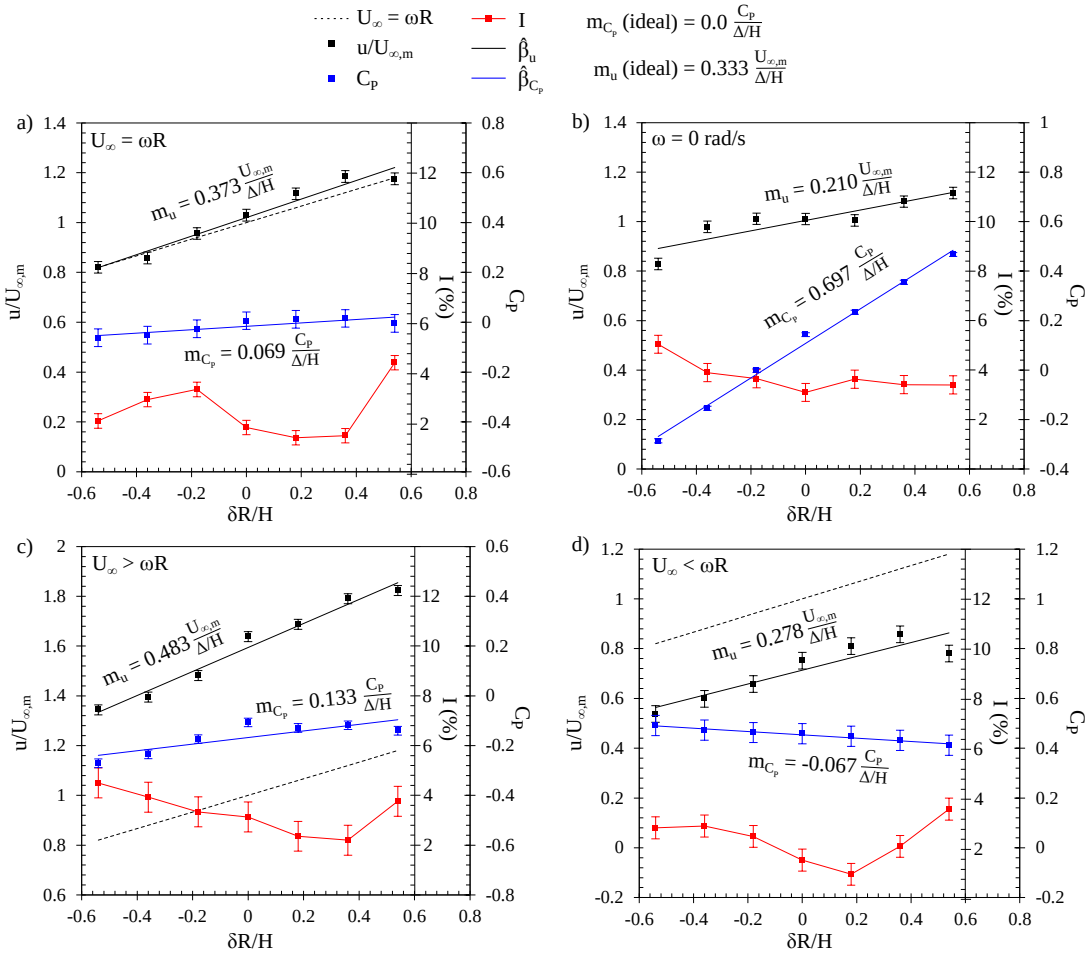

FIGURE 6.29: Velocity, static pressure, and turbulence intensity at z/H = 0, $\theta = 10°$ for a) $\omega = 6.28$rad/s, $U_{\infty,m} = 4.71$m/s, b) $\omega = 0$rad/s, $U_{\infty,m} = 4.71$m/s, c) $\omega = 6.28$rad/s, $U_{\infty,m} = 7.2$m/s, d) $\omega = 6.28$rad/s, $U_{\infty,m} = 3.2$m/s

Adopting a reduced freestream velocity resulted in a reduced gradient of 0.28 $U_{\infty,m}$/H. When the freestream flow velocity is less than ωR, the curvature within the absolute reference frame is in the opposite direction to the physical curvature of the test-section. Thus the inner surface acts as a pressure surface while the outer becomes a suction. The static pressure gradient thus became negative with a mild decline of -0.067 $\frac{C_P}{\delta R/H}$ across the width. A further effect was an increase in the measured static pressure value for this condition. Due to the rotating reference frame a dynamic pressure gradient will occur proportional to the radius. The lower flow velocity within the test-section thus resulted in decelerated flow with respect to the surrounding room, causing a corresponding increase in the static pressure due to the reduced dynamic component, which can be observed in Fig. 6.29d)

For the conditions shown in Fig. 6.29c) and d), turbulence intensity was calculated with respect to the measured velocity profile as opposed to the ωR value. This was to ensure

that increased or decreased freestream velocity did not produce a misrepresentation of the turbulence intensity. The increased freestream velocity, shown in Fig. 6.29c) resulted in an increase in the mean turbulence intensity to a value of 3.28%. For the reduced freestream condition the intensity decreased to a mean value of 2.29%. In both cases increased uniformity was identified to occur across the width of the section which was attributed to the path of the flow no longer following the curvature of the test-section, which caused increased turbulent mixing.

6.7 Limitations and Future Potential

The initial motivation of the present design was to develop a concept that would allow automotive aerodynamic testing within a continuous curved path. However, inadvertently the design would also permit a range of other additional new experimental investigations. As a concept it represents a unique new way to create an environment of relative flow curvature in the absence of a static pressure gradient.

In comparison to a traditional wind tunnel the necessity of a rotor component would make it more difficult to scale due to the additional mechanical complexity. As the air within the test-section is stationary relative to the surrounding reference frame it must be considered that the desired relative freestream velocity becomes equivalent to the tangential velocity of the test-section itself.

The proof-of-concept design is limited to testing only one corner radius. It would be possible to test different relative corner radii by using different scale models, and then conducting analysis at a common Reynolds number by running the experiment at different speeds, as is shown in Fig. 6.30. If a new version were to be constructed it would be likely that the most simple method to aid toward overcoming this limitation would be to use a high aspect ratio test-section, with enough width for the model to be swept through different radii. Another, likely more complex, solution would be the use of flexible walls for the sections. A change in curvature radii would need to accommodate the test-section being positioned further from the centre of rotation, so the diffuser and contraction would also need to be flexible, and increase or decrease in length as required.

The high turbulence intensity and non-uniformity are undesirable for immediate experimental analysis in its current state. The inclusion of turbulence screens would be an effective method to improve these shortcomings. Screens would need to be non-uniform to ensure a uniform static pressure drop within the non-uniform velocity field. Barlow et. al [24] gave guidelines on calculating the pressure drop across screens, and this can

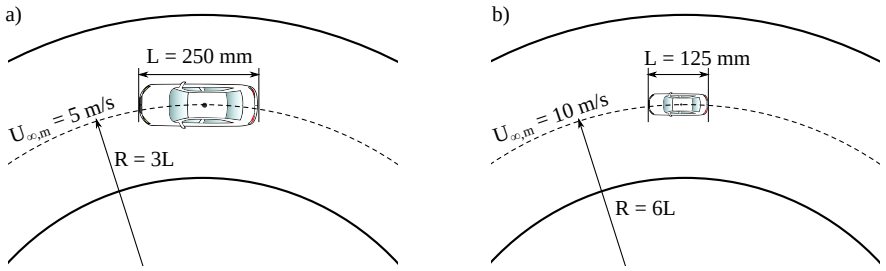

FIGURE 6.30: Illustration of how different effective corner radii could be achieved within a fixed curvature test-section at the same Re showing a a) 3L radius corner, and b) 6L radius corner

be modified to calculate the appropriate wire width and change in cell size required for a given velocity gradient.

The omission of any screens in this initial phase was deliberate to ensure that any effects due to tunnel features were not masked by screens, and the velocity field was achieved without requiring the correction provided by non-uniform screens, as has been used previously in a stationary wind tunnel test-section [25, 26]. Thus while this resulted in non-uniformity of the turbulence intensity, it permitted improved understanding of the flow characteristics.

A contraction ratio of only 2:1 would have also contributed to the high turbulence intensities. Three-dimensional contraction designs indicated potential for improved flow quality however they presented further manufacturing challenges and weren't further pursued in this instance.

Another design decision affecting flow quality was the open-circuit configuration. A return circuit was investigated, but significantly increased the complexity of the design and was unnecessary towards achieving the initial outcome.

Regions for future development include improving the contraction shape and the turning vane cascade, as well as investigating suitable techniques for boundary layer control. Frequency analysis of the velocity signal indicated the likely occurrence of trailing edge separation over the inner side of the turning vanes due to an over-expansion of the flow. A solution would be increasing the inlet area to the corner. This would result in a net contraction over the cascade, and would reduce the expansion ratio on the inner side, while still maintaining the relative contraction-to-expansion variation across the span to produce the correct velocity distribution. A second option would be entry of the flow into a diffuser with a more slight curvature, and thus a milder velocity gradient and contraction-to-expansion variation. A limitation of this approach would be that the test-section curvature would likely also be more restricted.

For automotive-specific testing a moving ground is an important feature. This will typically be achieved by using a belt positioned underneath the model that moves at the same speed as the freestream flow. For the present design the air within the test-section is stationary within the absolute reference frame, so the moving ground would need to be a stationary platform rather than a moving belt. This is not a feature present on the current design but is something that could be accommodated for in a future version.

An important final note is that the experimental rig is not required to be entirely built as its own dedicated facility. Provided there is sufficient room to accommodate the desired rotor size, the design could potentially (but not easily) be incorporated into an existing wind tunnel circuit. Dependent on a variety of circumstantial factors, this may be achieved most easily as an additional branch off the main circuit or an in-line configuration.

6.8 Summary

A new method developed for creating continuous and repeatable curved flow has been proposed and investigated through the construction and experimental analysis of a proof-of-concept. Results demonstrated the concept was capable of achieving flow conditions that were representative of the theoretical flow properties for a 750 mm mean radius corner. The design uniquely achieved these conditions in the absence of a significant static pressure gradient, or using non-uniform screens to correct the freestream velocity distribution.

The design was capable of maintaining the flow conditions consistently throughout the test-section in the vertical and downstream directions, and achieved these in a rotating, non-inertial reference frame. The results were achieved across a range of mean freestream velocities from 3.53 m/s to 5.89 m/s. Where a mild dependency on Reynolds number was attributed to the external disturbances and their effect toward the outlet condition, in addition to outer boundary effects.

The experiment established the requirement of an equivalent relationship between the freestream velocity, the angular velocity, and radius toward achieving the correct flow conditions. Overall it demonstrated that by using a rotational, non-inertial reference frame, relative flow curvature can be achieved in the absence of acceleration acting on the freestream flow.

Chapter 7

Conclusions and Future Work

7.1 Conclusions

An investigation was conducted into the aerodynamic effects of the cornering conditions for automotive applications, with a focus on steady-state constant-radius corners. The characteristics of the cornering flowfield were established and identified to have several attributes which differentiated them from the commonly investigated straight-line condition. Due to the curved path travelled by a vehicle through a corner, the relative freestream flow assumes a curvature and results in a change in the angle of yaw both along the length and across the width. Within the reference frame of the vehicle, the motion occurs within a rotating reference frame, and thus the freestream velocity increases proportional to the radial displacement, and is coupled with a radially orientated centrifugal acceleration.

A reference automotive bluff-body, the Ahmed body, was utilised to investigate several different cornering parameters using numerical simulation. Wall-resolved Large Eddy Simulations with a Smagorinsky Sub-Grid Scale model were used and were validated against existing experimental data in both the straight-line and yawed conditions. The numerical method was demonstrated as capable of capturing both the time-averaged aerodynamic effects and transient flow mechanisms within the highly turbulent flowfield.

The bluff body was investigated at constant angles of yaw to first establish flow effects attributed purely to a change in flow angle. At a constant angle of yaw the drag coefficient was identified to increase and occurred primarily due to the effective increase in frontal area and a larger wake region. There was also the introduction of a side force and yawing moment which acted positively in the direction of the flow angle. These effects were the result of enhanced suction due to increased curvature of the flow around

on the leeward side of the nose, and a comparative reduction on the opposing windward side.

The flow angle resulted in a leeward shift of flow structures with a heightened sensitivity in the separated regions. The change in freestream conditions enhanced the circulation of the windward C-pillar vortex with a comparatively minor reduction on the leeward side. Over the upper windward edge a longitudinal vortex formed and continued downstream over the upper surface of the body. This additional longitudinal vortex interacted with the backlight region, in conjunction with the C-pillar vortices, to promote attached flow. The effect reduced local surface pressure and resulted in an enhanced suction peak at the upper edge of the rear slanted surface, where the net effect caused a lift coefficient increase of a similar magnitude to that of drag. As a further effect, the reduction in size of the backlight separation bubble caused an increase in frequency of the periodic enlargement and contraction of the structure within that region, and the corresponding fluctuations in the pressure field.

Due to the curved flow of the cornering condition the flow angle was opposite at the front and rear of the body. The forebody angle resulted in outboard suction due to increased acceleration of the flow around the outboard side of the nose, this then caused the formation of larger separated vortical structures due to an enlargement of the side separation bubble. The change in flow angle at the rear caused an enhanced pressure gradient which acted in the opposite direction over the aft portion of the two sides. The upper forebody separation bubble was skewed outboard and the emitted vortices remained over the upper surface of the body due to the curved freestream direction. These features re-energised the backlight region, promoting earlier reattachment of the backlight separation bubble.

The cornering condition resulted in an increase in drag that was attributed primarily to the force component acting in the longitudinal axis of the body. The acceleration due to the rotating non-inertial reference frame resulted in a radially-orientated buoyancy which caused a reduced surface pressure on the inboard side and outboard increase. The resultant effect was a net side force that acted toward the centre of rotation. An inboard contraction of separated region at the trailing face occurred, in addition to increased circulation of the lower wake structure. The additive influence of the radially-orientated pressure gradient further reduced the inboard core pressure of the spanwise orientated wake recirculations. This then affected the primary transient mechanism of the periodic bursting of the upper and lower recirculations. The instantaneous structure revealed pronounced expansions and contractions within the lower wake region with an increased inboard component of lateral expansion as the corner radius decreased.

The effects eventuated in a decrease in the trailing face surface pressure distribution, concentrated toward the inboard side.

An increased yaw angle sensitivity was identified to occur in the cornering condition. The most conservative difference in force and moment coefficient effects occurred when the flow angle was equal and opposite at the front and rear, and highlighted the potentially more dramatic effects that could occur in reality. A positive yaw angle increment resulted in an increase in lift coefficient that was more than three times greater than the equivalent change for the pure yawed condition. This occurred due to increased circulation over the outboard edge and the correspondingly greater production of rearward lift. For practical applications the potential effect of vehicle dynamics was identified as significant, and thus emphasized the importance of replicating vehicle dynamic behaviour for development within the condition.

The yawed condition and cornering conditions were identified to exhibit limited likeness, which was primarily the result of cumulative effects attributed to flow interactions which occurred along the length of the body. Similarity in flow structures and surface pressure distribution was observed to occur in the forebody region, where local changes were predominantly due to the oncoming flow angle. Direct comparison of the flowfields identified the longitudinal vortex structure to primarily cause the cumulative effects which differentiated the two conditions.

Inherent to the cornering condition was the acceleration due to the rotating reference frame and the resultant pressure gradient within the boundary layer. In addition, a greater contraction of the spanwise orientated wake recirculations occurred causing a larger increase in the drag component acting in the x-direction. A comparison based purely on the absolute difference in force and moment magnitudes (ignoring the opposing trends which occurred in lift, yawing moment, and pitching moment) was used to crudely equate the two conditions and identified a yaw angle to curvature ratio of $\psi = 25.12\,\kappa$. Results indicated that development of any vehicle within the yawed condition could translate poorly to the cornering condition.

A limitation for development within the cornering condition has been the absence of an experimental method that is capable of recreating the correct conditions. To overcome this a new experimental method was conceived which was designed to enable continuous and repeatable cornering conditions to be achieved within a controlled experimental environment. A prototype was constructed to simulate a 750 mm constant radius corner within an accelerating non-inertial reference frame. The concept achieved these conditions by delivering flow to a rotating test-section in the absence of flow acceleration. With the correct relationship maintained between the freestream and angular velocity the design was able to maintain accurate conditions throughout the test-section for three

different Reynolds numbers. The development of this method would thus permit a wide variety of unique new analyses, as well as open the possibility for future experimental studies to supplement the numerical findings detailed throughout the present work.

7.2 Future Work

Inevitably through conducting this investigation, a number of areas have been identified that would be of interest to pursue in future studies.

The flowfield that occurs relative to a vehicle in the cornering condition has little resemblance to most other practically investigated flowfields. Analysis of specific flow structures in near-isolation, such as turbulent boundary layers, separation bubbles, and vortices, would likely reveal specific properties that were not apparent in the present study. To further build on the present findings, future analyses should consider other reference geometries. This would enable better understanding of how different vehicle types are affected within the condition, and allow an assessment of the universality of the cornering flow phenomena identified in the present study.

How these cornering-specific effects differ when analysing a vehicle with wheels, and tyre deformation, would be particularly interesting, and could result in substantial changes to the flowfield. Cornering analyses should also not remain restricted to passenger vehicles. Motorsport is an example where aerodynamic performance in the cornering condition is most critical, and analysis of such vehicles would be of high industrial relevance. There are also related external applications that are yet to be areas of extensive research. Such an example would be submarines, where a very large angular variation will occur over its ellipsoidal surface during manoeuvring.

The present work only considers steady-state, constant radius corners. A logical progression would be to conduct analyses which also consider the entry and exit of the cornering condition, and progress to further scenarios. It would be expected that flowfield hysteresis would result in an interesting varied temporal response of the cornering-specific effects. It would be important that this progression adopts a systematic approach, as prior research has demonstrated that simulating the multiple curvatures of a specified path has been able to reveal little about cornering-specific flow phenomena.

The experimental method that was designed has indicated future potential to investigate the cornering flowfield within controlled conditions. The method would permit unique new analyses of a range of objects assuming a curved path in a rotating non-inertial reference frame; not be restricted to cornering vehicles. Feasibly this method could be further developed into a experimental rig that is far more adaptable to allow analysis of a

wider variety of different flow curvature and conditions. Such a development would then permit complementary experimental investigations to corroborate the present numerical findings. The specific regions of development for the experiment itself are discussed in detail within Chapter 6 but should generally focus on improving the turning vane cascade and reducing the turbulence intensity in the test-section, as well as looking toward a more versatile future design.

Appendix A

Calculation of Aerodynamic Drag

Aerodynamic drag, by definition, is the resistance to motion through the freestream air. As any object assumes a path that is no longer orientated in a straight-line, the aerodynamic resistance to its motion does the same. The drag coefficient for an object moving in a curved path becomes proportional to the tangential force causing the moment which acts in the opposite direction about the centre of rotation.

The following section details the method for numerical simulation results where the drag force was calculated using the freestream flow angle, and surface orientation with respect to that direction, to calculate an equivalent aerodynamic drag coefficient which could directly compared to the straight-line result.

Pressure drag was calculated by integrating the surface static pressure at each cell over the frontal area normal to the flow angle. Viscous drag was evaluated in a similar fashion using wall shear components integrated over the planar surface area relative to flow.

The velocity at any given point in the flow-field was described with respect to the instantaneous centre of rotation shown at (x_c, y_c).

$$U_\infty = \omega \times \sqrt{(y - y_c)^2 + (x - x_c)^2} \tag{A.1}$$

Thus the pressure coefficient (C_P) was defined where U_∞ now varies:

$$C_P = \frac{p}{0.5 \times \rho \times U_\infty^2} \tag{A.2}$$

The flow angle relative to the x-direction is given by:

$$tan\psi_{flow} = \frac{x - x_c}{y - y_c} \tag{A.3}$$

The angle of the cell face is determined by the projected face area of the cell in the x (A_{fx}) and y (A_{fy}) directions :

$$tan\psi_{face} = \frac{A_{fx}}{A_{fy}} \tag{A.4}$$

Thus the differential angle between the freestream flow angle and face angle is given by:

$$\psi_p = \psi_{face} - \psi_{flow} \tag{A.5}$$

The total face area of the cell in the x-y plane is given by:

$$A_{fxy}^2 = A_{fx}^2 + A_{fy}^2 \tag{A.6}$$

The observed face area of a given cell with respect to the freestream flow will be given by:

$$A_{fo} = A_{fxy} sin(\psi) \tag{A.7}$$

The pressure drag component then becomes:

$$C_{DP} = \frac{\sum(C_p A_{fo})}{A_{ref}} \tag{A.8}$$

Where A_{ref} is the frontal area in the case of the Ahmed body. The coefficients of wall-shear in each direction ($C_{\tau x}, C_{\tau y}, C_{\tau z}$) are considerd to calculate the viscous component.

The face area tangential to the flow direction is given by:

$$A_{ft}^2 = A_{fz}^2 + (A_{fy} cos\psi_{flow} + A_{fx} cos\psi_{flow})^2 \tag{A.9}$$

The planar shear coefficient gives the wall-shear coefficient acting in the plane tangential to the direction of passage:

$$\psi_{shear} = C_{\tau x} cos\psi_{flow} + C_{\tau y} sin\psi_{flow} \tag{A.10}$$

As a result the viscous drag coefficient then becomes:

$$C_{Dv} = \frac{\sum(\psi_{shear} A_{ft})}{A_{ref}} \tag{A.11}$$

Drag coefficient is then equal to the sum of the pressure and viscous components:

$$C_D = C_{DP} + C_{Dv} \tag{A.12}$$

Appendix B

Experimental Uncertainty Analysis

A $\pm 2\sigma$ interval was calculated as shown in Table B.1 to determine measurement variability. Values were calculated with respect to the rotor angular velocity and mean flow velocity, which resulted in a minimum of 168 individual samples for each.

TABLE B.1: Calculated 2σ interval width for experimental results taken at specified test-section angular and mean flow velocity

		$2\sigma_{X-X_{mean}}$		
ω (rad/s)	$U_{\infty,m}$ (m/s)	Velocity (u/U_∞)	Static Pressure (C_P)	Turb. Intensity (%)
6.28	4.71	0.0176	0.0155	0.169
6.28	3.20	0.0247	0.0296	0.346
6.28	7.20	0.0173	0.0063	0.509
7.85	5.89	0.0169	0.0154	0.312
4.71	3.53	0.0225	0.0191	0.281
0	4.71	0.0179	0.0078	0.295

B.1 Fixed Velocity Uncertainty

Uncertainty in velocity was attributed to the temperature and its affect on the recorded voltage, in addition to the respective uncertainty due to both the angular velocity and radial position.

$$\delta U_X = \frac{\partial}{\partial X}\left(\left(\frac{\left(\frac{T_w - T_0}{T_w - T_a}\right)(A + BU_\infty^n) - A}{B}\right)^{\frac{1}{n}}\right)\delta X + \frac{\partial}{\partial X}(\omega R)\delta X \qquad \text{(B.1)}$$

The temperature correction was calculated with respect to the theoretical freestream velocity. A, B and n were the averaged coefficients extracted from the King's law curve fit in the form $E^2 = A + BU^n$

Components were calculated based on the respective uncertainty within each value: $\delta U_R, \delta U_\omega$, δU_{T_a}, and δU_{T_0}

$$\delta U_R = \omega \ \delta R \tag{B.2}$$

$$\delta U_\omega = R \ \delta \omega \tag{B.3}$$

$$\delta U_{T_a} = \frac{(A + BU_\infty^n)(T_0 - T_w)\left(\frac{\left(\frac{T_w - T_0}{T_w - T_a}\right)(A+BU_\infty^n) - A}{B}\right)^{(\frac{1}{n}-1)}}{Bn(T_a - T_w)^2}\delta T_a \tag{B.4}$$

$$\delta U_{T_0} = \frac{(A + BU_\infty^n)\left(\frac{\left(\frac{T_w - T_0}{T_w - T_a}\right)(A+BU_\infty^n) - A}{B}\right)^{(\frac{1}{n}-1)}}{Bn(T_a - T_w)}\delta T_0 \tag{B.5}$$

The absolute calibration error of 0.067 m/s was normalised to give an estimate of the associated uncertainty attributed to probe accuracy.

RSS $\delta U_{i,fixed}$ was calculated and normalised to give a fixed error estimate.

B.2 Fixed Static Pressure Uncertainty

Fixed static pressure uncertainty was calculated as a product of the error in relative total pressure attributed to the angular velocity, density, and radial position accuracy. The respective effects towards the pressure correction applied in both the radial and vertical positions were also included.

$$\delta p_X = \frac{\partial}{\partial X}\left(0.5\rho R^2\omega^2\right)\delta X + \frac{\partial}{\partial X}\left(\frac{\rho\omega^2 R^2}{2}\right)\delta X + \frac{\partial}{\partial X}\left(\rho g z\right)\delta X \tag{B.6}$$

Where ρ was calculated assuming an ideal gas:

$$\delta \rho_X = \frac{\partial}{\partial X}\left(\frac{P_{abs}}{287.058\ T_0}\right)\delta X \tag{B.7}$$

Components were then determined individually:

$$\delta p_R = \rho R\omega^2(1 + R)\delta R \tag{B.8}$$

$$\delta p_\omega = \rho R^2\omega(1 + \frac{2}{3}R)\delta\omega \tag{B.9}$$

$$\delta p_{T_0} = \frac{0.5\ P_{abs}}{-287.058\ T_0^2}(R^2\omega^2 + \frac{\omega^2 R^2}{2} + gz)\delta T \tag{B.10}$$

$$\delta p_{P_{abs}} = \frac{0.5}{287.058\ T_0}(R^2\omega^2 + \frac{\omega^2 R^2}{2} + gz)\delta P_{abs} \tag{B.11}$$

$$\delta p_z = \rho g\ \delta z \tag{B.12}$$

The absolute calibration error of 0.015 Pa was normalised with respect to the dynamic pressure to give a calibration error estimate. Components were combined to determine a normalised $RSS\ \delta p_{i,fixed}$.

B.3 Fixed Turbulence Uncertainty

Turbulence intensity was calculated with respect to the theoretical freestream velocity according to $U_\infty = \omega R$. Thus making the uncertainty dependent on the accuracy of radial position, angular velocity, and the recorded velocity RMSD (Root Mean Square Derivative).

$$\delta(I)_X = \frac{\partial}{\partial X}\left(\frac{U_{RMSD}}{\omega R}\right)\delta X \tag{B.13}$$

δU_{RMSD} was dependent on the fixed error of the velocity measurement ($\delta U_{i,fixed}$) applied over a $\pm 2\sigma$ range of measured instantaneous values.

$$\delta U_{RMSD} = 2\sigma_U(\delta U_{i,fixed}) \tag{B.14}$$

Thus component based contributions to uncertainty became:

$$\delta(I)_R = \left(\frac{U_{RMSD}}{\omega R^2}\right)\delta R \tag{B.15}$$

$$\delta(I)_\omega = \left(\frac{U_{RMSD}}{\omega^2 R}\right)\delta\omega \tag{B.16}$$

$$\delta(I)_{U_{RMSD}} = \left(\frac{1}{\omega R}\right)\delta U_{RMSD} \tag{B.17}$$

Bibliography

[1] Watkins, S., Saunders, J., and Hoffmann, P. Turbulence experienced by moving vehicles. Part I. Introduction and turbulence intensity. *Journal of Wind Engineering and Industrial Aerodynamics*, 57(1):1–17, 1995. ISSN 01676105. doi: 10.1016/0167-6105(94)00100-R.

[2] Watkins, S. and Vino, G. The effect of vehicle spacing on the aerodynamics of a representative car shape. *Journal of Wind Engineering and Industrial Aerodynamics*, 96(6-7):1232–1239, 2008. ISSN 01676105. doi: 10.1016/j.jweia.2007.06.042.

[3] Okada, Y., Nouzawa, T., Okamoto, S., Fujita, T., Kamioka, T., and Tsubokura, M. Unsteady Vehicle Aerodynamics during a Dynamic Steering Action: 1st Report, On-Road Analysis. April 2012. doi: 10.4271/2012-01-0446. URL `http://www.sae.org/technical/papers/2012-01-0446`.

[4] Tsubokura, M., Ikawa, Y., Nakashima, T., Okada, Y., Kamioka, T., and Nouzawa, T. Unsteady Vehicle Aerodynamics during a Dynamic Steering Action: 2nd Report, Numerical Analysis. April 2012. doi: 10.4271/2012-01-0448. URL `http://www.sae.org/technical/papers/2012-01-0448`.

[5] Nara, K., Tsubokura, M., Ikeda, J., and Fasel, U. Numerical Analysis of Unsteady Aerodynamics of Formula Car during Dynamic Cornering Motion. (June):1–11, 2014.

[6] Toet, W. Aerodynamics and aerodynamic research in Formula 1. *The Aeronautical Journal*, 117(1187):1–26, 2013.

[7] Katz, J. Aerodynamics of Race Cars. *Annual Review of Fluid Mechanics*, 38(1):27–63, January 2006. ISSN 0066-4189. doi: 10.1146/annurev.fluid.38.050304.092016. URL `http://www.annualreviews.org/doi/abs/10.1146/annurev.fluid.38.050304.092016`.

[8] Zhang, X., Toet, W., and Zerihan, J. Ground Effect Aerodynamics of Race Cars. *Applied Mechanics Reviews*, 59(1):33, 2006. ISSN 00036900. doi: 10.1115/

1.2110263. URL http://appliedmechanicsreviews.asmedigitalcollection.asme.org/article.aspx?articleid=1398447.

[9] Milliken, W. F. and Milliken, D. L. Race Car Vehicle Dynamics, 1995. URL https://docs.google.com/leaf?id=0B-b_sxKZve6oYTg3NWZiZDItMDBhZC00MWY0LWFhMjItOTNiMDU4ZWNhNDc2&hl=en_US.

[10] Sims-williams, D. B. and Dominy, R. G. Experimental Investigation into Unsteadiness and Instability in Passenger Car Aerodynamics. *SAE, Technical Paper Series*, (724), 1998. doi: 10.4271/980391.

[11] Keogh, J., Doig, G., Diasinos, S., and Barber, T. The influence of cornering on the vortical wake structures of an inverted wing. *Proceedings of the Institution of Mechanical Engineers, Part D: Journal of Automobile Engineering*, pages 1–13, 2015. ISSN 0954-4070. doi: 10.1177/0954407015571673. URL http://pid.sagepub.com/lookup/doi/10.1177/0954407015571673.

[12] Dijck, T. V. Computational Evaluation of Aerodynamic Forces on a Racing Motorcycle during High Speed Cornering. *SAE Technical Paper Series*, 2015. doi: 10.4271/2015-01-0097.Copyright.

[13] Albukrek, C., Doddegowda, P., Ivaldi, A., and Amodeo, J. Unsteady Flow Analysis of a Formula Type Open Wheel Race Car in Cornering. In *SAE Technical Paper Series*, number 724, pages 1–21, Dearborn, Michigan, 2006. ISBN 2006013661.

[14] Johansson, M. O. and Katz, J. Lateral Aerodynamics of a Generic Sprint Car Configuration. *SAE Technical Paper Series*, 01(3312):1–10, 2002.

[15] Collins, S. The secrets of Laurel Hill revealed. *Racecar Engineering*, 2014.

[16] Curtiss, H. C., Putman, W. F., and Traybar, J. J. The Princeton Dynamic Model Track. Technical report, Princeton University, 1963. URL http://dx.doi.org/10.2514/6.1964-1104.

[17] Curtiss, H. C., Sun, M., Putman, W. F., and Hanker, E. J. Rotor Aerodynamics in Ground Effect at Low Advance Ratios. *Journal of the American Helicopter Society*, 29(1):48, 1984. ISSN 00028711. doi: 10.4050/JAHS.29.48.

[18] Mason, W. H. Summary of Wind Tunnel Test Facilities. Technical report, Department of Aerospace and Ocean Engineering, Virginia Polytechnic Institute, Blacksburg, VA, 1981.

[19] Ito, H. Flow in curved pipes. *JSME international journal*, 30(262):543–552, 1987. ISSN 0913-185X. doi: 10.1299/jsme1987.30.543.

[20] Humphrey, J. a. C., Whitelaw, J. H., and Yee, G. Turbulent flow in a square duct with strong curvature. *Journal of Fluid Mechanics*, 103(-1):443, 1981. ISSN 0022-1120. doi: 10.1017/S0022112081001419.

[21] Daskopoulos, P. and Lenhoff, a. M. Flow in curved ducts: bifurcation structure for stationary ducts. *Journal of Fluid Mechanics*, 203:125, 1989. ISSN 0022-1120. doi: 10.1017/S0022112089001400.

[22] Daskopoulos, P. and Lenhoff, a. M. Flow in curved ducts. Part 2. Rotating ducts. *Journal of Fluid Mechanics*, 217(-1):575, April 1990. ISSN 0022-1120. doi: 10.1017/S0022112090000854. URL `http://www.journals.cambridge.org/abstract_S0022112090000854`.

[23] Prandtl, L. Attaining A Steady Stream in Wind Tunnels. *National Advisory Committee for Aeronautics Technical Note*, (726), 1933.

[24] Barlow, J., Rae, W. H., and Pope, A. *Low-Speed Wind Tunnel Testing*. John Wiley & Sons, 3rd edition, 1999.

[25] Chambers, J. R., Grafton, S. B., and Lutze, F. H. Curved Flow, Rolling Flow, and Oscillatory Pure-Yawing Wind-Tunnel Test Methods for Determination of Dynamic Stability Derivatives. *NATO AGARD Lecture Series No. 114 - Dynamic Stability Parameters*, 7, 1981.

[26] Bird, B. J. D., Jaquet, B. M., and Field, L. Effect of Fuselage and Tail Surface on Low-Speed Yawing Characteristics of a Swept-Wing Model as Determined in Curved-Flow Test-Section of Langley Stability Tunnel. Technical Report 2483, 1951.

[27] Orlik-Ruckemann, K. Methods of Measurement of Aircraft Dynamic Stability Derivatives. *National Research Council of Canada*, 1959.

[28] Foster, D. J. and Haynes, G. W. Rotary Stability Derivatives from Distorted Models. *Journal of the Royal Aeronautical Society*, 60, 1956.

[29] Gordes, A. Process for simulating curved airflows on wheeled vehicles in fluid flow channels with a straight measuring section, 2005.

[30] Baals, D. and Corliss, W. Wind Tunnels of NASA, 2014. URL `http://www.hq.nasa.gov/pao/History/SP-440/contents.htm`.

[31] Llewelyn-Davies, D. J. T. P. The Redesign of the College of Aeronautics Whirling Arm Facility. Technical Report 8702, College of Aeronautics, Cranfield Institute of Technology, 1987.

[32] Kumar, P. E. The College of Aeronautics Whirling Arm Initial Development Tests. Technical Report 174, College of Aeronautics, Cranfield University, 1967.

[33] Ericson, L. E. Reflections regarding recent rotary rig results. *Journal of Aircraft*, 24(1):25–30, 1987. ISSN 0021-8669. doi: 10.2514/3.45406.

[34] Pattinson, J., Lowenberg, M. H., and Goman, M. G. Multi-Degree-of-Freedom Wind-Tunnel Maneuver Rig for Dynamic Simulation and Aerodynamic Model Identification. *Journal of Aircraft*, 50(2):551–566, 2013. ISSN 0021-8669. doi: 10.2514/1.C031924. URL `http://arc.aiaa.org/doi/abs/10.2514/1.C031924$\delimiter"026E30F$nhttp://dx.doi.org/10.2514/1.C031924`.

[35] Beyers, M. Unsteady Wall Interference in Rotary Tests. In *AIAA 27th Aerospace Sciences Meeting*, pages 1–9, Reno, Nevada, 1989.

[36] Garry, K. P. and Cooper, K. R. Comparison of Quasi-Static and Dynamic Wind Tunnel Measurements on Simplified Tractor-Trailer Models. *Journal of Wind Engineering and Industrial Aerodynamics*, 22(2-3):185–194, 1986.

[37] Watkins, S., Toksoy, S., and Saunders, J. On the Generation of Turbulence for Road Vehicles. In *11th Australasian Fluid Mechanics Conference*, pages 223–226, Hobart, Australia, 1992.

[38] Duell, E., Kharazi, A., and Muller, S. The BMW AVZ Wind Tunnel Center. *SAE Technical Paper Series*, 01(118):1–32, 2010.

[39] Le Good, G. M. and Garry, K. P. On the Use of Reference Models in Automotive Aerodynamics. *SAE Technical Paper Series*, 01(1308), 2004.

[40] Ahmed, S. R., Ramm, G., and Faltin, G. Some Salient Features of the Time-Averaged Ground Vehicle Wake. *SAE Technical Paper Series*, 1984.

[41] Mankowski, O. *The Wind Tunnel Simulation and Effect of Turbulent Air flow on Automotive Aerodynamics*. PhD thesis, Durham University, 2013.

[42] D'Hooge, A., Palin, R., Rebbeck, L., Gargoloff, J., and Duncan, B. Alternative Simulation Methods for Assessing Aerodynamic Drag in Realistic Crosswind. *SAE Technical Paper Series*, 01(0599), April 2014. doi: 10.4271/2014-01-0599. URL `http://www.sae.org/technical/papers/2014-01-0599`.

[43] Docton, M. K. R. *The Simulation of Transient Cross Winds on Passenger Vehicles*. PhD thesis, University of Durham, 1997.

[44] Favre, T. *Aerodynamics simulations of ground vehicles in an unsteady crosswind*. 2011. ISBN 9789175011967.

[45] Tsubokura, M., Nakashima, T., Kitayama, M., Ikawa, Y., Doh, D. H., and Kobayashi, T. Large eddy simulation on the unsteady aerodynamic response of a road vehicle in transient crosswinds. *International Journal of Heat and Fluid Flow*, 31(6):1075–1086, December 2010. ISSN 0142727X. doi: 10.1016/j.ijheatfluidflow.2010.05.008. URL `http://linkinghub.elsevier.com/retrieve/pii/S0142727X10000974`.

[46] Volpe, R., Ferrand, V., Da, A., and Le, L. Forces and flow structures evolution on a car body in a sudden crosswind. *Journal of Wind Engineering and Industrial Aerodynamics*, 128:114–125, 2014. ISSN 0167-6105. doi: 10.1016/j.jweia.2014.03.006. URL `http://dx.doi.org/10.1016/j.jweia.2014.03.006`.

[47] Passmore, M. A., Richardson, S., and Imam, A. An experimental study of unsteady vehicle. *Proceedings of the Institution of Mechanical Engineers , Part D : Journal of Automobile Engineering*, 2001.

[48] Cheng, S. Y., Tsubokura, M., Nakashima, T., Okada, Y., and Nouzawa, T. Numerical quantification of aerodynamic damping on pitching of vehicle-inspired bluff body. *Journal of Fluids and Structures*, 30:188–204, 2012. ISSN 08899746. doi: 10.1016/j.jfluidstructs.2012.01.002. URL `http://dx.doi.org/10.1016/j.jfluidstructs.2012.01.002`.

[49] Cheng, S. Y., Tsubokura, M., Okada, Y., Nouzawa, T., Nakashima, T., and Doh, D. H. Aerodynamic stability of road vehicles in dynamic pitching motion. *Journal of Wind Engineering and Industrial Aerodynamics*, 122:146–156, 2013. ISSN 01676105. doi: 10.1016/j.jweia.2013.06.010. URL `http://dx.doi.org/10.1016/j.jweia.2013.06.010`.

[50] Mansor, S. and Passmore, M. Estimation of bluff body transient aerodynamics using an oscillating model rig. *Journal of Wind Engineering and Industrial Aerodynamics*, 96(6-7):1218–1231, June 2008. ISSN 01676105. doi: 10.1016/j.jweia.2007.06.043. URL `http://linkinghub.elsevier.com/retrieve/pii/S0167610507001675`.

[51] Watts, M. and Watkins, S. Aerodynamic Structure and Development of Formula 1 Racing Car Wakes. 2014. ISSN 19464002. doi: 10.4271/2014-01-0600. URL `http://www.sae.org/technical/papers/2014-01-0600`.

[52] Serre, E., Minguez, M., Pasquetti, R., Guilmineau, E., Deng, G. B., Kornhaas, M., Schäfer, M., Fröhlich, J., Hinterberger, C., and Rodi, W. On simulating the turbulent flow around the Ahmed body: A French-German collaborative evaluation of LES and DES. *Computers and Fluids*, 78:10–23, April 2013. ISSN 00457930.

doi: 10.1016/j.compfluid.2011.05.017. URL http://linkinghub.elsevier.com/retrieve/pii/S0045793011001885.

[53] Aljure, D. E., Lehmkuhl, O., Rodríguez, I., and Oliva, a. Flow and turbulent structures around simplified car models. *Computers and Fluids*, 96:122–135, 2014. ISSN 00457930. doi: 10.1016/j.compfluid.2014.03.013. URL http://dx.doi.org/10.1016/j.compfluid.2014.03.013.

[54] Guilmineau, E., Deng, G., and Wackers, J. Numerical simulation with a DES approach for automotive flows. *Journal of Fluids and Structures*, 27:807–816, July 2011. ISSN 08899746. doi: 10.1016/j.jfluidstructs.2011.03.010. URL http://linkinghub.elsevier.com/retrieve/pii/S0889974611000399.

[55] Minguez, M., Pasquetti, R., and Serre, E. High-order large-eddy simulation of flow over the "Ahmed body" car model. *Physics of Fluids*, 20(9):1–17, 2008. ISSN 10706631. doi: 10.1063/1.2952595. URL http://scitation.aip.org/content/aip/journal/pof2/20/9/10.1063/1.2952595.

[56] Han, T. Computational Analysis of Three-Dimensional Turbulent Flow Around a Bluff Body in Ground Proximity. *AIAA*, 27(9):1213–1219, 1989.

[57] Fares, E. Unsteady flow simulation of the Ahmed reference body using a lattice Boltzmann approach. *Computers & Fluids*, 35(8-9):940–950, September 2006. ISSN 00457930. doi: 10.1016/j.compfluid.2005.04.011. URL http://linkinghub.elsevier.com/retrieve/pii/S0045793005001581.

[58] Krajnovic, S. and Davidson, L. Flow Around a Simplified Car, Part 1: Large Eddy Simulation. *Journal of Fluids Engineering*, 127(September):907–918, 2005. ISSN 00982202. doi: 10.1115/1.1989371. URL http://fluidsengineering.asmedigitalcollection.asme.org/article.aspx?articleid=1430210.

[59] Krajnovic, S. and Davidson, L. Flow Around a Simplified Car, Part 2: Understanding the Flow. *Journal of Fluids Engineering*, 127(September):919–928, 2005. ISSN 00982202. doi: 10.1115/1.1989372. URL http://fluidsengineering.asmedigitalcollection.asme.org/article.aspx?articleid=1430211.

[60] Guilmineau, E., Chikhaoui, O., Deng, G., and Visonneau, M. Cross wind effects on a simplified car model by a DES approach. *Computers and Fluids*, 78:29–40, 2013. ISSN 00457930. doi: 10.1016/j.compfluid.2011.08.020. URL http://dx.doi.org/10.1016/j.compfluid.2011.08.020.

[61] Spalart, P. R., Jou, W. H., Strelets, M., and Allmaras, S. R. Comments on the feasibility of LES for wings and on a hybrid RANS/LES approach. *Advances in DNS/LES*, 1(JANUARY):4–8, 1997.

[62] Strachan, R. K., Knowles, K., and Lawson, N. J. The vortex structure behind an Ahmed reference model in the presence of a moving ground plane. *Experiments in Fluids*, 42(5):659–669, February 2007. ISSN 0723-4864. doi: 10.1007/s00348-007-0270-x. URL `http://link.springer.com/10.1007/s00348-007-0270-x`.

[63] Lienhart, H. and Becker, S. Flow and Turbulence Structure in the Wake of a Simplified Car Model. *SAE Technical Paper Series*, 01(0656), 2003.

[64] Bayraktar, I., Landman, D., and Baysal, O. Experimental and Computational Investigation of Ahmed Body for Ground Vehicle Aerodynamics. *SAE Technical Paper Series*, 1(2742), 2001.

[65] Krajnovic, S. and Davidson, L. Large-eddy simulation of the flow around simplified car model. *SAE Technical Paper Series*, 01(0227):1–10, 2004. URL `http://www.tfd.chalmers.se/~lada/postscript_files/SAE2004_sinisa_paper.pdf$\delimiter"026E30F$npapers3://publication/uuid/C2812030-8E61-4408-849C-33187CD7DDF6`.

[66] Vino, G., Watkins, S., Mousley, P., Watmuff, J., and Prasad, S. Flow structures in the near-wake of the Ahmed model. *Journal of Fluids and Structures*, 20(5): 673–695, July 2005. ISSN 08899746. doi: 10.1016/j.jfluidstructs.2005.03.006. URL `http://linkinghub.elsevier.com/retrieve/pii/S0889974605000514`.

[67] Conan, B., Anthoine, J., and Planquart, P. Experimental aerodynamic study of a car-type bluff body. *Experiments in Fluids*, 50:1273–1284, 2011. ISSN 07234864. doi: 10.1007/s00348-010-0992-z.

[68] Sims-williams, D. B. and Duncan, B. D. The Ahmed Model Unsteady Wake : Experimental and Computational Analyses. *SAE Technical Paper Series*, 01 (1315), 2003.

[69] Thacker, a., Aubrun, S., Leroy, a., and Devinant, P. Experimental characterization of flow unsteadiness in the centerline plane of an Ahmed body rear slant. *Experiments in Fluids*, 54, 2013. ISSN 07234864. doi: 10.1007/s00348-013-1479-5.

[70] Tunay, T., Sahin, B., and Ozbolat, V. Effects of rear slant angles on the flow characteristics of Ahmed body. *Experimental Thermal and Fluid Science*, 57:165–176, September 2014. ISSN 08941777. doi: 10.1016/j.expthermflusci.2014.04.016. URL `http://linkinghub.elsevier.com/retrieve/pii/S0894177714001137`.

[71] Fourrie, G., Keirsbulck, L., and Labraga, L. Wall shear stress characterization of a 3D bluff-body separated flow. *Journal of Fluids and Structures*, 42:55–69, 2013.

ISSN 08899746. doi: 10.1016/j.jfluidstructs.2013.05.014. URL http://dx.doi.org/10.1016/j.jfluidstructs.2013.05.014.

[72] Howard, R. J. a. and Pourquie, M. Large eddy simulation of an Ahmed reference model. *Journal of Turbulence*, 3, 2002. ISSN 1468-5248. doi: 10.1088/1468-5248/3/1/012.

[73] Joseph, P., Amandolèse, X., and Aider, J.-L. Drag reduction on the 25 degree slant angle Ahmed reference body using pulsed jets. *Experiments in Fluids*, 52 (5):1169–1185, December 2011. ISSN 0723-4864. doi: 10.1007/s00348-011-1245-5. URL http://link.springer.com/10.1007/s00348-011-1245-5.

[74] Kohri, I., Yamanashi, T., Nasu, T., Hashizume, Y., and Katoh, D. Study on the Transient Behaviour of the Vortex Structure behind Ahmed Body. *SAE Technical Paper Series*, 01(0597), 2014. ISSN 19464002. doi: 10.4271/2014-01-0597. URL http://www.sae.org/technical/papers/2014-01-0597.

[75] Wang, X. W., Zhou, Y., Pin, Y. F., and Chan, T. L. Turbulent near wake of an Ahmed vehicle model. *Experiments in Fluids*, 54(4):1490, April 2013. ISSN 0723-4864. doi: 10.1007/s00348-013-1490-x. URL http://link.springer.com/10.1007/s00348-013-1490-x.

[76] Zhang, B. F., Zhou, Y., and To, S. Unsteady flow structures around a high-drag Ahmed body. *Journal of Fluid Mechanics*, 777:291—-326, 2015. doi: 10.1017/jfm.2015.332.

[77] Spohn, A. and Gilliéron, P. Flow separations generated by a simplified geometry of an automotive vehicle. *IUTAM Symposium: unsteady separated flows*, 2002. URL http://www.ercoftac.org/fileadmin/user_upload/bigfiles/sig15/database/9.4/IUTAM_Spohn-Gillieron_2002.pdf.

[78] Basara, B. Case 9.4 Flow around a simplified car body (Ahmed body), 2001. URL http://www.ercoftac.org/fileadmin/user_upload/bigfiles/sig15/database/9.4/.

[79] Thacker, a., Aubrun, S., Leroy, a., and Devinant, P. Effects of suppressing the 3D separation on the rear slant on the flow structures around an Ahmed body. *Journal of Wind Engineering and Industrial Aerodynamics*, 107-108:237–243, August 2012. ISSN 01676105. doi: 10.1016/j.jweia.2012.04.022. URL http://linkinghub.elsevier.com/retrieve/pii/S0167610512001249.

[80] Heft, A. I., Indinger, T., and Adams, N. A. Investigation of Unsteady Flow Structures in the Wake of a Realistic Generic Car Model. In *29th AIAA Applied Aerodynamics Conference*, number June, pages 1–14, 2011.

[81] Smagorinsky, J. General Circulation Experiments with the Primitive Equations. *Monthly Weather Review*, 91(3):99–164, April 1963. ISSN 0036-8075. doi: 10.1126/science.27.693.594. URL http://www.ncbi.nlm.nih.gov/pubmed/17732006.

[82] Menter, F. R. Two-equation eddy-viscosity turbulence models for engineering applications. *AIAA Journal*, 32(8):1598–1605, August 1994. ISSN 0001-1452. doi: 10.2514/3.12149. URL http://arc.aiaa.org/doi/abs/10.2514/3.12149.

[83] Meile, W., Ladinek, T., Brenn, G., Reppenhagen, a., and Fuchs, a. Non-symmetric bi-stable flow around the Ahmed body. *International Journal of Heat and Fluid Flow*, 57:34–47, 2016. ISSN 0142727X. doi: 10.1016/j.ijheatfluidflow.2015.11.002. URL http://linkinghub.elsevier.com/retrieve/pii/S0142727X15001320.

[84] Gohlke, M., Beaudoin, J. F., Amielh, M., and Anselmet, F. Experimental analysis of flow structures and forces on a 3D-bluff-body in constant cross-wind. *Experiments in Fluids*, 43(4):579–594, July 2007. ISSN 0723-4864. doi: 10.1007/s00348-007-0341-z. URL http://link.springer.com/10.1007/s00348-007-0341-z.

[85] Volpe, R., Devinant, P., and Kourta, A. Experimental characterization of the unsteady natural wake of the full-scale square back Ahmed body: flow bi-stability and spectral analysis. *Experiments in Fluids*, 56(5):1–22, 2015. ISSN 0723-4864. doi: 10.1007/s00348-015-1972-0. URL http://link.springer.com/10.1007/s00348-015-1972-0.

[86] Krentel, D. and Nitsche, W. Investigations on Active Drag Control on a Bluff Body with Cross-Wind. *New Results in Numerical and Experimental Fluid Mechanics*, 121:177–184, 2013. ISSN 16122909. doi: 10.1007/978-3-642-35680-3. URL http://www.scopus.com/inward/record.url?eid=2-s2.0-84873639141&partnerID=tZOtx3y1.

[87] Mullarkey, S. P. *Aerodynamic stability of road vehicles in sidewinds and gusts*. PhD thesis, Imperial College London (University of London), 1990.

[88] Fuller, J., Best, M., Garret, N., and Passmore, M. The importance of unsteady aerodynamics to road vehicle dynamics. *Journal of Wind Engineering and Industrial Aerodynamics*, 117:1–10, 2013. ISSN 01676105. doi: 10.1016/j.jweia.2013.03.006. URL http://dx.doi.org/10.1016/j.jweia.2013.03.006.

[89] Ferrand, V. Forces and Flow Structures on a Simplified Car Model Exposed to an Unsteady Harmonic Crosswind. *Journal of Fluids Engineering*, 136(1):011101, 2013. ISSN 0098-2202. doi: 10.1115/1.

4025466. URL http://fluidsengineering.asmedigitalcollection.asme.org/article.aspx?doi=10.1115/1.4025466.

[90] Baker, C. J. Ground Vehicles in High Cross-Winds Part 1: Steady Aerodynamic Forces. *Journal of Fluids and Structures*, pages 69–90, 1991.

[91] Howell, J. Aerodynamic Drag of Passenger Cars at Yaw. *SAE International Journal of Passenger Cars - Mechanical Systems*, 8(1):2015–01–1559, 2015. ISSN 1946-4002. doi: 10.4271/2015-01-1559. URL http://papers.sae.org/2015-01-1559/.

[92] Loh, E. Motor Trend. URL http://www.motortrend.com/.

[93] Piomelli, U. and Chasnov, J. R. Large-eddy simulations theory and applications. In *Turbulence and Transition Modelling*, chapter 7, pages 269–336. Springer, Netherlands, 1996.

[94] Comte, FréDÉRic Ducros, P. and Lesieur, M. Large-eddy simulation of transition to turbulence in a boundary layer developing spatially over a flat plate. *Journal of Fluid Mechanics*, 326, 1996. ISSN 0022-1120. doi: 10.1017/S0022112096008221.

[95] Piomelli, U. Large-eddy simulation : achievements and challenges. 35:335–362, 1999.

[96] Meneveau, C., Lund, T. S., and Cabot, W. H. A Lagrangian dynamic subgrid-scale model of turbulence. *Journal of Fluid Mechanics*, 319(-1):353, 1996. ISSN 0022-1120. doi: 10.1017/S0022112096007379.

[97] Krajnovic, S. LES Investigation of Passive Flow Control Around an Ahmed Body. In *ASME 2013 International Mechanical Engineering Congress and Exposition*, pages 1–12, 2013.

[98] ANSYS. ANSYS Fluent 14.5 User Guide, 2015.

[99] Lilly, D. K. On the application of the eddy viscosity concept in the inertial sub-range of turbulence. *National Centre for Atmospheric Research Manuscript*, 123, 1966.

[100] Lilly, D. K. A Proposed Modification of the Germano-Subgrid-Scale Closure Method. *Physics of Fluids a-Fluid Dynamics*, 4(3): 633–635, 1992. ISSN 08998213. doi: 10.1063/1.858280. URL http://links.isiglobalnet2.com/gateway/Gateway.cgi?GWVersion=2&SrcAuth=mekentosj&SrcApp=Papers&DestLinkType=FullRecord&DestApp=WOS&KeyUT=A1992HE35000018$\delimiter"026E30F$npapers2://publication/uuid/370956C1-0EC3-417A-9983-0380AECBEA57.

[101] Canuto, V. M. and Cheng, Y. Determination of the Smagorinsky–Lilly constant Cs. *Physics of Fluids*, 9(1997):1368, 1997. ISSN 10706631. doi: 10.1063/1.869251. URL `http://link.aip.org/link/PHFLE6/v9/i5/p1368/s1&Agg=doi`.

[102] Krajnovic, S. and Davidson, L. Development of large-eddy simulation for vehicle aerodynamics. In *ASME International Mechanical Engineering Congress and Exposition*, number 1993, pages 1–8, 2002.

[103] Van Doormaal, J. P. and Raithby, G. D. Enhancements of the Simple Method for Predicting Incompressible Fluid Flows. *Numerical Heat Transfer*, 7(2):147–163, 1984. ISSN 0149-5720. doi: 10.1080/01495728408961817.

[104] Leonard, B. P. The ultimate conservative difference scheme applied to unsteady one-dimensional advection. *Comp. Methods Appl. Mech. Eng.*, 88:17–74, 1991.

[105] Krajnovic, S. and Davidson, L. Influence of floor motions in wind tunnels on the aerodynamics of road vehicles. *Journal of Wind Engineering and Industrial Aerodynamics*, 93:677–696, September 2005. ISSN 01676105. doi: 10.1016/j.jweia.2005.05.002. URL `http://linkinghub.elsevier.com/retrieve/pii/S0167610505000450`.

[106] Barber, T. J. and Leonardi, E. Causes for Discrepancy in Ground Effect Analyses. *The Aeronautical Journal*, 106(1066):653–668, 2002.

[107] Strachan, R. K. *The aerodynamic interference effects of side walll proximity on a generic car model*. PhD thesis, Cranfield University, 2010. URL `http://dspace.lib.cranfield.ac.uk/handle/1826/4643`.

[108] Pope, S. B. *Turbulent Flows*. Cambridge University Press, 2000.

[109] Robinson, S. K. Coherent motions in the turbulent boundary layer. *Annual Review of Fluid Mechanics*, 31(23):601–639, 1991. ISSN 00664189. doi: 10.1146/annurev.fluid.23.1.601.

[110] Schlatter, P. and Örlü, R. Assessment of direct numerical simulation data of turbulent boundary layers. *Journal of Fluid Mechanics*, 659:116–126, 2010. ISSN 0022-1120. doi: 10.1017/S0022112010003113.

[111] Na, Y. and Moin, P. Direct numerical simulation of a separated turbulent boundary layer. *Journal of Fluid Mechanics*, 374:379–405, 1998. ISSN 0022-1120. doi: 10.1017/S0022112002002173.

[112] Chapman, D. R. Computational aerodynamics development and outlook. *AIAA Journal*, 17(12):1293–1313, 1979. ISSN 0001-1452. doi: 10.2514/3.61311.

[113] Choi, H. and Moin, P. Grid-point requirements for large eddy simulation : Chapman ' s estimates revisited. Technical Report White 2005, Centre for Turbulence Research, 2011.

[114] Kolář, V. Brief notes on vortex identification. *Proc of the 8th WSEAS Intl Conf on Fluid Mechanics*, pages 23–28, 2011.

[115] Jeong, J. and Hussain, F. On the identification of a vortex. *Journal of Fluid Mechanics*, 285(-1):69, April 2006. ISSN 0022-1120. doi: 10.1017/S0022112095000462. URL `http://www.journals.cambridge.org/abstract_S0022112095000462`.

[116] Haller, G. An objective definition of a vortex. *Journal of Fluid Mechanics*, 525: 1–26, February 2005. ISSN 0022-1120. doi: 10.1017/S0022112004002526. URL `http://www.journals.cambridge.org/abstract_S0022112004002526`.

[117] Hunt, J. C. R., Wray, A. A., and Moin, P. Eddies, Streams and Convergence Zones in Turbulent Flows. In *Centre for Turbulence Research Proceedings of the Summer Program*, pages 193–208, 1988.

[118] Hinton, D. A. and Tatnall, C. R. A Candidate Wake Vortex Strength Definition for Application to the NASA Aircraft Vortex Spacing System (AVOSS). *NASA Technical Memorandum*, (110343), 1997.

[119] Holm, V. *Methods for Vortex Identification*. PhD thesis, Lund University, 2012.

[120] Perry, A. E. and Chong, M. S. A Description of Eddying Motions and Flow Patterns using Critical-Point Concepts. *Annua*, 19:125–155, 1987.

[121] Lienhart, H., Stoots, C., and Becker, S. DGLR Fach Symposium Der AG STAB. Technical report, Stuttgart University, 2000.

[122] Welch, P. D. The use of Fast Fourier Transform for the estimation of power spectra: A method based on time averaging over short, modified periodograms. *IEEE Transactions on Audio and Electroacoustics*, AU-15(2):70–73, 1967.

[123] Kiya, M. and Sasaki, K. Structure of Large-Scale Vortices and Unsteady Reverse Flow in the Reattaching Zone of a Turbulent Separation Bubble. *Journal of Fluid Mechanics*, 154:463–491, 1985.

[124] Maskell, E. A Theory of the Blockage Effects on Bluff Bodies and Stalled Wings in a Closed Wind Tunnel. *Ministry of Aviation, Aeronautical Research Council Reports and Memoranda*, page 27, 1965.

[125] Corioilis, P. G. Sur les equations du mouvement relative des systemes de corps, 1835.

[126] Robins, B. Resistance of the Air and Experiments Relating to Air Resistance. *Philosophical Transactions of the Royal Society*, 47, 1746.

[127] Gelder, T. F., Moore, R. D., Sanz, J. M., and McFarland, E. R. Wind Tunnel Turning Vanes of Modern Design. *NASA Technical Memorandum*, 87416, 1986.

[128] Lindgren, B. and Johansson, A. V. Evaluation of a new wind tunnel with expanding corners. *Experiments in Fluids*, 36(1):197–203, 2004. ISSN 0723-4864. doi: 10.1007/s00348-003-0705-y. URL `http://link.springer.com/10.1007/s00348-003-0705-y`.

[129] Su, Y.-x. Flow Analysis and Design of Three-Dimensional Wind Tunnel Contractions. *AIAA Journal*, 29(11):1912–1920, 1990.

[130] King, L. V. On the convection of heat from small cylinders in a stream of fluid. *Philosophical Transactions of the Royal Society*, 214:373–432, 1914.

[131] Jø rgensen, F. E. How to measure turbulence with hot-wire anemometers - a practical guide. Technical report, 2002.

[132] First Sensor. LDE Series Digital low differential pressure sensors. Technical report, 2014.

[133] Bell, G., Gibbings, D., and Patterson, J. An absolute determination of the Gravitational Acceleration at Sydney, Australia. *Metrologia*, 9:47–61, 1973.

[134] Moffat, R. J. Describing the uncertainties in experimental results. *Experimental Thermal and Fluid Science*, 1(1):3–17, 1988. ISSN 08941777. doi: 10.1016/0894-1777(88)90043-X.

[135] Bender, T. J. The New Lola Cars 50 % Scale Aerodynamic Wind Tunnel. *SAE Technical Paper Series*, 01(3547), 2000.

[136] Walter, J., Bordner, J., Nelson, B., and Boram, A. The Windshear Rolling Road Wind Tunnel. (October 2007):265–288, April 2012. doi: 10.4271/2012-01-0300. URL `http://www.sae.org/technical/papers/2012-01-0300`.

[137] Watkins, S. A Review of the Wind Conditions Experienced by a Moving Vehicle. *SAE Technical Paper Series*, (981182), 1998.

[138] Huang, R. F. and Lin, C. L. Vortex shedding and shear-layer instability of wing at low-Reynolds numbers. *AIAA Journal*, 33(8):1398–1403, 1995. ISSN 0001-1452. doi: 10.2514/3.12561.